SYNTHESIS OF NANO-SCALE OXIDE COMPOUND OF TITANIUM AND VANADIUM APPLIED AS ENERGY STORAGE MATERIALS

CHOKCHAI KAHATTHA

A THESIS SUBMITTED IN PARTIAL FULFILLMENT

OF THE REQUIREMENT FOR THE DEGREE OF

DOCTOR OF PHILOSOPHY IN NANOSCIENCE AND NANOTECHNOLOGY

COLLEGE OF NANOTECHNOLOGY

KING MONGKUT'S INSTITUTE OF TECHNOLOGY LADKRABANG

2014

KMITL-2014-NT-D-001-002

หัวข้อวิทยานิพนธ์	**การสังเคราะห์สารประกอบออกไซด์ของไททาเนียมและวานาเดียมระดับนาโนเพื่อประยุกต์เป็นวัสดุกักเก็บพลังงาน**
นักศึกษา	**นายโชคชัย คหัฏฐา**
รหัสประจำตัว	53670102
ปริญญา	**ปรัชญาดุษฎีบัณฑิต**
สาขาวิชา	**นาโนวิทยาและนาโนเทคโนโลยี**
พ.ศ.	2556
อาจารย์ที่ปรึกษาวิทยานิพนธ์	รศ.ดร.วิษณุ เพชรภา

บทคัดย่อ

วิทยานิพนธ์ฉบับนี้มุ่งเน้นการสังเคราะห์สารประกอบออกไซด์ระดับนาโนของไททาเนียมและวานาเดียมเพื่อประยุกต์ใช้เป็นวัสดุกักเก็บพลังงาน ไททาเนียมไดออกไซด์ที่เจือด้วยวานาเดียมสามารถเตรียมด้วยวิธีการโซโนเคมิคอลและวานาเดียมออกไซด์สามารถเตรียมด้วยวิธีการไฮโดรเทอร์มอล สมบัติทางโครงสร้างของสารประกอบออกไซด์วิเคราะห์ด้วยวิธีการเลี้ยวเบนของรังสีเอ็กซ์ กล้องจุลทรรศน์อิเล็กตรอนแบบเลื่อนกราดและกล้องจุลทรรศน์อิเล็กตรอนแบบส่องกราด สมบัติทางเคมีของสารประกอบวิเคราะห์ด้วยวิธีการรามานสเปกโตรสโกปี ฟูเรียร์ทรานสฟอร์มอินฟราเรดสเปกโตรสโกปีและเอ็กซ์เรย์โฟโตอิมิสชันสเปกโตรสโกปี สมบัติทางแสงของสารประกอบวิเคราะห์ด้วยเครื่องยูวี-วิซิเบิลสเปกโตรมิเตอร์ จากนั้นศึกษาผลกระทบของเวลาในการสั่นด้วยคลื่นเหนือเสียง อุณหภูมิในการเผาและปริมาณการเจือวานาเดียมต่อสมบัติทางกายภาพและทางแสงของไททาเนียมไดออกไซด์ ศึกษาผลกระทบของระยะเวลาที่ใช้ในกระบวนการไฮโดรเทอร์มอล อุณหภูมิที่ใช้ในกระบวนการไฮโดรเทอร์มอลและชนิดของตัวลดทอน(Reductants)ต่อสมบัติทางกายภาพของวานาเดียมออกไซด์ วัสดุประกอบของไททาเนียมไดออกไซด์ที่เจือด้วยวานาเดียมกับวานาเดียมออกไซด์ถูกเตรียมด้วยวิธีการผสมไททาเนียมไดออกไซด์ที่เจือด้วยวานาเดียมและวานาเดียมออกไซด์ด้วยเครื่องกวนแบบแม่เหล็กโดยใช้สารละลายไฮโดรคลอริคและไทรทัลเอ็กซ์ 100 เป็นตัวประสาน ชั้นของวัสดุกักเก็บพลังงานที่เตรียมจากวัสดุประกอบของไททาเนียมไดออกไซด์ที่เจือด้วยวานาเดียมกับวานาเดียมออกไซด์ถูกเตรียมด้วยวิธีการปาดเคลือบลงบนกระจกนำไฟฟ้าทินออกไซด์ที่เจือด้วยฟลูออรีน ผลการทดลองชี้ให้เห็นว่าสามารถสังเคราะห์ไททาเนียมไดออกไซด์ที่มีโครงสร้างแบบอะนาเทสด้วยวิธีการโซโนเคมิคอลโดยไม่ต้องผ่านกระบวนการเผา ผลการทดลองเมื่อผ่านกระบวนการเผาพบว่าไททาเนียมไดออกไซด์เริ่มเกิดการเปลี่ยนโครงสร้างจากอะนาเทสเป็นรูไทล์ที่อุณหภูมิประมาณ 700 องศาเซลเซียส และเกิดการเปลี่ยนแปลงโครงสร้างเป็นรูไทล์อย่างสมบูรณ์เมื่ออุณหภูมิ 800 องศาเซลเซียส จากภาพถ่ายด้วย

กล้องจุลทรรศน์อิเล็กตรอนแบบเลื่อนกราดและส่องกราดพบว่าอนุภาคไททาเนียมไดออกไซด์มีลักษณะกึ่งทรงกลมขนาดเส้นผ่านศูนย์กลางประมาณ 20-30 นาโนเมตร และเกิดการรวมตัวกันของอนุภาคจากระดับนาโนเมตรเป็นระดับไมโครเมตรหลังจากผ่านกระบวนการเผาจากอุณหภูมิ 500 ถึง 1000 องศาเซลเซียส ผลการวิเคราะห์การเลี้ยวเบนของรังสีเอ็กซ์ของไททาเนียมไดออกไซด์ที่เจือด้วยวานาเดียมพบว่าแลตทิสของไททาเนียมไดออกไซด์ถูกเจือด้วยวานาเดียมเนื่องจากขนาดของวานาเดียมไอออน (0.72 อังสตรอม)มีขนาดเล็กกว่าไททาเนียมไอออน (0.75 อังสตรอม) ผลการวิเคราะห์ด้วยเทคนิคยูวี-วิซิเบิลสเปคโตรสโคปีชี้ให้เห็นว่าการเจือด้วยวานาเดียมทำให้อนุภาคนาโนไททาเนียมไดออกไซด์สามารถดูดซับแสงในช่วงวิซิเบิลได้ดีขึ้นและสามารถลดช่องว่างแถบพลังงานต้องห้ามของอนุภาคนาโนไททาเนียมไดออกไซด์ ในขณะที่กระบวนการไฮโดรเทอร์มอลสามารถใช้ในการสังเคราะห์แท่งนาโนวานาเดียมไดออกไซด์ที่มีโครงสร้างแบบโมโนคลินิกได้ ผลการทดลองพบว่าความเป็นผลึกและรูปร่างของวานาเดียมไดออกไซด์ขึ้นกับชนิดของตัวลดทอนที่ใช้ในกระบวนการไฮโดรเทอร์มอล จากภาพถ่ายด้วยกล้องจุลทรรศน์อิเล็กตรอนแบบเลื่อนกราดชี้ให้เห็นว่าวานาเดียมไดออกไซด์มีลักษณะคล้ายแท่ง ใบไม้และแท่งขนาดสั้น ที่มีเส้นผ่านศูนย์กลาง 80-100 นาโนเมตร และมีความยาวประมาณ 2-10 ไมโครเมตร ทำให้ทราบว่ากระบวนการไฮโดรเทอร์มอลสามารถช่วยในการเปลี่ยนเฟสของวานาเดียมเพนทอกไซด์เป็นวานาเดียมไดออกไซด์และลดขนาดของสารตั้งต้นให้อยู่ในระดับ 1 มิติได้ สมบัติการเก็บประจุของวัสดุประกอบไททาเนียมไดออกไซด์ที่เจือด้วยวานาเดียมกับวานาเดียมออกไซด์ภายใต้การฉายแสงอาทิตย์เสมือนมีประสิทธิภาพในการเก็บประจุดีขึ้นเมื่อทำการเปลี่ยนแปลงปริมาณไททาเนียมไดออกไซด์ที่เจือด้วยวานาเดียมออกไซด์เนื่องจากได้รับโฟโตอิเล็กตรอนมากขึ้นจากไททาเนียมไดออกไซด์ที่เจือด้วยวานาเดียมเมื่ออยู่ภายใต้แสงอาทิตย์เสมือน

คำสำคัญ : ไททาเนียมไดออกไซด์ วานาเดียมออกไซด์ กระบวนการโซโนเคมิคอล กระบวนการไฮโดรเทอร์มอล และ วัสดุกักเก็บพลังงาน

Thesis Title	SYNTHESIS OF NANO-SCALE OXIDE COMPOUND OF TITANIUM AND VANADIUM APPLIED AS ENERGY STORAGE MATERIALS
Student	Mr. Chokchai Kahattha
Student ID	53670102
Degree	Doctor of Philosophy
Program	Nanoscience and Nanotechnology
Year	2013
Thesis Advisor	Assoc. Prof. Dr. Wisanu Pecharapa

ABSTRACT

This thesis focuses on the synthesis of nano-scale oxide compound of titanium and vanadium that can be applied as energy storage materials. The V-doped TiO_2 nanoparticles and VO_2 were synthesized using sonochemical and hydrothermal process, respectively. Structural properties of the compound materials were characterized by X-ray diffraction technique, Scanning Electron Microscope and Transmission Electron Microscope. Chemical properties of the nanocomposites were investigated by Raman spectroscopy, Fourier Transform Infrared spectroscopy and X-ray photoemission spectroscopy. Optical properties of the samples were studied using UV-Vis spectrophotometer. The effects of sonication time, calcinations temperature and vanadium doping content on physical and optical properties of TiO_2 were studied. The influence of reaction time, reaction temperature and reducing agent types on the physical properties of VO_2 were investigated. V-doped TiO_2/V_2O_5 nanocomposite was prepared by mixing V-doped TiO_2 with V_2O_5 using hydrochloric solution and Triton-X 100 as the binder. Storage layers were spreaded onto F-doped tin oxide (FTO) substrate using doctor-blade technique. The results revealed that the anatase phase of TiO_2 nanoparticles can be synthesized by sonochemical process without calcinations process. Post calcinations process results indicated that the transformation of anatase to rutile phase initiated at 700 °C and completely transformed into rutile phase initiated at 800 °C. The SEM and TEM images disclose that the precipitated powders from sonochemical-assisted process have a quasi-spherical structure with diameter 20-30 nm and aggregated form nanosize to

microsize after calcinations temperature elevates from 500 °C to 1000 °C. For doping with V elements, the XRD results indicated that V ions can suitably be doped into TiO_2 lattice due to the proper replacement of smaller ionic radius of V^{4+} (0.72 Å) at specific content on some of Ti^{4+} (0.75 Å) sites. UV-Vis spectroscopy results indicated that V doping could extend the visible light absorption and decrease optical band gap of TiO_2 nanoparticles. Meanwhile, the monoclinic structure of VO_2 can be synthesized using hydrothermal process. The crystalline structure and phase of the VO_2 are highly dependent on the reductant types. The SEM images enclose that as-prepared samples possess different morphologies consisted of rod-like, leaf-like and short-rod like with a diameter of 80-100 nm and a length of 2-10 μm. The significant variation of charge storage properties of the nanocomposites under solar irradiation were obtained by varying V-doped TiO_2 content in the composite. Corresponding results suggest that V-doped TiO_2 can generate photoelectrons under solar irradiation, which can effectively assist the storage performance of V_2O_5.

Keywords: Titanium dioxide, Vanadium oxide, Sonochemical process, Hydrothermal process and Energy storage material.

ACKNOWLEDGMENT

This thesis were succesfully completed by supporting of my best advisor, Assoc. Prof. Dr. Wisanu Pecharapa. I would like to thank to him for his great supporting everything in my life and my thesis.

I would like to thank National Nanotechnology Center (NANOTEC), NSTDA, Ministry of Science and Technology, Thailand, through its program of Center of Excellence Network for scholarship and College of Nanotechnology, KMITL for public utility and research fund.

I would like to thank Energy Policy and Planning Office, Ministry of Energy, Thailand, for research funding support.

I would like to thank Rajamangala University of Technology Thanyaburi (RMUTT) for XRD and SEM measurement.

Chokchai Kahattha

CONTENTS

CONTENTS (CONT.)

CONTENTS (CONT.)

LIST OF TABLES

Table **Page**

LIST OF FIGURES

Figure **Page**

LIST OF FIGURES (CONT.)

Figure **Page**

LIST OF FIGURES (CONT.)

Figure **Page**

LIST OF FIGURES (CONT.)

Figure **Page**

LIST OF FIGURES (CONT.)

Figure **Page**

LIST OF FIGURES (CONT.)

Figure **Page**

LIST OF FIGURES (CONT.)

Figure **Page**

LIST OF FIGURES (CONT.)

Figure **Page**

LIST OF FIGURES

Figure **Page**

CHAPTER 1

INTRODUCTION

1.1 Motivation

In the past few decades, nanomaterials have received increasing attentions because of their fascinating properties that can be enhanced when their dimensions are in nanoscale. Numerous nanostructures including nanoparticles, nanosheets, nanotubes, nanowires and nanodotshave been extensively investigated. Among nanomaterials, Vanadium oxide (V_xO_y) has been intensively studied due to its excellent properties for various applications such as sensors, catalysts, magnetic materials, storage material and thermochromic applications [1]. Previously, many methods have been developed to synthesize the V_xO_y nanostructure such as ion beam sputtering, atmospheric chemical vapour deposition, co-precipitation and hydrothermal method [2]. Haihong Yin *et al.*[3] synthesized VO_2 by hydrothermal process and studied field emission properties of the nanostructure. V_2O_5 was selected as source material and oxalic acid as reductant. The results indicated that the nanostructure of this material can be changed by variation of oxalic acid concentration and the nanobundles have the best field emission performance. P. Evans *et al.* [4] reported thermochromic properties of VO_2 thin films prepared by atmospheric chemical vapour deposition and the corresponding results indicated that their transmission spectra in infrared region drastically reduced up to 80% when the films were heated at 65 °C. Graham Armstrong *et al.* [5] reported on lithium intercalation electrochemistry of VO_2 synthesized by hydrothermal process. The results indicated that VO_2 nanowires were obtained after kept in stainless-steel autoclave at 180 °C for 48 h and had a capacity to intercalate lithium of 265 $mAhg^{-1}$ at a rate of 10 mAg^{-1}. M.B. Sahana *et al.* [6] prepared V_2O_5 by spin coating and observed electrochemical properties of the thin films. Metal organic, organic and inorganic were selected as the sol-gel precursors. The results indicated that the Li^+ intercalation capacity and Li^+ diffusion coefficient was increased by an order of magnitude in the non-stoichiometric films. A. Dhayal *et al.* [7] reported on gas sensing properties of V_2O_5 hollow spheres made up of self-assembled nanorods synthesized by solvothermal method and the corresponding results indicated that V_2O_5 nanorods had superior

sensing response against ethanol when compared to that of ammonia. Keng-Che *et al.* [8] gave a report on electrochromic properties of V_2O_5 nanowires using commercial V_2O_5 powder. The deposition of V_2O_5 nanowires were carried out by thermal evaporation onto ITO substrate and the results indicated that V_2O_5 nanowires were obtained after kept in a pressure of 8 x 10^{-4} Torr and 650 °C. The transmittance spectrum change of V_2O_5 nanowires is 37.4% at 415 nm. From literatures, the electrical and optical behaviors of these materials could be improved depending on sample size and morphologies.

To enhance the properties of V_xO_y, the composites with functional materials have been dramatically attended. Among many metal oxide compounds, TiO_2 has been attracted numerous attentions due to its wide band gap about 3.20 eV and excellent response in ultraviolet region. From this ability, TiO_2 can generate photoelectrons under UV irradiation, which can effectively assist the electrochemical performance of V_xO_y. Due to the limitation of its properties such as rather high recombination of photogenerated electron-hole pairs and the weak absorption in visible region, the finding of study examining the doping with various elements such as N, Cu, Ag and Pd could be the promising method for resolve these problems [9]. Among transition metal ions, vanadium (V) is attractively potential candidate as an effective additive into TiO_2 due to the close ionic radius between these two elements. Recently, there have been a number of research works focusing on the effective techniques for synthesizing TiO_2 such as hydrothermal process [10], flame spray pyrolysis [11], co-precipitation process [12] and sonochemical process [13]. Among these techniques, the sonochemical process is well suited for the synthesis of these materials because of its simplicity, low equipment cost, comfort of synthesis and doping.

In this thesis, we focused on the improvement of charge storage properties of V_2O_5 using V-doped TiO_2 nanoparticles in from of functional composite. The effect of photoillumination of V-doped TiO_2/V_2O_5 on photo-electrochemical properties of the products were studied and discussed.

1.2 Objective

This thesis is conducted in order to

1.2.1 Study the synthesis of V-doped TiO_2 via the sonochemical process.

1.2.2 Study the synthesis of VO_2 via the hydrothermal process.

1.2.3 Study the storage properties of V_2O_5 and V-doped TiO_2/V_2O_5 nanocomposite.

1.3 Scope of Thesis

The scope of this thesis is as follows,

1.3.1 Characterize V-doped TiO_2synthesized via the sonochemical process and investigate the effect of sonication time, calcination temperature and vanadium doping content on physical and optical properties of TiO_2.

1.3.2 Characterize VO_2 synthesized via hydrothermal process and study the effects of reaction time, reaction temperature and type of reductant on physical properties of the material.

1.3.3 Prove and analyze the storage properties of V_2O_5 and V-doped TiO_2/V_2O_5 nanocomposite.

1.4 Expected Results

1.4.1 The relevant parameters of the synthesis such as sonication time, calcinations temperature vanadium doping content, reaction time, reaction temperature and type of reductant will be notified.

1.4.2 The meaning of charge storage mechanisms of the materials under optical irradiation will be clearly understood.

1.4.2 The improvement of charge storage properties in the nanocomposite material and the enhancement of the efficiency of device will be clarified.

REFERENCES

[1] Wentao, J., Juan, N., Ke, Y. and Ziqiang, Z. Hydrothermal synthesis and electrochemical characterization of VO_2 (B) with controlled crystal structures, Applied Surface Science 257, 2011, 3253–3258.

[2] Sorapong, P., Yoshikazu, S., Athapol, K., Sommai, P. and Susumu, Y. Synthesis and characterization of vanadium oxides nanorods, Journal of Solid State Chemistry 178, 2005, 2152–2158.

[3] Haihong, Y., Juan, N., Wentao J., Zhengli, Z. and Ke, Y. Synthesis, field emission and humidity sensing characteristics of monoclinic VO_2 nanostructures, Physica E 43, 2011, 1720–1725.

[4] P. Evans, M.E. Pemble, D.W. Sheel and H.M. Yates. Multi-functional self-cleaning thermochromic films by atmospheric pressure chemical vapour deposition, Journal of Photochemistry and Photobiology A: Chemistry 189, 2007, 387–397.

[5] Graham, A., Jesus, C., A. Robert, A. and Peter, G. B. The synthesis and lithium intercalation electrochemistry of VO_2(B) ultra-thin nanowires, Journal of Power Sources 178, 2008, 723–728.

[6] M.B. Sahana., C. Sudakar., C. Thapa.,G.Lawes., V.M. Naik., R.J. Baird., G.W. Auner., R. Naik., and K.R. Padmanabhan. (2007) 'Electrochemical properties of V_2O_5 thin films deposited by spin coating'.*Mat. Sci. Eng. B. Solid.*, vol. 143, pp. 42-50.

[7] A. Dhayal Raj., T. Pazhanivel., P. Suresh Kumar., D. Mangalaraj., D. Nataraj., N. Ponpandian. (2010) 'Self assembled V_2O_5nanorods for gas sensors'. *Curr. Appl. Phys.*, vol. 10, pp. 531-537.

[8] Keng-Che, C., Fu-Rong, C., and Ji-Jung, K. (2006) 'V_2O_5 nanowires as a functional material for electrochromic device'. *Sol. Energ. Mat. Sol. C.*, vol. 90, pp. 1156-1165.

[9] K.S. Rane, R. Mhalsiker, S. Yin, T. Sato, K. Cho, E. Dunbar, P. Biswas, Visible light-sensitive yellow $TiO_{2-x}N_x$ and Fe–N co-doped $Ti_{1-y}Fe_yO_{2-x}N_x$ anatase photocatalysts, J. Solid. State. Chem. 179 (2006) 3033–3044.

[10] S. S. Mali, P. S. Shinde, C.A. Betty, P. N. Bhosale, W. J. Lee, P. S. Patil, Nanocoral architecture of TiO_2 by hydrothermal process: Synthesis and characterization, Appl. Surf. Sci. 257 (2011) 9737– 9746.

[11] K. K. Akurati, A. Vital, J.-Philippe Dellemann, K. Michalow, T. Graule, D. Ferri, A. Baiker, Flame-made WO_3/TiO_2 nanoparticles: Relation between surface acidity, structure and photocatalytic activity, Appl. Catal. B-Environ. 79 (2008) 53–62.

[12] R. Zanella, S. Giorgio, C. H. Shin, C. R. Henry, C. Louis, Characterization and reactivity in CO oxidation of gold nanoparticles supported on TiO_2 prepared by deposition-precipitation with NaOH and urea, J. Catal. 222 (2004) 357–367.

[13] L. G. Reyes, I. H. Perez, L. D. Barriga-Arceo, H. D. Rosales, E. A. Estrada, R. S. Parra, J.J. Cruz-Rivera, Temperature effects during Ostwald ripening on structural and bandgap properties of TiO_2 nanoparticles prepared by sonochemical synthesis, Mat. Sci. Eng. B-Solid.175 (2010) 9–13.

CHAPTER 2

THEORETICAL BACKGROUND AND LITERATURE REVIEWS

The objective of this chapter is to investigate the properties of titanium dioxide, vanadium pentoxide and vanadium dioxide, the meaning of composite, the synthesis techniques and application of energy storage. In this chapter, the relevant theories are explained.

2.1 Nanostructure for high-performance electrochemical capacitor

The excited characteristic weather change, the limited reserves of fuels and energy security concerns, have activated internationally unexpected interest in developing renewable energy technologies from sustainable and renewable energy resources. In fact, there is a rapid increasing in renewable energy productions from solar energy, the most numerous and easily available resources [1,2]. Efficient energy storage systems are critically needed to make the best of the electricity generated from these sources since they can promote the effective using of the power system (generation, transmission and distribution) by storing. Among various energy storage systems, the most prominent is electrochemical energy storage (EES) system, including batteries, electrochemical capacitors (ECs) and fuel cells [3,4]. These three device systems share the ''electrochemical similarities'' and common features that the energy produced processes occur at the phase boundary at the electrode/electrolyte interface. The performance of EES devices has been improved by developing new materials and better understanding of the fundamental electrochemical processes at the interface.

The key parameters to evaluate the performance of EES systems and their potential for applications include energy density (Wh/kg or Wh/L: energy storage per unit weight and volume), power density (W/kg or W/L), specific capacitance (F/g): specific capacity (mAh/g) and cycle life, meanwhile cost and environmental safety [5,6]. To compare the power and energy capabilities, Figure 1 shows the Ragone plot of specific power versus specific energy for the most important EES systems. Fuel cells and batteries are considered to be high-energy systems, while ECs

(supercapacitors) and conventional electrostatic capacitors are considered to be high-power systems. Among these various energy storage systems, batteries and ECs are two significant technological systems that have found a broad range of applications. Typically batteries are designed to take high energy density by storing charge in bulk electrodes (bulk storage) through faradaic reactions and they have been the technology for many applications with all portable electronics on energy stored chemically in them. However, due to physical changes in materials/structures between the charge state and the discharge state, current battery technologies have performance limitations such as short cycle life and slow charge/discharge rates (limited power capability) [7]. In the other hand, ECs are designed to take advantage of near-surface charge storage mechanisms (based on electrochemical doublelayer capacitance or redox pseudocapacitance) to realize much greater power density at some spending of their energy density. Although limited in specific energy, ECs can provide the capability to store and release the energy within time frame of a few seconds compared to tens of minutes or more needed to charge/discharge for batteries. In addition, ECs exhibit better cycle life that is measured in hundreds of thousands to millions of cycles, better than batteries. Moreover, ECs also offer high confidence and better safety versus batteries, leading to a much lower maintenance cost [8,9]. With high power ability, extraordinary cycle life and reliability, ECs have been used in a variety of applications ranging from portable electronics, computer memory backup systems, to hybrid electric vehicles and all-electric vehicles, and to large industrial scale power and energy management [10].

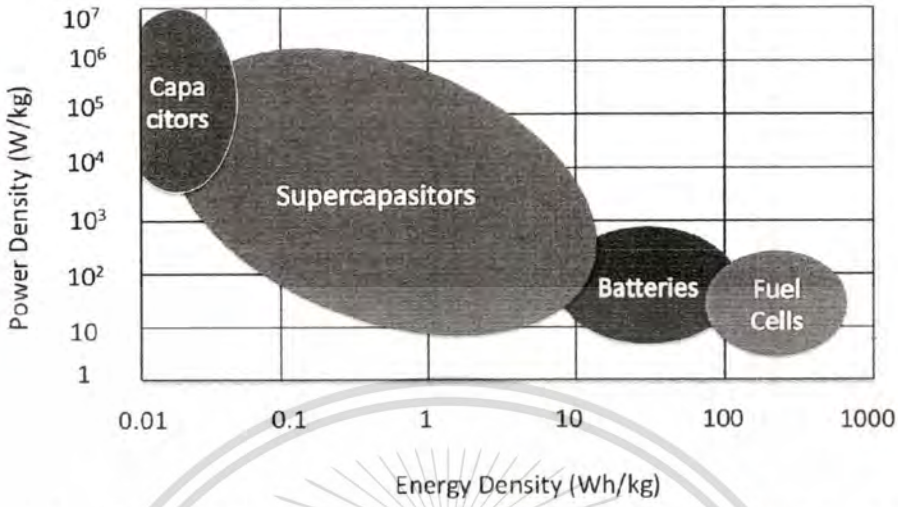

Figure 2.1 Ragone plot of power density versus energy density for various electrochemical energy storage devices [7].

The fast charge/discharge characteristics and long cycle life make ECs especially suitable for recycling energy, leading to the improved energy efficiency. In the past decade, EC technology has interested growth in the increasing of performance to the discovery of new electrode materials, various nanomaterial structures and the design of new hybrid systems that combine faradaic and capacitive electrodes. For enhancement electrical properties, mechanical and surface properties due to confined dimensions of nanostructured materials have been important for electrochemical energy storage [11,12]. The significant advantages include electron and ion transport short path, large surface area between electrode and electrolyte and new reactions not possible in bulk materials.

ECs store charges at the electrochemical interfaces between the high surface area, porous electrode material and the electrolyte. The effective capacitances of ECs are typically several orders of magnitude greater than conventional capacitors because of much larger specific surface area (500–2000 m^2/g for ECs) and shorter distance between the electrode and electrolyte ions (in the order of nanometer, 10^{-9} m).

Depending on the energy storage mechanisms, ECs can be classified into two general categories such as electrochemical double-layer capacitors (EDLCs) and pseudocapacitors (Figure 2.2). EDLCs can be stored charges electrostatically by reversible ion absorption at the electrode/electrolyte interface (Figure 2.2 a). In

contrast, pseudocapacitors use fast and reversible redox reactions at the surface of electroactive materials for charge storage (Figure 2.2 b).

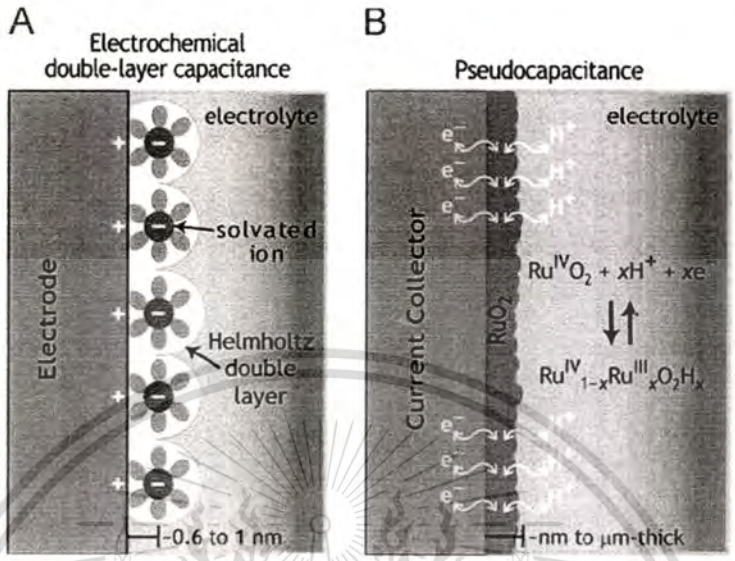

Figure 2.2 Schematic of two different charge storage mechanisms via (A) electrochemical double-layer capacitance (EDLC) or (B) redox reactions based pseudocapacitance [18].

Various techniques are employed to synthesize and modify nanomaterials for enhancement electrode performance. Recently, Yong Zhang and his groups [13] synthesized MnO_2 electrode material for supercapacitors using low temperature solid state reaction dual $KMnO_4$ and $MnCl_4$ as the precursors. The effect of molar ratio between dual precursors on electrochemical properties was investigated. They found that all obtained MnO_2 is α-MnO_2 phase and the molar ratio of 3:2 exhibits the highest specific capacitance at 258.7 Fg^{-1} under charge/discharge rate 100 mAg^{-1}, and the discharge capacitance is 145.9 Fg^{-1} after 200 cycles under rate 300 mAg^{-1} (as shown in Fig. 2.3). They recommended that the specific surface area of this material is significant effected on its capacitance properties.

K. Jeyalakshmi *et al.* deposited Ni-doped β-V_2O_5 thin films by sol-gel spin coating technique using V_2O_5 powder and $Ni(Ac)_2 \cdot 4H_2O$ as the vanadium source and dopant materials, respectively. The results indicated that The film with 5 wt.% of Ni exhibited the maximum specific capacitance of 417 Fg^{-1} at scan rate of 5 mV/s. The possibly phenomenon, is due to the rearrangement of the V_2O_5 structure caused by the

substitution of Ni^{2+} ions and the formation of nanopores, which induced the growth of nanorods [14].

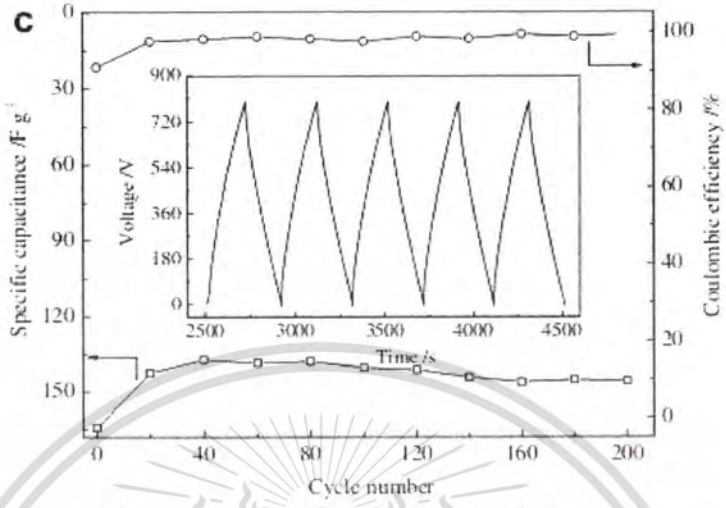

Figure 2.3 Specific capacitance of MnO_2 electrode prepared with a mole ratio 3:2 in 1 M Na_2SO_4 as a function of cyclic number at a constant current of 300 mAg^{-1} [13].

Zhiyong Huang *et al.* synthesized V_6O_{13} by sol-hydrothermal method using commercial bulk V_2O_5 as starting material and octylamine as reductant. Results indicated that hollow flowers-like V_6O_{13} can deliver a capacitance of 417 Fg^{-1} at a scan rate of 5 mVs^{-1}. This value decreases to 400 Fg^{-1} after 1000 cycles in potential range from 0 to 0.8 V versus saturated calomel electrode (SCE) in 1 M $NaNO_3$ aqueous electrolyte at pH of 2. These high performances could be contributed to the large specific surface area of the sample. The special shape of hollow-flowers would promote active material to contact with electrolyte sufficiently and increase the effective availability of active material [15].

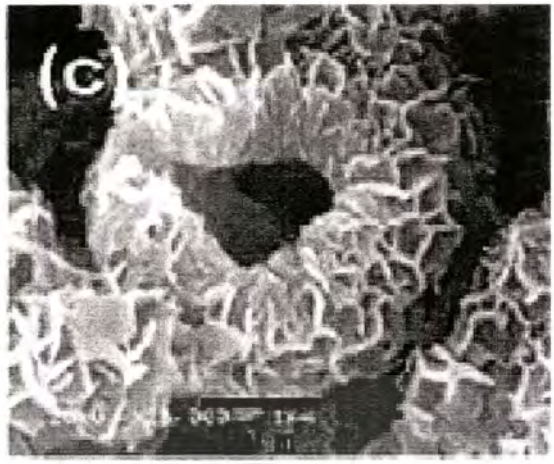

Figure 2.4 SEM images and specific capacitance of hollow flowers-like V_6O_{13} synthesized by sol-hydrothermal method [15].

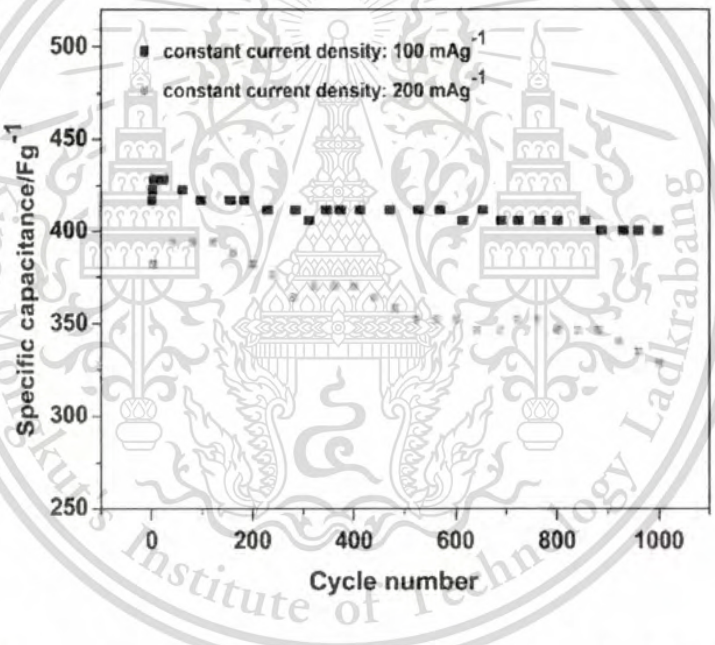

Figure 2.5 SEM images and specific capacitance of hollow flowers-like V_6O_{13} synthesized by sol-hydrothermal method [15].

To take full advantage of EDLC and pseudocapacitance, the hybrid capacitors are fabricated with transition metal oxides as positive electrode materials and activated carbon (AC) as negative electrode material, so the hybrid capacitors deliver high power density as well as acceptable energy density. Therefore, many efforts are made to search for alternative materials. Vanadium oxide is one of the attractive candidates because of its layered structure, high capacity, ease of preparation.

Liying Liang *et al.* fabricated $VO_2(B)$ hybrid with multiwalled carbon nanotubes (MWCNT) is synthesized by sol-gel method assisted with freeze-drying process. The $VO_2(B)$/CNTs composite exhibits far better rate capability and charge storage compared to $VO_2(B)$ electrode which does not contain MWCNT. Particularly, a highest specific capacitance of 250 Fg^{-1} obtained on MWCNT:$VO_2(B)$ is 0.25:1 composite material under 0.5 Ag^{-1} charge–discharge test [16].

Jeliza S. Bonso *et al.* fabricated exfoliated graphite nanoplatelet (xGnP) and V_2O_5 nanotube (VNT) composite electrode by sol-gel technique using commercial XGnP and ammonium metavanadate as the starting materials. Specific capacitance value of 226 Fg^{-1} was measured in 1 M LiTFSI in acetonitrile for the xGnP–VNT composite. Meanwhile, the specific capacitance of bare VNT was 70 Fg^{-1} and bare xGnP was 42.5 Fg^{-1}, demonstrating the helping effect of combining the two materials [17].

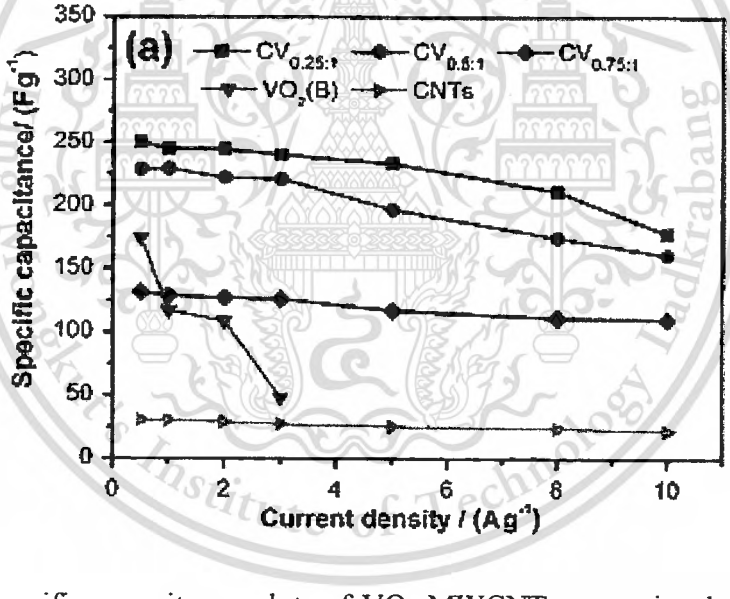

Figure 2.6 Specific capacitance plots of VO_2-MWCNT composites hybrid electrode with different MWCNT content at various current densities [17].

2.2 Supercapacitor parameters

The specific stored energy and the specific power that can be delivered to the load are the crucial characteristics of a super capacitor device along with others, such as its cycling life, self discharge current and efficiency. The double layer capacitance C_{dl} at each electrode interface is given by:

$$C_{dl} = \frac{\varepsilon A}{4\pi t} \quad (2.1)$$

Where ε is the dielectric constant of the electrical double layer region, A is the surface area of the electrode and t is the thickness of the electrical double layer. The specific energy E and specific power P of supercapacitors are calculated according to

$$E = \frac{1}{2}CV^2 \quad (2.2)$$

$$P = \frac{V^2}{4R} \quad (2.3)$$

Where C is the dc capacitance in Farads, V the nominal voltage and R is the equivalent series resistance (ESR) in ohms. The average capacitance C is calculated from C-V plot using the following relation as,

$$C = I(dV/dt) \quad (2.4)$$

Where I is the average current in ampere and dV/dt is the voltage scanning rate. The interfacial capacitance C_i is calculated using the relation,

$$C_i = C/A \quad (2.5)$$

Where A is the area of active material dipped in the electrolyte. The specific capacitance C_{SC} is given by the equation,

$$C_{sc} = C/W \quad (2.6)$$

Where W is the weight of active material on the substrate. The capacitance of a device is largely dependent on the characteristics of the electrode material particularly, the surface area and the pore-size distribution [18]

2.3 Metal oxide based supercapacitor

Literature reviews of supercapacitors show that varieties of metal oxide have been employed. These materials include of RuO_2, MnO_2, NiO, V_2O_5, etc.

2.3.1 Ruthenium Oxide based supercapacitor

Among numerous transition metal oxides, RuO_2 has been attracted great attention using as an electrode materials for supercapacitors due to its advantages of a wide potential window of highly reversible redox reactions, high specific capacitance and long cycle life [19].

In recent years [19] the use of ruthenium oxide as an electrode material was investigated. It was found that hydrous ruthenium oxide film deposited by the galvanostatic method was a promising for electrochemical capacitor with high power density and energy density. A specific capacitance of 276 F/g has been obtained from an amorphous hydrous ruthenium oxide prepared by this method [20].

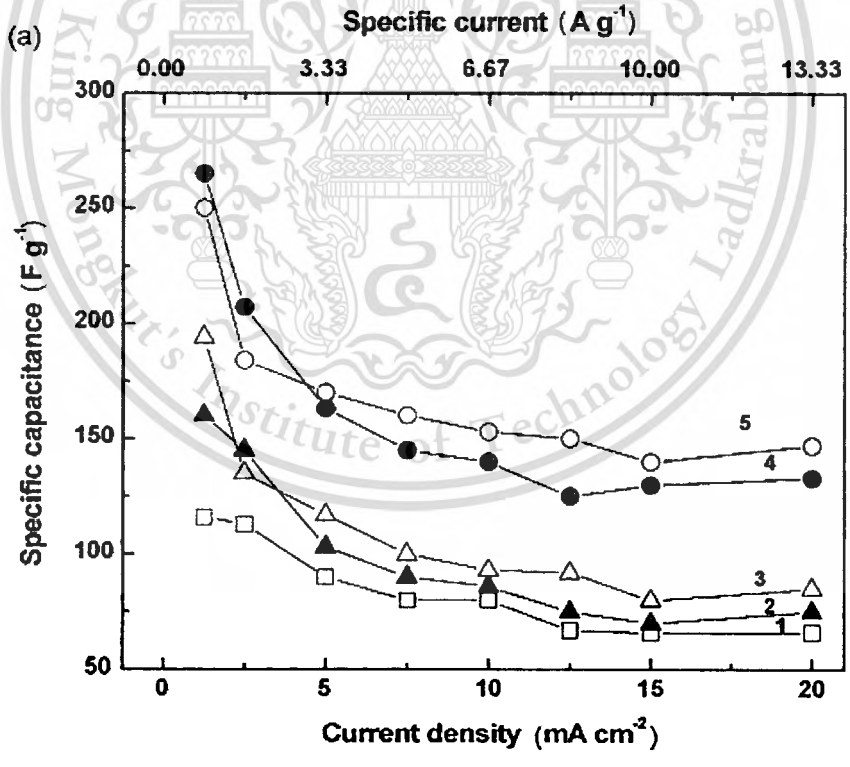

Figure 2.7 Specific capacitance versus charge–discharge current density for RuO_2/Stainless steel electrodes prepared in (a) 0.01 M $RuCl_3$+ 0.1 M HCl electrolyte at (1)15, (2) 20, (3) 25, (4) 30 and (5) 35 mA/cm^2 [20].

In thin film form, T.P. Gujar *et al.* [19] have successfully employed spray deposited ruthenium oxide thin film for electrochemical supercapacitors with specific capacitance of 551 F/g). Fang *et al.* [21] have prepared ruthenium oxide film electrode by organic precursor method and obtained maximum specific capacitance of 593 F/g and interfacial capacitance of 4 F/cm^2. Kim *et al.* [22] have prepared ruthenium oxide film electrode with an average specific capacitance of 863 F/g and good high rate capability by colloidal method. Though the hydrous ruthenium oxide exhibits excellent pseudocapacitive behavior with large specific capacitance and good reversibility, the low abundance and high cost of the precious metal are major limitations to commercial application [23].

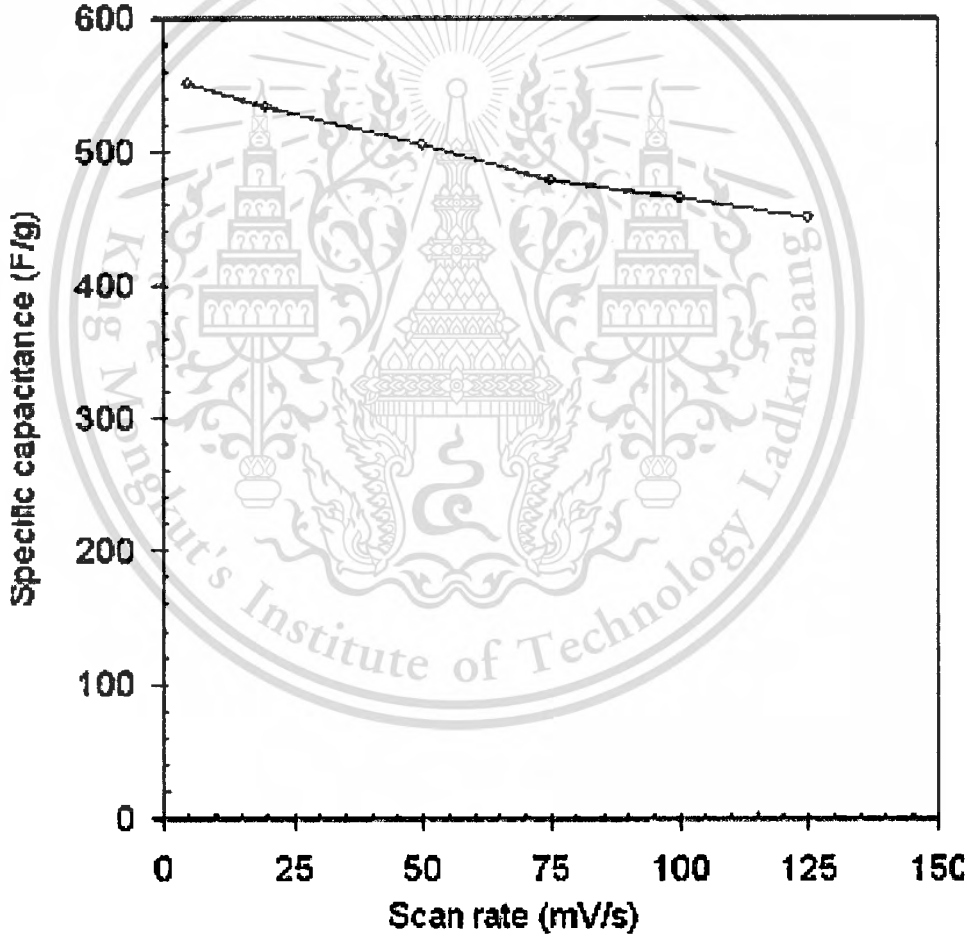

Figure 2.8 Specific capacitance variation of ruthenium oxide electrode at different scan rate with concentration of H_2SO_4 electrolyte was 0.5 M [19].

2.3.2 Manganese Oxide based supercapacitor

Manganese oxide provides a lower cost and lower toxicity replacement for ruthenium oxide in supercapacitor applications. Composite electrodes based on manganese oxide and containing carbon microsphere [24], graphene [25], polyaniline [26] and other conducting materials are under investigation for application in supercapacitors [27]. Manganese oxide thin films have been prepared using various synthesis methods, such as sol-gel [28], electrochemical deposition [29], chemical bath deposition [30] and microwave-hydrothermal method [31].

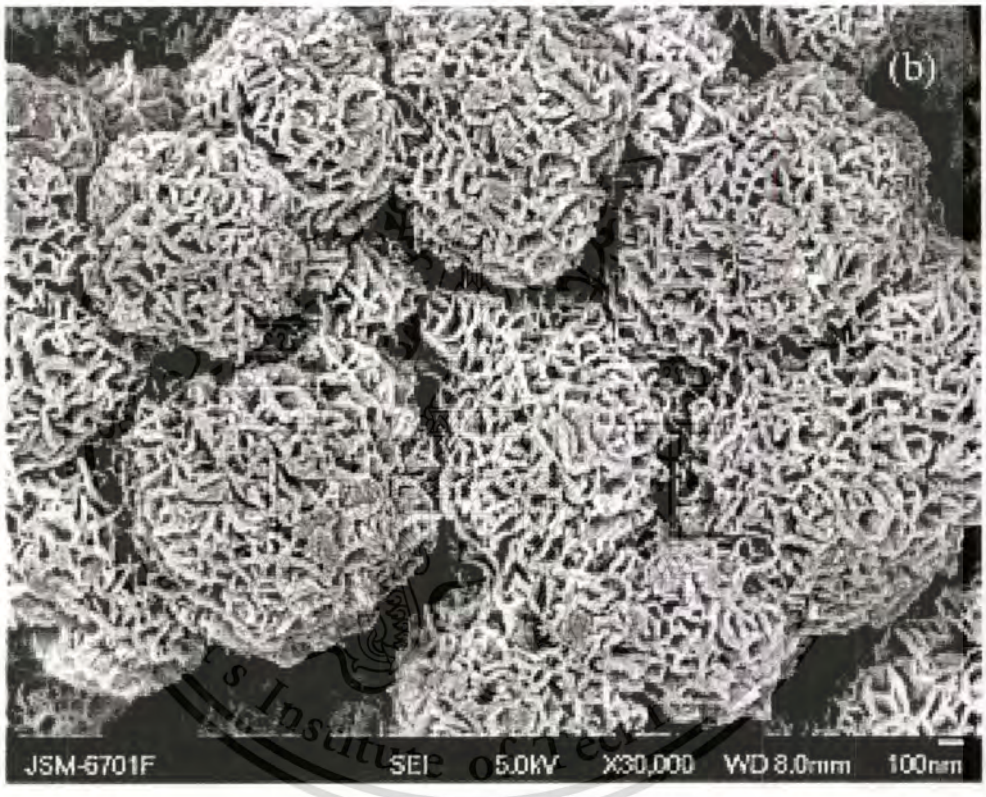

Figure 2.9 SEM images of CMS/MnO_2 composites prepared by hydrothermal method [24].

Jianyun Cao *et al.* have prepared MnO_2 as positive electrode and graphene as negative electrode with high energy density of 25.2 Wh/kg at a power density of 100 W/kg and exhibits capacitance retention of 96% after 500 cycles by reducing $KMnO_4$ in N,N-dimethylformamid (DMF) [32]. Ramchandra S. *et al.* prepared MnO_2 powder with various nanostructures using hydrothermal method. They found that the flakes-shaped MnO_2 exhibits the higher capacitance than other nanostructures with specific capacitance of 455 F/g in $LiPF_6$ electrolyte [33]. Yu Hu *et al.* prepared nanoporous

layered δ-MnO_2 thin film with specific capacitance 447 F/g for flexible supercapacitor using chemical bath deposition method from ethanol and $KMnO_4$ [34].

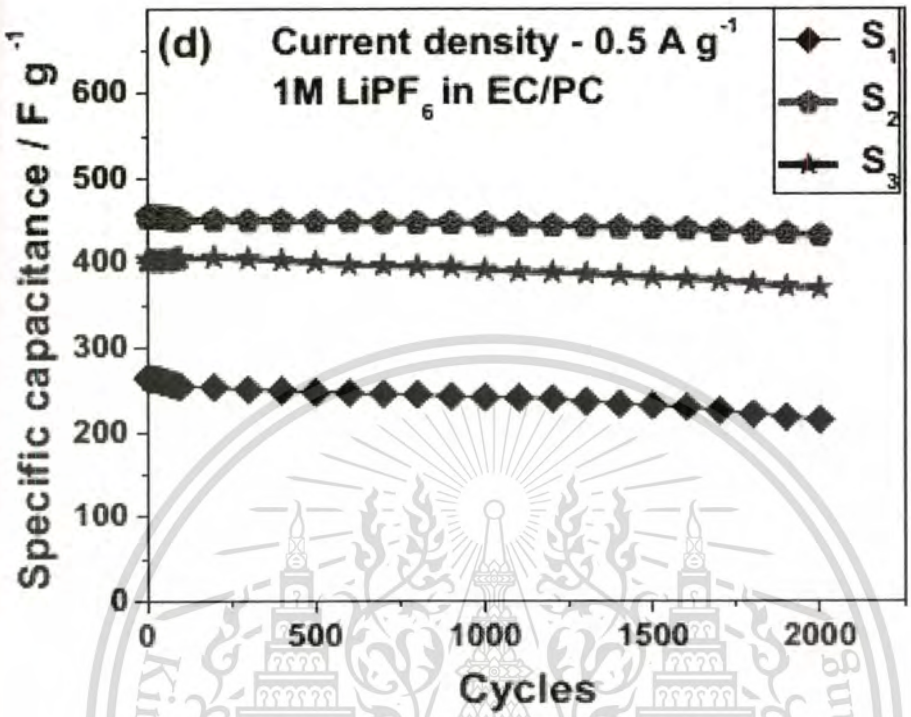

Figure 2.10 Specific capacitance with cycle measured for S1, S2 and S3 electrodes in 1.0 M $LiPF_6$ (EC:DMC) electrolyte [33].

2.3.3 Nickel Oxide based supercapacitor

Nickel oxidefilms have been prepared by hydrothermal method [35], electrospinning process [36], ethanol-water system [37], chemical bath deposition [38] and one-step electrochemical technique [39]. Jianhui Zhu *et al.* prepared nickel oxide nanowall arrays grown on flexible Fe-Co-Ni alloy with specific capacitance of 270 F/g and exhibited cycle lifetime with 93% specific capacitance kept after 4000 cycles [40].

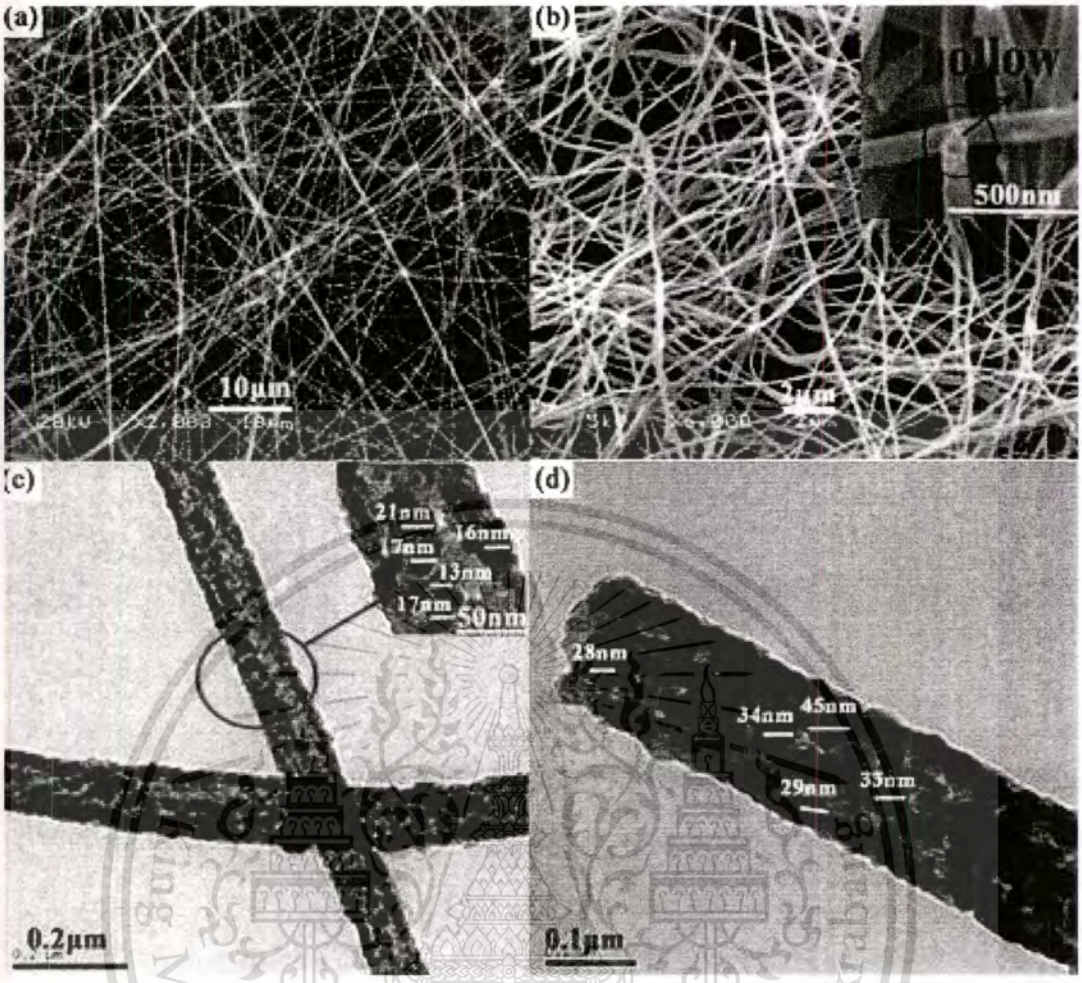

Figure 2.11 (a) SEM image of the as-prepared precursor fibers NiO/CA; (b) SEM image of the as-prepared precursor fibers NiO/CA annealed at 500 °C; (c) TEM image of as-prepared precursor fibers NiO/CA after annealed at 500 °C; (d) TEM image of as-prepared precursor fibers NiO after annealed at 500 °C [36].

Dandan Han *et al.* synthesized hollow core-shell nickel oxide microspheres with specific capacitance 448 F/g by chemical precipitation method using nickel sulfate as a precursor. Zeheng Yang *et al.* synthesized multishelled nickel oxide hollow nanospheres with specific capacitance 612.5 F/g by layer-by-layer self-assembly method [41].

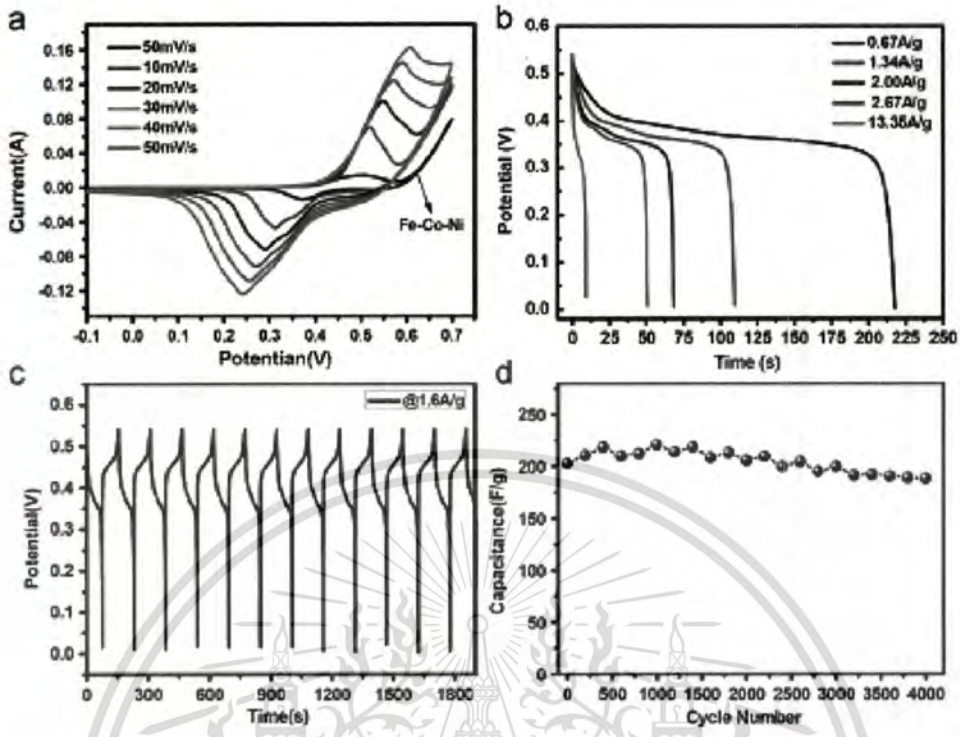

Figure 2.12 CV curves of NiO NWAs grown on alloy at various scanning rates. The black curve is the CV curve of Fe–Co–Ni substrate at the scanning rate of 50 mV/s. (b) Galvanostatic discharge curves of NiO NWAs at various discharge current densities. (c) Galvanostatic charge/discharge tests of NiO NWAs with a current density of 1.6 A/g. (d) Cycling performance [40].

2.3.4 Vanadium Oxide based supercapacitor

Vanadium oxide has attracted a lot of attention as electrode materials for supercapacitor. Wentao Jiang *et al.* [42] synthesized three different VO_2 nanostructures using hydrothermal process with different concentration of oxalic acid at 180 °C and studied the capacitance performance. It was found that the urchin-like VO_2 had the highest lithium ion intercalation and also best capacity retention. The capacity fading of the nanoscaled VO_2 is probably due to the fact that nanosized VO_2 form has large specific surface areas and high surface energies, making it easier to form the agglomerated state during the electric cycling, thus increasing the charge transfer resistance and partial fracture of its shape and structural degradation after the

redox cycles might be another important factor that was studied during the charge–discharge process of other vanadium oxide nanostructure.

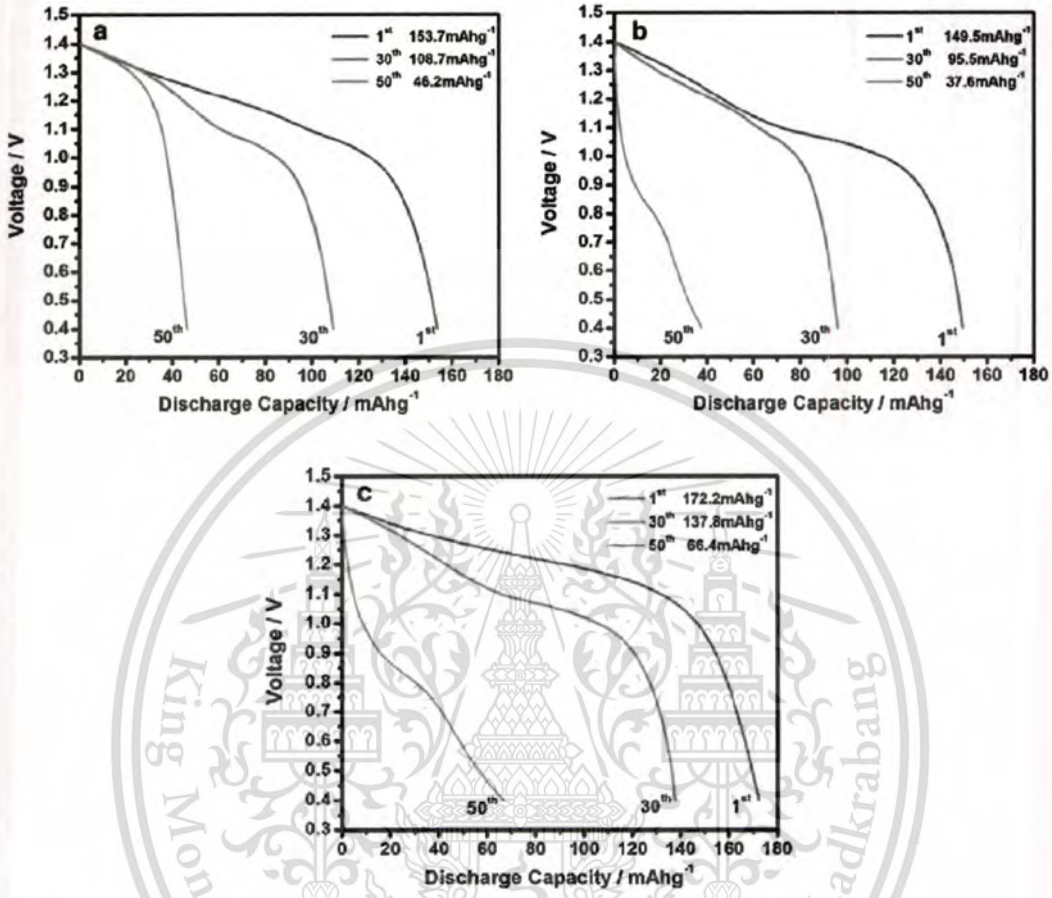

Figure 2.13 Voltage VS discharge capacity cure of the as-prepared VO_2 with different morphologies (a) VO_2 honeycombs, (b) VO_2 nanorods and (c) urchin-like VO_2 [42].

M.B. Sahana *et al.* [43] prepared V_2O_5 by spin coating and observed the crucial electrochemical properties of the thin films. Metalorganic, organic and inorganic were selected as the starting precursors in this process. The results indicated that the Li^+ intercalation capacity and Li^+ diffusion coefficient was increased by an order of magnitude in the non-stoichiometric films.

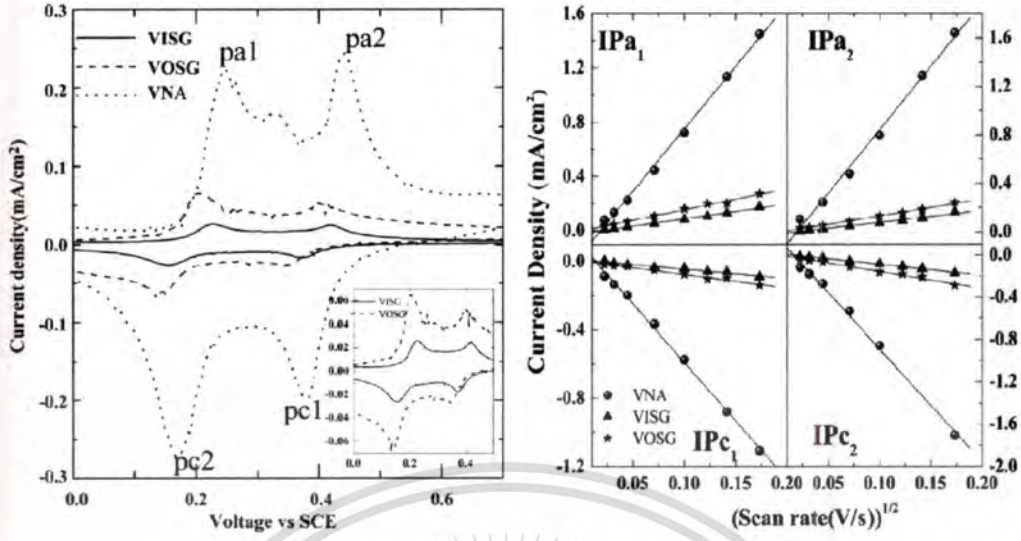

Figure 2.14 Right image, cyclic voltammograms and left image, Randles-Sevčik plot for the two cathodic and anodic of the thin films were deposited by spin coating using metal-organic (VNA), organic (VOSG) and inorganic (VISG) as the precursors [43].

2.4 Titanium dioxide

In 1791, English mineralogist, William Gregor discovered a black sandy substance in his neighborhood in England. He studied this substance and after he was assured that it was a mineral. Four years later, Martin H. Klaproth respected that these mineral combined with a new chemical element and later named it Titanium. He was not able to synthesize the pure titanium. However, the suitable structure and useful material is in the form of titanium oxide (TiO_2) [44]. In 1972, Fujishima and Honda discovered the phenomenon of photocatalytic splitting of water on a TiO_2 electrode under ultraviolet (UV) light [45]. Since then, TiO_2 have attracted much interest to research in the two main areas such as photovoltaics and photocatalysis.

Titanium dioxide with chemical formula TiO_2, also known as titanium (IV) oxide or titania. It is well known that TiO_2 forms three distinct polymorphs such as Rutile, Anatase and Brookite (seen in Fig. 2.15), composed of Ti ions with an octrahedal coordination. The crystalline structures of anatase and rutile phase are tetragonal but brookite phase is orthorhombic structure. In nature, the metastable phase of TiO_2 is anatase phase meanwhile most stable phase rutile can be obtained via the thermal treatment process over 600 °C [46].

The prominent properties of TiO_2 includes wide optical band gap (3.02-3.20 eV), strong ultraviolet absorptivity, non-toxicity, long-term chemical stability, good photocatalysis and high energy conversion efficiency. TiO_2 is utilized in various applications ranging from photocatalyst for organic pollutants degradation in water treatment process, the filler in pigment matrix for enhancement their self-cleaning properties and electron transport layer in optoelectronic device applications such as the working electrode material in solar cell.

Figure 2.15 TiO_6 polyhedra for TiO_2 phase (a) rutile, (b) anatase and (c) brookite, where Ti-white and O-red. The lattice parameter a = b = 4.45937 Å and c = 2.9581 Å for rutile; a = b = 3.7842 Å, c = 9.5146 Å for anatase and a = 9.16 Å, b = 5.43 Å, c = 5.13 Å for brookite [47].

2.4.1 Synthesis of titanium dioxide

In the past decade, many research groups have concentrated on synthesis titanium dioxide nanostructure and studied the properties of these unique nanostructures. Among the unique properties of titanium dioxide nanostructures, the movement of electrons and holes in semiconductor nanostructures is governed by the well-known quantum confinement, and the transport properties related to phonons and photons are largely affected by the size and geometry of the materials [48]. The specific surface area and surface-to-volume ratio increase dramatically as the size of a material decreases. From literatures, numerous techniques have been employed for synthesis titanium dioxide nanostructures.

Chunlan Cao and his groups [49] fabricated TiO_2 nanorod arrays on FTO substrate by hydrothermal technique using titanium butoxide and hydrochloric acid as

the titanium source and reductant, respectively. The diameter, length, and density of the TiO_2 nanorods with rutile phase could be varied by changing the growth parameters, such as time, temperature, and initial reactant concentration (as shown in Fig. 2.16).

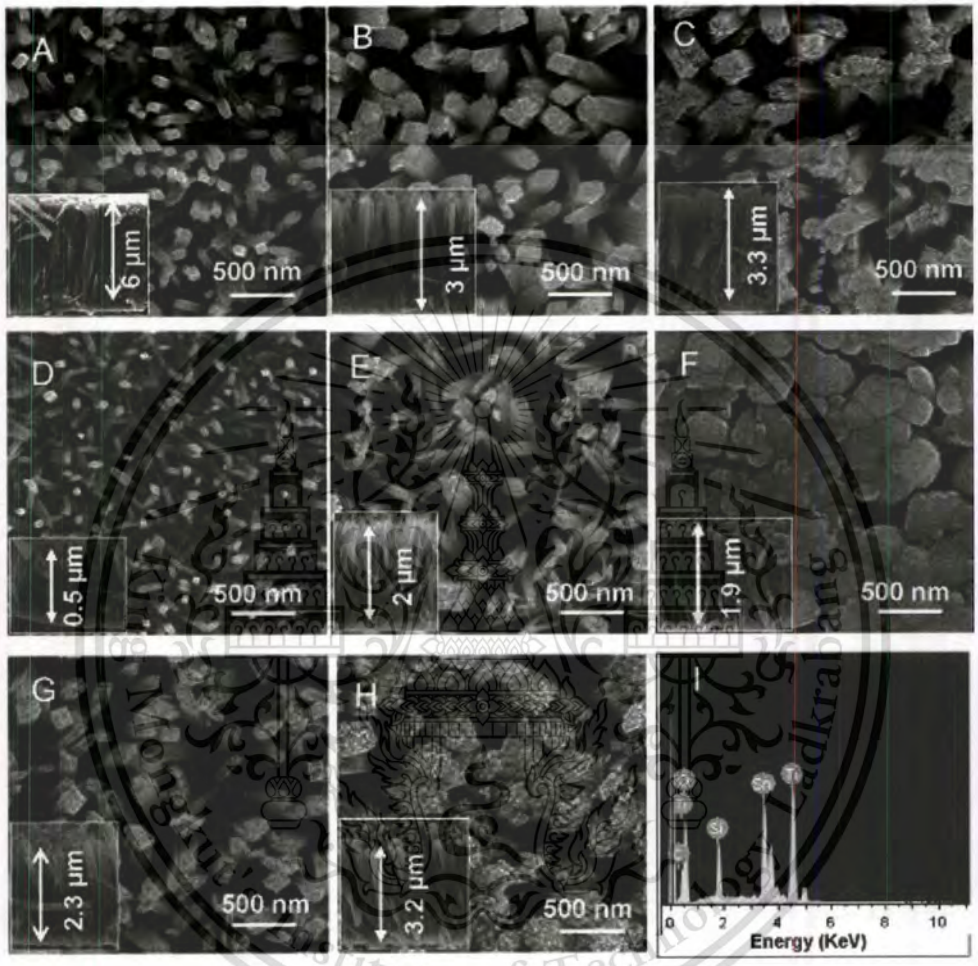

Figure 2.16 FESEM images of the samples, (a) S-a, (b) S-b, (c) S-c, (d) S-d, (e) S-e, (f) S-f, (g) S-g and (h) S-h. (i) The EDS spectra of S-h. The insets are the corresponding cross-sectional views of each sample [49].

Y.F. You *et al.* prepared TiO_2 powder with crystalline sizes of the synthesized TiO_2 powder in the range of 20-65 nm by sol-gel method using Butyl titanate and oxalic acid as Ti source and catalyst, respectively. TiO_2 powder has been synthesized with the sol-gel method from hydrolysis of a titanium precusor. This process normally proceeds via an acid-catalyzed hydrolysis step of titanium(IV) alkoxide followed by condensation. The development of Ti-O-Ti chains is favored with low content of

water, low hydrolysis rates and excess titanium alkoxide in the reaction mixture. Three dimensional polymeric skeletons with close packing result from the development of Ti-O-Ti chains. The formation of $Ti(OH)_4$ is favored with high hydrolysis rates for a medium amount of water. The presence of a large quantity of Ti-OH and insufficient development of three-dimensional polymeric skeletons lead to loosely packed first-order particles. Polymeric Ti-O-Ti chains are developed in the presence of a large excess of water. Closely packed first order particles are yielded via a three-dimensionally developed gel skeleton [50]. The reactions rate is as follow:

$$Ti - OR + H_2O \rightarrow Ti - OH + R - OH \qquad \text{Hydrolysis (2.7)}$$

$$Ti - OH + RO - Ti \rightarrow Ti - O - Ti + R - OH \qquad \text{Alcohol condensation (2.8)}$$

$$Ti - OH + HO - Ti \rightarrow Ti - O - Ti + H_2O \qquad \text{Water condensation (2.9)}$$

S.R. Shirsath and co-worker [51] synthesized TiO_2 nanoparticles by sonochemical process using titanium isopropoxide as the titanium source. They found that, after calcinations process at 450 °C, the anatase phase of TiO_2 was obtained and during ultrasonic irradiation, microjets formed due to the cavitational activity helps to form the resultant inorganic oxide particles with smaller and more uniform particles size. The primary particle size of sonochemically synthesized TiO_2 nanoparticles was in the rage of 10-50 nm (as shown in Fig. 2.17) and the individual particles aggregated to form secondary particles of larger size.

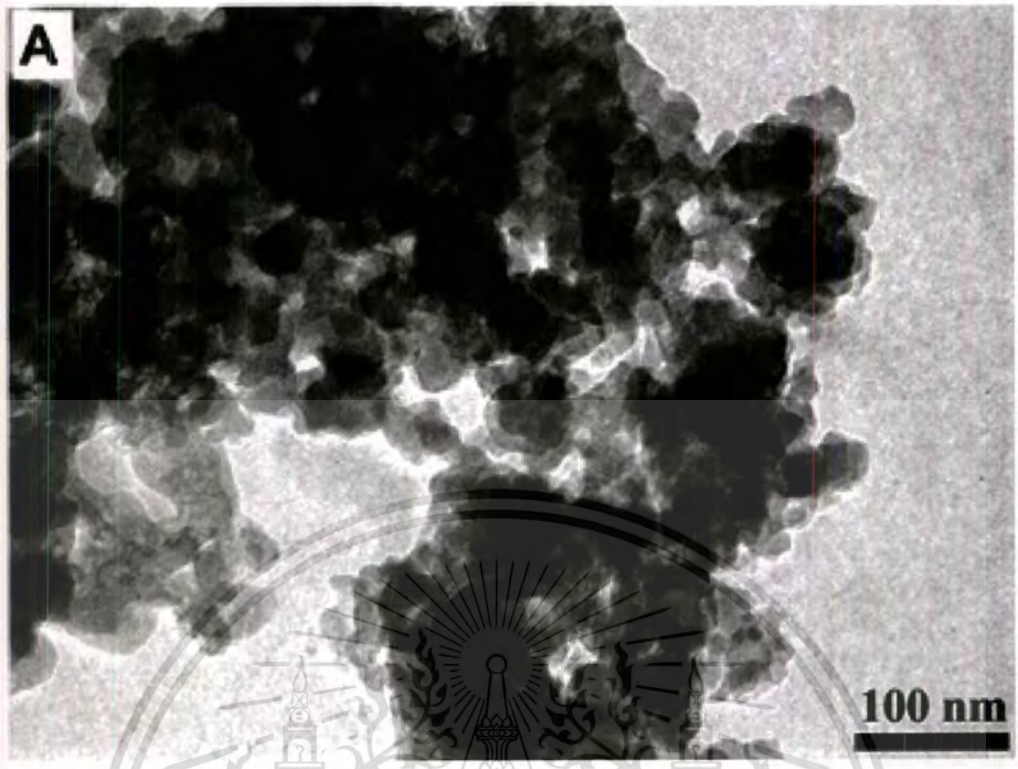

Figure 2.17 Illustrates the transmission electron microscopy (TEM) images of anatase phase TiO_2 nanoparticles synthesized by sonochemical process [51].

2.4.2 Effect of calcinations temperature on physical properties of TiO_2

Qinghua Chen and his group [52] prepared TiO_2 nanobelts by anodization and calcined at different temperature range from 350-750 °C in air. From XRD pattern analysis, a phase transition from anatase to rutile phase coccurred at 650 °C. In addition, the transformation sequence and thermodynamic phase stability between the two titania polymorphs anatase and rutile depend on the initial particle sizes. For equally sized particles, anatase is more thermodynamically stable at particle size < 11 nm, and rutile is more thermodynamically stable at particle size > 35 nm [53].

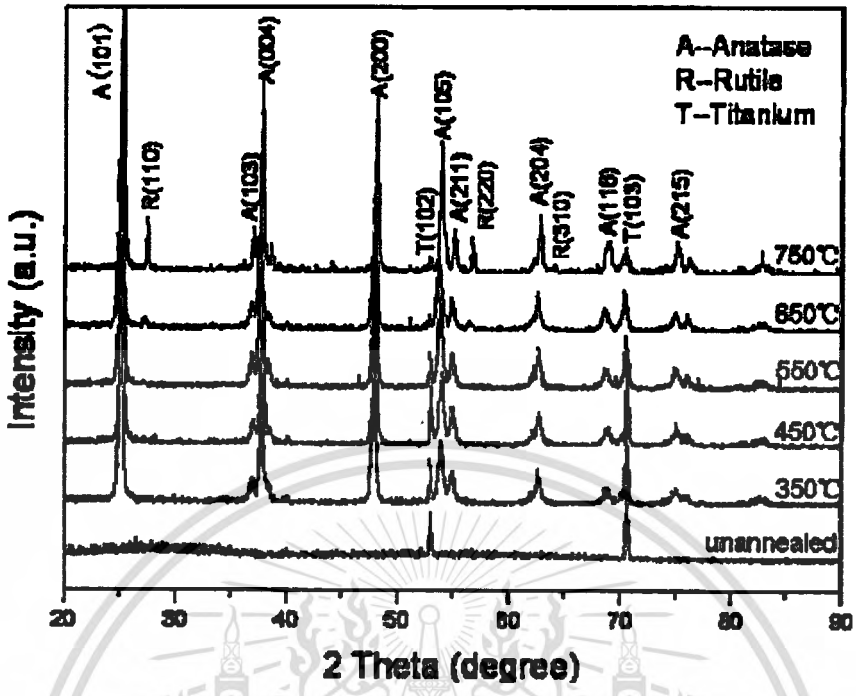

Figure 2.18 XRD patterns of TiO_2 NBs without and with calcination at different temperatures [52].

Phase composition and crystallite size of TiO_2 nanobelts could be calculated from Spurr equation and Scherrer equation as following:

$$F_R = \frac{1}{1+0.8[I_{A(101)}/I_{R(110)}]} \times 100 \quad (2.10)$$

Where F_R is the mass fraction of rutile, $I_{A(101)}$ and $I_{R(110)}$ are the integrated intensities of anatase (101) and rutile (110) peaks, respectively.

$$D = \frac{K\lambda}{\beta cos\theta} \quad (2.11)$$

Where D is average crystalline size, K is the shape factor, λ is the wavelength of Cu Kα radiation (0.15418 nm), β is the full-width at half –maximum (FWHM) of main intensity peak and θ is the diffraction angle peak. The energetics of the two polymorphs are sufficiently close, they can be reversed by small differences in surface energy. Once rutile crystallite is formed, it grows much faster than anatase. Thus, it is reasonable to conclude that under calcination treatment at 650 °C the anatase

crystallites first turn into rutile phase, leading to the decrease of average crystallite size of anatase. Moreover, once the formation of rutile crystallite is excited, crystallite size of rutile increases sharply, which can be confirmed by the results of crystalline rutile grew from 28.02 to 106.33 nm at 750 °C (as shown in Table 1.).

Table 2.1 Phase composition and crystallite size of TiO_2 nanobelts as a function of various calcinations temperature [52].

Calcination temperature (°C)	Phase content (%)		Crystallite size (nm)	
	Anatase	Rutile	Anatase	Rutile
350	100	-	32.12	-
450	100	-	33.51	-
550	100	-	33.78	-
650	95.18	4.82	23.32	28.02
750	88.08	11.92	47.16	106.33

In the other hand, the transition temperature from anatase to rutile phase depends on process condition and materials used in process. Dong Jin Kim *et al.* used hydrochloric acid as a catalyst to prepared titania sols and TiO_2 thin films in the sol-gel process. They found that the transition temperature from anatase to rutile phase is 1000 °C for 1 h in air. While, the transition temperature of TiO_2 thin films were prepared by sol-gel process using diethanolamine (DEA), nitric acid and sulfuric acid as the catalyst started at 500 °C in air that reported by Mehdi Alzamani and his group [54].

2.4.3 Effect of doping with metal on physical and optical properties

Due to the limitation of absorption only in ultraviolet region, the doping with various elements such as Ag, Fe, N, Mo and V [55,56] could be the promising method for effective extension of the optical absorption toward the visible region. Doping with transition elements are attractively potential candidate as an effective additive into TiO_2 due to the close ionic radius between these two elements and the appropriate formation of a trap energy level within the forbidden band gap of TiO_2 induced by proper substitution of Ti by these ions [57].

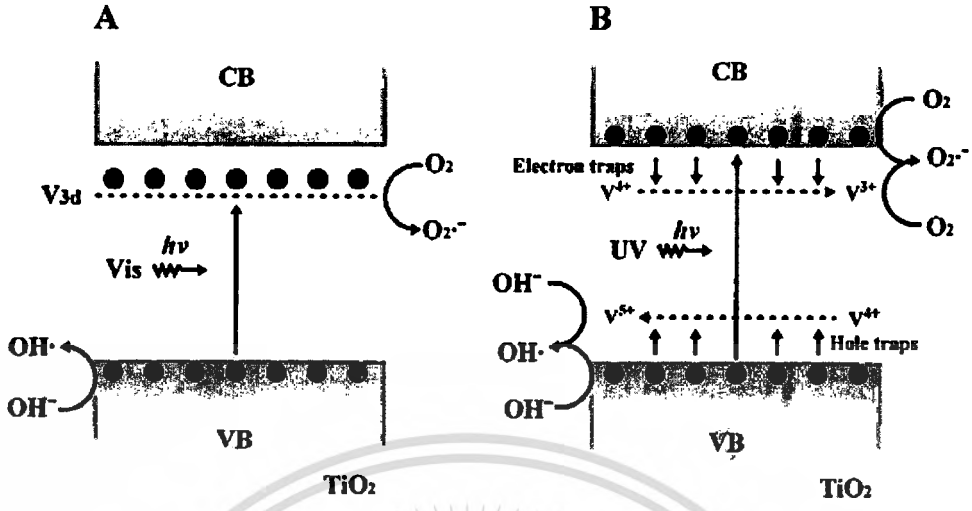

Figure 2.19 The energy band diagram of V-doped TiO_2 nanofiber that purpose by Zhenyi Zhang and his group [57].

Recently, there have been a number of research works focusing on the effective technique for doping with transiton ions into TiO_2. A.H. Ghanbari Niaki *et al.* [58] synthesized Zn-doped TiO_2 thin films with Zn dopant contents 0-10% they found that neither zinc oxide and zinc titanates were detected for Zn-doped TiO_2 thin films due to low concentration of dopant and XRD patterns showed slight shift to lower angle with Zn incorporation since the ionic radius of Zn^{2+} (0.074 nm) is higher than Ti^{4+} (0.061 nm). It indicates that Zn could incorporate into TiO_2 lattice and can be observed that the phase composition of Zn-doped TiO_2 films depends on dopant concentration.

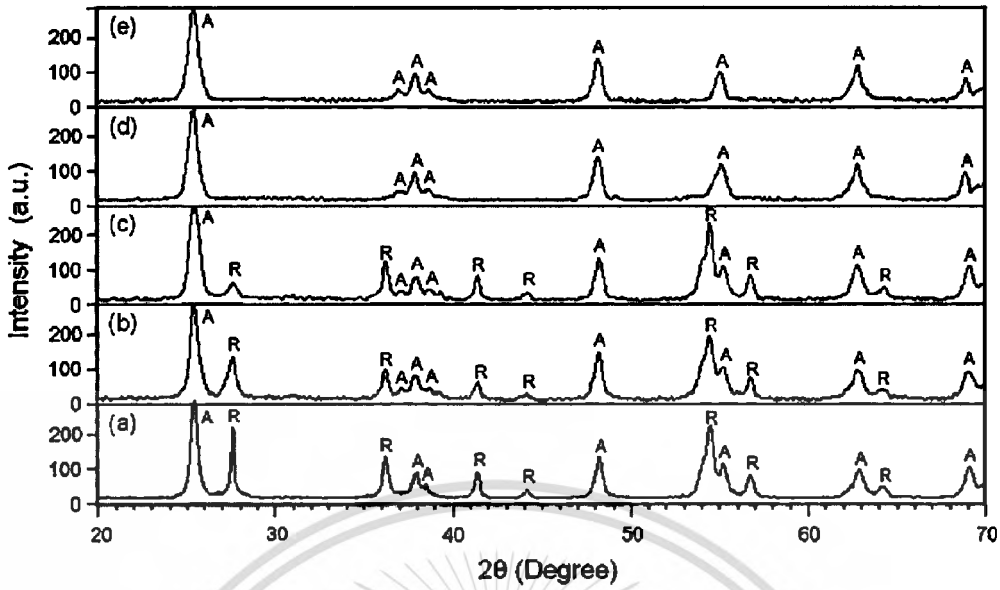

Figure 2.30 XRD patterns of Zn-doped TiO_2 thin films with Zn contents 0-10% (a) 0% (b) 2% (c) 5% (d) 7% and (e) 10% [58].

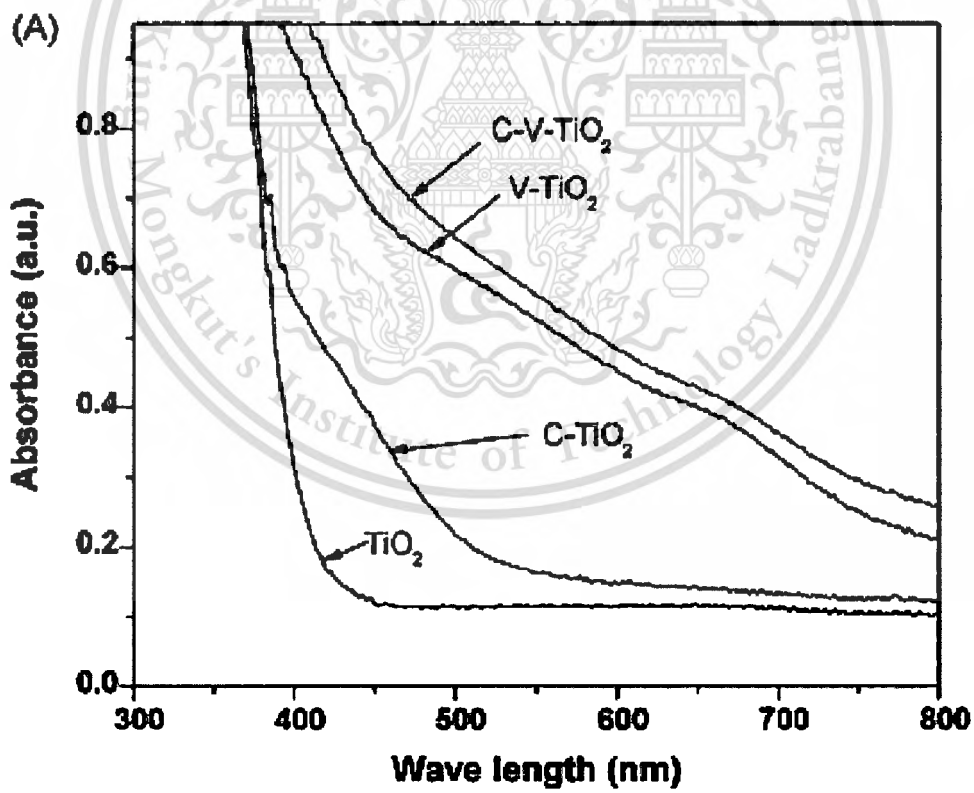

Figure 2.31 UV-Vis diffuse reflectance spectra of bare TiO_2, V-doped TiO_2, C-doped TiO_2 and C-V-doped TiO_2 [59].

X. Yang *et al.* [59] employed sol-gel technique to synthesize C- and V-doped TiO_2 with visible-light enhancement for acetaldehyde degradation. As was demonstrated in Fig. 2.31, C–doped TiO_2 exhibited absorption in visible light region and its absorption edge was around 550 nm, which had a red-shift compared with TiO_2. This phenomenon may be due to that the doped elemental carbon acted as a photosensitizer and caused a significant decrease in the overall energy gap of anatase TiO_2. For V-doped TiO_2 case, the spectra of V–doped TiO_2 showed a red-shift of the band-gap. The absorption enhancement in the visible light region was ascribed to the 3d-orbital of vanadium which may change the band-gap of TiO_2. The visible absorption of TiO_2 doped with metals was caused by the formation of a dopant energy level within the band-gap of TiO_2. For C–V–doped TiO_2 case, owing to the combined effect of carbon species acting as a photosensitizer and vanadium species forming a dopant energy level, the absorption curve of the co-doped TiO_2 extended to 700 nm. This absorption was attributed to the charge transfer between the valence band and the t_{2g} level of vanadium, which lied just below the conduction band. The electronic transitions from the valence band to dopant level or from the dopant level to the conduction band can cause an effectively red-shift of the absorption edge threshold.

2.5 Vanadium oxide

Vanadium dioxide (VO_2) is a traditional binary compound with different polymorphs. The allotropic phases in this system include VO_2(R), VO_2(M), VO_2(B), VO_2(A) and VO_2(C). VO_2 undergoes the evident transition material from a semiconductor to a metal around 70 °C, accompanied by a structural change [60]. Above this temperature, VO_2 exhibits the tetragonal rutile structure with typical lattice constant a = b = 4.55 Å and c = 2.85 Å, which is metallic [61]. Below the transition temperature, VO_2 is monoclinic structure with typical lattice constant a = 12.09 Å, b = 3.702 Å, c = 6.433 Å and β = 106.6°, because of the pairing of V atoms (seen in Fig. 2.32), and this is associated with semiconducting behavior, with a band gap ~0.7 eV. The resistivity of VO_2 in its metallic state is in the range of 2×10^{-4} to 5×10^{-4} $\Omega \cdot cm^3$ and displays a sudden and large increase when cooled below the transition temperature. Changes in electrical properties drive large changes in optical properties between the low- and high-temperature phases; the low-temperature monoclinic structure is somewhat infrared (IR)-transparent, whereas the tetragonal phase is opaque.

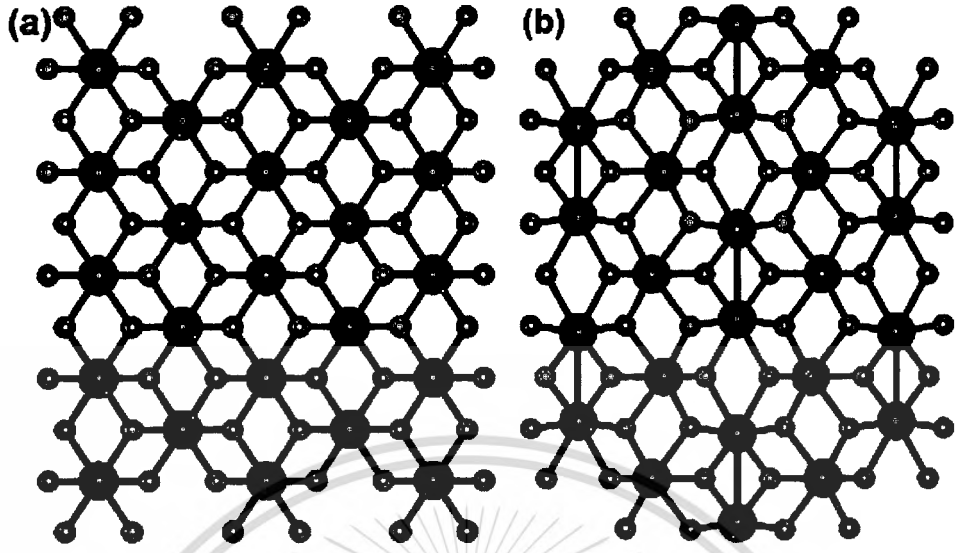

Figure 2.32 Structure of (a) tetragonal rutile form of VO_2 and (b) monoclinic form, showing alternating short (indicated by bonds) and long V-V distances. The large dark spheres are vanadium atoms and the small lighter spheres are oxygen atoms [62].

VO_2 has been considered as a smart material for many applications due to its fascinating structure that can be transformed from a semiconductor to a metal at modurate transition temperature at about 70 °C. Above this transition temperature, it adopts the tetragonal rutile structure and is typically metallic. On contrary, it is in semiconductor behavior with monoclinic structure at below transition temperature. Conversion in electrical properties pushes large changes in optical properties. At lower transition-temperature the monoclinic structure is transparent in infrared region, whereas the tetragonal rutile structure is reflective at higher transition temperature. Because of this interesting property, it has been widely utilized in many applications such as humidity sensor [63], thermochromic window [64] and optical switching devices [65]. More recently, there have been a number of research works focusing on the effective techniques for synthysizing VO_2 such as radio frequency sputtering [66], thermal reduction [67], ion beam sputtering [68], atmospheric pressure chemical vapor deposition [69] and hydrothermal process [70].

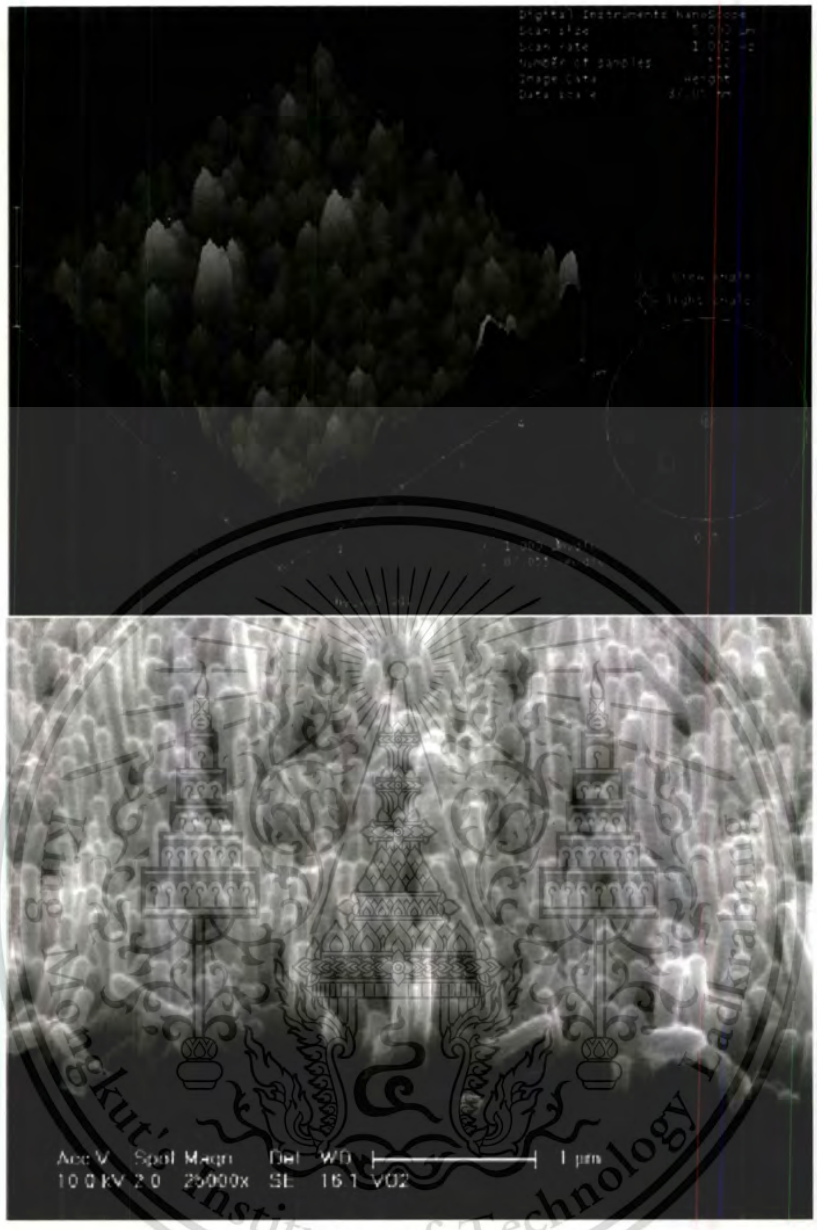

Figure 2.33 AFM and SEM images of VO_2 films were deposited by atmospheric pressure chemical vapor deposition using vanadium tetrachloride as the precursor at 450 °C [69].

Kimson C. Kam *et al.* [71] synthesized VO_2 nanorods via the hydrothermal process using NH_4VO_3 as the vanadium source and investigated the thermochromic properties of as-synthesized nanorods. They found that the thermochromic transition temperature of the VO_2 nanorods was about 10 °C higher compared to bulk VO_2.

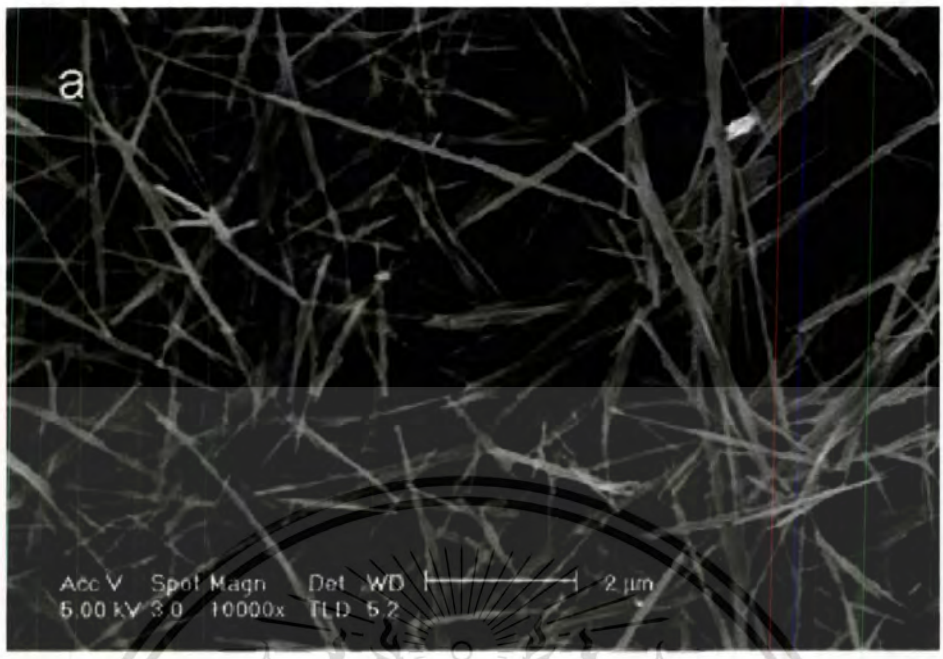

Figure 2.34 SEM images and transmittance in IR regions of VO_2 nanorods were synthesized by hydrothermal method using NH_4VO_3 as the vanadium source at reaction temperature 180 °C for 48 h [71].

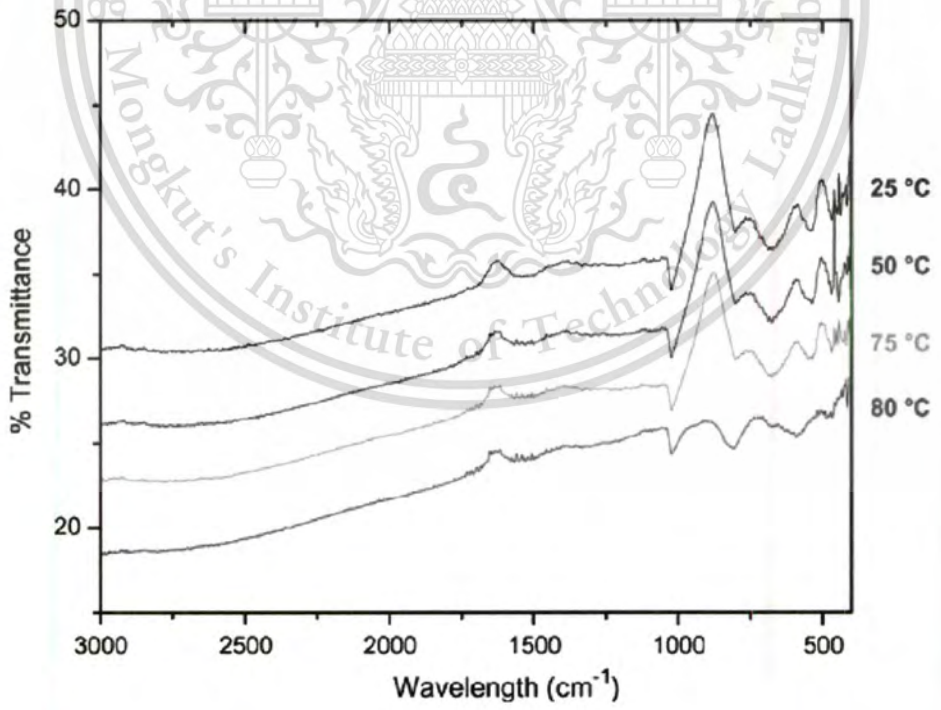

Figure 2.34 SEM images and transmittance in IR regions of VO_2 nanorods were synthesized by hydrothermal method using NH_4VO_3 as the vanadium source at reaction temperature 180 °C for 48 h [71].

2.5.1 Synthesis of vanadium oxide

In the past decade, many research groups have concentrated on synthesis vanadium oxide nanostructures and studied the properties of these unique nanostructures. Among the unique properties of vanadium oxide nanostructures the specific surface area and surface-to-volume ratio increase dramatically as the size of a material decreases. From literatures, numerous techniques have been employed for synthesis vanadium oxide nanostructures. Xueliang Li and co-workers [72] synthesized VO_2 nanorod arrays by hydrothermal technique using V_2O_5 powder and *n*-butanol as a precursor and reducing agent without using template. From XRD results (as shown in Fig. 2.35), they found that with the reaction temperature increasing from 120 to 180 °C the intensity diffraction peak of (110) gradually increase and V_2O_5 has no diffraction peak presented in XRD pattern of the sample with reaction temperature at 180 °C, it is indicated that V_2O_5 gradually was deoxidized into VO_2 with temperature increase. Temperature plays a very important role in the formation of pure crystal and is one of the necessary factors of crystal growth.

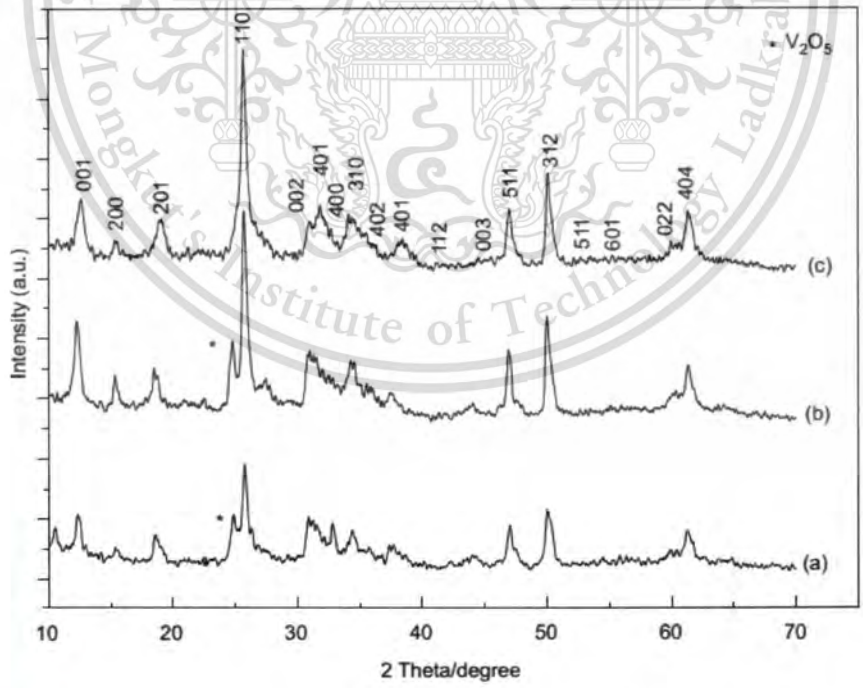

Figure 2.35 XRD patterns of samples obtained at (a) 120 °C, (b) 150 °C and (c) 180 °C for 36 h by hydrothermal method using V_2O_5 powder and *n*-butanol as the precursor and reducing agent, respectively [72].

Based on above experimental results, a possible reaction process demonstrating the synthesis of VO_2 nanorods array can be proposed:

$$V_2O_5 + CH_3\text{-}(CH_2)_3\text{-}OH \rightarrow 2VO_2 + CH_3\text{-}(CH_2)_2\text{-}CHO + H_2O \quad (2.12)$$

$$V_2O_5 + CH_3\text{-}(CH_2)_2\text{-}CHO + 2H_2O \rightarrow 2VO_2H_2O + CH_3\text{-}(CH_2)_2\text{-}COOH \quad (2.13)$$

$$VO_2H_2O \rightarrow VO_2 + H_2O \quad (2.14)$$

It is indicated that both *n*-butanol and temperature played crucial role in forming nanocrystals during the growth process of nanorods. In the mechanism, the ratio of *n*-butanol/H_2O is a very important factor in the reaction. If it is too small, V_2O_5 cannot be fully deoxidized. Meanwhile, function of structure-template of chain of alkyl will weaken. The details were as follows: there were lots of interfaces in suspension due to properties differences of oil/water. It was the interfaces that had led to the orientation of growing of nanorods, and intensified function of structure-template of chain of alkyl. Compared with CH_3–$(CH_2)_2$–COOH, CH_3–$(CH_2)_2$–CHO had less stability and was oxidized into CH_3–$(CH_2)_2$–COOH. Particles of VO_2,VO_2•H_2O, V_2O_5 and ions of VO_2^+ preferentially adhered to the chain of alkyl because of the electrostatic attraction and chemical reactions. Haihong Yin and his group [73] synthesized VO_2 nanostructures via facile hydrothermal process using V_2O_5 and oxalic acid as source material and reductant, respectively. Three nanostructures of nanorods, nanocarambolas and nanobundles were found existing in the obtained samples and a changing of their morphology was found in the synthesis process, during which the proportion of these three types of nanostructures can be adjusted by altering the concentrations of oxalic acid.

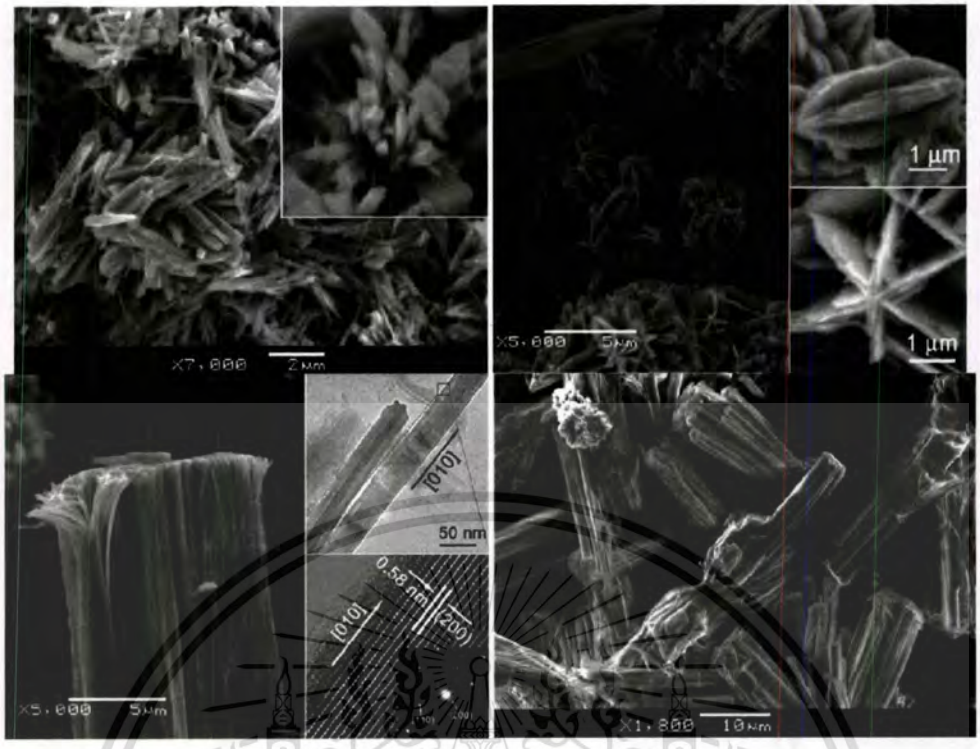

Figure 2.36 SEM images of VO_2 nanostructures via facile hydrothermal process using V_2O_5 as source material with different concentrations of oxalic acid as reductant [73].

A proposed mechanism for the evolution of VO_2 nanowire bundles is presented in Fig. 2.37. With the concentration of oxalic acid increasing, the reaction rate increased, and V_2O_5 were reduced and formed VO^{2+}, then some tiny VO_2 nanowire nucleus formed. And because these nanowires were very close to each other, these nanowires self-assembled into VO_2 nanobundle nucleus. Finally, these VO_2(B) nanobundle nucleuses grew along the axial direction and formed nanobundles.

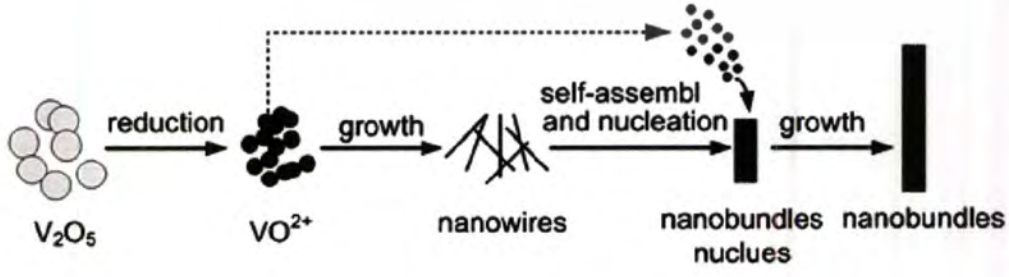

Figure 2.37 Schematic illustration of the growth mechanism of self-assembled VO_2(B) nanowire bundles [73].

2.5.2 Effect of reaction temperature on physical properties of V_xO_y

Shidong Ji *et al.* synthesized VO_2 via hydrothermal process using V_2O_5 as a source material and oxalic acid as a reducing agent with different reaction temperature 180 °C to 270 °C for 24 h. Pure VO_2(A) could be obtained when the hydrothermal treatment temperature was higher than 230 °C, while lower temperature was beneficial for the formation of VO_2(B) phase. In our experiments, pure VO_2(B) could be obtained by hydrothermal treatment at 180 °C. Transformation from VO_2(B) to VO_2(A) could occur during the temperature range from 180 to 230 °C. Besides temperature, system pressure was found to be a very important factor, which has a great influence on the formation of the final polymorphs [74].

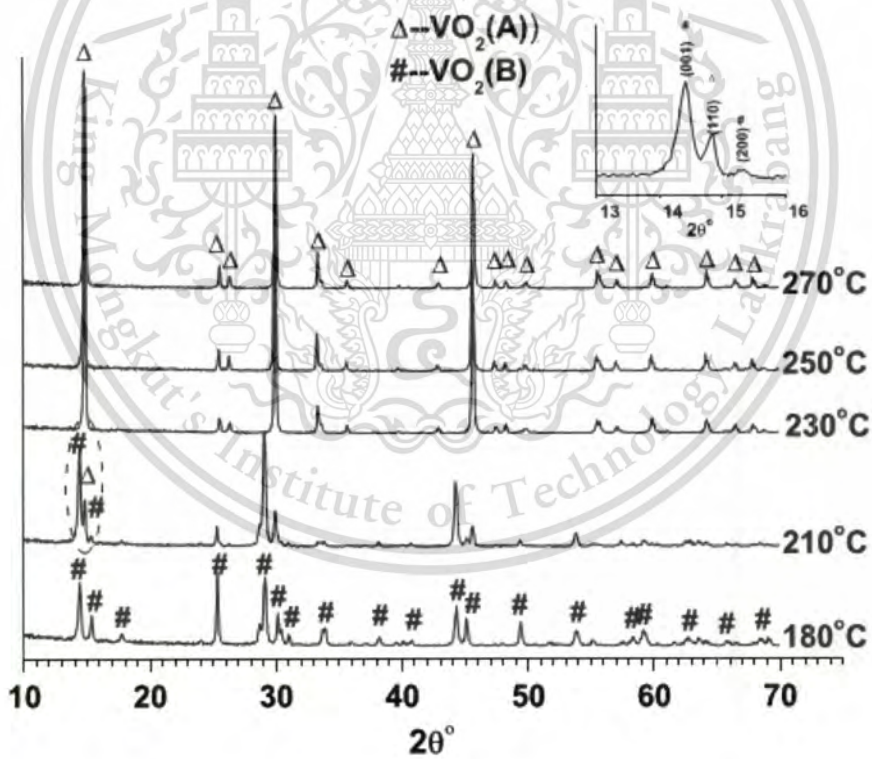

Figure 2.38 XRD pattern of VO_2 have been synthesized by hydrothermal process [74].

X.H. Cheng *et al.* synthesized VO_2 by hydrothermal process via the reduction of V_2O_5 by oxalic acid with difference reaction temperature 180 °C to 250 °C. They

found that monoclinic VO_2(B) nanobelt was always firstly formed and then transformed into tetragonal VO_2(A) nanorods by assembling and following the crystal adjustment as the increase of system temperature [75].

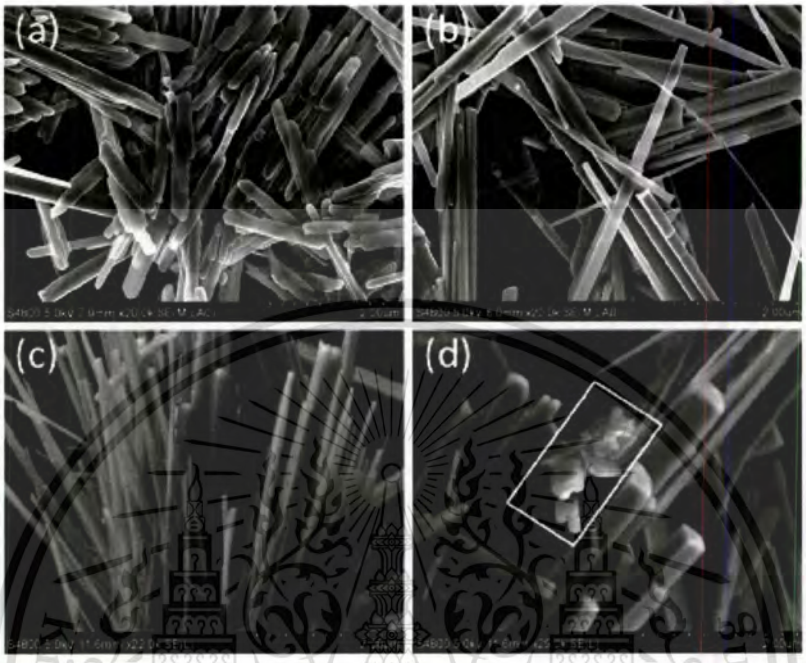

Figure 2.39 SEM image of as-synthesized VO_2 at difference reaction temperature for 24 h (a) 180 °C, (b) 210 °C, (c) 230 °C and (d) 250 °C [75].

2.5.3 Effect of reaction time on physical properties of V_xO_y

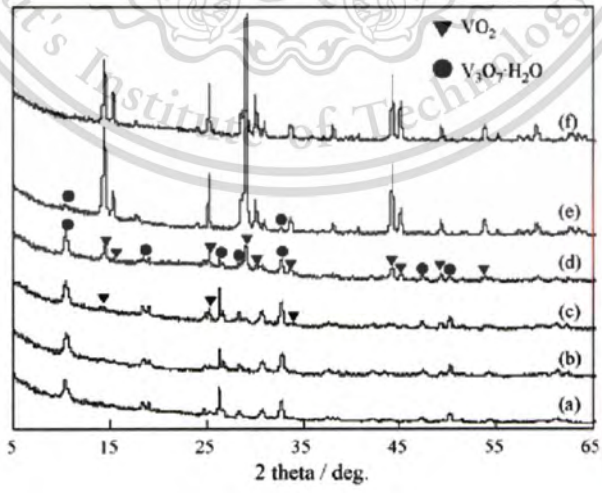

Figure 2.40 XRD patterns of VO_2(B) nanorods by hydrothermal process using dual V_2O_3 and V_2O_5 as a starting material and ethanol as a reductant at 180 °C for (a) 3, (b) 6, (c) 12, (d) 24, (e) 48 and (f) 72 h [76].

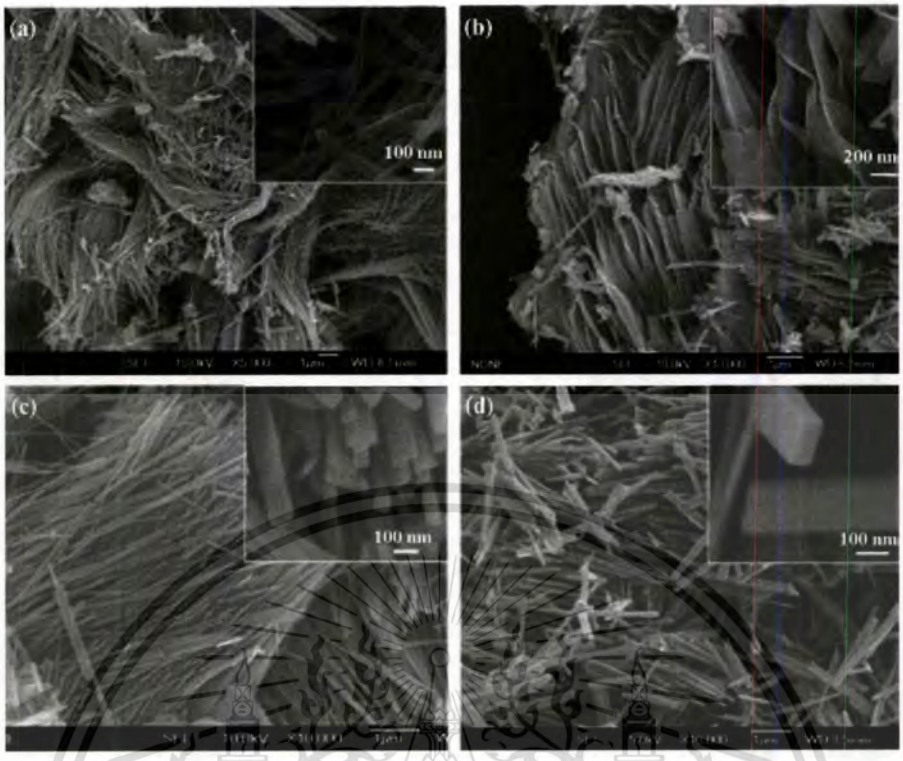

Figure 2.41 XRD patterns of VO_2(B) by hydrothermal process using dual V_2O_3 and V_2O_5 as a starting material and ethanol as a reductant at 180 °C for (a-b) 6, (c) 24 and (d) 72 h [76].

Zhanjun Chen *et al.* synthesized VO_2(B) nanorods by hydrothermal process using dual V_2O_3 and V_2O_5 as a starting material and ethanol as a reductant at 180 °C for 3-72 h. They found that after the reaction time was further increased, the phase of $V_3O_7 \cdot H_2O$ tends to disappear and the pure VO_2(B) was formed. Thus, $V_3O_7 \cdot H_2O$ is an intermediate product for the formation of VO_2(B) [76].

2.5.4 Effect of calcinations temperature on physical properties of V_xO_y

Tina F.-R. Shen *et al.* [77] employed the hydrothermal process for synthesizing VO_2 at different hydrothermal treatment temperatures and different thermal treatment under ambient argon. They found that VO_2 were obtained as hydrothermal treatment temperature was above 160 °C and the thermal treatment was a crucial process to change its structure.

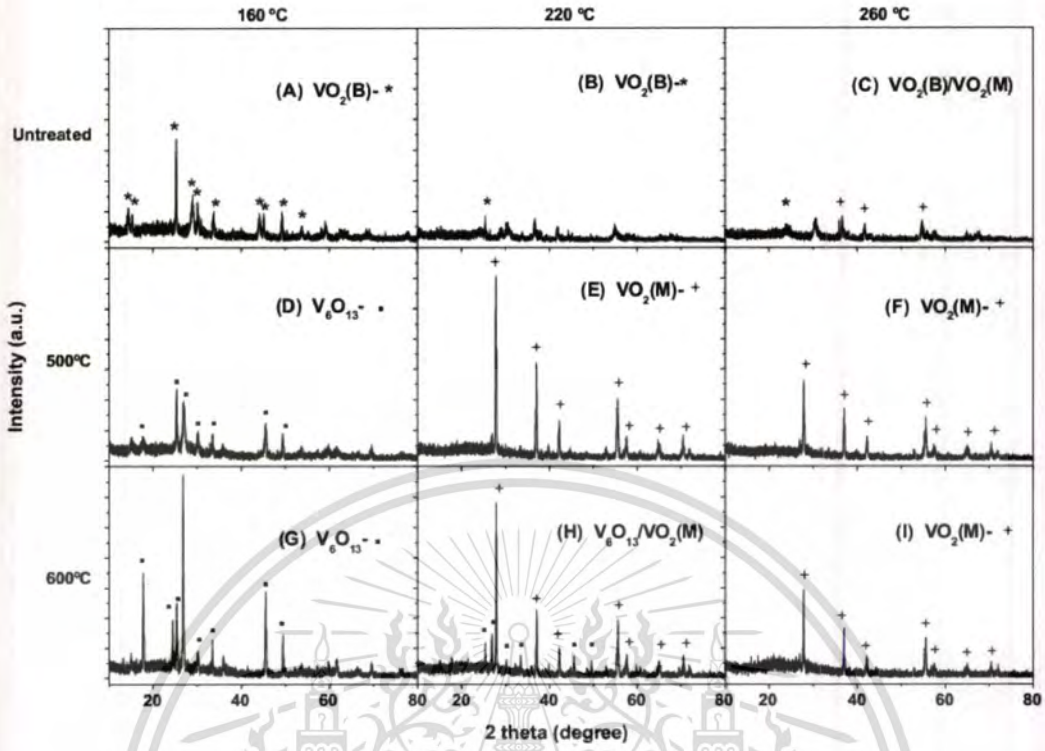

Figure 2.42 XRD patterns of Vanadium oxide were synthesized by hydrothermal method using V_2O_5 as the vanadium source with different reaction temperature (160-260 °C) and different thermal treatment (500-600 °C) under Argon flow for 3 h [77].

David Alie *et al.* synthesized VO_2 via hydrothermal reaction using V_2O_5 powder as the source material and oxalic acid as the reducing agent. Structure studied after heat treatment 40-450 °C in air confirmed that full conversion of VO_2 to V_2O_5 was observed at 450 °C, indicating that the VO_2 phase is thermally stable up to 300 °C [78].

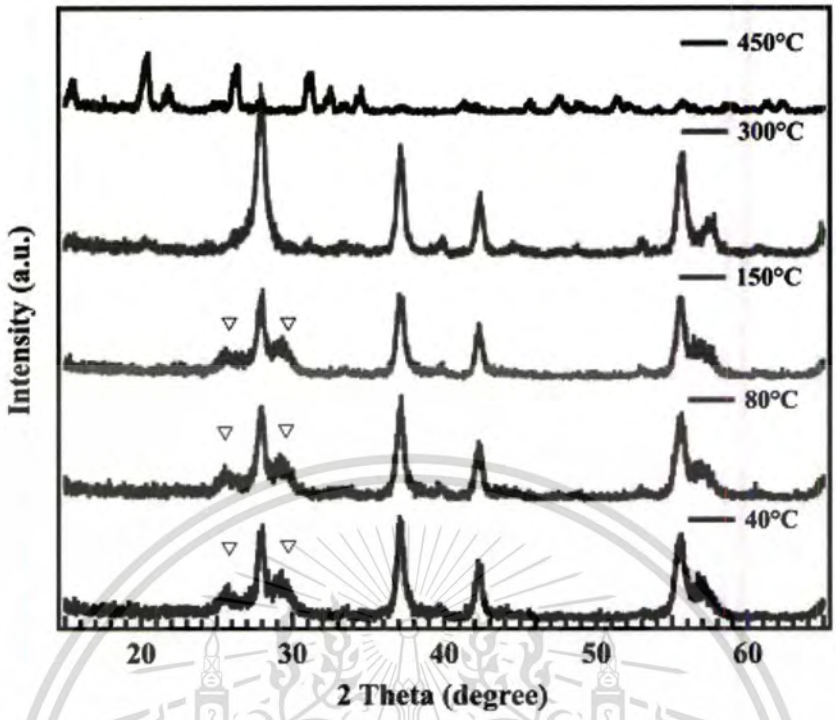

Figure 2.43 XRD data of VO_2 sample heated treatment from 40 °C to 450 °C in air [78].

Sorapong Pavasupree *et al.* purposed the reaction mechanism of V_2O_5 after heat treatment as-synthesized VO_2 at 400 °C for 4 h in air as following:

$$2VO_2 + 1/2O_2 \rightarrow V_2O_5 \quad (2.15)$$

From TGA/DTG results compared with above equation, there is an exothermic peak at around 380-410 °C (DTG data) and weight increase from 86% to 90% (TGA data) caused by the formation of crystallization of V_2O_5 [79].

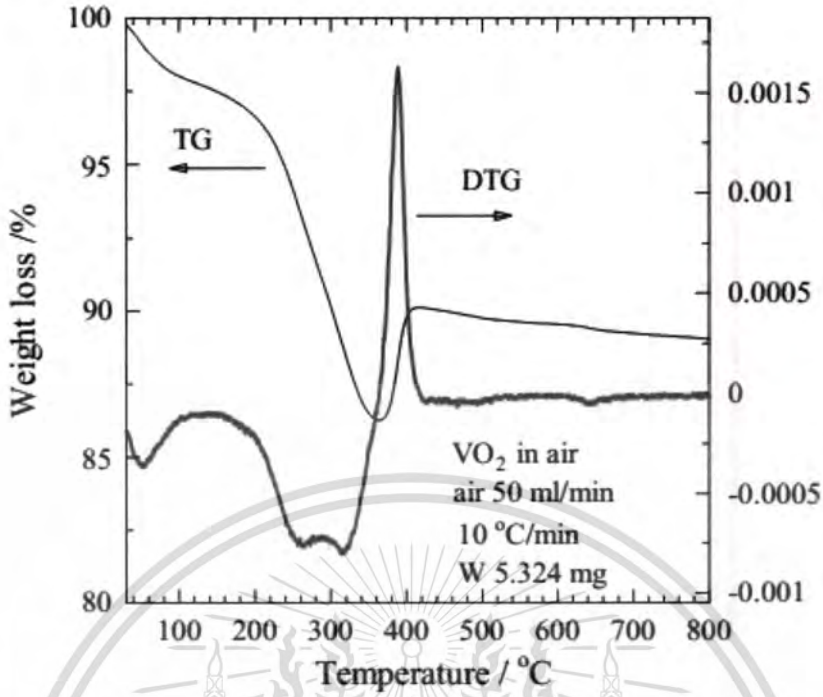

Figure 2.44 TGA/DTG data of the as-synthesized VO_2 [79].

Vanadium pentoxide (V_2O_5) has been intensively studied in the field of nanomaterial due to its excellent and suitable properties for various applications such as sensors, catalysts, cathode materials for batteries and electrochemical applications [80,81]. Previously, many techniques such as sputtering, atmospheric chemical vapor deposition, co-precipitation and hydrothermal method [82,83] have been successfully employed to synthesize functional V_2O_5 nanostructures.

A. Dhayal *et al.* [84] reported on gas sensing properties of V_2O_5 hollow spheres made up of self-assembled nanorods synthesized by solvothermal method and the corresponding results indicated that V_2O_5 nanorods had superior sensing response against ethanol when compared to that of ammonia. They stated that, before allowing the test gas into the sensing chamber, the electrons on the surface of the V_2O_5 nanorods are trapped on the surface by atmospheric oxygen and get released as the test gas is allowed inside the chamber. The reducing gas molecules react with the surface oxygen ions and remove them, releasing the trapped electrons on the surface of the pelletized V_2O_5 nanorods. As a result, the resistance of the sensing element reduces and there by the conductance increases.

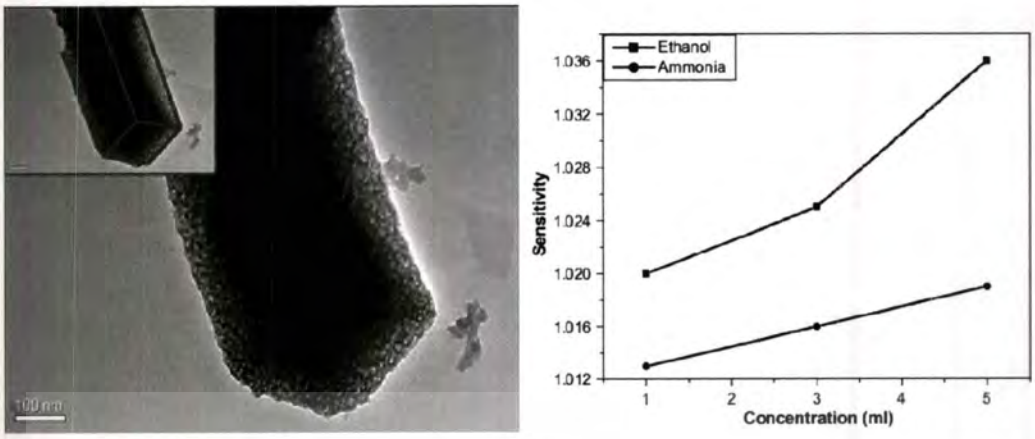

Figure 2.45 TEM image of V_2O_5 nanorod synthesized by solvothermal treatment using ammonium metavanadate and ethylene glycon as precursors (a) and (b) the ethanol and ammonia concentration as a function of sensitivity using V_2O_5 nanorods [84].

Keng-Che *et al.* [85] gave a report on electrochromic properties of V_2O_5 nanowires derived from commercial V_2O_5 powder. The deposition of V_2O_5 nanowires were carried out by thermal evaporation onto ITO substrate and the results indicated that V_2O_5 nanowires were obtained after kept in a pressure of 8×10^{-4} Torr and 300 °C. The transmittance spectrum change of V_2O_5 nanowires is 37.4% at 415 nm. The higher electrochromic efficiencies of V_2O_5 nanowires are expected as the intercalation/deintercalation of Li^+ between the V_2O_5 nanowires layers in the electrode can be explained by the following redox reaction:

$$V_2O_5 + xLi^+ + xe^- \leftrightarrow Li_xV_2O_5 \quad (2.16)$$

$$V^{5+} \text{ (Beige-yellow)} + e^- \leftrightarrow V^{4+} \text{ (Brownish violet)} \quad (2.17)$$

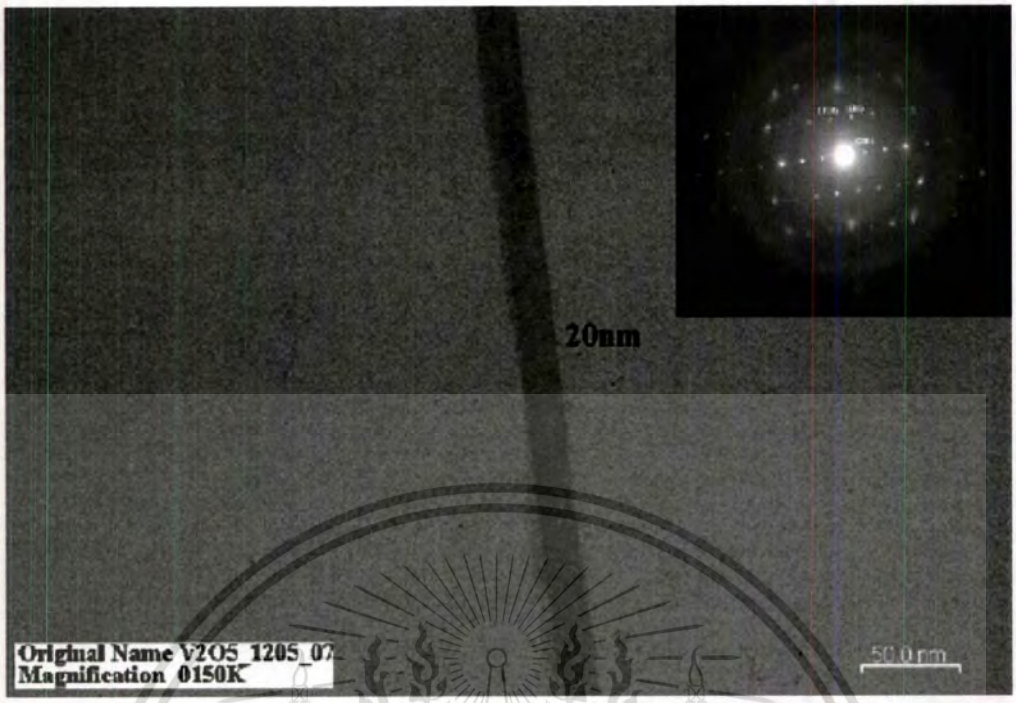

Figure 2.46 TEM image and colored-bleached stage of V_2O_5 nanowires were deposited by thermal evaporation onto ITO substrate [85].

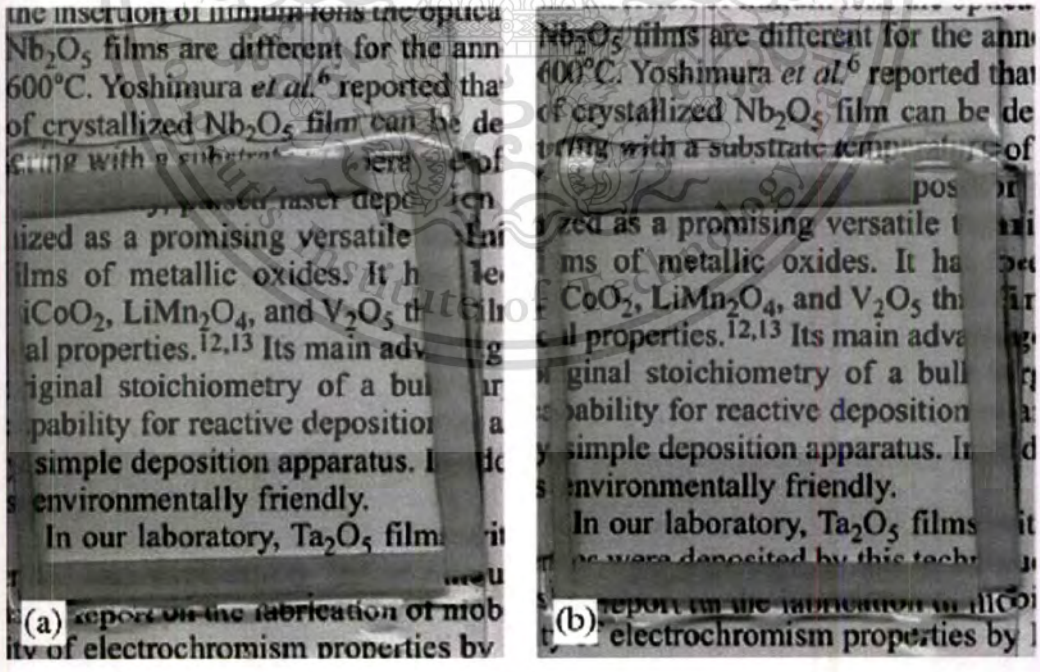

Figure 2.47 The V_2O_5 nanowires electrochemical device (a) colored state and (b) bleached state [85].

2.6 Composite and Nanocomposite

Composite is the combinations of two or more materials in microstructure that are non-soluble in each other. The main material is called matrix and the adding material for enhancing matrix properties that is the most of reinforcing material is called guest phase. The matrix materials are a continuous and homogenous structure meanwhile the guest phase material may be in form of particles, flakes and fibers. The materials in composite form are more effective their performances than traditional form, for example, the enhancement of the strong property of concrete by the reinforcement with steel and the increase of efficiency in epoxy by the reinforcement with graphite fibers. Composite forms are classified in 3 types by the reinforcement material; particle, platelets and fibrous materials. The structures of these composites are shown in Fig. 2.48.

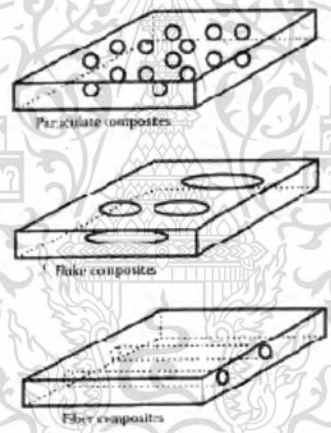

Figure 2.48 Types of composites based on reinforcement shape.

- Particulate composites

Particulate composites are the guest particles that randomly immersed in matrix phase such as alloys and ceramic. The advantages of particulate composites are improved strength, increased operating temperature and oxidation resistance. The examples of this composite type include aluminum particles in rubber, silicon carbide particles in aluminum, gravel, sand and cement to make concrete.

- Flake composites

Flake composites are the flat reinforcements in matrix phase. The advantages of flake composites are high out-of-plane flexural modulus, high strength, and low

cost. However, the efficiency of flake composites is limited by the difficult orientation in the matrix and a few materials for the guest materials.

• Fibrous composites

Fibrous composites are the reinforcement in form of short or long fiber mixed in matrix phase. The examples of fibrous reinforcement are carbon and aramides. The types of matrices include polymer (epoxy), metal (aluminum), ceramic (calcium-alumino silicate) and carbon.

Nanocomposites consist of materials in the range of nanometers (10^{-9} m) that scale agreement in nanometer range is less than 100 nm. The properties of materials in nanoscale show excellent performance different from bulk materials, for example the improvement of elastic modulus, transmission rate for water vapor and the decrease of toughness and impact strength.

Min Young Song *et al.* prepared V_2O_5/TiO_2 nanoparticles onto glass beads by chemical vaper deposition. From XRD results, they found that the nanocomposites consisted of dual diffraction peaks of TiO_2 and V_2O_5 [86]. Yuan Wang *et al.* [87] prepared TiO_2/V_2O_5 nanoheterostructures via electrospinning technique. The samples exhibited the characteristic diffraction peaks of rutile phase of TiO_2 and orthorhombic V_2O_5. This result indicates that rutile TiO_2 and orthorhombic V_2O_5 are all observed in the TiO_2/V_2O_5 nanoheterostructures.

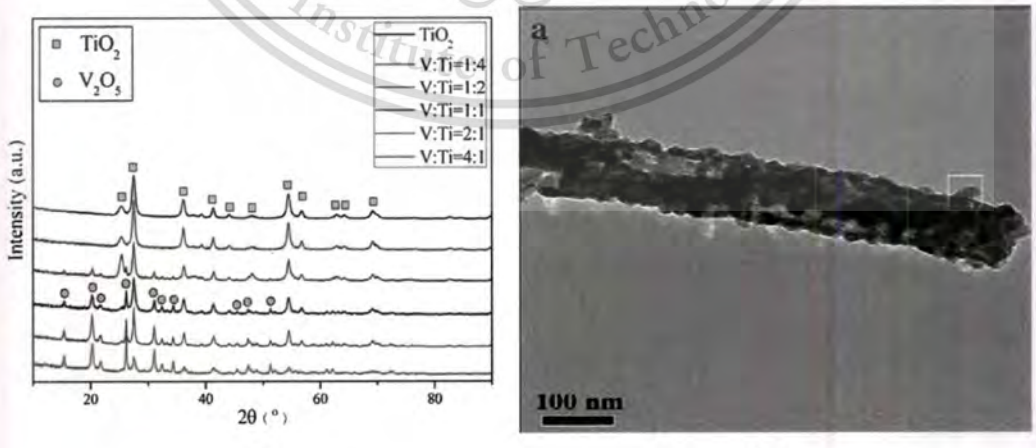

(a) (b)

Figure 2.49 (a) XRD patterns and (b) TEM image of TiO_2/V_2O_5 synthesized by electrospinning technique [87].

Kezhen Lv *et al.* [88] synthesized and investigated the optical properties of WO_3/TiO_2 hollow spheres with average diameter of 320 nm and shell thickness of 50 nm using glucose as a carbon template. They found that the absorption edge of the WO_3/TiO_2 was shifted towards and absorbed stronger in the visible region compared to pure TiO_2. The red-shift in the absorption spectrum of the WO_3/TiO_2 hollow spheres may be attributed to some reasons. The indirect band gap energy of anatase phase TiO_2 was about 3.2 eV and 2.8 eV for WO_3. When WO_3 and TiO_2 form a coupled photocatalyst, the formation of defective energy levels within the forbidden band of WO_3 and TiO_2 could decrease the band gap energy of WO_3/TiO_2.

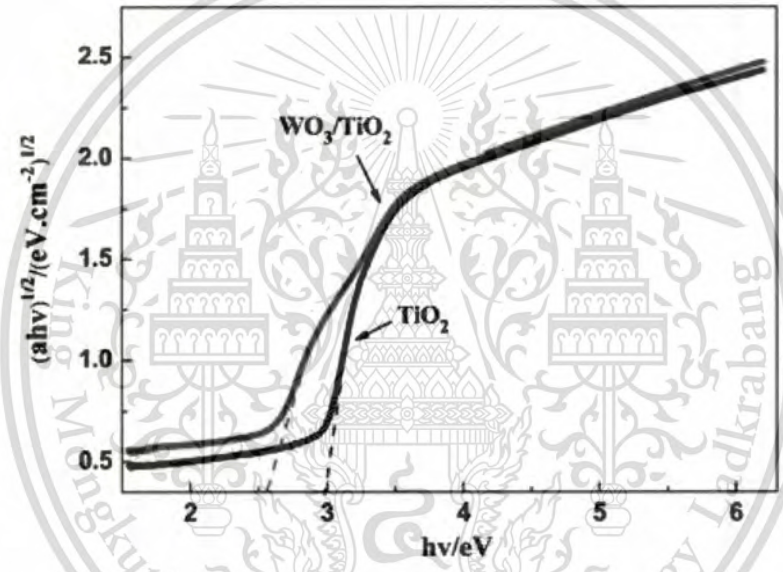

Figure 2.50 Plot of $(\alpha hv)^{1/2}$ versus photon energy of TiO_2 and WO_3/TiO_2 nanocomposites [88].

The increased photocatalytic activity of the nanocomposites photocatalyst was primarily attributed to enhancements in charge separation efficiency because a junction was formed by the decoration of WO_3 with TiO_2, which plays an important role in the separation of photogenerated electron–hole pairs.

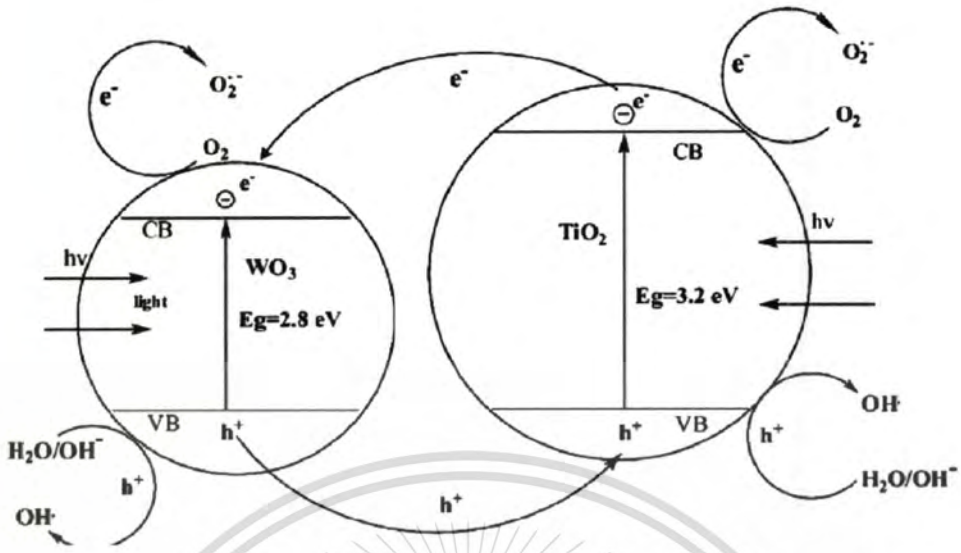

Figure 2.51 Schematic representation of charge carrier separation in the photoexcited WO_3/TiO_2 nanocomposites [88].

2.7 Sonochemical synthesis

Ultrasound is classified as sound beyond the frequency that can be detected by the human ear. The normal range of human hearing is between 16 Hz and 20 kHz. Sometimes called 'silent sound', the ultrasound range is from 20 kHz to 10 MHz. This range can be roughly subdivided into three main regions: low frequency, high power ultrasound (20-100 kHz); intermediate frequency, medium power ultrasound (100 kHz-2 MHz); and high frequency, low power ultrasound (2-10 MHz). The frequency range from 20 kHz to *ca.* 2 MHz is used in sonochemistry.

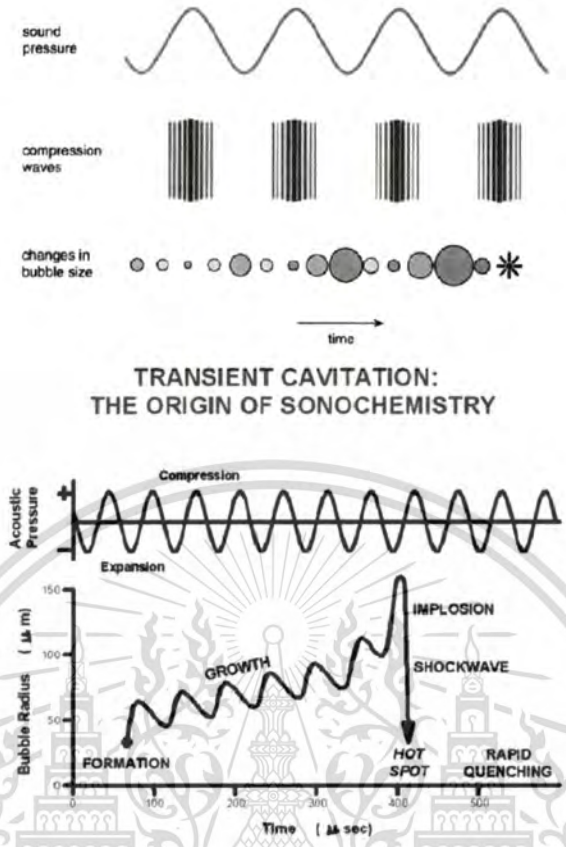

Figure 2.52 Liquids irradiated with ultrasound can produce bubbles. These bubbles oscillate, growing a little more during the expansion phase of the sound wave than they shrink during the compression phase. Under the proper conditions these bubbles can undergo a violent collapse, which generates very high pressures and temperatures. This process is called cavitation [89].

Ultrasound is very useful in the synthesis of a wide range of nanostructured materials, including high-surface-area transition metals, alloys, carbides, oxides, and colloids. The chemical effects of ultrasound do not come from a direct interaction with molecular species. Instead, sonochemistry arises from acoustic cavitation: the formation, growth, and implosive collapse of bubbles in a liquid. Cavitational collapse produces intense local heating (about 5000 K), high pressures (about 1000 atm), and enormous heating and cooling rates ($>10^9$ K/s). Such extraordinary conditions permit access to range of chemical reaction space normally not accessible, which allow for the synthesis of a wide variety of unusual nanostructured material.

When the acoustic cavitation bubble collapses close to or on a solid surface it can only do so asymmetrically because the surface provides resistance to liquid flow from that side. This leads to a microjet of liquid being directed towards the surface of the material at speeds of up to 200 m/s (shown in Fig. 2.53). This effect is equivalent to high-pressure jetting and is the reason why ultrasound is used in sonochemistry synthesis. The jets can be sufficiently powerful to cause pitting of the surface (erosion).

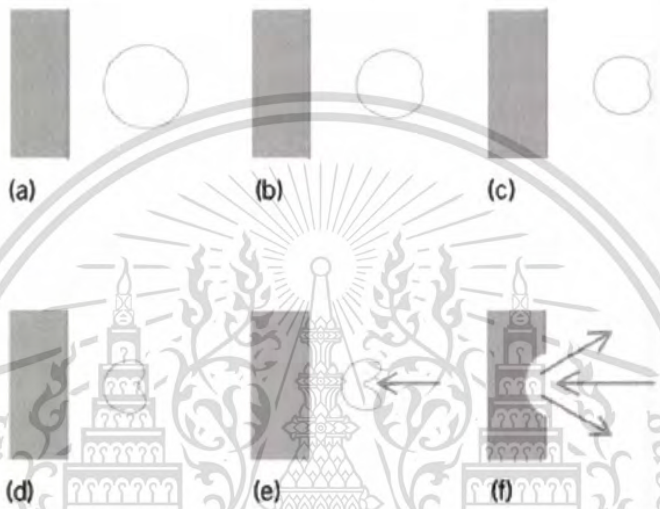

Figure 2.53 Sequence *a–f* of a single bubble collapsing during cavitation near a surface [90].

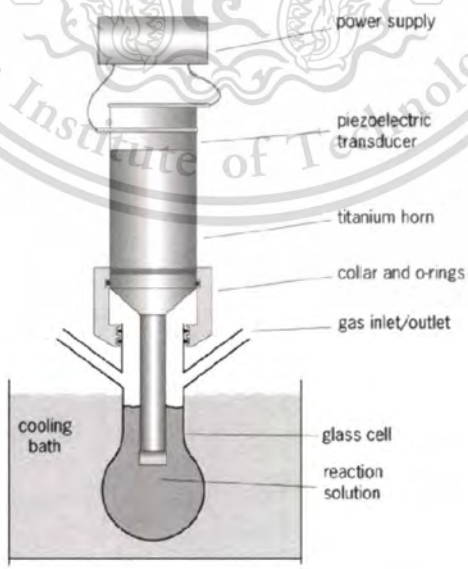

Figure 2.54 Typical commercial laboratory apparatus for sonochemical reactions [90].

The most intense source of ultrasound generally used in the chemical laboratory is the direct immersion ultrasonic horn (as shown in Fig. 2.54). These devices are available from several manufacturers at modest cost. A variety of sizes of power supplies and titanium horns are available, thus allowing flexibility in sample size. The acoustic intensities are easily and reproducibly variable; the acoustic frequency is well controlled, albeit fixed (typically at 20 KHz). Since power levels are quite high, counter-cooling of the reaction solution is essential to provide temperature control; cooling of the piezoelectric ceramic may also be necessary, depending on the configuration. One potential disadvantage in corrosive media is the erosion of the titanium tip; this is generally a very slow process without chemical consequences, given the high tensile strength and low reactivity of Ti metal. This configuration may be used for both homogeneous and heterogeneous sonochemistry.

2.8 Hydrothermal synthesis

The hydrothermal technique has become one of the most important tools for advanced materials processing, especially owing to its advantages in the processing of nanostructural materials for a wide variety of technological applications such as electronics, optoelectronics, catalysis, ceramics, magnetic data storage, etc. The term 'hydrothermal' is purely of geological origin. This reaction describes the action of water at elevated temperature and pressure, in bringing about changes in the earth's crust leading to the formation of various rocks and minerals.

Hydrothermal synthesis is normally conducted in steel pressure vessels called autoclaves with or without Teflon liners under controlled temperature and/or pressure with the reaction in aqueous solutions. The temperature can be elevated above the boiling point of water, reaching the pressure of vapor saturation. The temperature and the amount of solution added to the autoclave largely determine the internal pressure produced. It is a method that is widely used for the production of small particles in the ceramics industry.

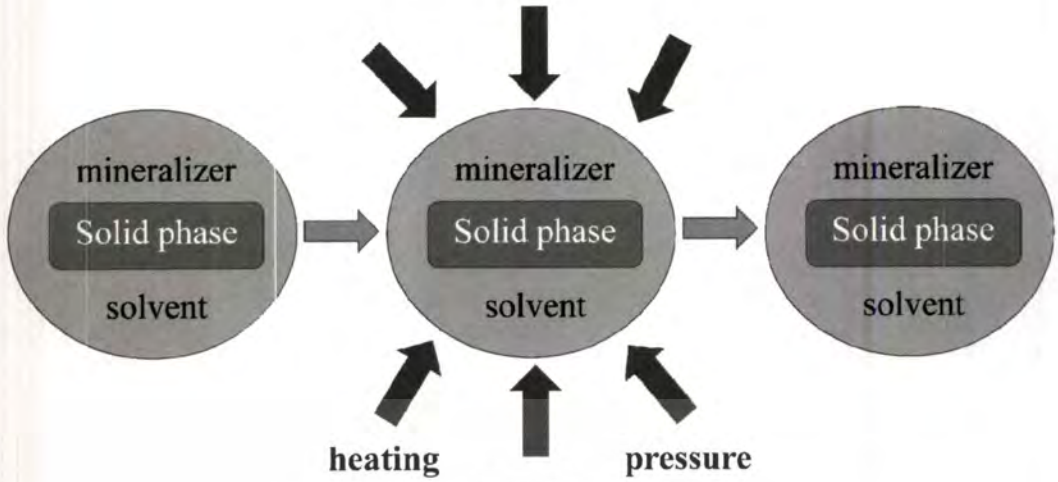

Figure 2.55 Typical hydrothermal reaction is in the general autoclave.

The hydrothermal processing of materials is a part of solution processing and it can be described as super heated aqueous solution processing. Fig. 2.56 shows the PT map of various materials processing techniques [91]. According to this, the hydrothermal processing of advanced materials can be considered as environmentally benign. Besides, for processing nanomaterials, the hydrothermal technique offers special advantages because of the highly controlled diffusivity in a strong solvent media in a closed system. Nanomaterials require control over their physical-chemical characteristics, if they are to be used as functional materials. As the size is reduced to the nanometer range, the materials exhibit peculiar and interesting mechanical and physical properties: increased mechanical strength, enhanced diffusivity, higher specific heat and electrical resistivity compared to their conventional coarse grained counter-parts due to a quantization effect [92].

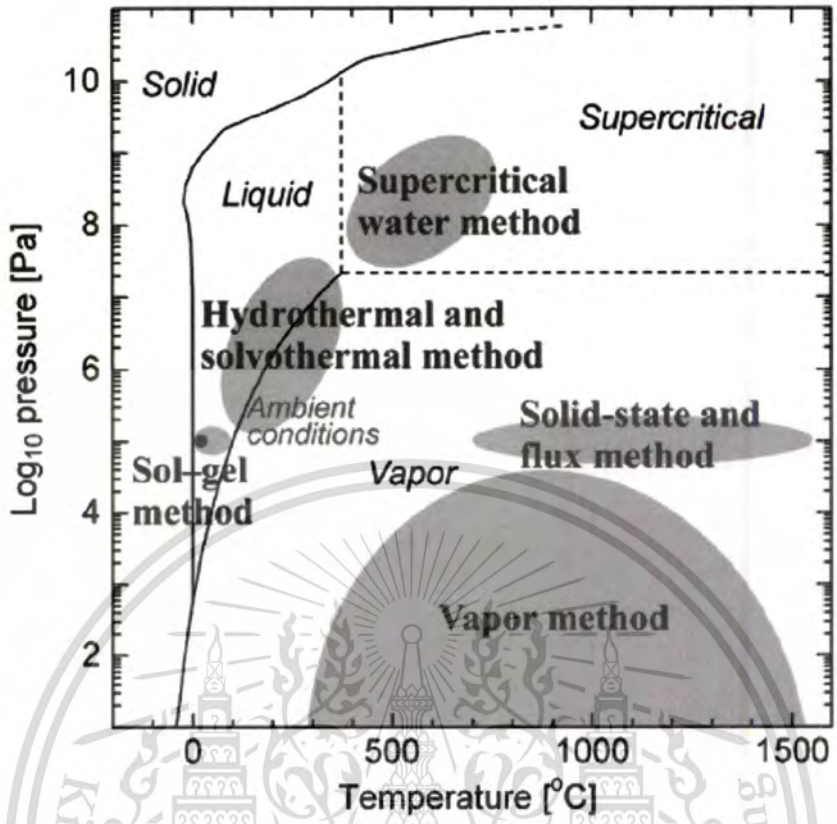

Figure 2.56 Temperature and pressure (T-P) conditions for zinc silicate synthesis methods according to process category. The phase diagram of water is overlaid on the T-P diagram to help distinguish between the various methods that use water as a solvent [91].

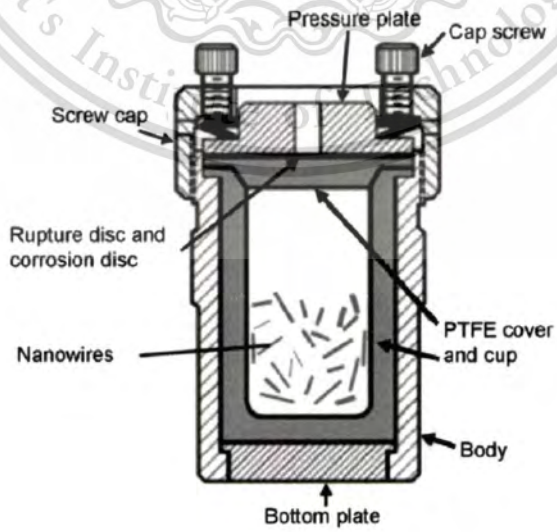

Figure 2.57 Schematic diagram of a typical laboratory autoclave from Parr [93].

Supercritical water (SCW) and supercritical fluids (SCF) provide an excellent reaction medium for hydrothermal processing of nanoparticles, since they allow varying the reaction rate and equilibrium by shifting the dielectric constant and solvent density with respect to pressure and temperature, thus giving higher reaction rates and smaller particles. The reaction products are to be stable in SCF leading to fine particle formation. The hydrothermal technique is ideal for the processing of very fine powders having high purity, controlled stoichiometry, high quality, narrow particle size distribution, controlled morphology, uniformity, less defects, dense particles, high crystallinity, excellent reproducibility, controlled microstructure, high reactivity with ease of sintering.

2.9 X-ray Diffraction

X-ray Diffraction (XRD) is a family of non-destructive analytical techniques which reveal information about the crystal structure, chemical composition, and physical properties of materials and thin films. These techniques are based on observing the scattered intensity of an X-ray beam hitting a sample as a function of incident and scattered angle, polarization and wavelength or energy.

X-ray diffraction is based on constructive interference of monochromatic X-rays and a crystalline sample. X-ray beams are generated by a cathode ray tube, filtered to produce monochromatic radiation, collimated to concentrate, and directed toward the sample. When the incident beam passes through matter and interacts with the electrons in the atoms resulting to the scattering beam that illustrated in Fig. 2.58. If the atoms are organized in planes (i.e., the matter is crystalline) and the distances between the atoms are of the same magnitude as the wavelength of the X-rays, constructive and destructive interference will occur. These results in diffraction where X-rays are emitted at characteristic angles based on the spaces between the atoms organized in crystalline structures called planes. The interaction of the incident rays with the sample produces constructive interference (and a diffracted ray) when conditions satisfy Bragg's Law.

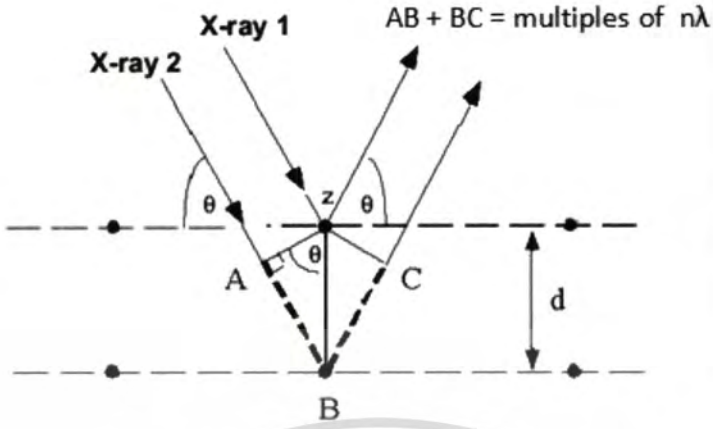

Figure 2.58 Diffraction of X-Ray in crystal.

From

$$n\lambda = AB + BC$$

$$AB = BC$$

$$n\lambda = 2AB$$

$$\sin\theta = AB / d$$

$$AB = d\sin\theta$$

$$n\lambda = 2d\sin\theta \qquad (2.18)$$

Where n is an integer, λ is the wavelength of incident wave, d is the distance between the planes in the atomic lattice and θ is the angle between the incident ray and the scattering planes.

The crystalline size of the solid material can be calculated from XRD peak in a diffraction pattern from Scherrer's equation followed as:

$$D = \frac{k\lambda}{\beta\cos\theta} \qquad (2.19)$$

Where D is crystalline size, k is constant depend on crystal shape (et. 0.94 for spherical crystals with cubic symmetry), λ is wavelength of X-ray, β is full width at half maximum and θ is Bragg angle

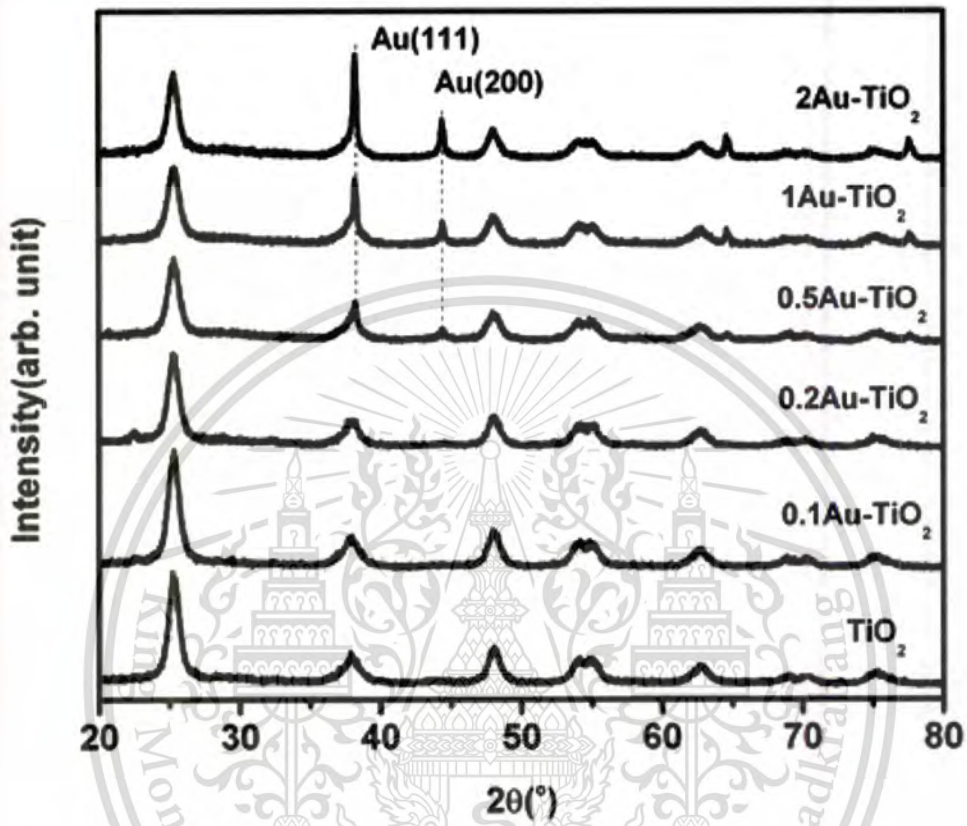

Figure 2.59 XRD patterns of Au-doped TiO_2 prepared via the co-polymer sol-gel method [94].

For example, Fig. 2.59 shows typical XRD patterns of Au-doped TiO_2 nanocomposites. It did not show any peak shift, indicating that the TiO_2 matrix was well maintained as the anatase phase. The average TiO_2 crystallite sizes were calculated using scherrer equation of all samples are quite similar, indicating that the introduced gold does not alter the crystalline properties of the TiO_2 matrix. The samples with 0.5% Au, 1%Au and 2%Au showed two characteristic peaks of metallic gold. But when the Au concentration is too low (<0.5%), the gold peaks were not observed due to the weak signal beyond the instrument detection limit [94].

2.10 Scanning Electron Microscopy

Scanning Electron Microscopy (SEM) is a microscope that uses electron source instead of light for inspecting topographies of specimens at high magnification. The signals derived from electron-sample interactions reveal the information of the sample including external morphology (texture), chemical composition, and crystalline structure and orientation of materials. SEM has allowed researchers to examine a much bigger variety of specimens for example, electronic device or the materials in the medical and physical science communities. The advantages of SEM are more over than traditional microscopes. Large depth of field in SEM, a large amount of a specimen can be in focus at one time and produces three-dimension image of specimen. Closely spaced specimens can be magnified at much higher levels that controlled by electromagnets. All of these advantages, as well as the actual strikingly clear images, make the scanning electron microscope one of the most useful instruments in research today.

The starting SEM operation, incident accelerated electrons are produced in electron beam at the top of the microscope by an electron gun. The electron beam follows a vertical path through the microscope in a vacuum system. The beam travels through electromagnetic fields and lenses, which focus the beam down toward the sample. When the bombarding electrons (primary electrons) collide with the sample, electrons and X-rays are ejected from the sample. X-rays, backscattered electrons, and secondary electrons are collected by detectors and converted into a signal that sent to a screen similar to a television screen for the production of final image. These phenomena are illustrated in Fig. 2.60.

The variety of signals are produced by primary electrons-sample interactions including secondary electrons (SE), backscattered electrons (BSE), diffracted backscattered electrons (EBSD), photons (characteristic X-rays), visible light (cathodoluminescence; CL), and heat that shown in Fig. 2.61. The production of SEM images is occurred by SE and BES phenomena; morphology and topography on samples are performed by secondary electrons and backscattered electrons are most valuable for illustrating contrasts in composition in multiphase samples. SEM analysis is considered to be "non-destructive"; that is, x-rays generated by electron interactions do not lead to volume loss of the sample, so it is possible to analyze the same materials repeatedly.

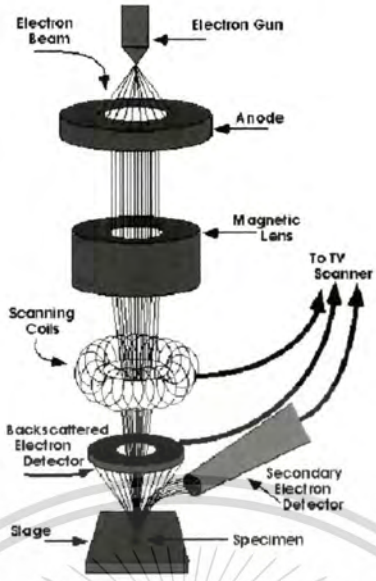

Figure 2.60 Diagrams of the operation in SEM [95].

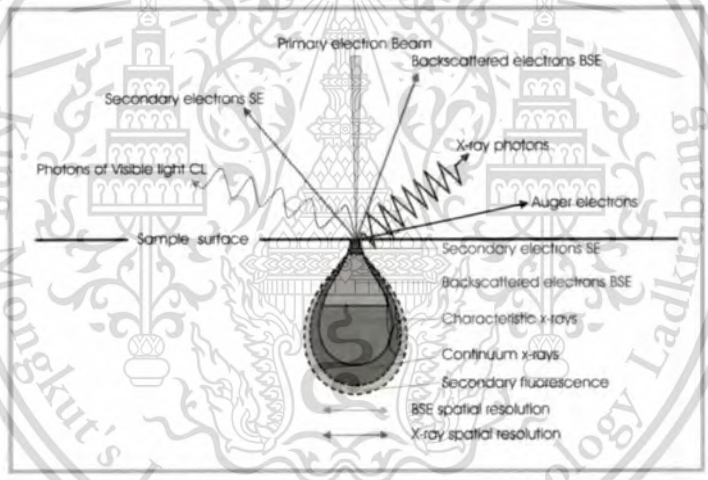

Figure 2.61 Interaction of the electron beam and sample's atom in SEM [96].

Because SEM utilizes vacuum conditions and uses electrons to form an image, special preparations must be done to the sample. All water must be removed from the samples because the water would vaporize in the vacuum. All metals are conductive and require no preparation before being used. All non-metals need to be made conductive by covering the sample with a thin layer of conductive material. This is done by using a device called a "sputter coater." The sputter coater uses an electric field and argon gas. The sample is placed in a small chamber that is at a vacuum. Argon gas and an electric field cause an electron to be removed from the argon, making the atoms positively charged. The argon ions then become attracted to a

negatively charged gold foil. The argon ions knock gold atoms from the surface of the gold foil. These gold atoms fall and settle onto the surface of the sample producing a thin gold coating.

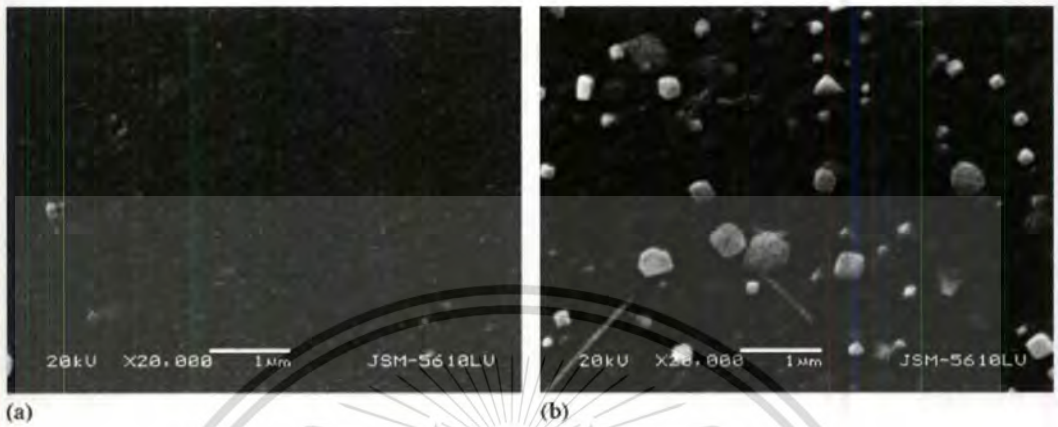

(a) (b)

Figure 2.62 Example of SEM image of TiO_2 (a) and Ag-doped TiO_2 (b) thin films prepared by liquid phase deposition technique. It could be seen that the pure TiO_2 film had a flat texture. Meanwhile, Ag–doped TiO_2 composite thin films displayed rougher surface morphologies and contained larger aggregated particles [97].

2.11 Transmission Electron Microscopy

Transmission Electron Microscopy (TEM) is one of techniques that using electron beam for the imaging sample. Outstanding image resolution in bright and dark field modes, the element mapping and the characterization of crystallographic phases and their orientation can be obtained by TEM analysis.

The electron beam is generated at the top of the microscope by electron gun and traveled in the vacuum system in column. Electromagnetic lenses are used for controlling size of electron beam. The electron beam is focused on the sample. Depending on the density of materials, some of transmitted electrons are detected at the bottom of microscope and hit to the fluorescent. The shadow image of the sample is occurred in varied darkness according to their intensity. The image can be studied directly by the operator or photographed with the camera. The components and operation of TEM are illustrated in Fig. 2.63.

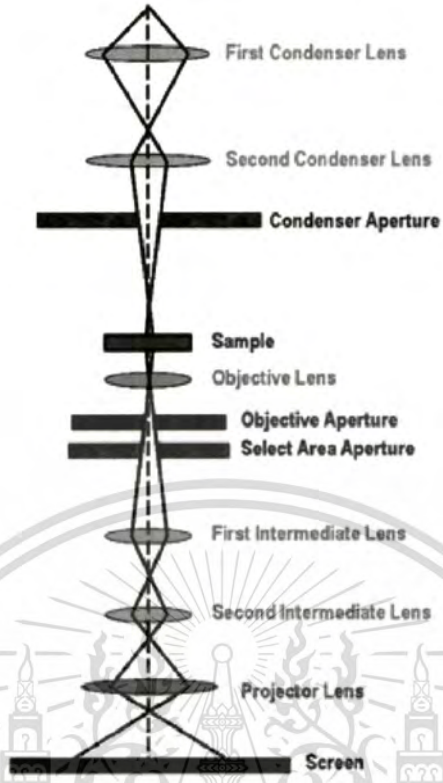

Figure 2.63 TEM instrument and its schematic of the operation [98].

Spots on the diffraction pattern are arranged as points of reciprocal lattice of investigated crystal. It is possible to determine the crystallographic orientation and type of material by the measurements of the spacing between spots and direct beam and measurements of angles between g vectors.

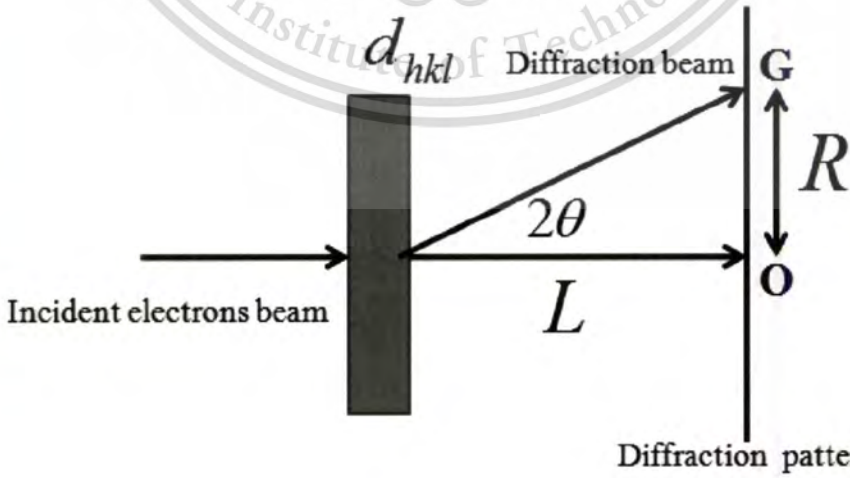

Figure 2.64 Geometric configuration of electron diffraction on single crystal.

From Bragg equation;

$$n\lambda = 2d\sin\theta$$

In a different form;

$$(\frac{1}{2})(\frac{1}{d}) = (\frac{1}{\lambda})\sin\theta$$

At very small Bragg angle, above equation transform into;

$$d = (\lambda L)/R \qquad (2.20)$$

Where λL is a camera constant; characteristic feature of microscope and depends also on magnification of a diffraction pattern

R is a distance between spot coming from direct beam and spot coming from lattice plane (hkl) diffracting the beam (OG line in Fig. 2.64)

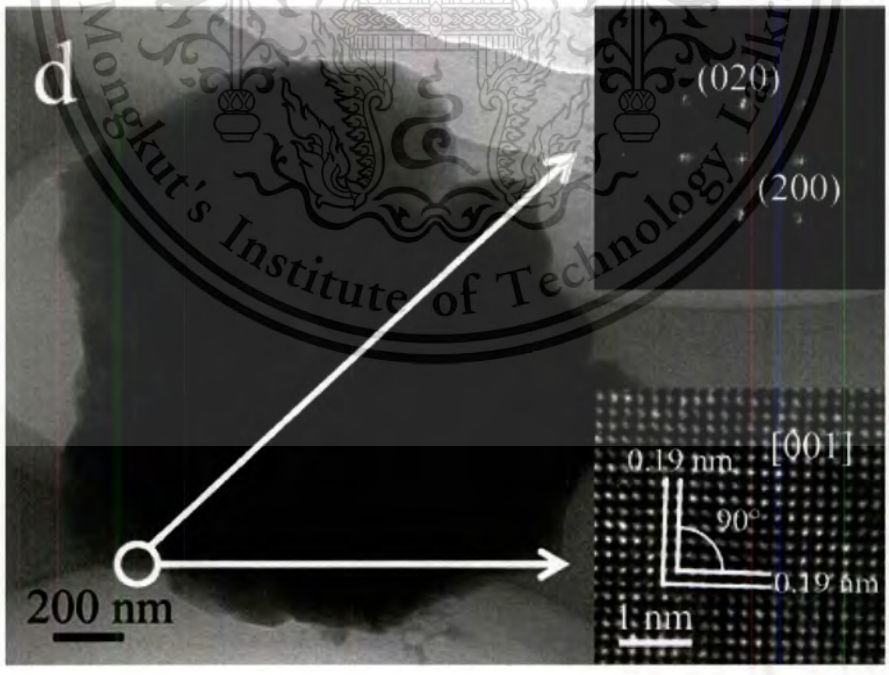

Figure 2.65 TEM image and SAED of single crystal TiO_2 hollow microsphere synthesized by one-step hydrothermal using Ti powder, H_2O_2, HF and H_2O as the precursors [99].

2.12 Optical band gap measurement

The measurement of the optical band gap of materials is important in the semiconductor, nanomaterial and solar applications. This section demonstrates how the optical band gap of a material can be determined from its ultraviolet-visible (UV-Vis) absorption spectrum. The term "optical band gap" refers to the energy difference between the top of the valence band to the bottom of the conduction band (as shown in Fig. 2.66); electrons are able to jump from one band to another. In order for an electron to jump from a valence band to a conduction band, it requires a specific minimum amount of energy for the transition. A diagram illustrating the optical band gap is shown in Fig. 2.66. The optical band gap is a major factor determining the electrical conductivity of a solid. Substances with large band gaps are generally insulators, those with smaller band gaps are semiconductors, while conductors or metal either have very small band gaps or no band gap (because the valence and conduction bands overlap as shown in Fig. 2.66).

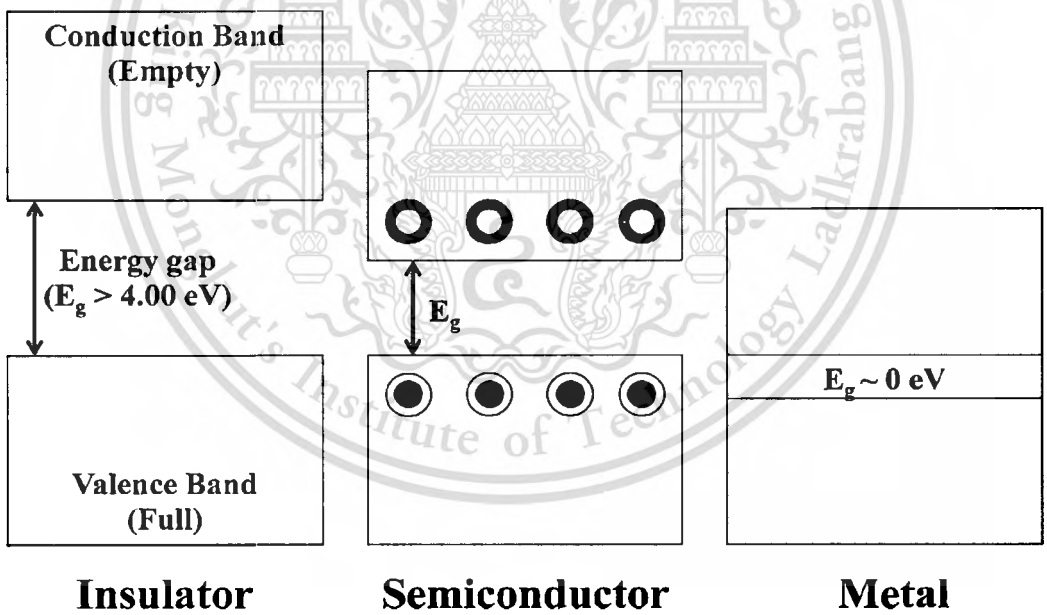

Figure 2.66 Electronic band diagrams in solid [100].

A semiconductor is characterized by a valence band that is filled by electrons and a conduction band that is separated in energy by an amount of forbidden (energy gab) energy from the upper edge of the valence band.

Semiconductors are transparent to photons whose energies lie below their band gap energy and are strongly absorbing for photons whose energies matched or exceed the band gap energy. Band-to-band absorption involves excitation of an electron from the valence band to the conduction band, resulting in creation of electron-hole pair.

The band gap energy of a semiconductor may be determined by observing the transmission or absorption of light of various wavelengths. Because of absorption the light intensity decreases through the sample as the photons are absorbed. The dependence of light transmitted through the sample is:

$$I = I_0 e^{-\alpha d} \tag{2.21}$$

Where I is the intensity of transmitted light through the sample of thickness d and I_0 is the incident light intensity. The absorption coefficient α strongly depends on wavelength. Semiconductors can have high absorption up to 10^5 for photons with energies match or exceed the band gap energy, and very low absorption for photons having energy below the band gap energy. It is also convenient to define a transmittance as:

$$T = \frac{I}{I_0} \tag{2.22}$$

Absorbance is then given by:

$$A = \alpha d = -\ln(T) \tag{2.23}$$

The absorbance spectrum of a semiconductor may be observed carrier out of monochromatic light (Fig. 2.67). Light from the lamp passing through the monochromator will be reflected at different angles for different wavelengths by a grating inside the monochromator. By rotating the grating it is possible to tune the wavelength of transmitted light through the exit slit of monochromator.

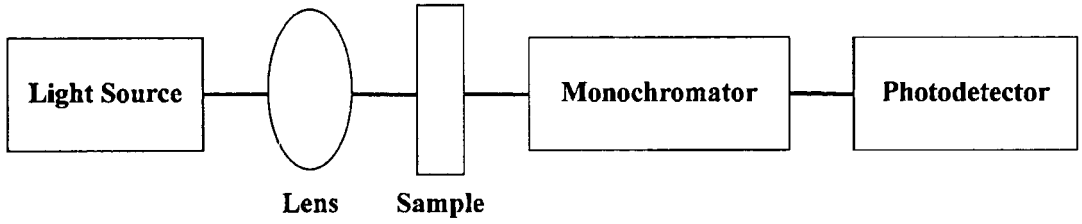

Figure 2.67 Optical instruments for absorption spectrum measurement.

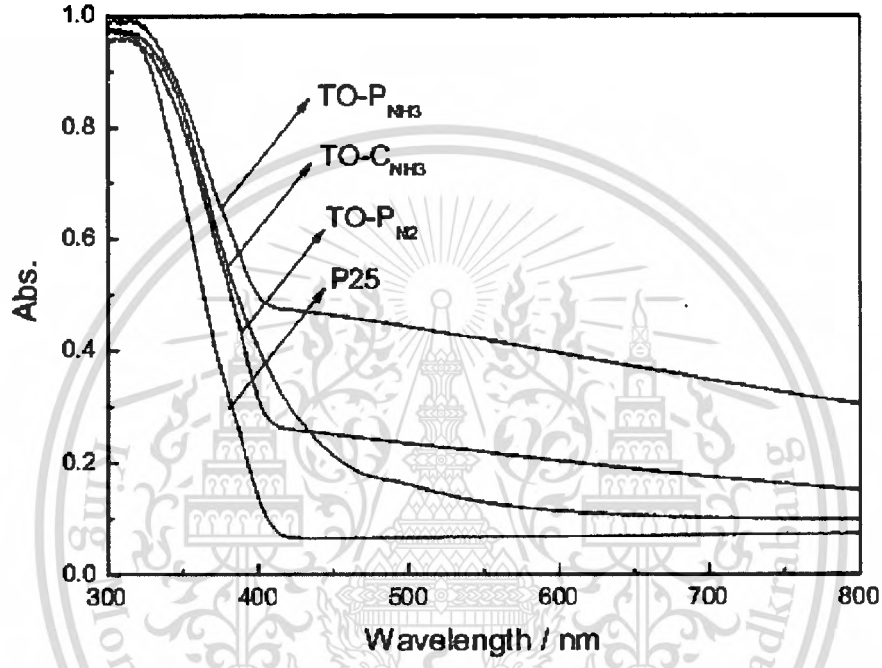

Figure 2.68 Absorption spectra of P25 and prepared N-doped TiO_2 nanopowders [101].

The optical absorption edge of a parabolic band bulk semiconductor with allowed direct transitions can be fit using Tauc equation where the absorption coefficient is described by;

$$\alpha h\nu = A(h\nu - E_g)^n \tag{2.24}$$

Where

α is the absorption coefficient measured as a function of photon energy $h\nu$

$h\nu$ is the photon energy in eV unit defined by $1240/\lambda(nm)$

A is a constant factor determined by the transition probability

E_g is the band gap energy

n is a number that depends on the type of transition process where $1/2, 2, 3/2$ or 3 for allowed direct, allowed indirect, forbidden direct and forbidden indirect electronic transition, respectively

Since the transitions in semiconductors are allowed direct, the Tauc equation requires $n = 1/2$ for calculations. Therefore, a straight line fit to a plot of $(\alpha h\nu)^2$ versus $h\nu$ gives a linear proportion of the Tauc equation;

$$(\alpha h\nu)^2 = (h\nu - E_g) \tag{2.25}$$

The x-intercept of the line fit to the data corresponds to the optical band gap energy.

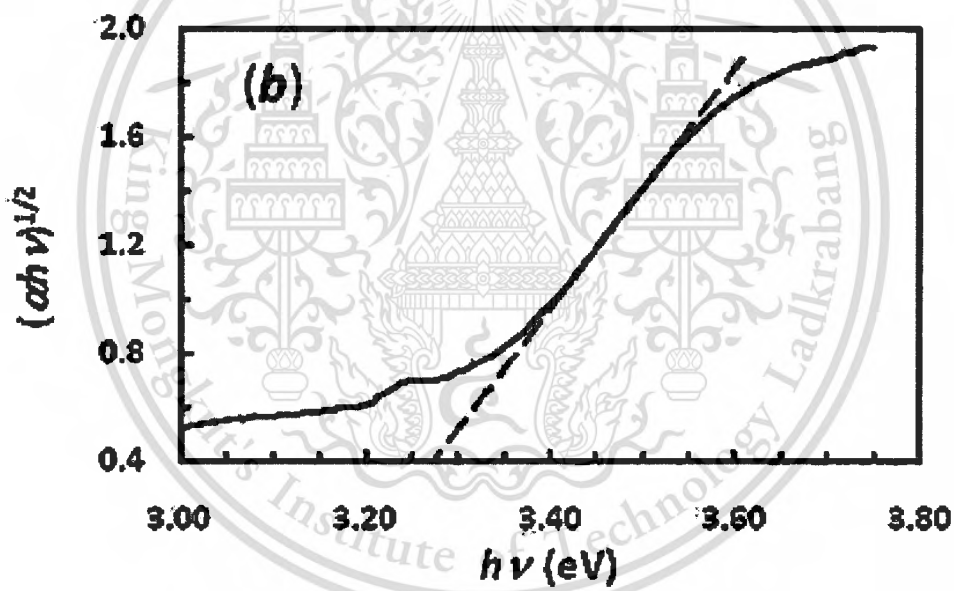

Figure 2.69 Tauc's plot of sheet likes TiO_2 nanoparticles for DSSC application [102].

In the limiting case of an infinitely thick sample, thickness and sample holder have no influence on the value of reflectance (R). In this case, the Kubelka-Munk equation at any wavelength can be employed:

$$\frac{K}{S} = \frac{(1-R_\infty)^2}{2R_\infty} \equiv F(R_\infty) \tag{2.26}$$

F (R_∞) is the so-called remission or Kubelka-Munk function, where R_∞ = $R_{sample}/R_{standard}$. In the parabolic energy band structure, the optical band gap E_g and absorption coefficient α of a direct band gap semiconductor are related through the well known equation:

$$\alpha h\nu = C_1(h\nu - E_g)^{1/2} \tag{2.27}$$

Where α is the linear absorption coefficient of the material, $h\nu$ is the photon energy and C_1 is a proportionality constant. When the material scatters in perfectly diffused manner (or when it is illuminated at 60° incidence), the K-M absorption coefficient K becomes equal to 2α (K=2α). In this case, considering the K-M scattering coefficient S as constant with respect to wavelength and using the remission function in Eq. (2.27) we obtain the expression:

$$[F(R_\infty)h\nu]^2 = C_2(h\nu - E_g) \tag{2.28}$$

The band gap energy can be measured by the Kubelka–Munk plots of $(1-R_\infty)^2/2R_\infty$ versus photon energy, where the x-axis intercepted value is the optical band gap energy [103].

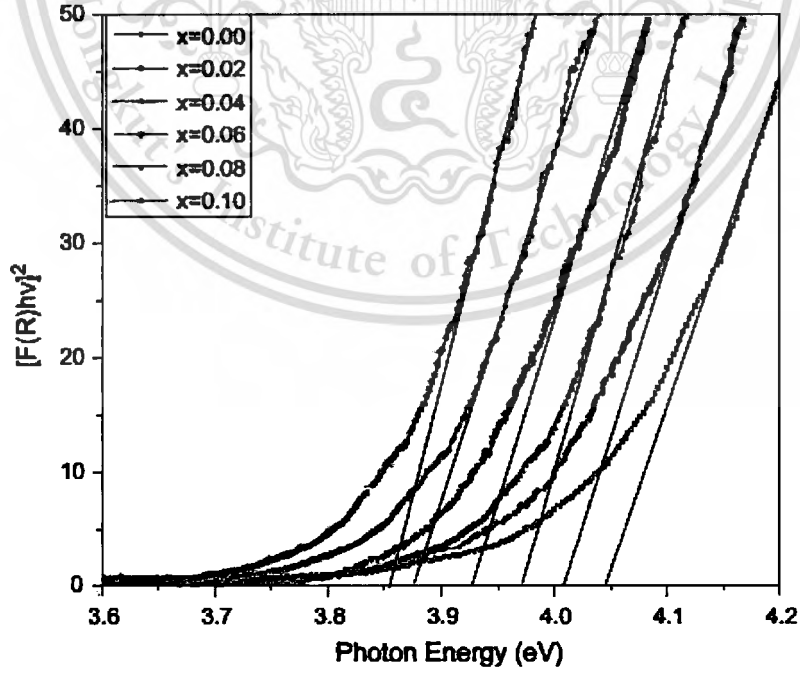

Figure 2.70 Kubelka–Munk plots and band gap energy estimation for $Zn_{0.97-x}Al_xCr_{0.03}S$ nanoparticles [103].

REFERENCES

[1] D. Ginley, M.A. Green, R. Collins, "Solar Energy Conversion Toward 1 Terawatt" MRS Bulletin 33 (2008) 355-364.

[2] V.S. Arunachalam, E.L. Fleischer, "The global Energy Landscap" MRS Bulletin 33 (2008) 264-288.

[3] M. Winter, R.J. Brodd, "What are Batteries, Fuel Cells, and Supercapacitor?" Chemical Reviews 104 (2004) 4245.

[4] Z. Yang, J. Zhang, M.C.W. Kintner-Meyer, X. Lu, D. Choi, J.P. Lemmon, J. Liu, "Electrochemical Energy Storage for Green Grid" Chemical Reviews 111 (2011) 3577.

[5] A. Burke, "Ultracapacitors: Why, how, and where is the technology" Journal of Power Sources 91 (2000) 37.

[6] D.R. Rolison, L.F. Nazar, "Electrochemical energy storage to power the 21st century" MRS Bulletin 36 (2011) 486.

[7] J.R. Miller, A.F. Burke, "Electrochemical capacitors: Challenges and opportunities for real-world applications" Electrochemical Society Interface 17 (2008) 53.

[8] P. Simon, Y. Gogotsi, "Materials for electrochemical capacitor" Nature Materials 7 (2008) 845.

[9] J.R. Miller, P. Simon, "Electrochemical capacitors for energy management" Science 321 (2008) 651.

[10] A. Burke, "Ultracapacitor technologies and application in hybrid and electric vehicles" International Journal of Energy Research 34 (2010) 133-151.

[11] M.D. Stoller, R.S. Ruoff, "Best Practice Methods for Determining and Electrod Material's Performance for Ultracapacitor" Energy & Environmental Science 3 (2010) 1294-1301.

[12] Y. Gogotsi, P. Simon, "True Performance Metrics in Electrochemical Energy Storage" Science 334 (2011) 917-918.

[13] Yong Zhang, G uang-yin Li, Yan Lv, Li-zhen Wang, Ai-qin Zhang, Yan-hua Song and Bei-li Huang, "Electrochemical investigation of MnO_2 electrode material for supercapacitors" international journal of hydrogen energy 36 (2011) 11760-11766.

[14] K. Jeyalakshmi, S. Vijayakumar, K.K. Purushothaman and G. Muralidharan, "Nanostructured nickel doped β-V_2O_5 thin films for supercapacitor applications" Materials Research Bulletin article in press correct proof.

[15] Zhiyong Huang, Hongmei Zeng, Li Xue, Xiangge Zhou, Yan Zhao and Qiongyu Lai, "Synthesis of vanadium oxide, V_6O_{13} hollow-flowers materials and their application in electrochemical supercapacitors" Journal of Alloys and Compounds 509 (2011) 10080-10085.

[16] Liying Liang, Haimei Liu and Wensheng Yang, "Fabrication of VO_2(B) hybrid with multiwalled carbon nanotubes to form a coaxial structure and its electrochemical capacitance performance" Journal of Alloys and Compounds 559 (2013) 167-173.

[17] Jeliza S. Bonso, Abdelaziz Rahy, Sanjaya D. Perera, Nijem Nour, Oliver Seitz, Yves J. Chabal, Kenneth J. Balkus Jr., John P. Ferraris and Duck J. Yang, "Exfoliated graphite nanoplatelets-V_2O_5 nanotube composite electrodes for supercapacitors" Journal of Power Sources 203 (2012) 227-232.

[18] C.D. Lokhande, D.P. Dubal, Oh-Shim Joo, "Metal oxide thin film based supercapacitors" Current Applied Physics 11 (2011) 255-270.

[19] T.P. Gujar, V.R. Shinde, C.D. Lokhande, Woo-Young Kim, Kwang-Deog Jung, Oh-Shim Joo, "Spray deposited amorphous RuO_2 for an effective use in electrochemical supercapacitor" Electrochemistry Communication 9 (2007) 504-510.

[20] Sujit Kumar Mondal, N. Munichandraiah, "Anodic deposition of porous RuO_2 on stainless steel for supercapacitor studies at high current densities" Journal of Power Sources 175 (2008) 657-663.

[21] Q.L. Fang, D.A. Evans, S.L. Roberson, J.P. Zheng, "Ruthenium Oxide Film Electrodes Prepared at Low Temperatures for Electrochemical Capacitors" Journal of Electrochemical Society 148 (2001) A833.

[22] Hansung Kim and Branko N. Popov, "Charaterization of hydrous ruthenium oxide/carbon nanocomposite supercapacitor prepared by colloidal method" Journal of Power Sources 104 (2002) 52-61.

[23] Mengqiang Wu, Graeme A. Snook, George Z. Chen, Derek J. Fray, "Redox deposition of manganese oxide on graphite for supercapacitors" Electrochemistry Communications (2004) 499-504.

[24] Xuanxuan Zhang, Fen Ran, Huili Fan, Yongtao Tan, Lei Zhao, Xiaoming Li, Lingbin Kong, Long Kang, "A dandelion-like carbon microsphere/MnO_2 nanosheets composite for supercapacitors" Journal of Energy Chemistry 23 (2014) 82-90.

[25] SiXu Deng, Dan Sun, ChunHui Wu, Hao Wang, JingBing Liu, YuXiu Sun, Hui Yan, "Synthesis and electrochemical properties of MnO_2 nanorods/graphene composites for supercapacitor applications " Electrochimica Acta 111 (2013) 707-712.

[26] Sepideh Amjad Iranagh, Ladan Eskandarian, Rahim Mohammadi, "Synthesis of MnO_2-polyaniline nanofiber composites to produce high conductive polymer" Synthetic Metals 172 (2013) 49-53.

[27] Pintu Sen, Amitabha De, Ankan Dutta Chowdhury, S.K. Bandyopadhyay, Nidhi Agnihotri, M. Mukherjee, "Conducting polymer based manganese dioxide nanocomposite as supercapacitor" Electrochimica Acta 108 (2013) 265-273.

[28] Wen-Jay Liu, Yong-Ming Dai, Jih-Mirn Jehng, "Synthesis, characterization and electrochemical properties of Fe/MnO_2 nanoparticles prepared by using sol–gel reaction" Journal of the Taiwan Institute of Chemical Engineers Volume 45 (2014) 475-480.

[29] Debasmita Das, Pratik Kumar Sen, Kaushik Das, "Mechanism of potentiostatic deposition of MnO_2 and electrochemical characteristics of the deposit in relation to carbohydrate oxidation " Electrochimica Acta 54 (2008) 289-295.

[30] Dongliang Yan, Zilong Guo, Guisheng Zhu, Huijuan Yang, Ronghua Wei, Huarui Xu, Aibing Yu, "Electrochemical properties of 3D MnO_2 film prepared by chemical bath deposition at room temperature" Materials Letters 82 (2012) 156-158.

[31] Zhong Chen, Jianling Li, Yu Chen, Yakun Zhang, Guofeng Xu, Jun Yang, Ye Feng, "Microwave-hydrothermal preparation of a graphene/hierarchy structure MnO_2 composite for a supercapacitor" Particuology, In Press, Corrected Proof, Available online 7 March 2013.

[32] Jianyun Cao, Yaming Wang, Yu Zhou, Jia-Hu Ouyang, Dechang Jia, Lixin Guo, "High voltage asymmetric supercapacitor based on MnO_2 and graphene electrodes" Journal of Electroanalytical Chemistry 689 (2013) 201-206.

[33] Ramchandra S. Kalubarme, Harsharaj S. Jadhav, Chan-Jin Park, "Electrochemical characteristics of two-dimensional nano-structured MnO_2 for symmetric supercapacitor" Electrochimica Acta 87 (2013) 457-465.

[34] Yu Hu, Jun Wang, Xionghua Jiang, Yanfeng Zheng, Zhenxing Chen, "Facile chemical synthesis of nanoporous layered δ -MnO_2 thin film for high-performance flexible electrochemical capacitors" Applied Surface Science 271 (2013) 193-201.

[35] Xiaoyan Yan, Xili Tong, Jian Wang, Changwei Gong, Mingang Zhang, Liping Liang, "Synthesis of mesoporous NiO nanoflake array and its enhanced electrochemical performance for supercapacitor application" Journal of Alloys and Compounds 593 (2014) 184-189.

[36] Bo Ren, Meiqing Fan, Qi Liu, Jun Wang, Dalei Song, Xuefeng Bai, "Hollow NiO nanofibers modified by citric acid and the performances as supercapacitor electrode" Electrochimica Acta 92 (2013) 197-204.

[37] Changzhou Yuan, Xiaogang Zhang, Quanfu Wu, Bo Gao, "Effect of temperature on the hybrid supercapacitor based on NiO and activated carbon with alkaline polymer gel electrolyte" Solid State Ionics 177 (2006) 1237-1242.

[38] Xiaoyan Yan, Xili Tong, Jian Wang, Changwei Gong, Mingang Zhang, Liping Liang, "Rational synthesis of hierarchically porous NiO hollow spheres and their supercapacitor application" Materials Letters 95 (2013) 1-4.

[39] D.V. Leontyeva, I.N. Leontyev, M.V. Avramenko, Yu.I. Yuzyuk, Yu.A. Kukushkina, N.V. Smirnova, "Electrochemical dispergation as a simple and effective technique toward preparation of NiO based nanocomposite for supercapacitor application" Electrochimica Acta 114 (2013) 356-362.

[40] Jianhui Zhu, Jian Jiang, Jingping Liu, Ruimin Ding, Hao Ding, Yamin Feng, Guangming Wei, Xintang Huang, "Direct synthesis of porous NiO nanowall arrays on conductive substrates for supercapacitor application" Journal of Solid State Chemistry 184 (2011) 578-583.

[41] Zeheng Yang, Feifei Xu, Weixin Zhang, Zhousheng Mei, Bo Pei, Xiao Zhu, "Controllable preparation of multishelled NiO hollow nanospheres via layer-by-layer self-assembly for supercapacitor application" Journal of Power Sources 246 (2014) 24-31.

[42] Wentao Jiang, Juan Ni, Ke Yu, et al., Hydrothermal synthesis and electrochemical characterization of VO_2(B) withcontrolled crystal structures. Appl. Surf. Sci.257, 3253-3258(2011).

[43] M.B. Sahana., C. Sudakar., C. Thapa.,G.Lawes., V.M. Naik., R.J. Baird., G.W. Auner., R. Naik., and K.R. Padmanabhan. (2007) 'Electrochemical properties of V_2O_5 thin films deposited by spin coating'.Mat. Sci. Eng. B. Solid., vol. 143, pp. 42-50.

[44] www.chemicool.com

[45] Akira Fujishima and Donald A. Tryk, "Photochemical and Photoelectrochemical Water Splitting" Energy Carriers and Conversion Vol. 1.

[46] J. García-Serrano, E. Gómez-Hernández, M. Ocampo-Fernández and U. Pal, "Effect of Ag doping on the crystallization and phase transition of TiO_2 nanoparticles" Current Applied Physics 9 (2009) 1097-1105.

[47] M Landmann, E Rauls and W G Schmidt, "The electronic structure and optical response of rutile, anatase and brookite TiO_2" J. Phys.: Condens. Matter 24 (2012) 195503 (6pp).

[48] Taro Toyoda, Junya Kobayashi and Qing Shen, "Correlation between crystal growth and photosensitization of nanostructured TiO_2 electrodes using supporting Ti substrates by self-assembled CdSe quantum dots" Thin Solid Films 516 (2008) 2426-2431.

[49] Chunlan Cao, Chenguo Hu, Xue Wang, Shuxia Wang, Yongshu Tian, Hulin Zhang, "UV sensor based on TiO_2 nanorod arrays on FTO thin film" Sensors and Actuators B 156 (2011) 114-119.

[50] Y.F. You, C.H. Xu, S.S. Xu, S. Cao, J.P. Wang, Y.B. Huang, S.Q. Shi, "Structural characterization and optical property of TiO_2 powders prepared by the sol–gel method" Ceramics International 40 (2014) 8659-8666.

[51] S.R. Shirsath, D.V. Pinjari, P.R. Gogate, S.H. Sonawane and A.B. Pandit, "Ultrasound assisted synthesis of doped TiO_2 nano-particles: Characterization and comparison of effectiveness for photocatalytic oxidation of dyestuff effluent" Ultrasonics Sonochemistry 20 (2013) 277-286.

[52] Qinghua Chen, Huiling Liu, Yanjun Xin, Xiuwen Cheng, "TiO_2 nanobelts-Effect of calcination temperature on optical, photoelectrochemical and photocatalytic properties" Electrochimica Acta 111 (2013) 284-291.

[53] H.Z. Zhang, J.F. Banfield "Understanding polymorphic phase transformation behavior during growth of nanocrystalline aggregates: insights from TiO_2 " J. Phys. Chem. B, 104 (2000), pp. 3481–3487.

[54] Mehdi Alzamani, Ali Shokuhfar, Ebrahim Eghdam, Sadegh Mastali, "Influence of catalyst on structural and morphological properties of TiO_2 nanostructured films prepared by sol–gel onglass" Progress in Natural Science: Materials International 23 (2013) 77-84.

[55] Khaled, M.; Odheiba, S. A.; and Issa, A.; 2009; Effect of M-doping (M = Fe, V) on the photocatalytic activity of nanorod rutile TiO_2 for Congo red degradation under the sunlight; Ceramics International; 35; 433-439.

[56] Christophe, C.; Thierry, P.; Jean-Charles, D.; and Sylvie, L.; 2010; N-doped TiO_2 by low temperature synthesis: Stability, photo-reactivity and singlet oxygen formation in the visible range; Journal of Photochemistry and Photobiology A: Chemistry; 216; 201-208.

[57] Zhenyi Zhang, Changlu Shao, Lina Zhang, Xinghua Li, Yichun Liu, "Electrospun nanofibers of V-doped TiO_2 with high photocatalytic activity" Journal of Colloid and Interface Science 351 (2010) 57-62.

[58] A.H. Ghanbari Niaki, A.M. Bakhshayesh, M.R. Mohammadi, "Double-layer dye-sensitized solar cells based on Zn-doped TiO_2 transparent and light scattering layers: Improving electron injection and light scattering effect" Solar Energy 103 (2014) 210-222.

[59] Xiangxin, Y.; Chundi, C.; Keith, H.; Larry, E.; Ronaldo, M.; Dambar, H.; and Kenneth, K.; 2007; Highly visible-light active C- and V-doped TiO_2 for degradation of acetaldehyde; Journal of Catalysis; 252; 296-302.

[60] M. Benkahoul, M. Chaker, J. Margot, E. Haddad, R. Kruzelecky, B. Wong, W. Jamroz and P. Poinas, "Thermochromic VO_2 film deposited on Al with tunable thermal emissivity for space applications" Solar Energy Materials and Solar Cells 95 (2011) 3504-3508.

[61] Haihong Yin, Juan Ni, Wentao Jiang, Zhengli Zhang and Ke Yu, "Synthesis, field emission and humidity sensing characteristics of monoclinic VO_2 nanostructures" Physica E 43 (2011) 1720-1725.

[62] Yanfeng Gao, Hongjie, Zongtao Zhanga, Litao Kanga, Zhang Chen, Jing Du, Minoru Kanehira and Chuanxiang Caoa, "Nanoceramic VO_2 thermochromic

smart glass: A review on progress in solution processing" Nano Energy article in press correct proof.

[63] Jinhua Li and Ningyi Yuan, Temperature sensitivity of resistance of VO_2 polycrystallinefilms formed by modified ion beam enhanced deposition. Appl. Surf. Sci.233, 252-257(2004).

[64] M. Benkahoul, M. Chaker, J. Margot,et al., Thermochromic VO_2 film deposited on Al with tunable thermal emissivity forspace applications. Sol. Energ. Mat. Sol. C.95, 3504-3508(2011).

[65] KuangYue Tsai, Fong-Hsu Wu, Han-Ping DShieh, et al., Optical switching properties of VO2 films drivenby using WDM-aligned lasers. Mater. Chem. Phys.96, 331-336(2006).

[66] SébastienSaitzek, FrédéricGuinneton, Guillaume Guirleo,et al., VO_2 thin films deposited on silicon substrates from V_2O_5 target: Limits inoptical switching properties and modeling. Thin Solid Films.516, 891-897(2008).

[67] Ji Qi, Guiling Ning and Yuan Lin, Synthesis, characterization, and thermodynamicparameters of vanadium dioxide. Mat. Res. Bull.43, 2300-2307(2008).

[68] Xingjian Yi, Changhong Chen, Luqin Liu, et al., A new fabrication method for vanadium dioxidethin films deposited by ion beam sputtering. Infrared. Phys. Techn.44, 137-141(2003).

[69] P. Evans, M.E. Pemble and D.W. Sheel,et al., Multi-functional self-cleaning thermochromic films byatmospheric pressure chemical vapour deposition. J. Photoch. Photobio. A.189, 387-397(2007).

[70] Shidong Ji, Feng Zhang and Ping Jin, Selective formation of VO_2(A) or VO_2(R) polymorph by controllingthe hydrothermal pressure.J. Solid. State. Chem. 184, 2285-2292(2011).

[71] Kinson C. Kam and Anthony K. Cheetham, Thermochromic VO_2nanorods and other vanadiumoxides nanostructures. Mat. Res. Bull.41, 1015-1021(2006).

[72] Xueliang Li, Xueji Chen, Xiangying Chen, Changlong Han, Chengwu Shi, "Hydrothermal synthesis and characterization of VO_2 (B) nanorods array" Journal of Crystal Growth 309 (2007) 43-47.

[73] Haihong Yin, Ke Yu, Zhengli Zhang, Ziqiang Zhu, "Morphology-control of VO_2 (B) nanostructures in hydrothermal synthesis and their field emission properties" Applied Surface Science 257 (2011) 8840-8845.

[74] Shidong Ji, Feng Zhang, Ping Jin, "Selective formation of VO_2(A) or VO_2(R) polymorph by controlling the hydrothermal pressure" Journal of Solid State Chemistry 184 (2011) 2285-2292.

[75] X.H. Cheng, H.F. Xu, Z.Z. Wang, K.R. Zhu, G. Li, Shaowei Jin, "Synthesis, characterization and formation mechanism of metastable phase VO_2(A) nanorods" Materials Research Bulletin 48 (2013) 3383-3388.

[76] Zhanjun Chen, Shaokang Gao, Lilong Jiang, Mingdeng Wei, Kemei Wei, "Crystalline VO_2 (B) nanorods with a rectangular cross-section" Materials Chemistry and Physics 121 (2010) 254-258.

[77] Tina F.-R. Shen, Ming-Hong Lai, Thomas C.-K. Yang, et al., Photocatalytic production of hydrogen by vanadium oxides undervisible light irradiation. Journal of the Taiwan Institute of Chemical Engineers. 43, 95-101(2012).

[78] David Alie, Lynn Gedvilas, Zhiwei Wang, Robert Tenent, Chaiwat Engtrakul, Yanfa Yan, Sean E. Shaheen, Anne C. Dillon, Chunmei Ban, "Direct synthesis of thermochromic VO_2 through hydrothermal reaction" Journal of Solid State Chemistry 212 (2014) 237-241.

[79] Sorapong Pavasupree, Yoshikazu Suzuki, Athapol Kitiyanan, Sommai Pivsa-Art, Susumu Yoshikawa, "Synthesis and characterization of vanadium oxides nanorods" Journal of Solid State Chemistry 178 (2005) 2152-2158.

[80] Lian-Mei, C., Qiong-Yu, L., Yan-Jing, H., Yan, Z., and Xiao-Yang, J. (2009) 'Investigations on capacitive properties of the AC/V_2O_5 hybrid supercapacitor in various aqueous electrolytes'. J. Alloy. Compd., vol. 467, pp. 465-471.

[81] T. Ivanava., and A Harizanova. (2005) 'Electrochromic investigation of sol-gel derived thin films of TiO_2-V_2O_5'.Mat. Res. Bull., vol. 40, pp. 411-419.

[82] Navaneetha, K. N., and Edmund G. S. (2011) 'Low temperature chemical vapor deposition of nanocrystalline V_2O_5 thin films'. Thin. Solid.Films., vol. 519, pp. 3663-3668.

[83] Chuan, C., Dongsheng, G., and Ying, W. (2011) 'Solution processing of V_2O_5-WO_3 composite films for enhanced Li-ion intercalation properties'. J. Alloy. Compd., vol. 509, pp. 909-915.

[84] A. Dhayal Raj., T. Pazhanivel., P. Suresh Kumar., D. Mangalaraj., D. Nataraj., N. Ponpandian. (2010) 'Self assembled V_2O_5 nanorods for gas sensors'. Curr. Appl. Phys., vol. 10, pp. 531-537

[85] Keng-Che, C., Fu-Rong, C., and Ji-Jung, K. (2006) 'V_2O_5 nanowires as a functional material for electrochromic device'. Sol. Energ. Mat. Sol. C., vol. 90, pp. 1156-1165.

[86] Min Young Song, Young-Kwon Park, Jongsoo Jurng, "Direct coating of V_2O_5/TiO_2 nanoparticles onto glass beads by chemical vapor deposition" Powder Technology 231 (2012) 135-140.

[87] Yuan Wang, Jiawang Zhang, Lixin Liu, Chengquan Zhu, Xueqin Liu, Qing Su, "Visible light photocatalysis of V_2O_5/TiO_2 nanoheterostructures prepared via electrospinning" Materials Letters 75 (2012) 95-98.

[88] Kezhen Lv, Jie Li, Xiaoxia Qing, Wenzhang Li, Qiyuan Chen, "Synthesis and photo-degradation application of WO_3/TiO_2 hollow spheres" Journal of Hazardous Materials, Volume 189, Issues 1–2, 15 May 2011, Pages 329-335.

[89] THE CHEMISTRY OF ULTRASOUND by Kenneth S. Suslick from The Yearbook of Science & the Future 1994; Encyclopaedia Britannica: Chicago, 1994; pp 138-155.

[90] www.accessscience.com-encyclopydia

[91] M. Takesue et al. "Progress in Crystal Growth and Characterization of Materials" 55 (2009) 98-124.

[92] K. Byrappa and T. Adschiri, "Hydrothermal technology for nanotechnology" Progess in Crystal growth and Characterization of Materials 53 (2007) 117-166

[93] Rachel Grange, Fabrizia Dutto and Aleksandra Radenovic "Nanowires-Implementations and Applications", book edited by Abbass Hashim, Published: July 18, 2011.

[94] Jun Fang, Shao-Wen Cao, Zheng Wang, Mohammad Mehdi Shahjamali, Say Chye Joachim Loo, James Barber and Can Xue, "Mesoporous plasmonic Aue TiO_2 nanocomposites for efficient visible-light-driven photocatalytic water reduction" international journal of hydrogen energy 37 (2012) 17853-17861.

[95] Radiological and Environmental Management Purdeu University.

[96] Imaging Spectroscopy and Analysis Centre (ISAAC) University of Glasgow.

[97] Jiaguo Yu, Jianfeng Xiong, Bei Cheng and Shengwei Liu, "Fabrication and characterization of Ag–TiO_2 multiphase nanocomposite thin films with enhanced photocatalytic activity" Applied Catalysis B: Environmental 60 (2005) 211-221.

[98] www.nanoscience.gatech.edu

[99] Xiaoliang Wang, Huanlong He, Yan Chen, Jinqiu Zhao and Xiangyi Zhang, "Anatase TiO_2 hollow microspheres with exposed {001} facets: Facile synthesis and enhanced photocatalysis" Applied Surface Science 258 (2012) 5863-5868.

[100] www.webexhibits.org

[101] Shaozheng Hu, Fayun Li and Zhiping Fan, "The influence of preparation method, nitrogen source and post-treatment on the photocatalytic activity and stability of N-doped TiO_2 nanopowder" Journal of Hazardous Materials 196 (2011) 248-254.

[102] Ratna Chauhan, Reena Kushwaha and Lal Bahadur, "Highly efficient dye-sensitized solar cell developed by using sheet like TiO_2 prepared by a novel route" Materials Chemistry and Physics 139 (2013) 525-530.

[103] D. Amaranatha Reddy, Chunli Liu, R.P. Vijayalakshmi, B.K. Reddy "Structural, optical and magnetic properties of $Zn_{0.97-x}Al_xCr_{0.03}S$ nanoparticles" Ceramics International 40 (2014) 1279-1288.

CHAPTER 3

EXPERIMENTS

This chapter explains the preparations of V-TiO_2 nanoparticles and VO_2 nanorods using sonochemical process and hydrothermal synthesis, respectively. The fabrication of charges storage devices using V-TiO_2/V_2O_5 nanocomposites via doctor blade technique is preliminarily.

3.1 Preparation of V-TiO_2 nanoparticles via the sonochemical process

V-doped TiO_2 with various vanadium contents were synthesized by sonochemical-assisted process. Titanium isopropoxide [$Ti(C_6H_{14}O_2)_2$] and vanadyl acetylacetonate [$VO(C_5H_8O_2)]_2$ were used as starting source materials for Ti and V, respectively

3.1.1 Materials and equipment

1) Titanium isopropoxide [$Ti(C_6H_{14}O_2)_2$]
2) Vanadyl acetylacetonate [$VO(C_5H_8O_2)]_2$
3) Sodium hydroxide (NaOH)
4) Deionized water
5) Absolute ethanol
6) Magnetic bar and magnetic stirrer
7) Ultrasonic horn (VCX 750)
8) Calcination oven

3.1.2 Experimental details

1) 14.21 mL of titanium isopropoxide was dissolved into designated solution of 49 mL-absolute ethanol and 1 mL-acetylacetone and then stirred at room temperature for 1 h.

2) Vanadyl acetylacetonate (0-5 mol %) was dissolved into the stocked solution and then stirred at room temperature for 24 h until transparent pale yellow solution was obtained.

3) 50 mL of the stocked solution and 50 mL of deionized water was filled into the chamber and then the mixed liquid was irradiated with high intensity ultrasound (650 W 20 kHz) by a Sonics Model VCX 750 at room temperature in ambient air for 10-30 min.

4) After cooled down to room temperature, the resulting precipitates were washed with deionized water and ethanol.

5) The cleaned precipitates were calcined at 300-1000 °C for 4 h.

6) All samples were characterized by XRD, Raman spectroscopy, XPS, SEM, TEM and UV-Vis spectrophotometer.

Figure 3.1 Sonochemical apparatus using ultrasonic horn (VCX 750).

3.2 Preparation of VO_2 nanorods via the hydrothermal synthesis

The VO_2 nanorods were synthesized by hydrothermal method using commercials V_2O_5 powder as the source of vanadium and *n*-butanol, acetylacetone as the reducing agents.

3.2.1 Materials and equipment

1) Commercials vanadium pentoxide
2) *n*-butanol
3) Acetylacetone
4) Deionized water
5) Acetone
6) Ethanol
7) Magnetic bar and magnetic stirrer
8) Teflon-lined stainless autoclave

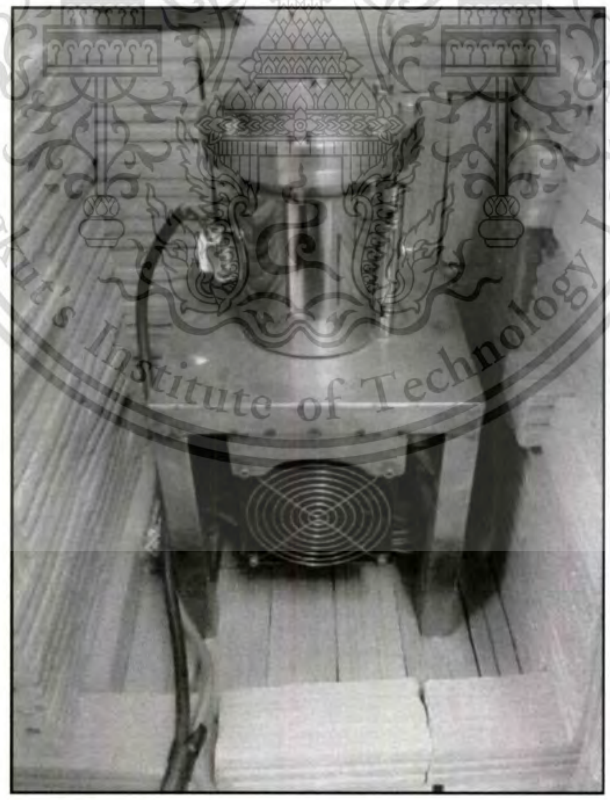

Figure 3.2 Hydrothermal apparatus with Teflon-line auto clave and magnetic stirrer.

3.2.2 Experimental details

1) 3.62 g of commercial V_2O_5 powder, 10 mL of *n*-butanol and 10 mL of acetylacetone were vigorously magnetically stirred at room temperature for 12 h.

2) The suspension was transferred into a 250 mL Teflon-lined stainless autoclave, which was then filled with deionized water up to 200 mL of total volume.

3) The autoclave was sealed and kept at 100-140 °C for 48 h and then cooled down to room temperature for 24 h.

4) The obtained dark blue precipitate was filtered and washed for several times with deionized water, acetone and absolute ethanol and dried in air at 80 °C for several time.

5) All samples were characterized by XRD, FTIR, XPS, SEM, TEM and UV-Vis spectrophotometer.

3.3 Fabrication of V-doped TiO_2/V_2O_5 nanocomposites films for charges storage application

The V-doped TiO_2/V_2O_5 charge storage layer was prepared by doctor blade technique using Triton X-100 as the binder.

3.3.1 Materials and equipment

1) V-TiO_2 nanoparticles were synthesized by sonochemical process
2) VO_2 nanorods were synthesized by hydrothermal process
3) Lithium perchlorate ($LiClO_4$)
4) Oxalic acid ($C_2H_2O_4$)
5) Methanol (CH_3OH)
6) Parapolymer film
7) Platinum film coated on FTO substrate
8) FTO glass
9) Triton X-100
10) Hydrochloric acid
11) Deionized water
11) Absolute ethanol
12) Magnetic bar and magnetic stirrer

13) Calcination oven with argon gas

3.3.2 Experimental details

1) V-doped TiO_2/V_2O_5 nanocomposites with different ratio of V-doped TiO_2:VO_2 were dissolved in the solution of hydrochloric acid, DI water and absolute ethanol.

2) The mixed solution was stirred at room temperature for 2 h.

3) 2 drops of Triton X-100 was dissolved into the slurry and continuously stirred for 3 h.

4) The well mixed suspension was slowly dropped and spread using doctor blade technique onto the FTO glass substrate.

5) The nanocomposites films were dried in air at 80 °C for 10 min to yield the as-prepared thick film.

6) The as-prepared nanocomposites films were further proceeded residual removal by heating at 500 °C in atmospheric nitrogen for 2 h to obtain the V-doped TiO_2/V_2O_5 nanocomposite film.

Figure 3.3 As-prepared V-doped TiO_2/V_2O_5 nanocomposites films as the working electrode.

7) Charges storage device was designed in the sandwich structure with V-doped TiO_2/V_2O_5 working electrode and platinum film coated on FTO counter electrode. The parapolymer film was inserted between both electrodes to prevent short circuit of the device.

8) Liquid electrolyte consisting of 0.1 M of $LiClO_4$ and 0.5 M of $(COOH)_2$ in methanol was finally filled in the device.

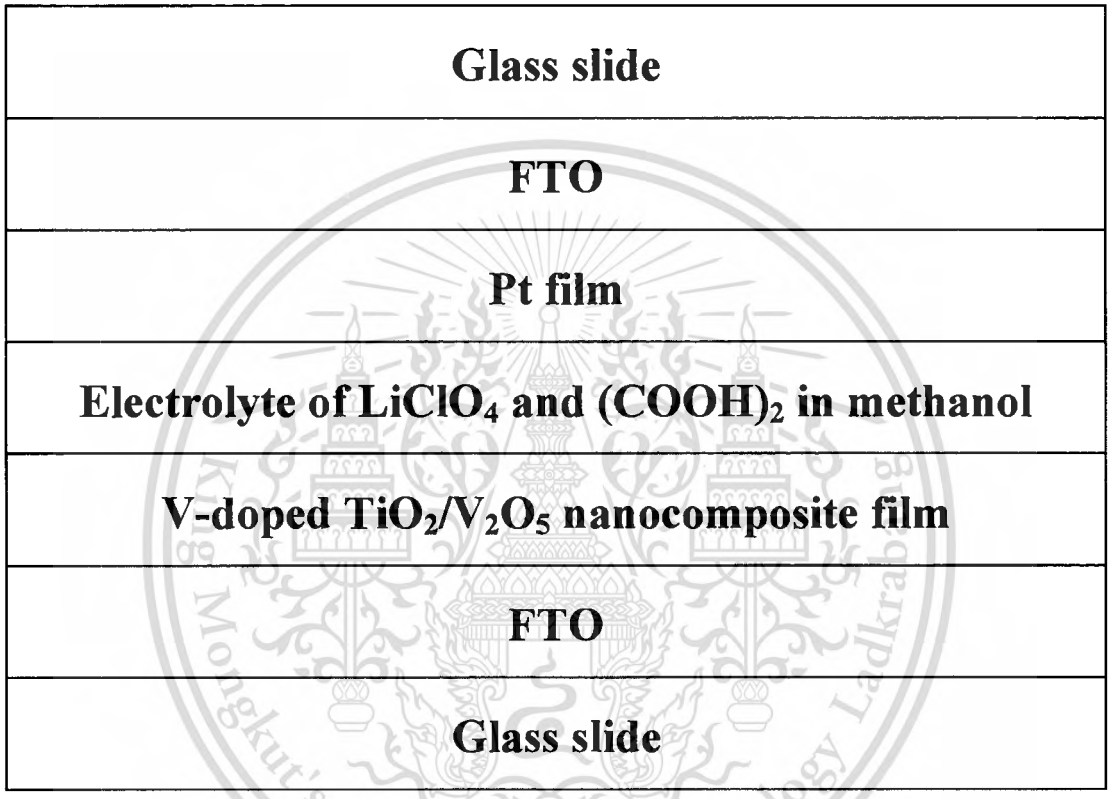

Figure 3.4 The schematic of V-doped TiO_2/V_2O_5 nanocomposite films for charges storage aplication.

3.4 Characterization

The crystal structure and phase identification of the samples were investigated by X-ray diffraction with a monochromatic source of Cu K_α (λ=0.15405 nm).

Raman spectroscopy (Thermo Scientific DXR Raman Microscope with 532 nm DPSS laser) was employed to verify the substitution of the Ti sites with V in the TiO_2 lattice.

X-ray photoelectron spectroscopy (AXIS Ultra DLD with dual anode Mg and Al K_α X-ray source) was applied to verify the chemical states of Ti and V.

Their morphologies were monitored with JEOL JSM-6340F field emission scanning electron microscope with an accelerating voltage of 5.0 kV.

Transmission electron microscopy images and selected area electron diffraction (SAED) patterns were taken with TECNAI G2 20 transmission electron microscope, using an accelerating voltage of 200 kV.

Chemical bonding of the materials was characterized by Fourier transform infrared spectroscopy (FTIR). FTIR studies were carried out in the range of 400-4000 cm^{-1} in the transmittance mode.

Photoelectrochemical measurement was conducted using Autolab PGSTAT302 with V-doped TiO_2/V_2O_5 nanocomposite film as the working electrode and Pt films as the counter electrode. Photocurrent measurement was carried out in the electrolyte of 0.1 M of $LiClO_4$ and 0.5 M of $(COOH)_2$ in methanol at room temperature. The current-potential curves were measured at a potential sweep rate of 20 mV/s in dark and under sun light irradiated by solar simulator lamp and Halogen lamp whose spectrum shown in Fig. 3.5.

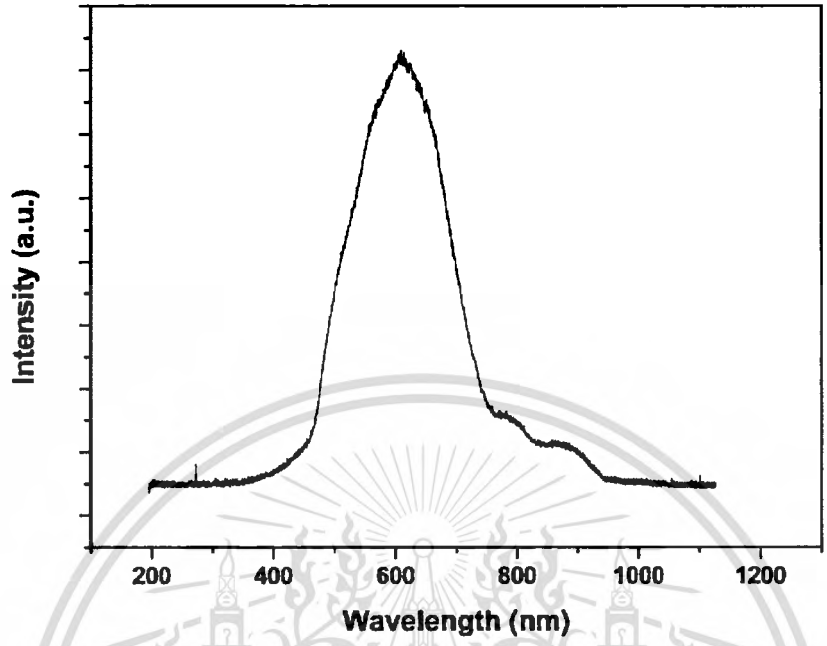

Figure 3.5 Spectrum of Halogen lamp.

CHAPTER 4

Results and Discussion

4.1 V-doped TiO_2 nanoparticles via the sonochemical process

In this sections, the results on the simple synthesis of V-doped TiO_2 nanoparticles by sonochemical precipitation process are reported. The effects of calcination temperature and vanadium content on crucial structural, physical and optical properties of as-prepared products were extensively scrutinized.

4.1.1 Effect of sonication time on physical properties of TiO_2 nanoparticles

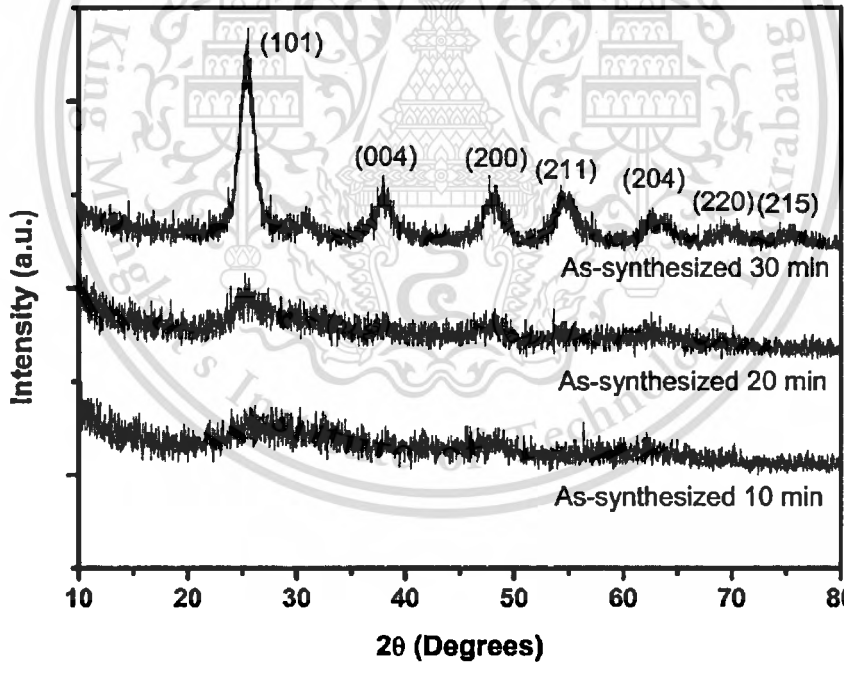

Figure 4.1 XRD patterns of the as-synthesized TiO_2 nanopowder irradiated with direct immersion of high intensity ultrasound titanium horn (750 W 20 kHz) with various sonication times 10-30 min.

The structural properties of as-synthesized TiO_2 nanopowders synthesized by sonochemical method with different sonication times were investigated by XRD

patterns as shown in Fig. 4.1. The XRD patterns of the products obtained with sonication times for 10 and 20 min do not show any sharp diffraction peaks with characteristics of crystalline phase. When the sonication time rises to 30 min, the sample shows prominent diffraction peaks situated at 2θ = 25.3°, 37.8°, 48.1°, 55.2°, 62.8°, 70.5° and 75.2°, which correspond to (101), (004), (200), (211), (204), (220) and (215) orientation plane with tetragonal structure of anatase phase (JCPDS File No. 89-4921), respectively. This result implies that as-sonochemically synthesized powder in anatase phase of TiO_2 can be produced by one-step sonochemical process using sonication time above 30 min without the heat treatment process [1].

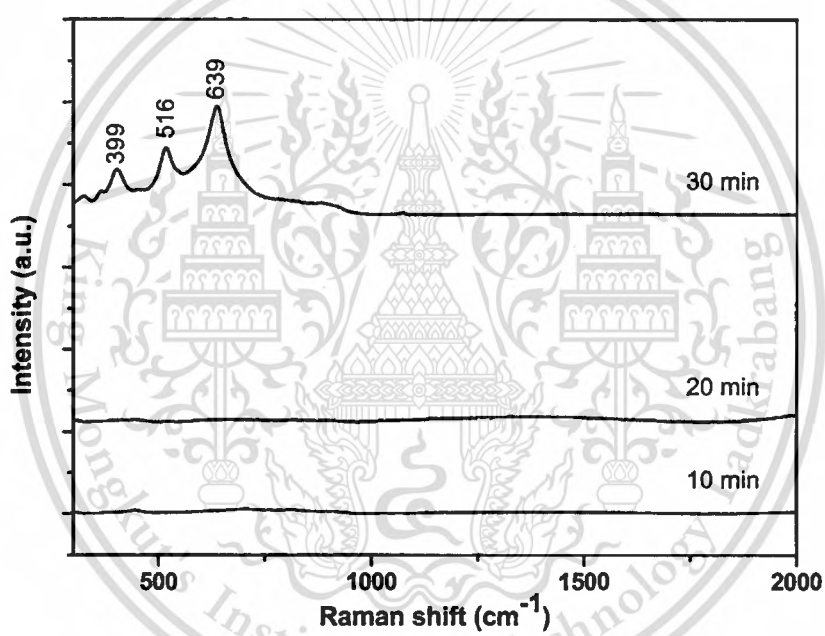

Figure 4.2 Raman spectra of the as-synthesized TiO_2 nanopowder irradiated with direct immersion of high intensity ultrasound titanium horn (750 W 20 kHz) with various sonication time 10-30 min.

Raman spectra of the samples synthesized at different sonication times are illustrated in Fig. 4.2. In Fig. 4.2, there is no characteristic peak of TiO_2 in Raman spectra of as-sonochemically obtained powder with sonication times for 10 and 20 min. Meanwhile, the samples sonicated with high intensity ultrasound for 30 min, the characteristic peaks at around 399, 516 and 639 cm^{-1} are attributed to B_{1g}, A_{1g} and E_g mode of anatase phase, respectively [2]. These results are in agreement with the

results revealed by XRD spectra. From XRD and Raman results, the formation mechanism of anatase TiO_2 particles initiated by sonochemical-assisted process is proposed. During dropping into deionized water, dissolved titanium isopropoxide in deionized water can proceed hydrolysis and condensation process to create functional hydrolyzed alcoxides, which have great amount of Ti-OH. The reaction is as follow:

$$Ti(OR)_4 + H_2O \rightarrow Ti(OH)_4 + 4R(OH) \text{ where R is } CH(CH_3)_2 \quad (4.1)$$

Simultaneously, rapid collision driven by high intensity ultrasound energy can sufficiently generate localized high temperature region, which is able to expedite the condensation reactions of hydroxyl groups to produce the nucleation of fine TiO_2 nanoparticles [3].

$$Ti(OH)_4 \rightarrow TiO_2 + 2H_2O \quad (4.2)$$

During ultrasonic irradiation, microjets formed due to the cavitational activity helps to form the resultant inorganic oxide particles with smaller and more uniform particle size. The proposed grown mechanism of TiO_2 nanoparticles via sonochemical process is shown in Fig. 4.3.

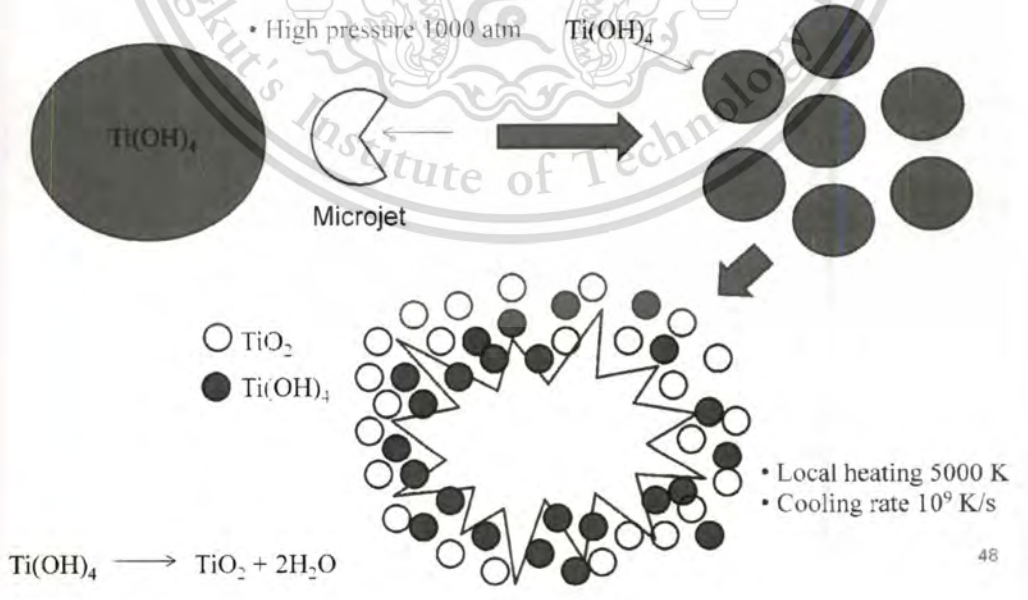

Figure 4.3 Growth mechanism of TiO_2 nanoparticles via sonochemical process.

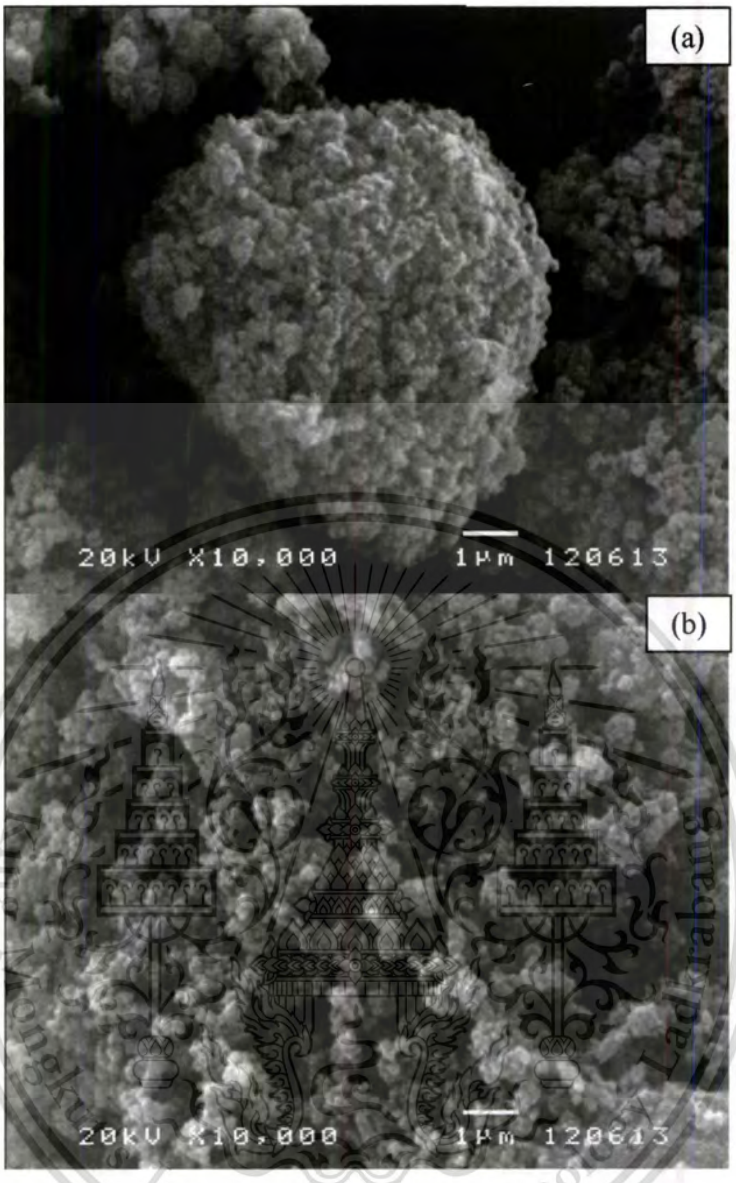

Figure 4.4 SEM images of TiO_2 synthesized by sonochemical-assisted process with (a) sonication time 10 min and (b) sonication time 30 min.

The SEM images illustrate the morphologies of TiO_2 synthesized by sonochemical-assisted process as demonstrated in Fig. 4.4. The SEM images disclose that the high intensity ultrasound can be reduced size of the powders from microsize to nanosize regime.

4.1.2 Effects of calcination temperature on physical properties of TiO_2 nanoparticles

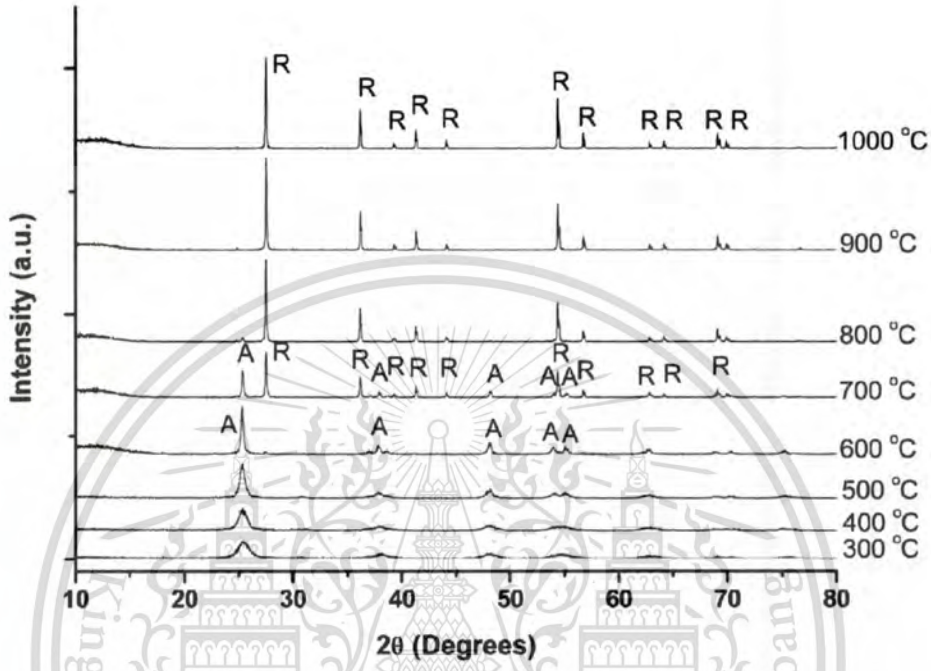

Figure 4.5 XRD patterns of TiO_2 nanoparticles synthesized by sonochemical-assisted process with different calcination temperatures 300-1000 °C.

Fig. 4.5 shows the XRD patterns of TiO_2 powders calcined at different temperatures from 300-1000 °C in air for 4 h. Noticeable diffraction peaks positioned at 2θ= 25.29°, 37.82°, 48.07°, 53.99° and 55.12° which are observed on the spectra of synthesized product calcined at 300-600 °C attribute to (101), (004), (200), (105) and (211) orientation plane of anatase-TiO_2 [JCPDS89-4921]. When the calcinations temperature elevated to 700 °C, the mixture peaks of the anatase and rutile phase were observed with rutile phase being the predominance and completely transformed to rutile phase as the temperature was over 800 °C. These results indicate that the phase transformation between anatase and rutile phase is activated at calcinations temperature higher than 600 °C. In addition, the transformation sequence and thermodynamic phase stability between the two titania polymorphs anatase and rutile depend on the initial particle sizes [4].

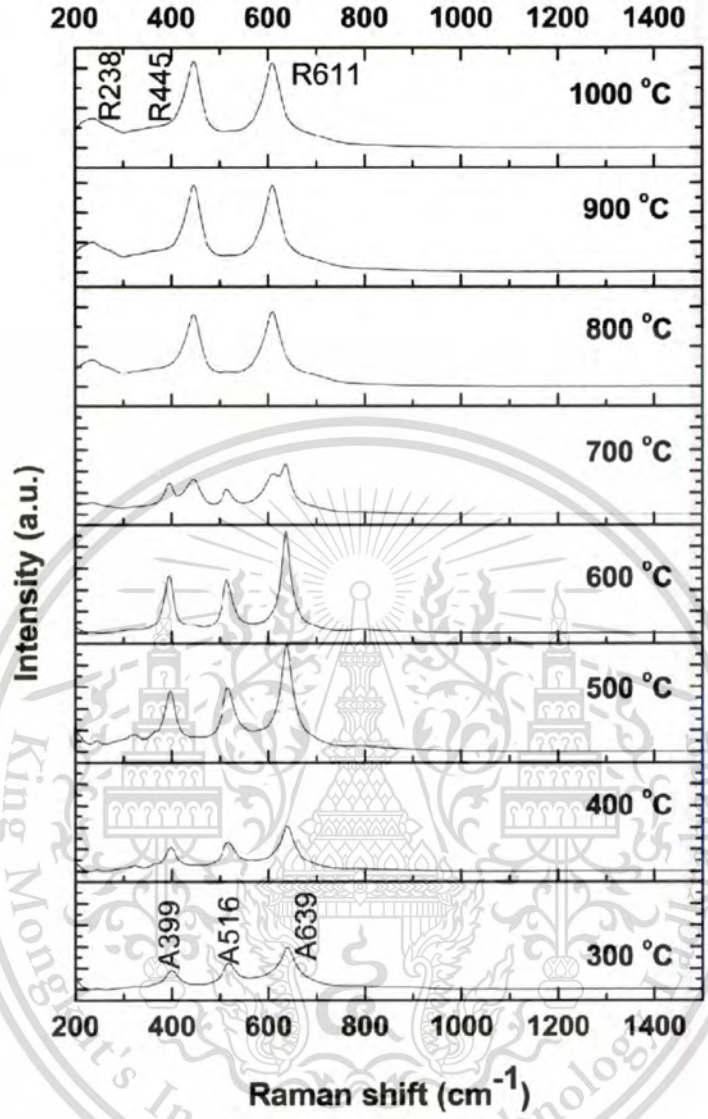

Figure 4.6 Raman spectra of TiO_2 nanparticles synthesized by sonochemical-assisted process at different calcination temperatures 300-1000 °C.

Raman spectra of the samples prepared at different calcinations temperature is illustrated in Fig. 4.6. In Fig. 4.6, for the sample calcined at 300-600 °C, the characteristic peaks at around 399, 516 and 639 cm^{-1} are attributed to B_{1g}, A_{1g} and E_g mode of anatase phase, respectively [5]. The rutile phase was obtained as the calcinations temperature ascended to 700 °C or even higher, the characteristic peaks of rutile phase at 235, 447 and 612 cm^{-1} ascribed to two-phonon scattering, E_g and A_{1g} mode of rutile phase are clearly noticed [5]. These results are in harmony with the results revealed by XRD spectra.

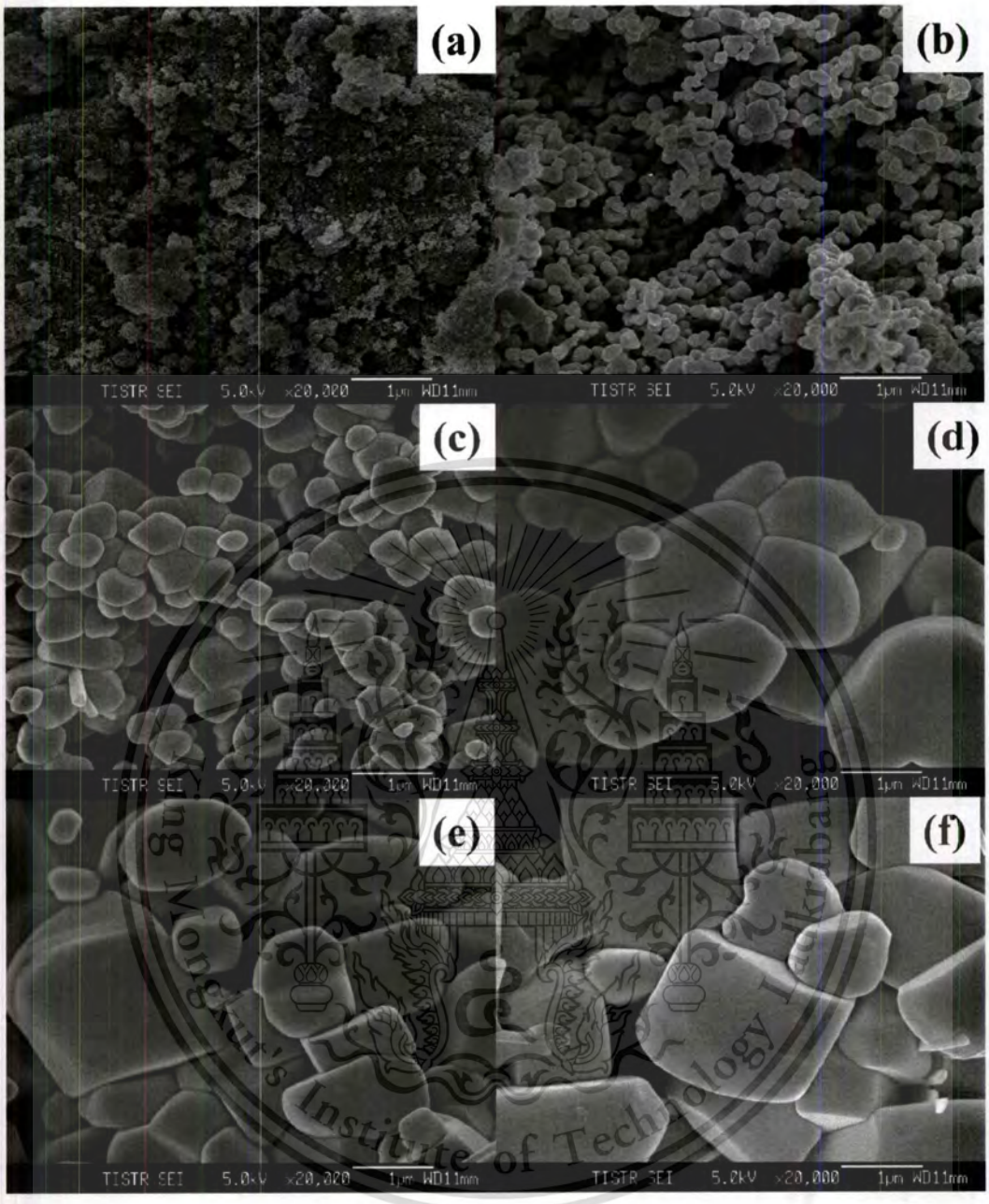

Figure 4.7 SEM images of TiO_2 synthesized by sonochemical-assisted process and calcined at (a) 500 °C, (b) 600 °C, (c) 700 °C, (d) 800 °C, (e) 900 °C and (f) 1000 °C.

The SEM images exhibiting the morphologies of TiO_2 powder calcined at different temperatures are demonstrated in Fig 4.7. The SEM images disclose that the precipitate powders from sonochemical-assisted process are aggregated form nanosize to microsize after calcinations temperature elevates from 500 °C to 1000 °C.

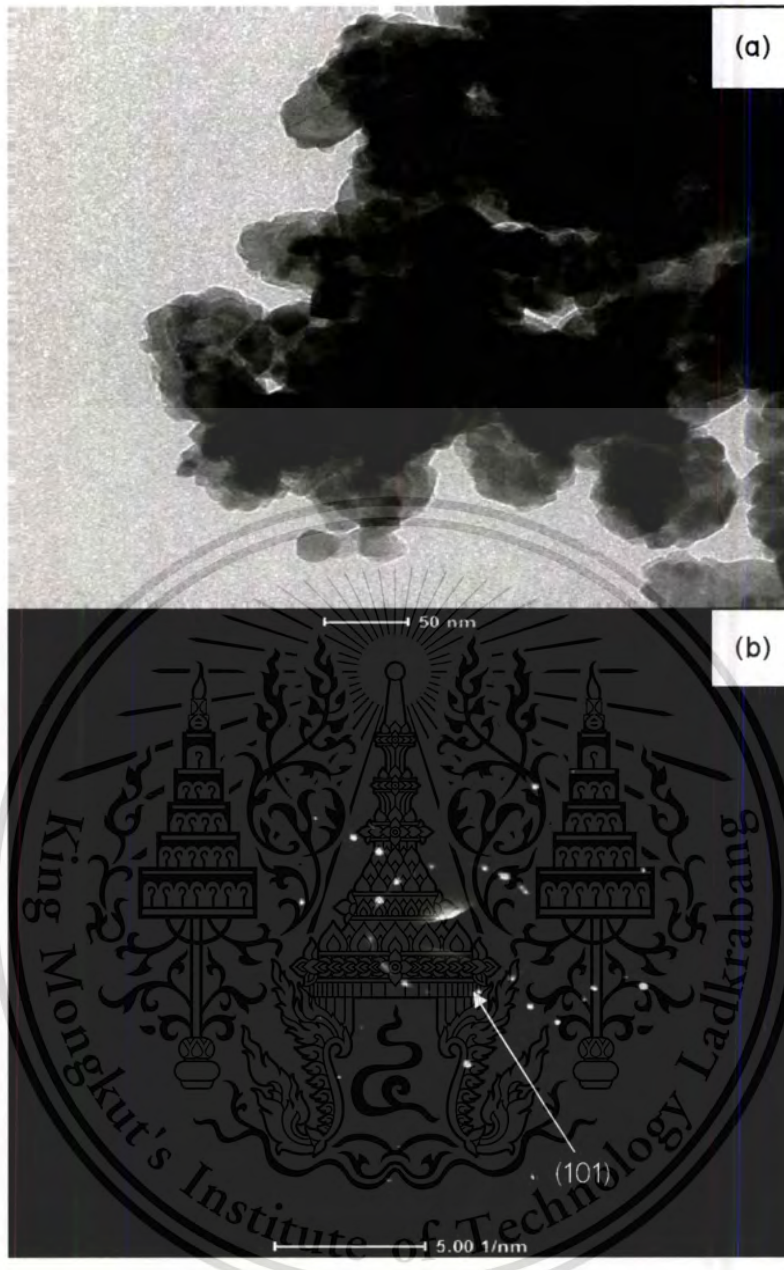

Figure 4.8 TEM images of (a) TiO_2 nanoparticles and (b) SAED image of TiO_2 synthesized by sonochemical-assisted process and calcined at 500 °C for 4 hr.

TEM images and electron diffraction patterns of TiO_2 nanopowders are shown in Fig. 4.8. It clearly seen that the TiO_2 have a quasi-spherical structure with diameter of 20-30 nm and show the polycrystalline after calcined at 500 °C as shown in Fig. 4.8 (a) and 4.8 (b).

4.1.3 Effects of vanadium doping content on physical and optical properties of V-doped TiO_2 nanoparticles

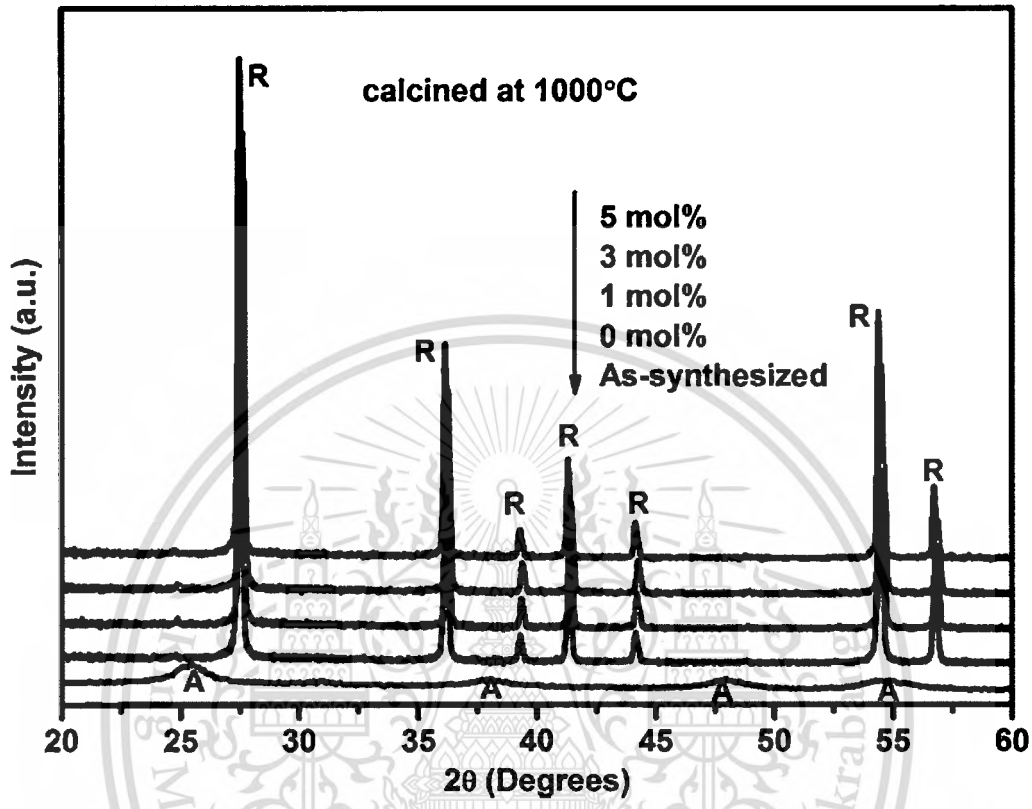

Figure 4.9 XRD patterns of the V-doped TiO_2 nanoparticles synthesized by sonochemical-assisted process with different vanadium doping contents.

Fig. 4.9 exhibits the XRD patterns of the V-doped TiO_2 with different V doping contents. As observed in all doped samples, the intense and sharp diffraction peaks situated at 2θ = 27.49°, 36.12°, 39.26°, 41.29°, 44.12°, 54.40° and 56.73° are assigned to (110), (101), (200), (111), (210), (211) and (220) plane of rutile phase [JCPDS89-4920]. No characteristic peaks ascribed to vanadium oxides (such as V_2O_5 or VO_2) were detected, indicating that the V ions can suitably be doped into TiO_2 lattice [6].

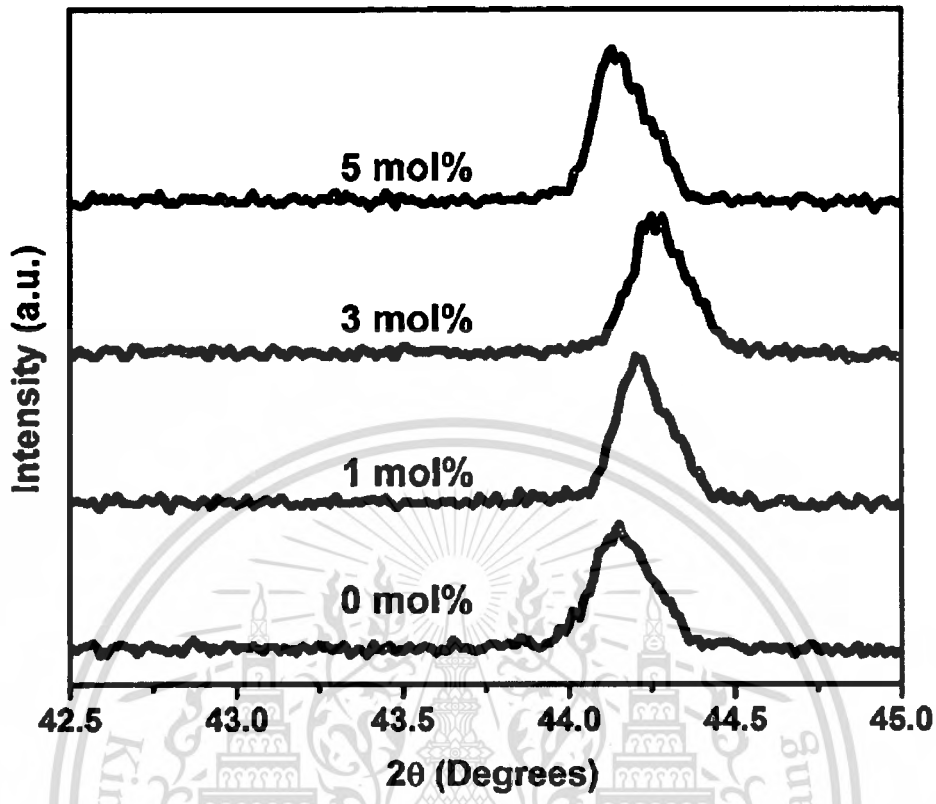

Figure 4.10 An enlargement of the rutile (200) peaks for undoped and V-doped TiO_2 nanoparticles synthesized by sonochemical process.

In addition, the significant shifts of peak positions to higher angle are observed (Fig. 4.10) as V doping content increases up to 3 mol% thereafter shifts back to lower angle, indicating the alternation of *d*-spacing of TiO_2 with specific V doping content. The inteplanar spacing (*d*-spacing) and crystallite size of the V-doped TiO_2 could be determined by Bragg's law and Scherrer equation as shown in Fig. 4.11. This alternation in *d*-spacing may attributable to the proper replacement of smaller ionic radius of V^{4+} (0.72 Å) at specific content on some of Ti^{4+} (0.75 Å) sites leading to the noticeable spacing shrinkage in TiO_2 [7].

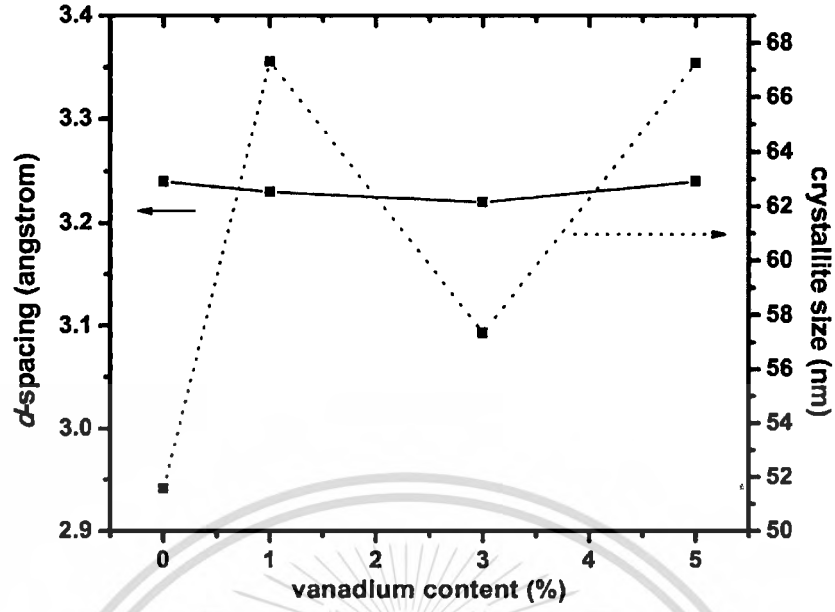

Figure 4.11 The effect of vanadium doping in the interplanar *d*-spacing and crystalline size of V-doped TiO_2 (5 % of vanadium) nanoparticles synthesized by sonochemical process.

Table 4.1 Characteristics of V-doped TiO_2 with different condition.

V-contents (mol%)	Temperature (°C)	*d*-spacing (Å)	Crystallite size (nm)
0	1000	3.24^{R}	51.57^{R}
1	1000	3.23^{R}	67.31^{R}
3	1000	3.22^{R}	57.35^{R}
5	1000	3.24^{R}	67.25^{R}

[A] calculated from (101) orientation plane of anatase.

[R] calculated from (110) orientation plane of rutile.

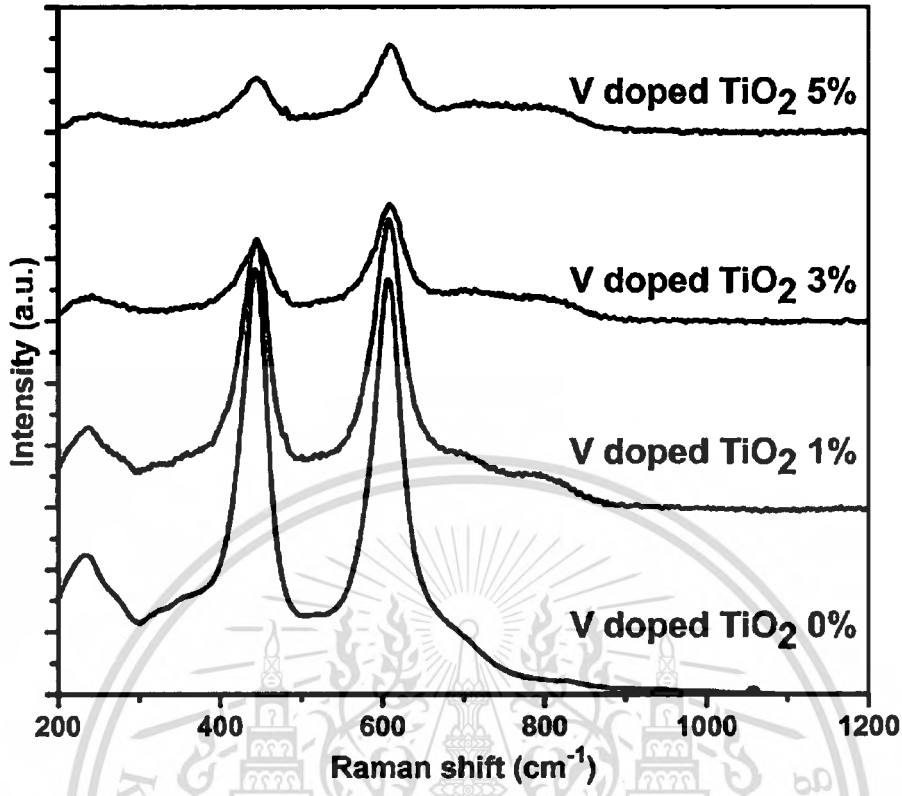

Figure 4.12 Raman spectra of the V-doped TiO_2 nanparticles synthesized by sonochemical process with different vanadium contents (calcined at 1000 °C for 4 h).

Fig. 4.12 displays the Raman scattering of the V-doped TiO_2 with different V doping contents and calcined at 1000 °C for 4 h. All results indicate the scattering peaks around 235, 447 and 612 cm^{-1} corresponded to the characteristic peaks of anatase phase and the intensities of all characteristic peaks decrease with increasing doping content. Furthermore, the scattering peaks associated to the V-O compounds were undetectable. These results also imply the suitable doping of vanadium into anatase TiO_2 [8], which well agreeable to the presumption from XRD results.

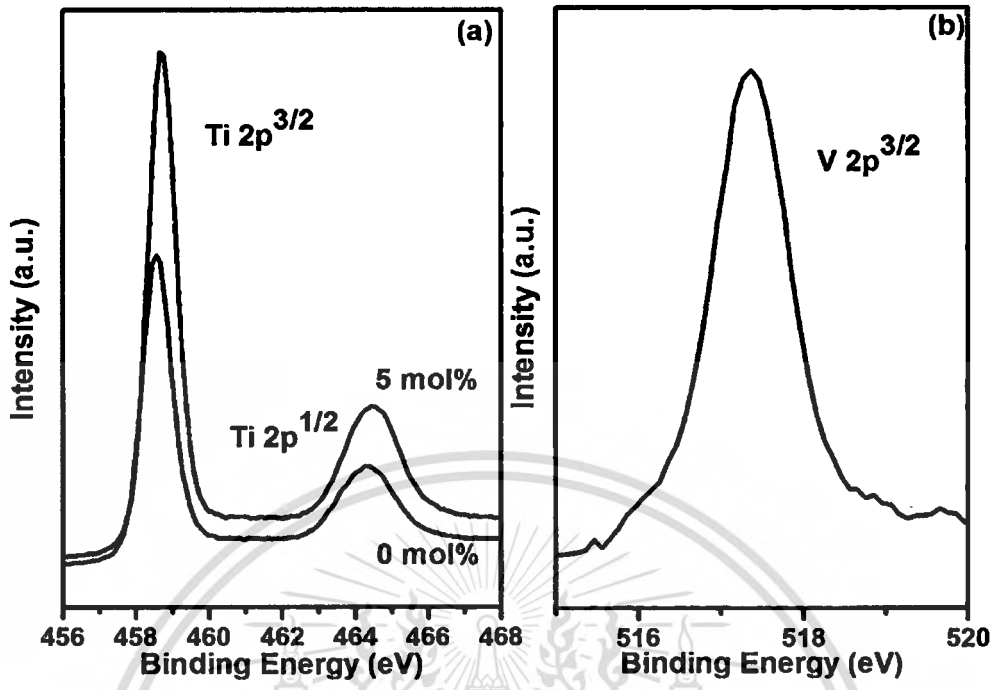

Figure 4.13 XPS spectra of the V-doped TiO_2 5 mol% calcined at 1000 °C for 4 hr synthesized by sonochemical process in (a) the Ti *2p* regime and (b) the V *2p* regime.

Additionally, the chemical composition of V-doped TiO_2 nanoparticle was analyzed by XPS as shown in Fig. 4.13. The peaks appearing at 458.7 and 464.3 eV are associated to Ti^{4+} $2p^{3/2}$ and Ti^{4+} $2p^{1/2}$, respectively [9]. It is an indication of the existence of Ti^{4+} ions in the sample. For V-doped TiO_2, The peak positions of Ti *2p* slightly shift to high binding energies, suggesting that V ions are incorporated into TiO_2 lattice [10]. In Fig. 4.13 (b), the peaks appearing at binding energies of 517.2 eV could be ascribed to the V^{4+} $2p^{3/2}$ [11]. It is confirmed that the V^{4+} ions exist in the V-doped TiO_2 but the vanishment of V $2p^{1/2}$ binding energy due to the low of V doping [11]. This result strongly confirmed that the V^{4+} were appropriately incorporated into TiO_2 lattice and substituted to Ti^{4+} site due to its close ionic radius (Ti^{4+} = 0.75 Å and V^{4+} = 0.72 Å) [12].

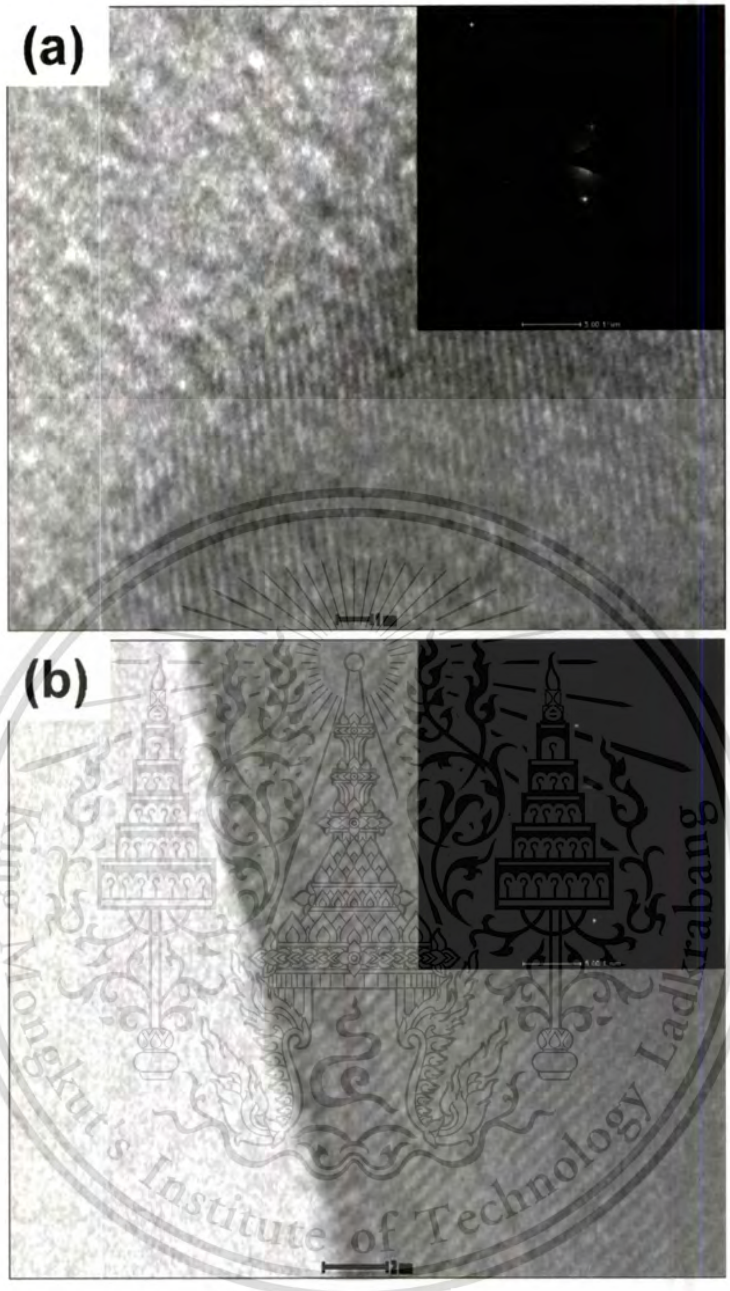

Figure 4.14 TEM images of TiO_2 (a) undoped TiO_2 and (b) 5 mol% V-doped TiO_2 synthesized by sonochemical process and calcined at 1000 °C for 4 h (scale bar 1 and 2 nm; the insert images are SEAD mode).

High magnification and Selected Area Electron Diffraction (SEAD) mode of undoped and 5 mol% V-doped TiO_2 nanoparticles are shown in Fig 4.14. The results reveal that the samples consist of interplanar spacing along the length direction of 3.27 Å and 3.25 Å for undoped and V-doped TiO_2, respectively. The TEM results

revealing the decrease of interplanar spacing of TiO_2 due to V dopant is in good accordance with the values calculated from XRD patterns.

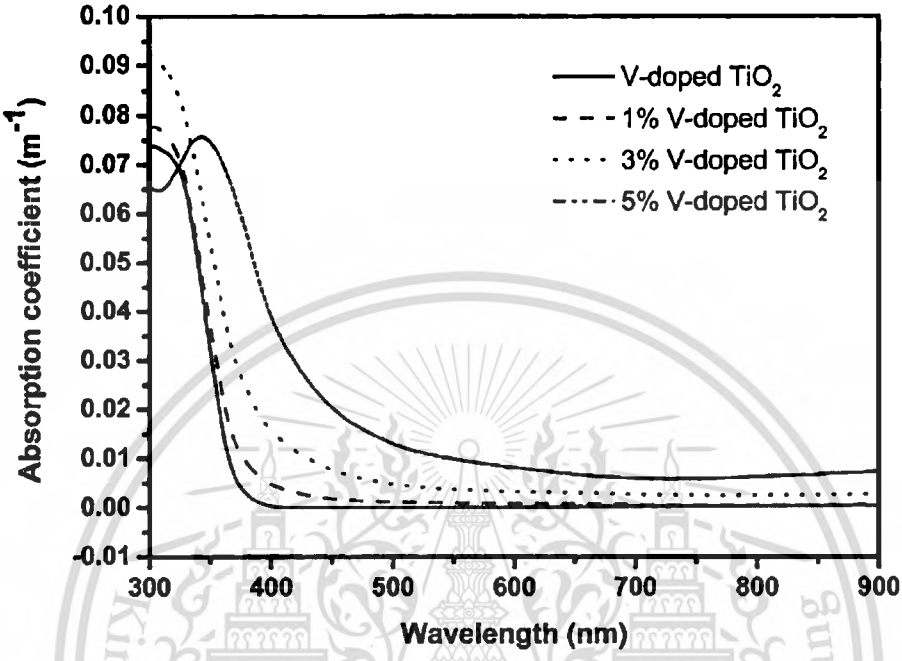

Figure 4.15 UV-Vis diffuse reflectance (DR) spectra of TiO_2 and V-doped TiO_2 nanoparticles with difference V doping of 0-5 mol%.

The UV-vis. absorption spectra of pure and V-doped TiO_2 with different V doping concentration were evaluated to investigate the shift of the light absorption edge after V doping in TiO_2. The obtained results are displayed in Fig. 4.15. Pure TiO_2 shows strong UV light absorption with absorption edge located at 375 nm but no visible light absorption is found. All the doped samples shifted their light absorption edges towards visible light region. In V-doped TiO_2 samples, along with visible light absorption, no decrease in UV light absorption was observed compared with that of pure TiO_2. V doping effectively narrows the band gap of TiO_2, which leads to the enhanced visible light absorption. The 5 mol% V-doped TiO_2 sample shows the highest absorption in the visible light range with absorption edge located at 450 nm. The effective visible light absorption of V-doped TiO_2 samples is mainly attributed to the existence of impurity states in the band gap of TiO_2 due to V doping, which narrows the band gap and then the electrons can be shifted from the valence band to

the conduction band excited by the visible light photons. With the increase of V doping concentration, the light absorption edges were shifted well to the visible light region [12].

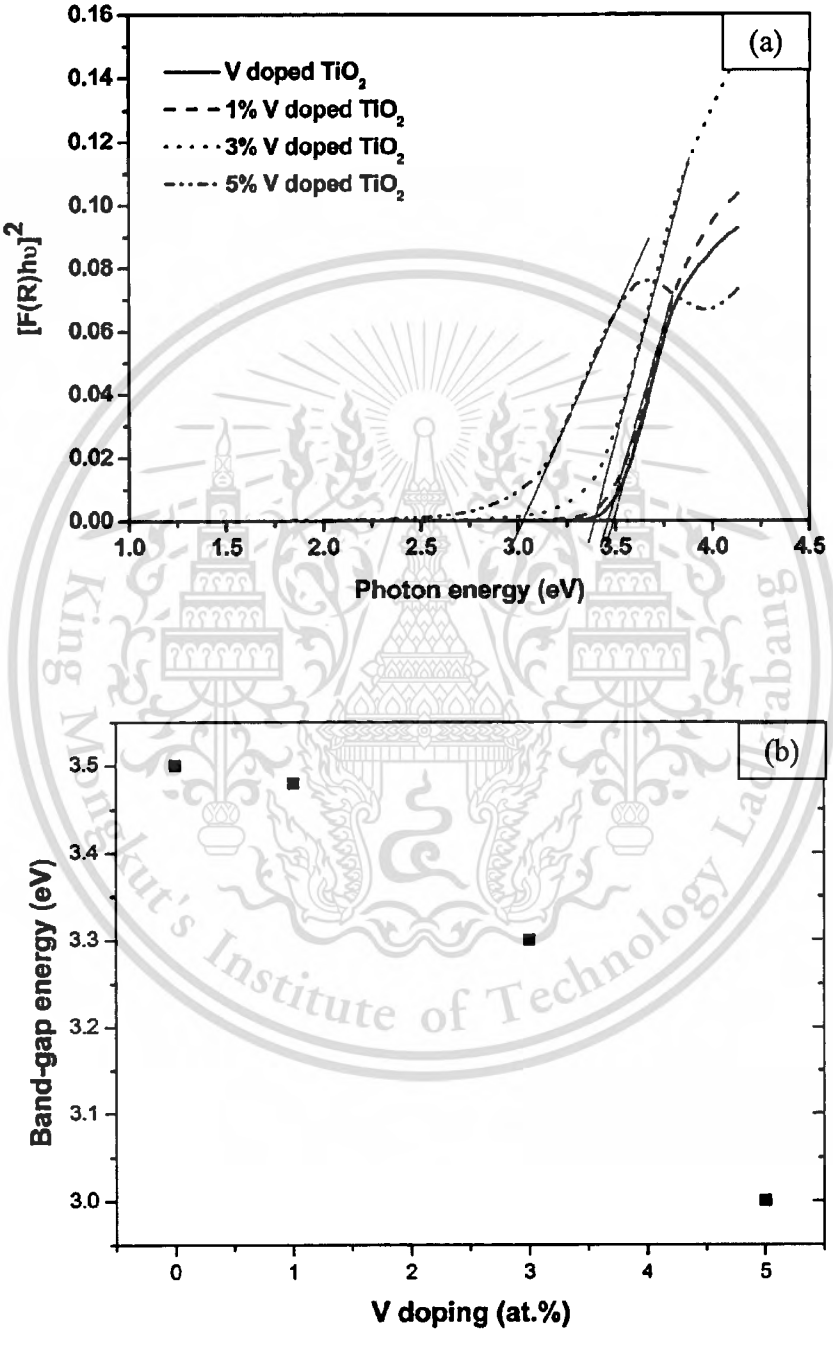

Figure 4.16 (a) Kubelka-Munk transformed reflectance spectra of V-doped TiO_2 nanoparticles with difference V doping 0-5 mol%. (b) Band gap as a function of V doping of V-doped TiO_2 nanoparticles.

Fig. 4.16 (a) illustrates the plot of Kubelka-Munk function as a function of photon energy of V-doped TiO_2 nanoparticles with difference V doping contents. Optical band gap can be calculated from the absorption spectrum. The Kubelka–Munk equation [13] for an "infinitely thick" layer is shown in equation (4.3);

$$\frac{K}{S} = \frac{(1-R_\infty)^2}{2R_\infty} \equiv F(R_\infty) \tag{4.3}$$

Where R_∞ is the absolute reflectance of the layer, S is the scattering coefficient and K is the molar absorption coefficient. The band gap energy can be measured by the Kubelka–Munk plots of $(1\text{-}R_\infty)^2/2R_\infty$ versus photon energy, where the x-axis intercepted value is the optical band gap energy. The measured band gap energies of V-doped TiO_2 nanoparticles are shown in the insert image. Undoped TiO_2 gives a optical band gap value of 3.50 eV, which is higher than the typical value of bulk TiO_2 (3.20 eV) due to the quantum size effect of the sample on the optical band gap energy [14].

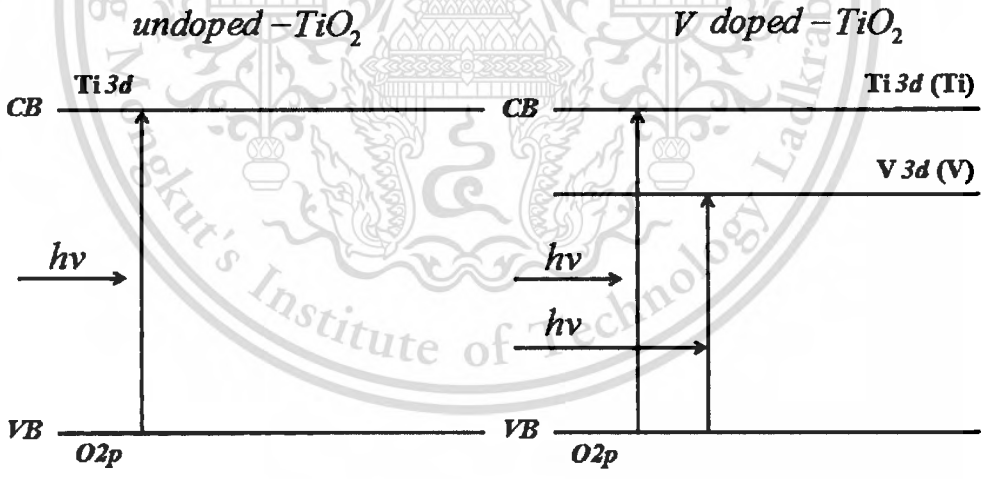

Figure 4.17 The suggested energy band structure of undoped and V-doped TiO_2.

Doping of 1-5 mol% V induces a decreasing of optical band gap energy to 3.49 ~ 3.10 eV. It is also worth to notice that for 1-5 mol% V-doped TiO_2 the light absorption in both UV and visible regions are greatly increased. The effective red shift of band gap and the evidently enhanced light absorption in UV–Visible region are beneficial to the photo-induced activity of V-doped TiO_2. Furthermore, the red

shift of the absorption edge and the light absorption in the visible light region increased with increasing the V-doping content in TiO_2 nanoparticles. It has been studied that the red shift of absorption edge for the sampless might be attributed to the electron transition from the valence band (O *2p*) to the V *3d* orbit and the visible light absorption might be related to the *d-d* transition of vanadium (as shown in Fig. 4.17). As observed Fig. 4.16 (b), the band gaps of V-doped TiO_2 nanoparticles decreased from 3.49 to 3.10 eV when the V doping contents of V-doped TiO_2 nanoparticles increased from 0 to 5 mol%. It was revealed that V doping could effectively extend the light absorption of TiO_2 into the visible region [15].

4.2 VO_2 nanostructures via the hydrothermal synthesis

This section reports the results on the synthesis of VO_2 nanostructures using hydrothermal method. The effects of types of reductant agents, reaction temperature, reaction time and thermal temperature on crucial structural and physical properties of as-prepared products were investigated.

4.2.1 Effects of types of reductant agents on the formation of VO_2 nanorods

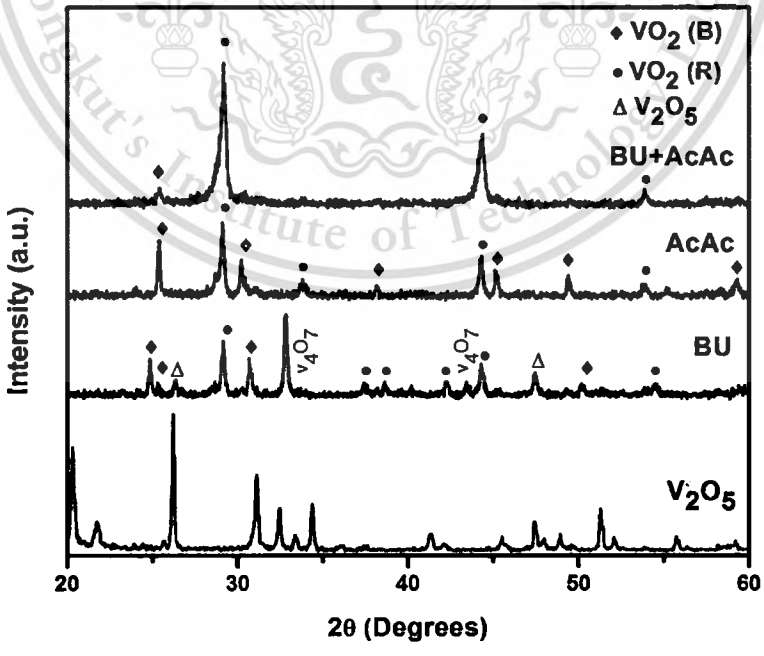

Figure 4.18 XRD patterns of the commercial V_2O_5 powders and VO_2 synthesized by hydrothermal method at 120 °C for 48 h using different reducing agents.

XRD patterns of as-synthesized vanadium oxide via the hydrothermal process at 120 °C for 48 h using different reductant agents are shown in Fig. 4.18. In the case of *n*-butanol as the reductant agent, the XRD pattern displays multi-diffraction peaks of mixed structures. The diffraction peaks positioned at 2θ = 26.1° and 47.3° are attributed to (110) and (600) orientation plane of orthorhombic structure of V_2O_5 [JCPDS file No. 89-2482]. This result suggests that the complete transformation of VO_2 phase could not be carried out by only *n*-butanol reducing agent. In contrast, the diffraction peaks of VO_2 are appeared in the XRD pattern of the as-synthesized product from process using acetylacetone as the reductant agent. The disappearance of diffraction peaks of V_2O_5 indicates that the starting material can be completely transformed into VO_2 with hydrothermal process using acetylacetone as the reductant agent. However, the diffraction peaks reveal the mixture phases of VO_2 (B) and VO_2 (R) with the monoclinic structures [16,17]. In the case of dual reductants of *n*-butanol and acetylacetone, the prominent diffraction peaks situated at around 2θ = 28.0°, 44.0° and 53.0° are assigned to (011), (021)/(012) and (102) orientation plane of VO_2 (R), respectively. In addition, a noticeable peak at around 2θ= 25.4° is attributable to (110) orientation plane of VO_2 (B). Based on XRD results, it can be deduced that *n*-butanol, acetylacetone and temperature are the important factors in the transformation of V_2O_5 to VO_2.

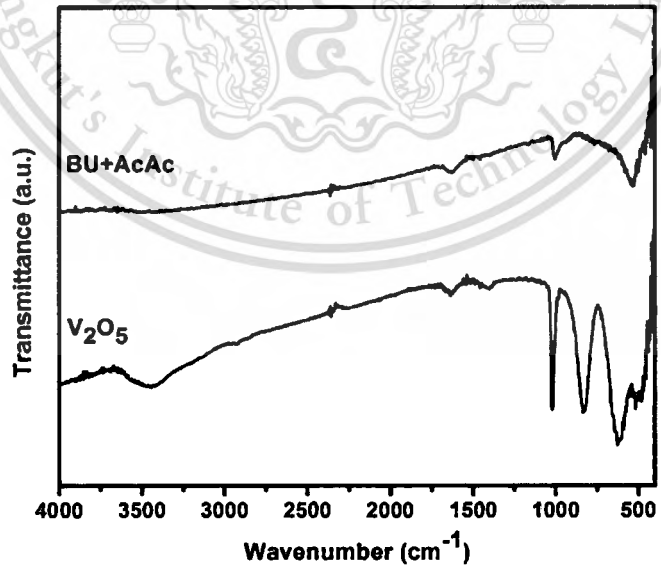

Figure 4.19 FTIR spectra of the commercial V_2O_5 powders and VO_2 powders synthesized by hydrothermal method at 120 °C for 48 h using dual reducing agents.

The chemical bonding of the starting materials and as-synthesized VO_2 nanorods carried out by hydrothermal process at 120 °C for 48 h using dual reductant agents are shown in Fig. 4.19. The prominent band situated at about 3460 and 1650 cm^{-1} are associated to the stretching and bending vibration mode of absorbed H_2O and O-H groups by KBr molecules, respectively [18]. The characteristic peaks of V_2O_5 are identified at around 1025, 830, 598 and 480 cm^{-1}. The peak at 1025 cm^{-1} relates to V=O stretching vibration mode, while the broad peak at around 830 cm^{-1} is attributed to coupled vibration mode between V=O and V-O-V [19]. The 1000 cm^{-1} peak observed in VO_2, which generally exists in many vanadium oxide compounds corresponds to another mediate oxidation state between V^{5+} in V_2O_5 and V^{4+} in VO_2. It is attributed to the stretching mode of short V=O bonds that are also presented in VO_2 [20]. The signal peak positioned at around 540 cm^{-1} in the FTIR spectrum of VO_2 is assigned to the vibrational bending mode of V-O-V [21], These FTIR results are in good accordance with the presumption from XRD results.

Meanwhile the possible mechanisms responsible for the formation of V_2O_5 nanorods via hydrothermal process are suggested. First, the starting V_2O_5 powders were dissolved and the oxidation state +5 of vanadium is reduced to +4 by the presence of *n*-butanol and acetylacetone acting as reducing agents. Possible reaction process demonstrating the synthesis of VO_2 nanorods can be proposed;

_n_-butanol as the reductant

$$V_2O_5 + CH_3(CH_2)_3OH \rightarrow 2VO_2 + CH_3(CH_2)_2CHO + H_2O \quad (4.4)$$

$$V_2O_5 + CH_3(CH_2)_2CHO + 2H_2O \rightarrow 2VO_2H_2O + CH_3(CH_2)_2COOH \quad (4.5)$$

$$VO_2H_2O \rightarrow VO_2 + H_2O \quad (4.6)$$

Acetylacetone as the reductant

$$V_2O_5 + CH_3COCH_2COCH_3 \rightarrow CH_3COCHO + CH_3COOH + 2VO_2 \quad (4.7)$$

Under hydrothermal, the intermediate species can undergo condensation and nucleation of vanadium oxide nuclei that can rapidly develop to various types of low dimensional nanostructures including nanorods and nanobelts [22]. It is suggested that the formation of VO_2 nanorods is reasonably explained by a nucleation and crystallization process which can be expressed by a detailed model as shown in Fig. 4.20. First, the VO_2^{+4} in the system is formed by the presence of *n*-butanol and acetylacetone acting as reducing agents. At the Simultaneous reaction, V(+4) is reduced to V(+5) and the VO_2^{+4} nuclei are formed and these nuclei develop into fragments under the hydrothermal reaction. Second, with the reaction time extending, the fragments are aggregated and combined, leading to the trend of nanorods.

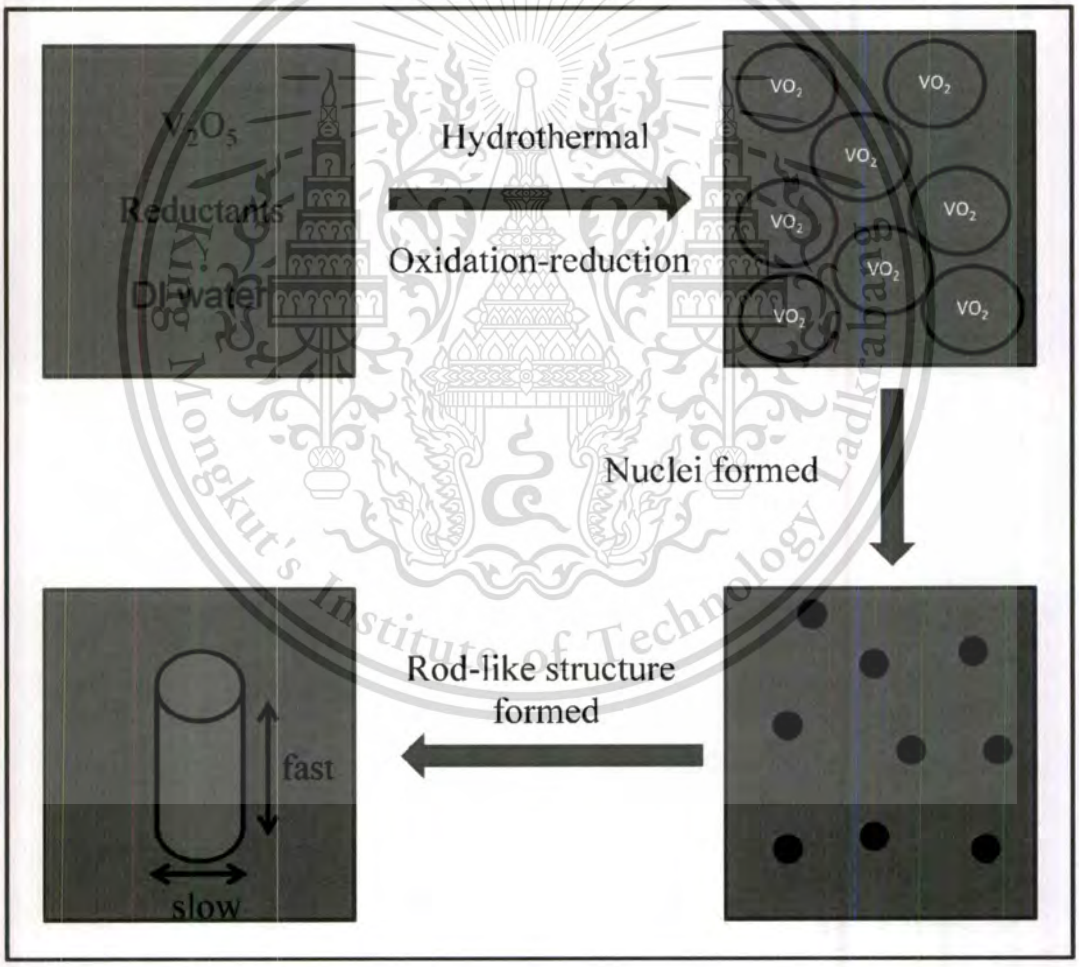

Figure 4.20 Schematic illustration of the growth mechanism of VO_2 nanorods.

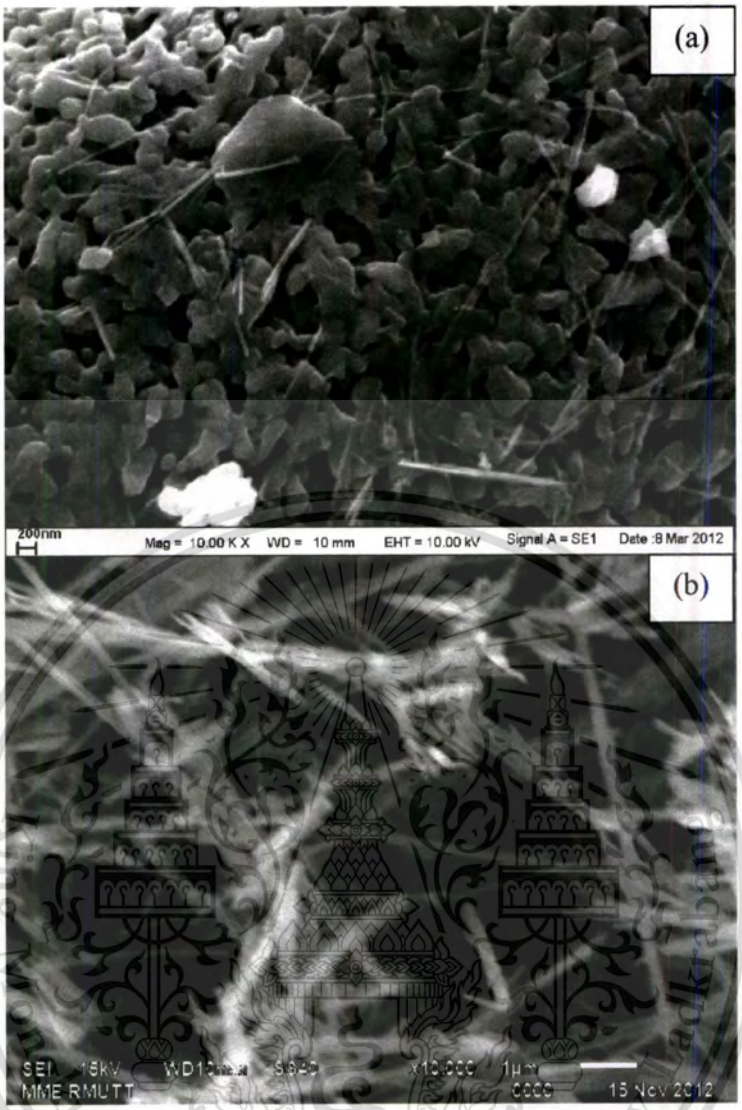

Figure 4.21 SEM images of (a) commercial V_2O_5 powders and VO_2 nanorods synthesized by facile hydrothermal method at 120 °C for 48 h using (b) *n*-butanol as reductant, (c) acetylacetone as a reductant and (d) dual *n*-butanol and acetylacetone as reductants.

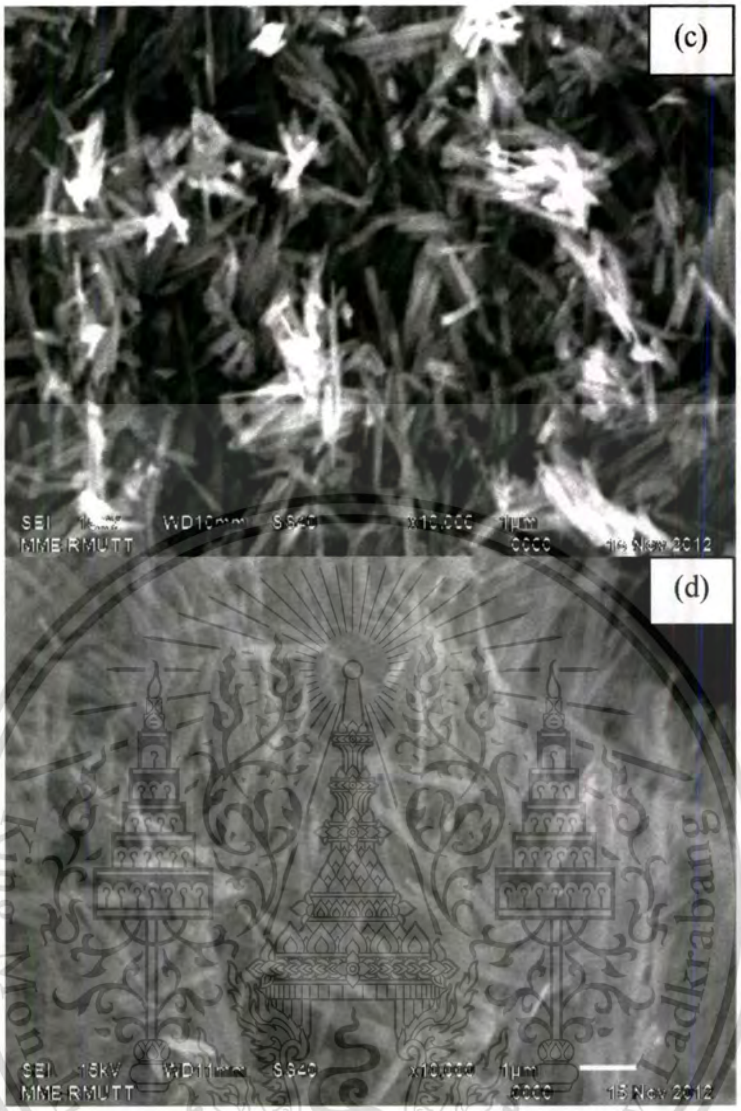

Figure 4.21 (cont.) SEM images of (a) commercial V_2O_5 powders and VO_2 nanorods synthesized by facile hydrothermal method at 120 °C for 48 h using (b) *n*-butanol as reductant, (c) acetylacetone as a reductant and (d) dual *n*-butanol and acetylacetone as reductants.

The SEM images as seen in Fig. 4.21 illustrate the morphologies of the V_2O_5 and VO_2 nanorods synthesized via the hydrothermal process at 120 °C for 48 h using dual reducing agents. It is clearly seen that the hydrothermal process not only evidently transform its crystal structure of V_2O_5 to VO_2 but also change physical structure of this material from brain-like to nanorod-like with strong influence of reductant types on size dimension of the rods.

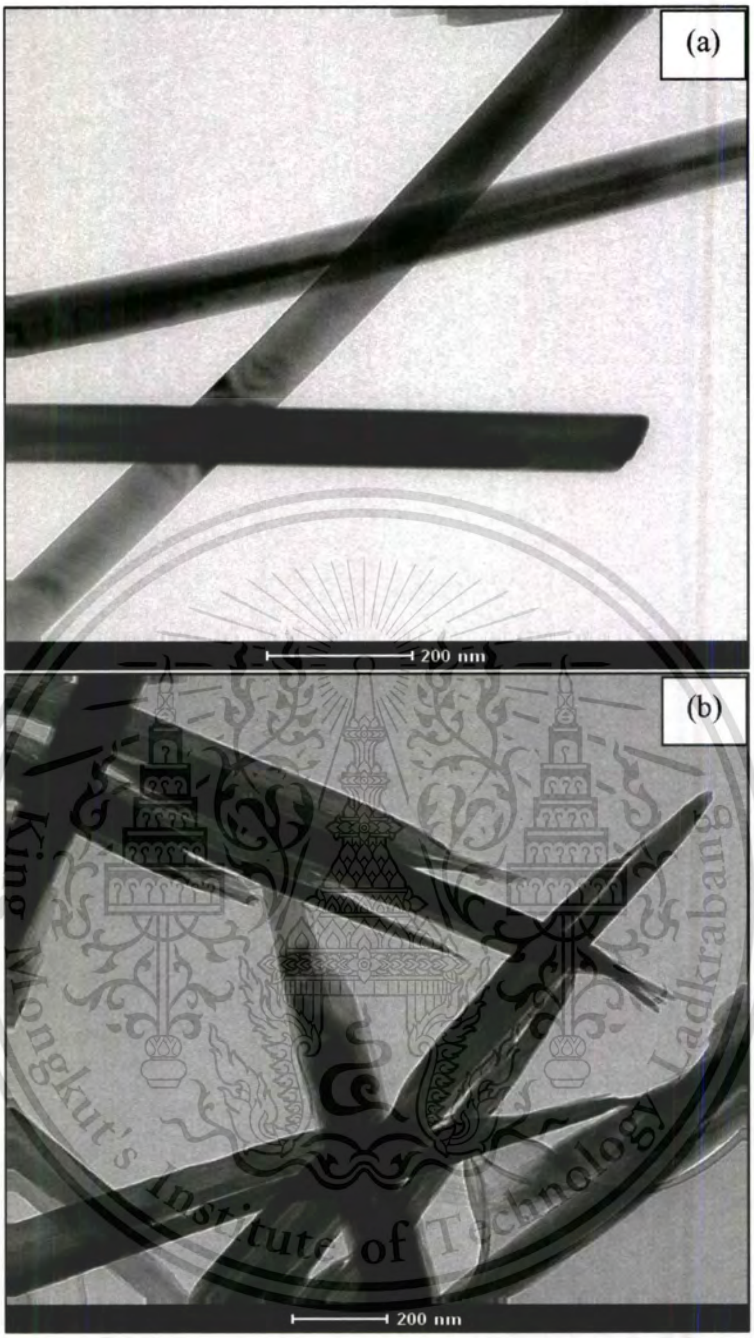

Figure 4.22 TEM images of VO_2 nanorods synthesized by facile hydrothermal method at 120 °C for 48 h with (a) *n*-butanol as the reductant, (b) acetylacetone as the reductant, (c) dual *n*-butanol and acetylacetone as the reductants and (d) SAED image of the sample using dual reductants.

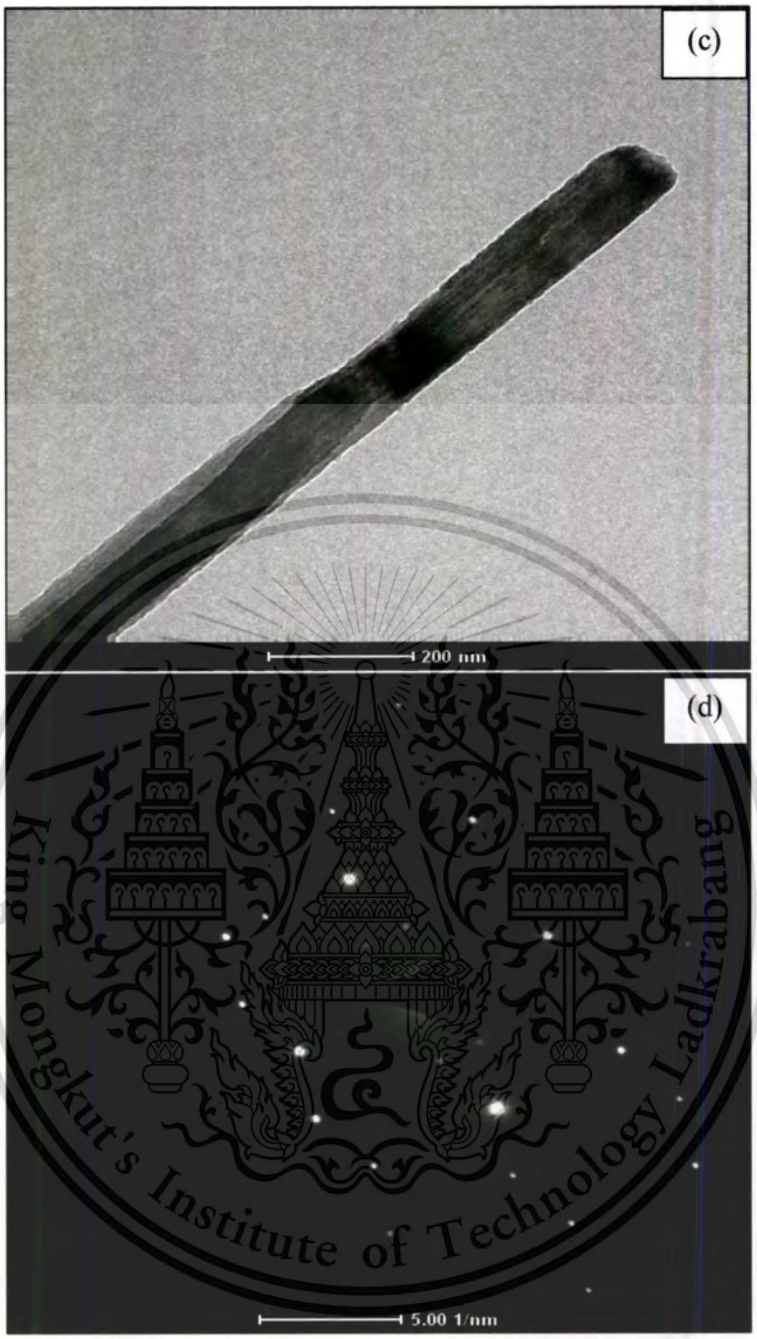

Figure 4.22 (cont.) TEM images of VO_2 nanorods synthesized by facile hydrothermal method at 120 °C for 48 h with (a) *n*-butanol as the reductant, (b) acetylacetone as the reductant, (c) dual *n*-butanol and acetylacetone as the reductants and (d) SAED image of the sample using dual reductants.

TEM images of as-synthesized sample using *n*-butanol as the reductant as seen in Fig. 4.22 (a) exhibits uniform rod-like structure with diameter of about 80 nm and

length over 10 μm. Meanwhile, Fig. 4.22 (b) shows the leaf-like structure of the sample using acetylacetone as a reductant, which appears to be an ultra thin cut of the parallel-piped with a diameter of 100 nm and a length of 2 μm. For the sample obtained by using dual *n*-butanol and acetylacetone as the reductants, Fig. 4.22 (c) exhibits the short-rod like structure with a diameter of 80 nm and a length 2-3 μm. Selected area electron diffraction (SAED) image as observed in Fig. 4.22 (d) can confirm that the as-synthesized VO_2 possesses high degree of crystallization. From SEM and TEM results, it is affirmed that the one-dimensional VO_2 can be synthesized by single-step hydrothermal method without any further post-treatment.

4.2.2 Effects of reaction temperatures on physical properties of VO_2 nanorods

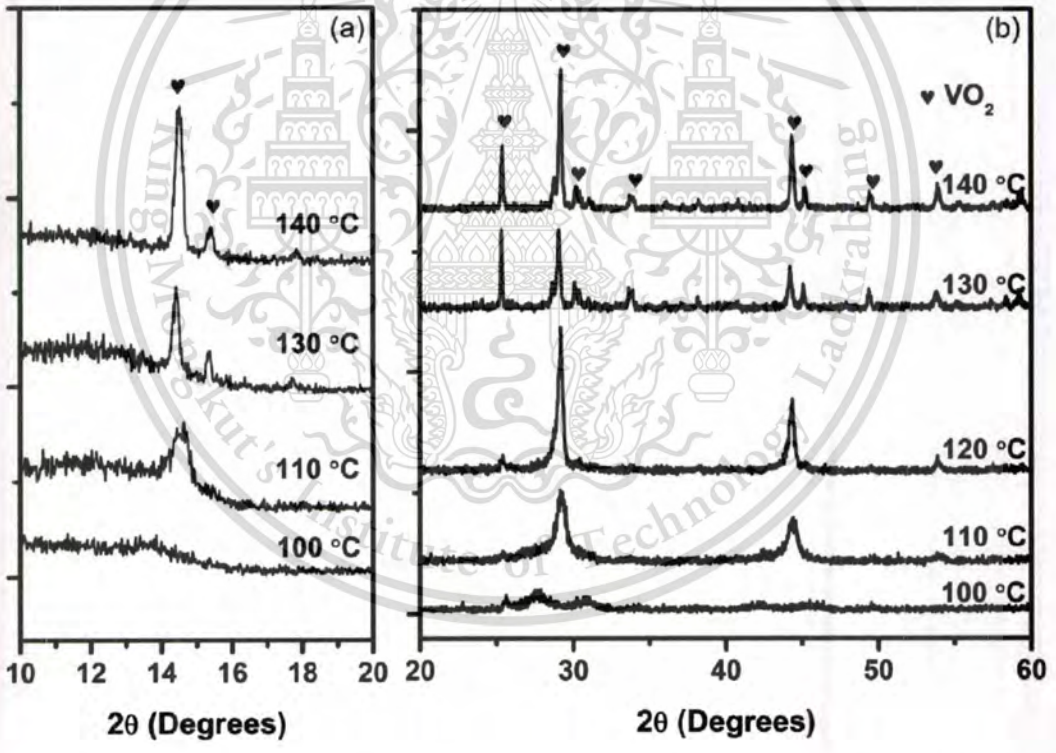

Figure 4.23 XRD patterns of the VO_2 synthesized by hydrothermal method at 100-120 °C for 48 h using dual butanol and acetylacetone as the reducing agents (a) at 2θ = 10-20° and (b) at 2θ = 20-60°.

Fig. 4.23 shows the XRD patterns of the samples synthesized by hydrothermal method at temperatures ranging from 100 and 140 °C for 48 h using dual butanol and

acetylacetonate as the reductant agents. In the case of 100 °C, XRD patterns show broadening peaks, indicating that the sample have an amorphous phase. In the case of 110 °C, the prominent diffraction peaks situated at around 2θ = 28.0°, 44.0° and 53.0° are assigned to (011), (021)/(012) and (102) orientation plane of VO_2 (R), respectively. In addition, a noticeable peak at around 2θ= 25.4° is attributable to (110) orientation plane of VO_2 (B). Based on XRD results, it can be concluded that reaction temperature at 110 °C for 48 h is the optimized factor in the complete transformation of V_2O_5 to VO_2.

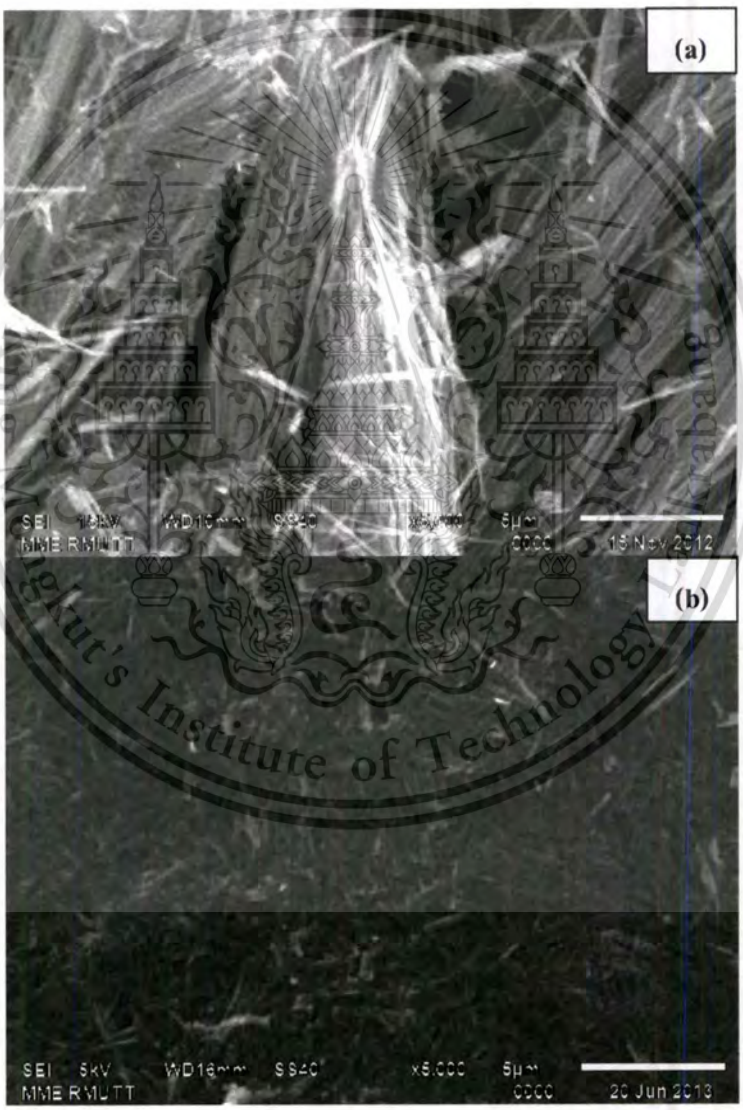

Figure 4.24 SEM images of the VO_2 synthesized by hydrothermal process at (a) 100 °C, (b) 110 °C, (c) 120 °C, (d) 130 °C and (e) 140 °C for 48 h using dual butanol and acetylacetone as the reducing agents.

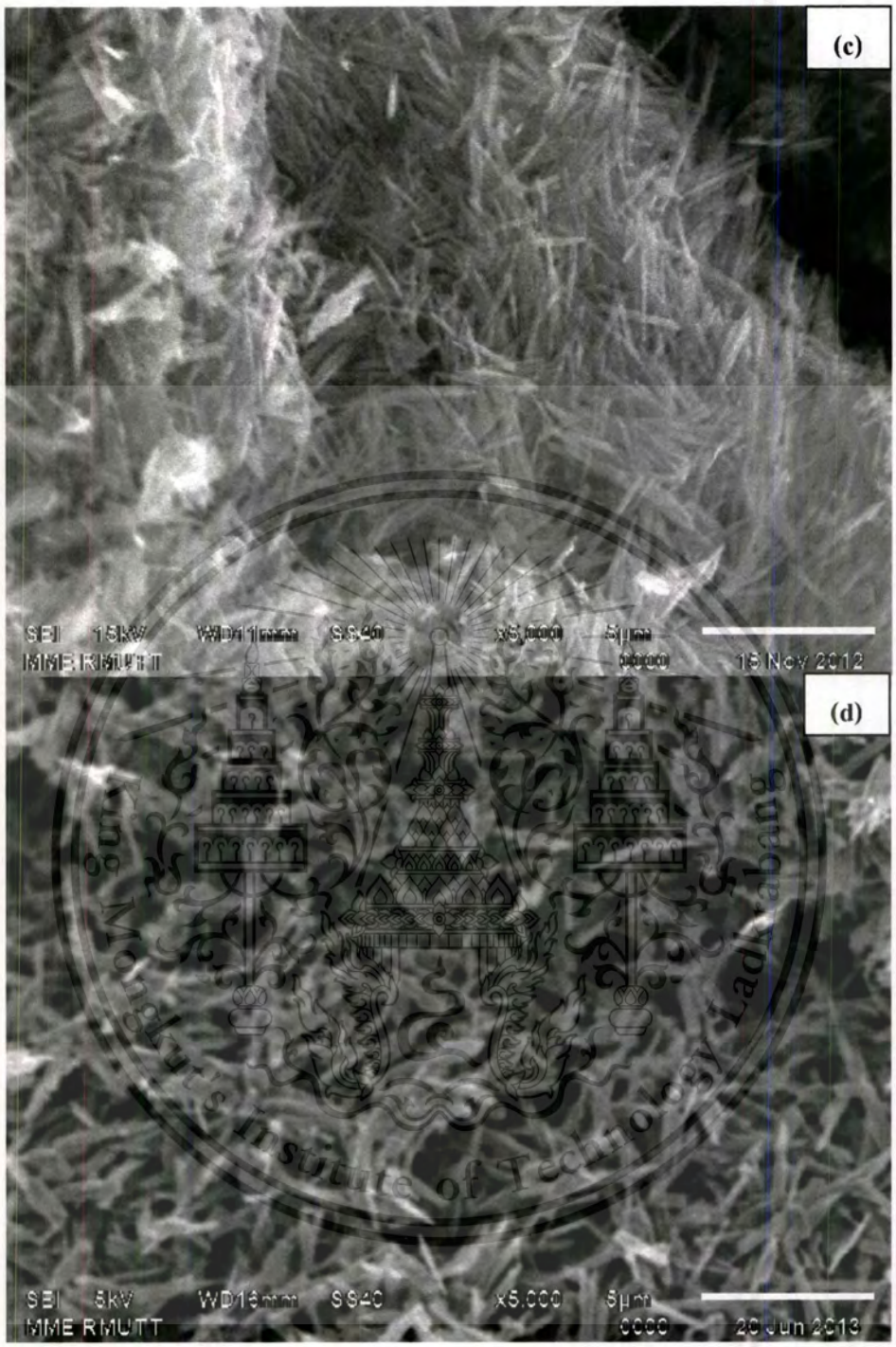

Figure 4.24 (cont.) SEM images of the VO_2 synthesized by hydrothermal process at (a) 100 °C, (b) 110 °C, (c) 120 °C, (d) 130 °C and (e) 140 °C for 48 h using dual butanol and acetylacetone as the reducing agents.

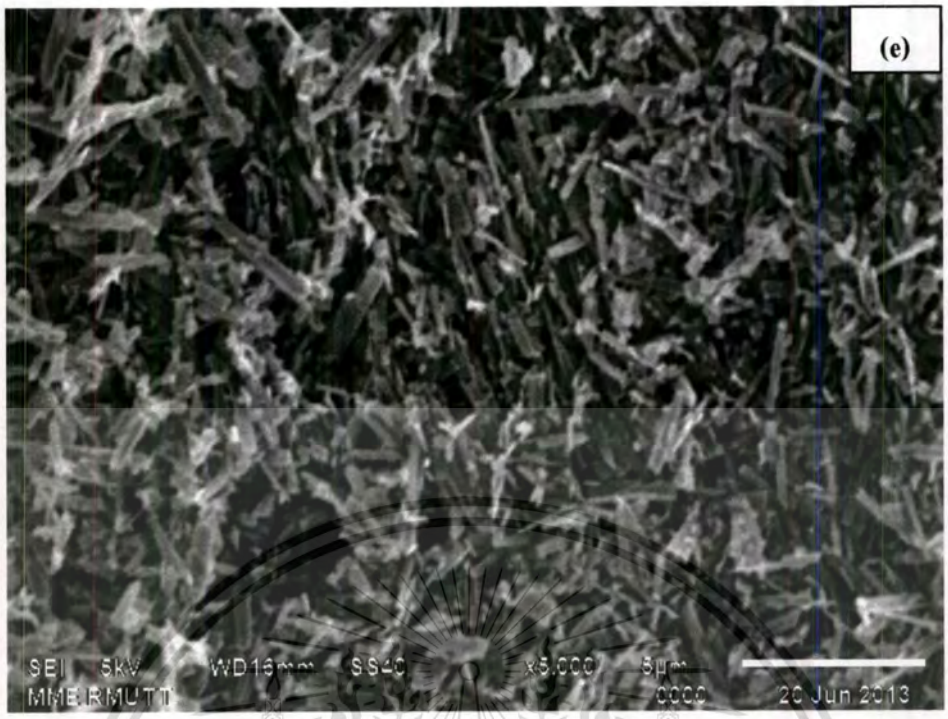

Figure 4.24 (cont.) SEM images of the VO_2 synthesized by hydrothermal process at (a) 100 °C, (b) 110 °C, (c) 120 °C, (d) 130 °C and (e) 140 °C for 48 h using dual butanol and acetylacetone as the reducing agents.

The SEM images as seen in Fig. 4.24 illustrate the morphologies of the VO_2 synthesized by hydrothermal method at 100-140 °C for 48 h using dual reducing agents. It is clearly seen that the reaction temperature not only evidently transform its crystal structure but also change physical structure of this material from nanostraw-like to nanobelt-like with increasing reaction temperature from 100-140 °C.

4.2.3 Effects of reaction time on physical properties of VO_2 nanorods

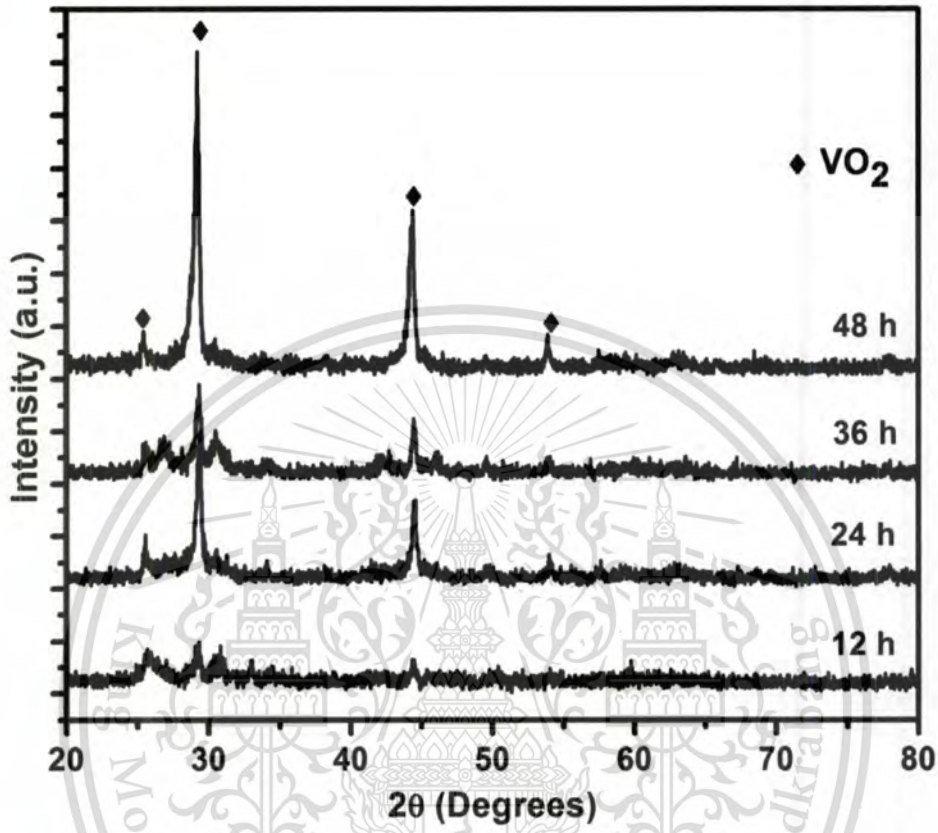

Figure 4.25 XRD patterns of the VO_2 synthesized by hydrothermal method at 120 °C with different reaction time using dual butanol and acetylacetone as the reducing agents.

The XRD patterns of the samples synthesized by hydrothermal process at 120 °C for different periods of reaction time are shown in Fig. 4.25. In the case of reaction time for 12 h, the XRD pattern consists of dual phase of VO_2(B) and VO_2(R), which corresponds to monoclinic structure. However, the noticeable diffraction peaks revealing other structures of vanadium oxide are unavailable in this pattern. This result indicates that monoclinic structure of VO_2 can be synthesized by hydrothermal treatment using dual *n*-butanol and acetylacetone at 120 °C for 12 h. In the case of long period reaction time, the intensity of diffraction peaks of VO_2(R) increases with increasing the hydrothermal treatment period. Meanwhile, the intensity of diffraction peak of VO_2(B) exhibit insignificant change. The previous analysis and these results

indicate that the high phase of monoclinic structure VO_2(R) phase can be obtained with increase in reaction temperature or the extension of reaction time at specific temperature.

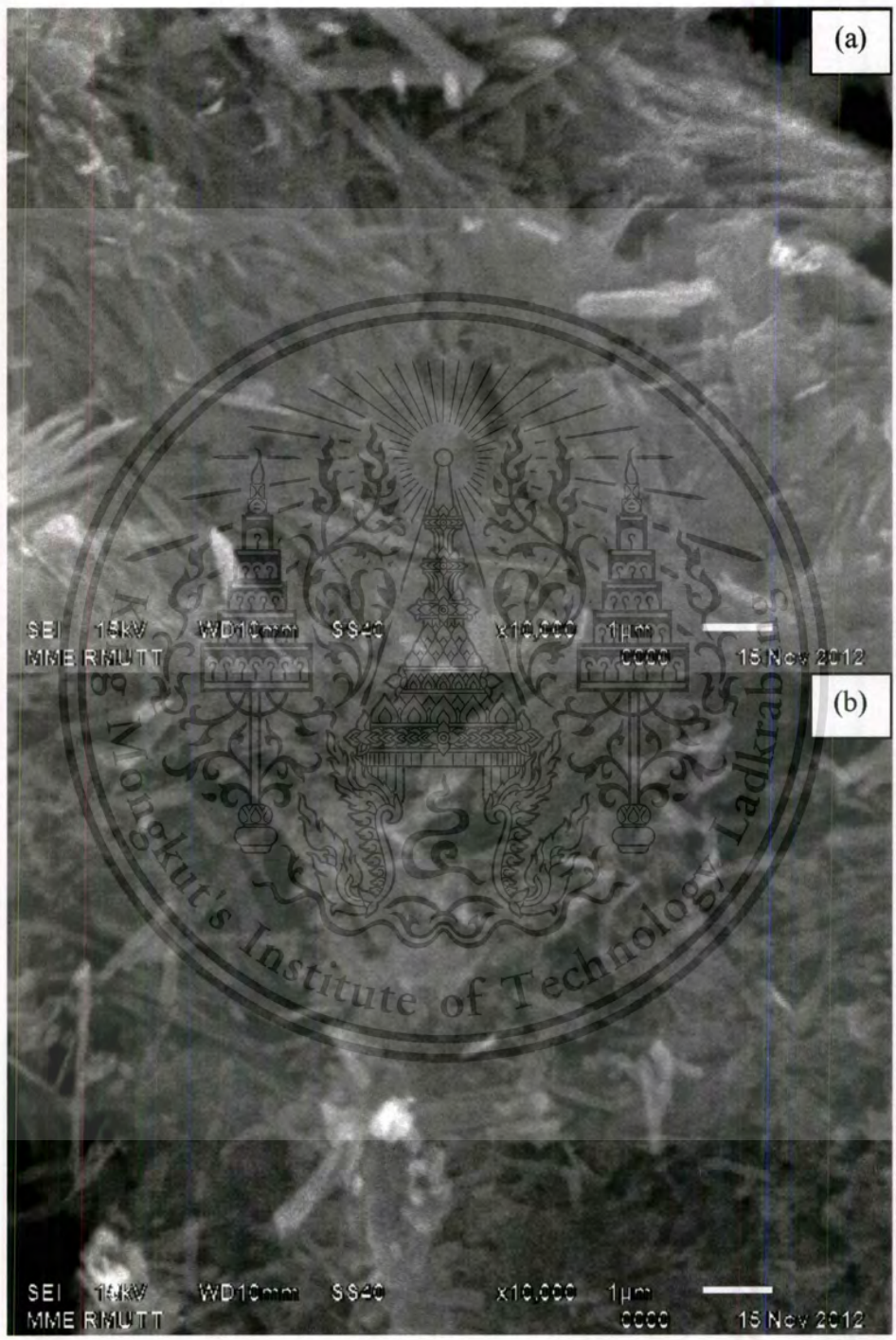

Figure 4.26 SEM images of the VO_2 synthesized by hydrothermal method at 120 °C with different reaction time (a) 12 hr, (b) 24 hr, (c) 36 hr and (d) 48 hr using dual butanol and acetylacetone as the reducing agents.

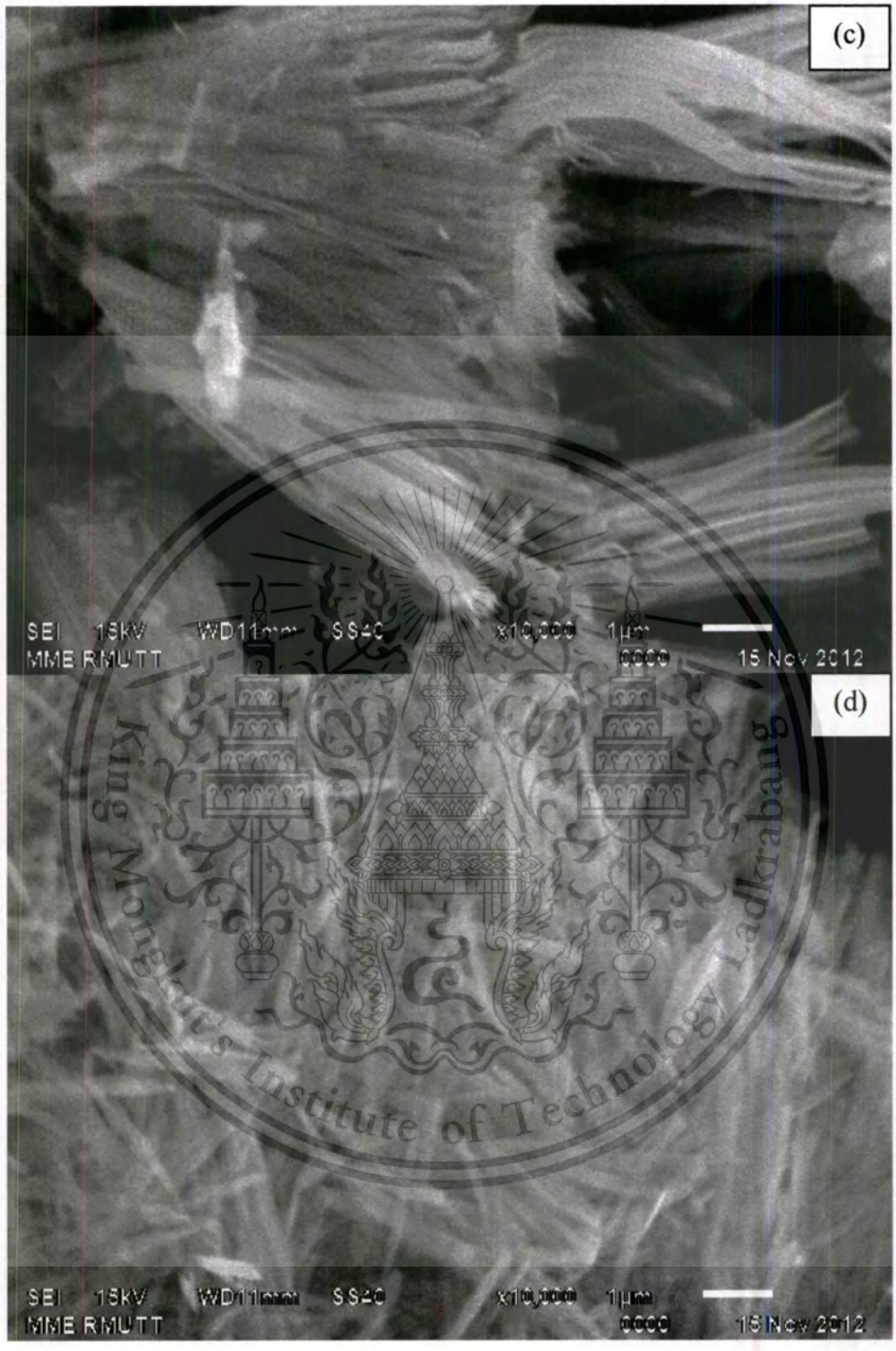

Figure 4.26 (cont.) SEM images of the VO_2 synthesized by hydrothermal method at 120 °C with different reaction time (a) 12 hr, (b) 24 hr, (c) 36 hr and (d) 48 hr using dual butanol and acetylacetone as the reducing agents.

The reaction time also plays an important role in controlling the morphologies of VO_2 nanostructures. Fig. 4.26(a)–(d) present SEM images of VO_2 nanocrystals synthesized by hydrothermal treatment at 120 °C for 12 h, 24 h, 36 h and 48 h, respectively. These four images display a series of typical VO_2 nanostructures under the different growth stages, the submicrometer size Chinese noodles-likes were obtained when the reaction period time was reached to 36 h and extracted to narrow nanorods with 100 nm in diameter and over 2 μm in length when the reaction time extends to 48 h.

4.3 Ti-V-O nanocomposite applied for energy storage device

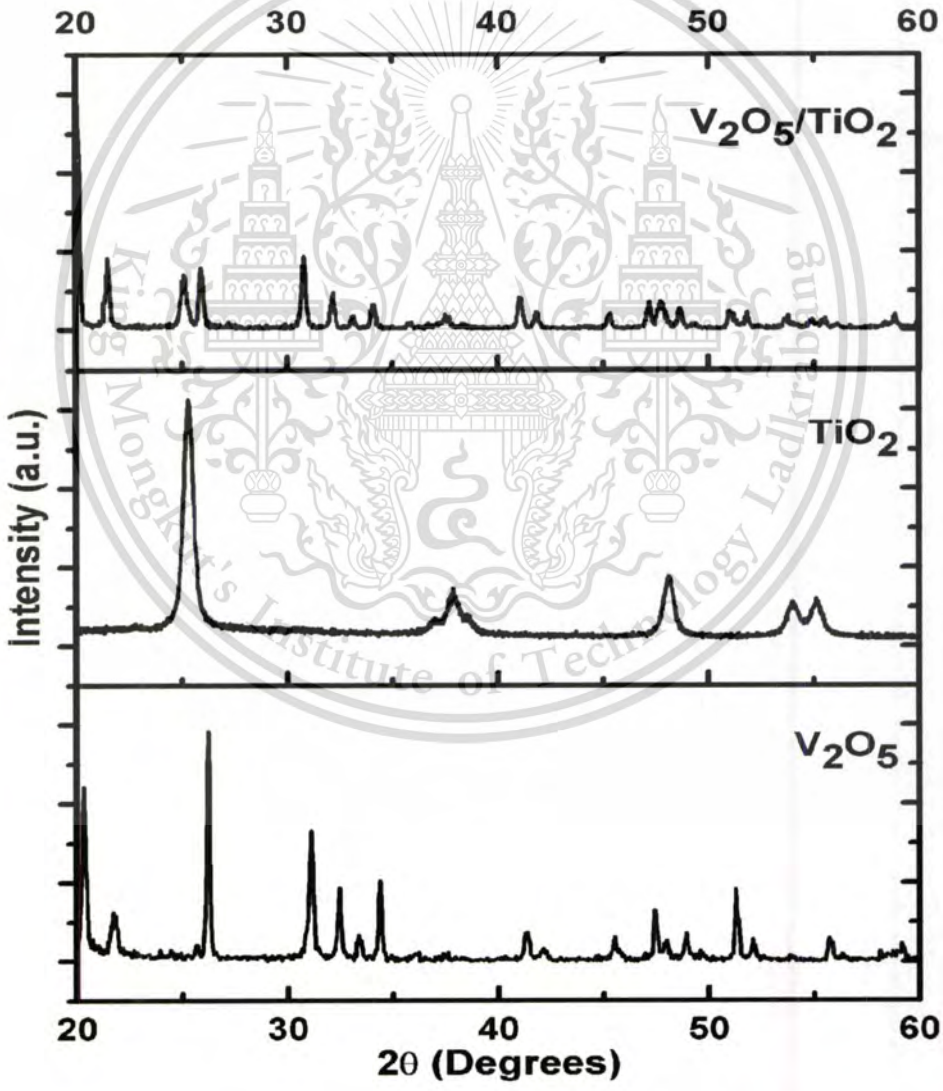

Figure 4.27 XRD patterns of TiO_2/V_2O_5 nanocomposite films.

The crystalline structure of the TiO_2/V_2O_5 nanocomposite films was investigated by XRD and their corresponding patterns are shown in Fig. 4.27. The noticeable diffraction peaks, which appeared in diffraction spectra of V_2O_5 synthesized by hydrothermal method and TiO_2 synthesized via the sonochemical process attributed to orientation plane of orthorhombic structure of V_2O_5 corresponded to JCPDS file No. 89-061 and anatase phase of TiO_2 corresponded to JCPDS file No. 89-4921. These results indicated that V_2O_5 orthorhombic structure and TiO_2 with pure anatase phase were obtained with calcinations route at 500 °C. Meanwhile, dual spectra were appeared in the diffraction peaks of TiO_2/V_2O_5 nanocomposite and disappearance of unusual diffraction peaks in the spectra. These results imply that the TiO_2/V_2O_5 nanocomposite can be obtained. The possible mechanisms anticipated to the formation of TiO_2 nanoparticles during sonochemical process are proposed. During the process, titanium isopropoxide dissolved in deionized water may transform to hydrolyzed alkoxides via hydrolysis and condensation processes. This intermediate form processes relevant functional groups that can further transform to fine TiO_2 nanoparticles by condensation process by the assistance of rapid collision driven by intense ultrasound energy provided by ultrasonic irradiation [23].

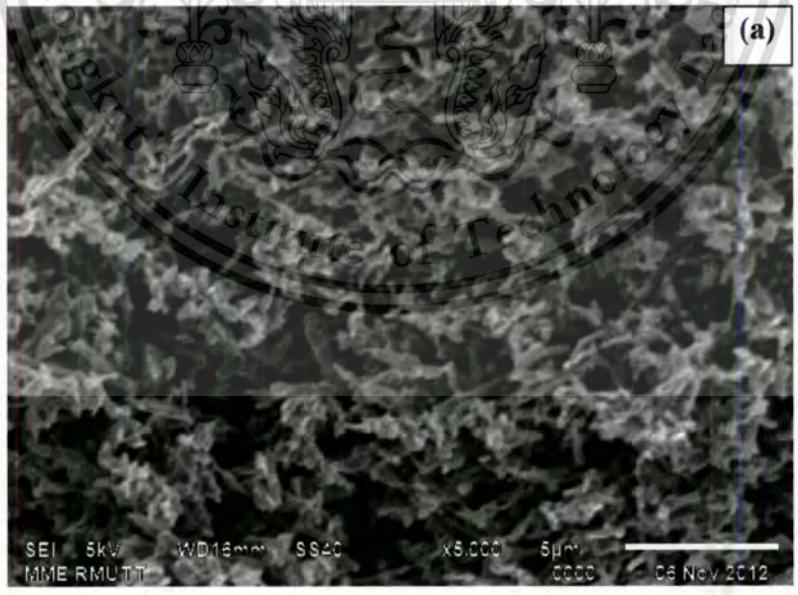

Figure 4.28 SEM images of (a) V_2O_5 nanorods, (b) TiO_2 nanoparticles and (c) TiO_2/V_2O_5 nanocomposites (the scale bar = 5 μm).

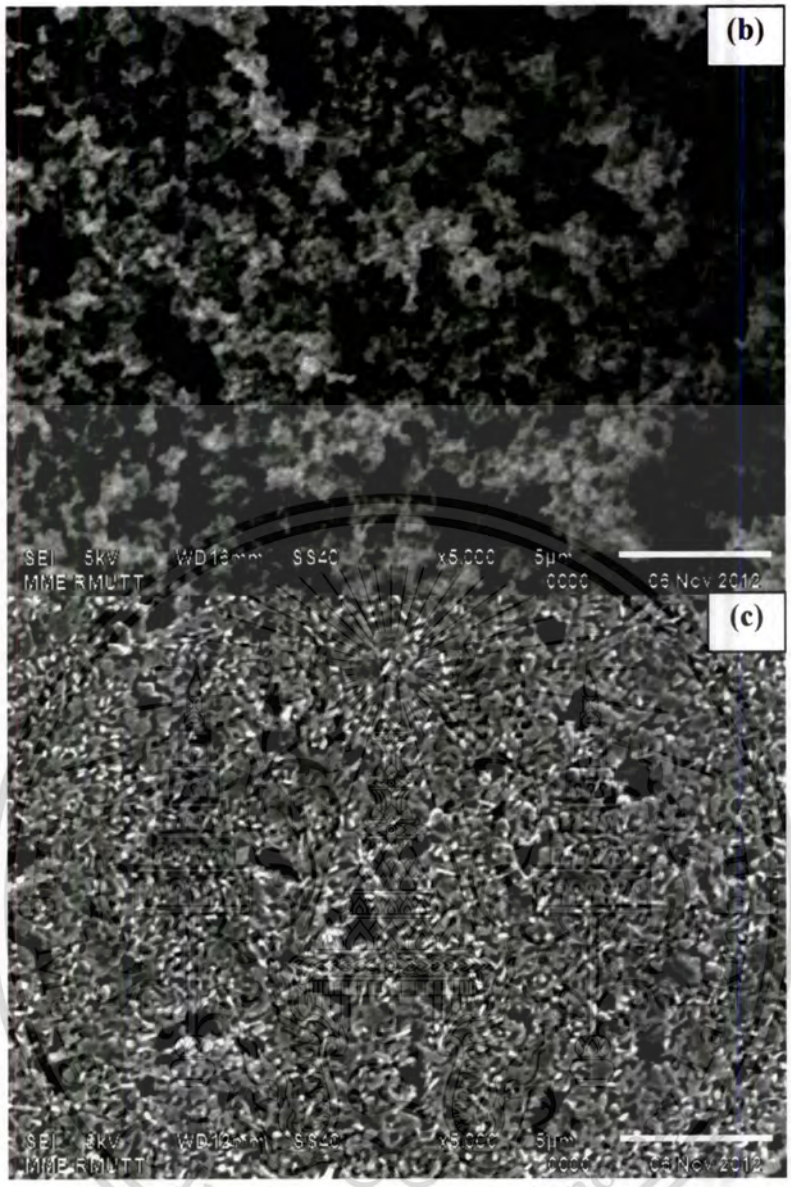

Figure 4.28 (cont.) SEM images of (a) V_2O_5nanorods, (b) TiO_2 nanoparticles and (c) TiO_2/V_2O_5 nanocomposites (the scale bar = 5 μm).

The SEM image of the nanorod-like V_2O_5 is shown in Fig. 4.28(a). Meanwhile the SEM image of TiO_2 nanoparticles synthesized by sonochemical-assisted process is exhibited in Fig. 4.28(b). Fig. 4.28(c) illustrates the morphology of TiO_2/V_2O_5 nanocomposite with weight ratio 0.9:0.1. It is clearly seen that the nanorod-like V_2O_5 with diameter about 200 nm can be synthesized by hydrothermal method. From Fig. 4.28(c), it is observed that TiO_2 nanoparticles are uniformly dispersed in V_2O_5 nanorod matrix. These results implied that TiO_2/V_2O_5 nanocomposite films can be prepared by mixing oxide materials.

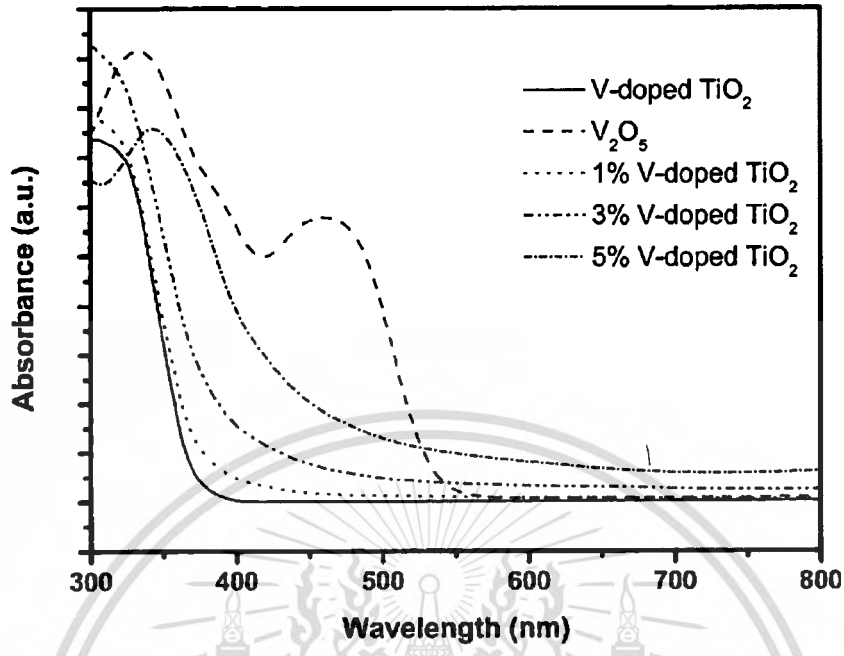

Figure 4.29 Optical absorption spectra of TiO_2 nanoparticles and V_2O_5 nanorods synthesized by sonochemical and hydrothermal method, respectively.

The optical absorption of TiO_2 and V_2O_5 was investigated by UV-Vis spectroscopy and the corresponding spectra are shown in Fig. 4.29. It clearly seen that the UV light in range 300-400 nm was absorbed by TiO_2 nanoparticle due to its typical optical band gap of TiO_2 [24]. Meanwhile, V_2O_5 can absorb light with photon energy in the range 450-470 nm. This characteristic feature was also observed in previous report [25]. From the result, the absorption in UV region of TiO_2 nanoparticles can initiate the generation of photoelectron under illumination, which support the photoelectrochemical process of V_2O_5.

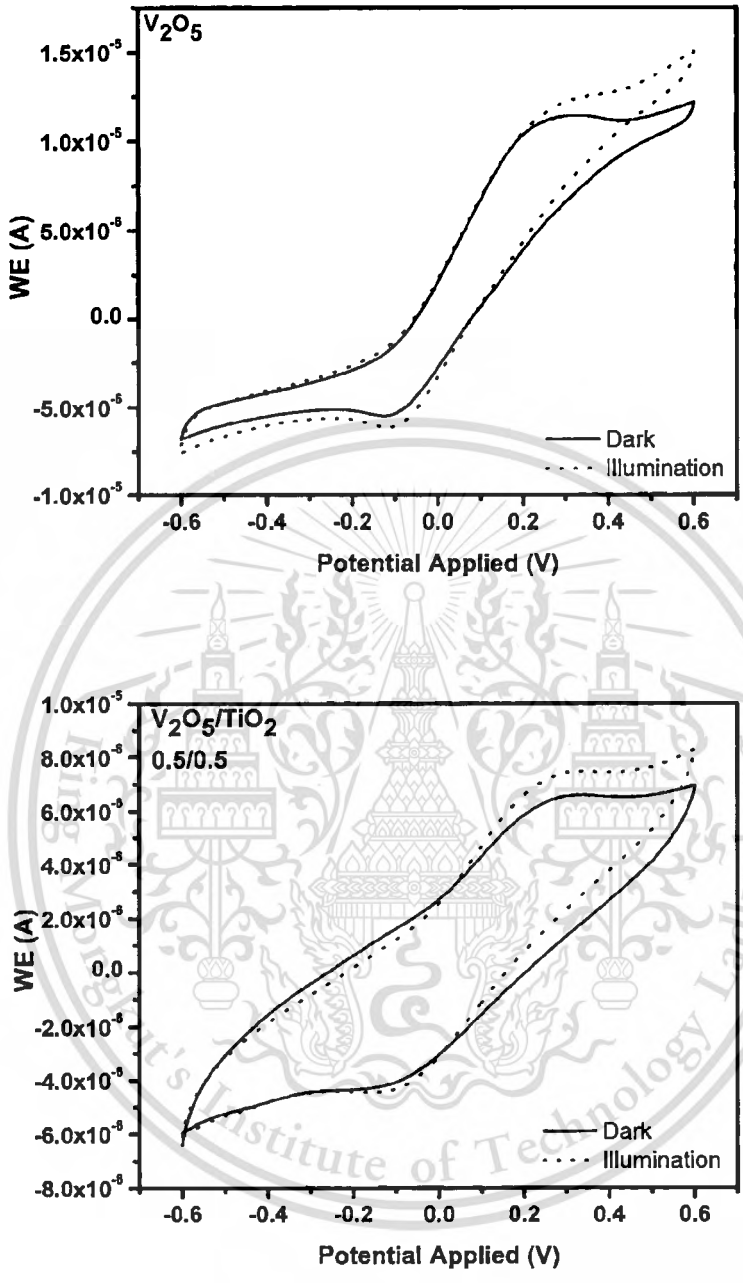

Figure 4.30 Cyclic voltammograms of TiO_2/V_2O_5 nanocomposites with different weight ratio at scan rate 20 mV/s. (Electrode area was 0.5x0.5 cm^2).

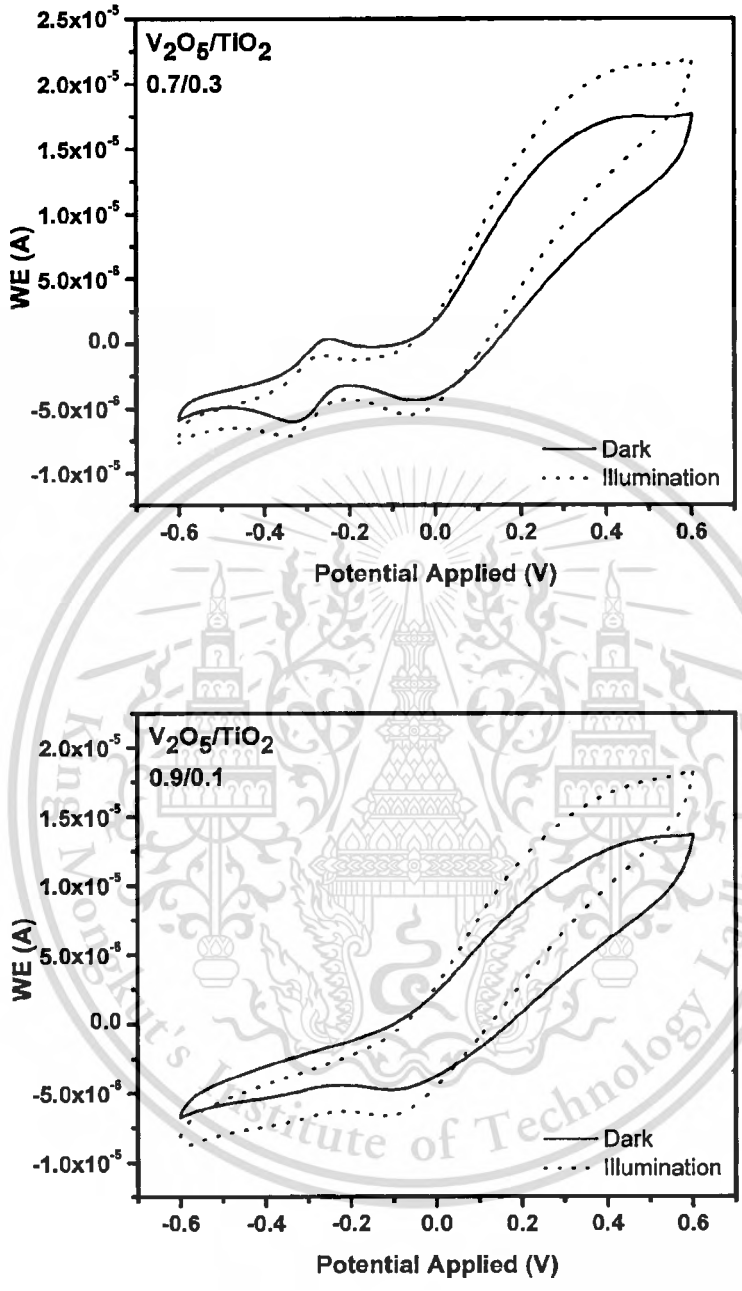

Figure 4.30 (cont.) Cyclic voltammograms of TiO_2/V_2O_5nanocomposites with different weight ratio at scan rate 20 mV/s. (Electrode area was 0.5x0.5 cm^2).

The photoelectrochemical properties of TiO_2/V_2O_5 nanocomposites with different weight ratio are shown in Fig. 4.30. For bare V_2O_5 case, it is noticed that the current density of the film increases when illuminated by solar simulator light due to

its absorption properties in the visible region of this material [26]. For all samples, both oxidation and reduction peak are observed in cyclic voltammogram revealing that the V_2O_5 nanorods exhibit charge capacitive behavior owing to intercalation/deintercalation of Li^+ in V_2O_5 matrix [25]. Furthermore, the changing of color on the V_2O_5 nanorods working electrode from brown to dark grey associated with the reduction of oxidation number of V^{5+} to V^{4+} is observed [27]. These phenomena allow us to conclude that electrons can accumulate in the V_2O_5 nanorods through intercalation of Li^+ and H^+ ions, as shown in Eq. (4.8).

$$V_2O_5 + xe^- + xM^+ \leftrightarrow M_xV_x^{4+}V_{2-x}^{5+}O_5$$
$$(M^+ = H^+ \; or \; Li^+) \qquad (4.8)$$

The increasing of current density in the composites used as working electrode is probably proceeded following the relative energies of the conduction bands of TiO_2 and V_2O_5. Under illumination, photo-generated electrons can easily be transferred from Ti(3d) to V(3d) orbitals, supporting the charges transfer and leading to the higher current density of the device. This presumption is supported by previous work that the performance of N_xTiO_{2-x}/NiO bilayer thin film electrodes was investigated [28]. It was found that the efficient separation of photogenerated charge carriers occurs in the interconnected N_xTiO_{2-x} and NiO thin film. This phenomenon implies that the enhancement in light-induced photoelectron generation can be achieved by the incorporation of TiO_2 into V_2O_5 due to the photoelectron generated by TiO_2 during illumination. The optimized weight ratio of V_2O_5/TiO_2 for superiority in current density is found to be 0.7:0.3. From the previous literatures, the photocurrents are produced not only from the band gap excitation in the TiO_2 nanoparticles, as revealed in Eq.(4.9), but also from the photo-anodic oxidation by holes injected into the electrolyte solution, according to the band bending for an n-type semiconductor [29]. In our work, the photo-oxidation of methanol or oxalic acid produces electrons, as Eqs.(4.10) and (4.11) show, and injection of these electrons into the TiO_2 nanoparticles gives rise to an increase in photocurrent, as following;

$$TiO_2 \xrightarrow{UV} TiO_2^*(e_{cb}^- + h_{vb}^+) \quad (4.9)$$

$$CH_3OH \xrightarrow{h^+} CH_2O + 2H^+ + 2e^- \quad (4.10)$$

$$(COOH)_2 \xrightarrow{h^+} 2CO_2 + 2H^+ + 2e^- \quad (4.11)$$

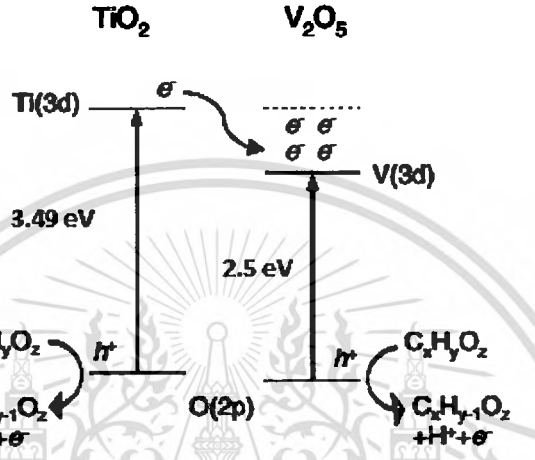

Figure 4.31 Schematic band energy diagram for the TiO_2/V_2O_5 nanocomposites ($C_xH_yO_z$ define as a methanol and carboxylic group).

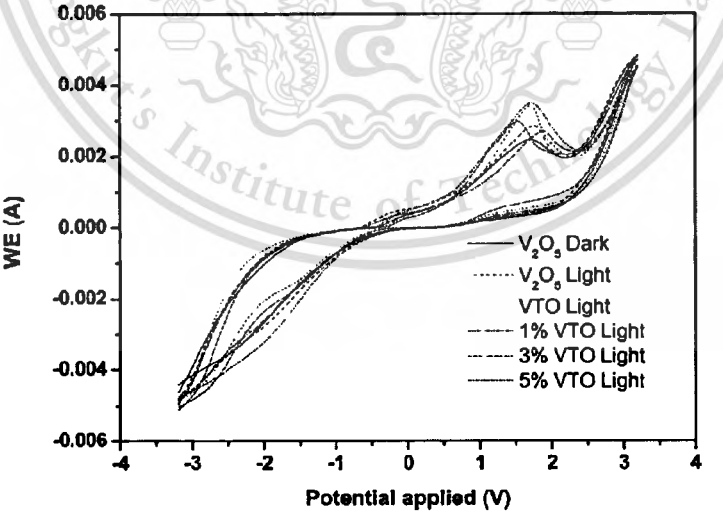

Figure 4.32 Cyclic voltammograms of V-doped TiO_2 /V_2O_5 nanocomposites at weight ratio 0.3:0.7 with different V doping contents at scan rate 20 mV/s in the electrolyte solution of 0.1 M $LiClO_4$ and 0.1 M $(COOH)_2$ in CH_3OH (Electrode area was 1.0x1.0 cm^2).

The photoelectrochemical properties of V-doped TiO_2/V_2O_5 nanocomposites at weight ratio 0.3:0.7 with difference V doping contents are shown in Fig. 4.32. From previous results, all samples, both oxidation and reduction peak are observed in cyclic voltammogram revealing that the V_2O_5 nanorods exhibit charge capacitive behavior owing to intercalation/deintercalation of Li^+ in V_2O_5 matrix. By Eq. (4.8)-(4.11), two main reasons of the increasing of current density in the V doped TiO_2 compared with undoped TiO_2 nanocomposites used as working electrode under illumination caused by; (1) After illumination by light, V-doped TiO_2 nanoparticles could absorb a greater number photons in visible region and generate the electron-hole greater than undoped TiO_2. (2) The reducing of recombination rate of electron-hole pairs by traps level inside forbidden energy gap which generated by doping with V ions into TiO_2 nanoparticles (described in V-doped TiO_2 section). The specific capacitance of samples is shown in Table 4.2.

Table 4.2 Specific capacitance of samples.

Samples	Illumination (On/Off)	Specific capacitance (F/g)
V_2O_5	Off	12.10
V_2O_5	On	15.67
V-doped TiO_2/V_2O_5	On	16.12
1% V-doped TiO_2/V_2O_5	On	20.92
3% V-doped TiO_2/V_2O_5	On	14.82
5% V-doped TiO_2/V_2O_5	On	16.06

REFERENCES

[1] C. Yu, J. C. Yu, M. Chan, "Sonochemical fabrication of fluorinated mesoporous titanium dioxide microspheres" J. Solid. State. Chem. 182 (2009) 1061–1069.

[2] L. González-Reyes, I. Hernández-Pérez, F.C. Robles Hernández, Effect of coarsening of sonochemical synthesized anatase on BET surface characteristics, Chem. Eng. Sci. 66 (2011) 721-728.

[3] K. Prasad, D.V. Pinjari, A.B. Pandit, S.T. Mhaske, Phase transformation of nanostructured titanium dioxide from anatase-to-rutile via combined ultrasound assisted sol–gel technique, Ultrason. Sonochem. 17 (2010) 409-415.

[4] Qinghua Chen, Huiling Liu, Yanjun Xin, Xiuwen Cheng, "TiO_2 nanobelts-Effect of calcinations temperature on optical, photoelectrochemical and photocatalytic properties" Electrochimica Acta 111 (2013) 284-291.

[5] X. Shen, J. Zhang, B. Tian, Microemulsion-mediated solvothermal synthesis and photocatalytic properties of crystalline titania with controllable phases of anatase and rutile, J. Hazard. Mater.192 (2011) 651– 657.

[6] X. Lü, J. Li, X. Mou, J. Wu, S. Ding, F. Huang, Y. Wang, F. Xu, Room-temperature ferromagnetism in $Ti_{1-x}V_xO_2$ nanocrystals synthesized from an organic-free and water-soluble precursor, J. Alloy. Compd. 499 (2010) 160–165.

[7] Z. Zhang, C. Shao, L. Zhang, X. Li, Y. Liu, Electrospun nanofibers of V-doped TiO_2 with high photocatalytic activity, J. Colloid. Interf. Sci. 351 (2010) 57–62.

[8] D. de la Cruz, J.C. Arevalo, G. Torres, R.G. Bautista Margulis, C. Ornelas, A. Aguilar-Elguezabal, TiO_2 doped with Sm^{3+} by sol–gel: Synthesis, characterization and photocatalytic activity of diuron under solar light, Catal. Today 166 (2011) 152–158.

[9] B. Tian, C. Li, J. Zhang, One-step preparation, characterization and visible-light photocatalytic activity of Cr-doped TiO_2 with anatase and rutile bicrystalline phases, Chem. Eng. J.191 (2012) 402– 409.

[10] R. Dholam, N. Patel, A. Miotello, Efficient H_2 production by water-splitting using indium-tin-oxide/V-doped TiO_2 multilayer thin film photocatalyst, Int. J. Hydrogen. Energ. 36 (2011) 6519-6528.

[11] X. Lü, J. Li, X. Mou, J. Wu, S. Ding, F. Huang, Y. Wang, F. Xu, Room-temperature ferromagnetism in $Ti_{1-x}V_xO_2$ nanocrystals synthesized from an organic-free and water-soluble precursor, J. Alloy. Compd. 499 (2010) 160–165.

[12] Z. Zhang, C. Shao, L. Zhang, X. Li, Y. Liu, Electrospun nanofibers of V-doped TiO_2 with high photocatalytic activity, J. Colloid. Interf. Sci. 351 (2010) 57–62.

[13] Amir Rastar, Mohamad E. Yazdanshenas, Abusaeed Rashidi, Seyed M. Bidoki, Estimation and prediction of optical properties of PA6/TiO2 nanocomposites, Arabian Journal of Chemistry, In Press, Corrected Proof, Available online 4 August (2012).

[14] H. Lin, C.P. Huang, W. Li, C. Ni, S. Ismat Shah, Yao-Hsuan Tseng, Size dependency of nanocrystalline TiO_2 on its optical property and photocatalytic reactivity exemplified by 2-chlorophenol, Applied Catalysis B: Environmental 68 (2006) 1-11.

[15] Baoshun Liu, Xuelai Wang, Guofa Cai, Liping Wen, Yanbao Song, Xiujian Zhao, Low temperature fabrication of V-doped TiO_2 nanoparticles, structure and photocatalytic studies, Journal of Hazardous Materials 169 (2009) 1112-1118.

[16] Haihong Yin, Ke Yu, Zhengli Zhang, Morphology-control of VO_2(B) nanostructures in hydrothermal synthesis and their field emission properties. Appl. Surf. Sci. 257, 8840–8845 (2011).

[17] ShidongJi, Feng Zhang and Ping Jin, Phase transition of single crystal VO_2(R) nanorods in solution revealed by reversiblechange in surface charge state and structure. Mater. Lett.65, 708 –711(2011).

[18] Lijuan Mao and Chunyan Liu, A new route for synthesizing VO_2(B) nanoribbons and1D vanadium-based nanostructures. Mat. Res. Bull. 43, 1384–1392(2008).

[19] ZHOU Ke-chao, CAO Du-meng and LI Zhi-you, Soft-chemical synthesis and high-temperature electrochemicalcharacteristics of VO_2. Trans. Nonferrous Met. Soc. China. 16, 517-521(2006).

[20] NagarajuGanganagappaa and AshokaSiddaramannab, One step synthesis of monoclinic VO_2 (B) bundles of nanorods:Cathode for Li ion battery. Mater Charact.68, 58–62 (2012).

[21] J.-C. Valmalette and J.-R. Gavarri, High efficiency thermochromic VO_2(R) resulting from theirreversible transformation of VO_2 (B). Mat. Sci Eng. B. 54,168–173(1998).

[22] Zhang, Y., Chen, C., Wu, W., Niu, F., Liu, X., Zhong, Y., Cao, Y., Liu, X., and Huang, C. 'Facile hydrothermal synthesis of vanadium oxides nanobelts by ethanol reduction of peroxovanadium complexes'.Ceram. Int., vol. 39, pp. 129-141 (2013).

[23] Jingbing, L., Lin, C., Jinshu, W., Mankang, Z., and Wenxiong, Z. (2010) 'A facile one-step approach to visible-light-sensitive vanadium-doped TiO_2 hollow microspheres'. Mat. Sci. Eng. B. Solid., vol. 172, pp. 142-145.

[24] Jingbing, L., Lin, C., Jinshu, W., Mankang, Z., and Wenxiong, Z. (2010) 'A facile one-step approach to visible-light-sensitive vanadium-doped TiO_2 hollow microspheres'. Mat. Sci. Eng. B. Solid., Vol. 172, pp. 142-145.

[25] Yan, L. C., Nutan, G., Stevin, S. P., Vanchiappan, A., Grace, W., and Madhavi, S. (2011) 'Morphology, structure and electrochemical properties of single phase electrospun vanadium pentoxidenanofibers for lithium ion batteries' J. Power. Sources., Vol. 196, No. 2, pp. 6465-6472.

[26] Boudaoud, L., Benramdane, N., Desfeux, R., Khelifa, B., and Mathieu, C. (2006) 'Structural and optical properties of MoO_3 and V_2O_5 thin films prepared by Spray Pyrolysis'. Catal.Today., Vol. 113, No. 3-4, pp. 230-234.

[27] Sooyeun, K., and Minoru, T. (2012) 'Electrochromic windows based on V_2O_5-TiO_2 and poly(3,3-dimethyl-3,4-dihydro-2H-thieno[3,4-b][1,4]dioxepine) coatings' Sol. Energ. Mat. Sol. C., Vol. 107, pp. 225-229.

[28] Huang, H., Jiang, L., Zhang, W.K., Gan, Y.P., Tao, X.Y., and Chen, H.F. (2010) 'Photoelectrochromic properties and energy storage of $TiO_{2-x}N_x$/NiO bilayer thin films' Sol. Energ. Mat. Sol. C., Vol. 94, No. 2, pp. 355-359.

[29] Haipeng Liu, Guangqing Xu, Jinwen Wang, Jun Lv, Zhixiang Zheng, Yucheng Wu, Photoelectrochemical properties of TiO_2 Nanotube Arrays Modified with BiOCl nanosheets, Electrochimica Acta 130 (2014) 213-221.

CHAPTER 5

CONCLUSIONS

In summary, TiO_2 nanoparticles were successfully synthesized by sonochemical-assisted process. The XRD and Raman results revealed that as-synthesized powder has an anatase phase of TiO_2 after sonication for 30 min. Furthermore, the calcinations temperature has significant influence on crystalline size and phase transformation. SEM and TEM results indicated that the quasi-spherical polycrystalline nanopowder with diameter 20-30 nm can be produced by sonochemical-assisted process and calcination at 600 °C.

V-doped TiO_2 nanoparticles were synthesized by sonochemical-assisted processs in combination with calcinations process in temperature range of 300-1000 °C. The XRD result disclosed that as-synthesized powder has an anatase phase of TiO_2. It was further notified that the calcinations temperature and the incorporation of V dopant have significant influence on physical properties of the powders. XRD and Raman spectra acknowledged that the transformation of anatase to rutile phase was activated after the calcinations was over 500 °C. The amelioration in crystallinity was achieved with increasing calcinations temperature accompanying XRD and SEM results. XPS results revealed that the existence of V ion incorporated into the TiO_2 lattice due to the close ionic radius between V^{4+} and Ti^{4+}. The noticeable interplanar spacing alternation was observed as the V doping content increased. UV-Vis spectroscopy revealed that the absorption activity in visible region can be improved by V doping.

VO_2 nanorods were successfully synthesized by facile hydrothermal method at 100-140 °C for 12-48 h using *n*-butanol and acetylacetone as the reductant. The XRD results revealed that the as-synthesized nanorods have the mixed phase VO_2 (B) and VO_2 (R) monoclinic structure when used single butanol and acetylacetone as a reductant. SEM and TEM results shown that the morphology of the as-synthesized VO_2 nanorods depend on the type of reductant agents, reaction temperature and reaction time.

TiO_2/V_2O_5 nanocomposites were successfully prepared by mechanical mixing method. The XRD results revealed that the diffraction spectrum of nanocomposites film consist of dual diffraction peaks of orthorhombicV_2O_5 and anatase TiO_2

structures. SEM results indicated that the TiO_2 nanoparticles are well-dispersed in V_2O_5 nanorodhost matrix. The photoelectrochemical results suggest that the performance of nanocomposite films utilized as working electrode can be enhanced by mixing V_2O_5 with TiO_2 nanorods and the maximum current is about 22 μA at the weight ratio is 0.3:0.7 The amelioration in their performance may due to the higher of charge transfer in the device with the presence of TiO_2 in the V_2O_5 matrix. For V-doped TiO_2/V_2O_5 nanocomposites, the photoelectrochemical results revealed that V-doped TiO_2 nanoparticles can enhance the photoelectrochimical properties of the device.

AUTHOR BIOGRAPHY

Mr. Chokchai Kahattha

DATE OF BIRTH	29 March 1982, Sakolnakhon
ADDRESS	50/24 Soi Prapa, Nittayo Road, Pang Khon, Sakolnakhon, Thailand 47160
EDUCATION	Bachelor degree of Science in Applied Physics and Industrial Instrument, Faculty of Science, King Mongkut's Institute of Technology Ladkrabang (KMITL), Bangkok, Thailand (2005). Master of Science in Applied Physics, Faculty of Science, King Mongkut's Institute of Technology Ladkrabang (KMITL), Bangkok, Thailand (2009).

PUBLICATION:

1. Prayut Potirak, **Chokchai Kahattha** and Wisanu Pecharapa, "Microwave-Assisted Synthesis and Characterization of Carbon Nanotube/Zinc Oxide composites", *Journal of Nanoscience and Nanotechnology*, Vol.11,No. 9, (2011) pp. 11195-11199. (IF: 1.352)
2. O. Thanomkiat, **C. Kahattha**, W. Pecharapa and W. Techitdheera, "Sol-gel based Deposition of $Ti_xV_{1-x}O$ Films for Thermally Controlled Optical Switching Applications", *Procedia Engineering*, 8, (2011), pp. 232-236.
3. K. Paipitak, **C. Kahattha**, W. Techitdheera, S. Porntheeraphat, W. Pecharapa, "Characterization of Sol-gel Derived Ti-doped Tungsten Oxide Electrochromic Thin Films", *Energy Procedia*, 9, (2011), pp. 446-451.
4. **C. Kahattha**, N. Wongpisutpaisan, N. Vittayakorn and W. Pecharapa, "Physical properties of V-doped TiO_2 nanoparticles synthesized by sonochemical-assisted process", *Ceramics International*, Vol. 39, supplement 1, (2013) pp. S389-S393.

(IF: 1.751)

5. **Chokchai Kahattha** and Wisanu Pecharapa, "Effects of Reductant on Physical Properties and Formation of Vanadium Oxide Compounds Prepared by Hydrothermal Route", *Integrated Ferroelectrics,* (2013) (IF: 0.375)
6. **C. Kahattha**, W. Techitdheera, N. Vittayakorn and W. Pecharapa, "Titanium dioxide/Vanadium oxide nanocomposites synthesized via sonochemical and hydrothermal process for energy storage application", *International Journal of Nanotechnology*, (2013) (IF: 1.087)
7. **C. Kahattha**, N. Vittayakorn and W. Pecharapa, "Effect of sonication time and calcination temperature on physical properties of Titanium dioxide synthesized via sonochemical-assisted process", *Advanced Materials Research*, 802 (2013) pp. 252-256.
8. Wisanu Pecharapa, **Chokchai Kahattha**, Papitchaya Woointranont, and Thanawee Chodjarusawand, "A study of acid-treated multiwall carbon nanotubes by electron microscopy and Raman Spectroscopy", ***Journal of the Microscopy Society of Thailand***, 24 (2), pp.133-135, 2010.
9. W. Pecharapa, **C. Kahattha**, W. Techitdeera, **"**Optical Properties of MgZnO Alloyed Films Characterized by Transmission Spectroscopy", ***Thai Journal of Physics***, Series 5, pp. 393-395, 2010.
10. **Chokchai Kahattha,** and Wisanu Pecharapa, **"**Physical Properties of Titanium dioxide/Vanadium oxide composites Synthesized by Ball-Milling Process**,** ***Journal of the Microscopy Society of Thailand***, 4 (1), pp.53-55, 2011.
11. N. Wongpisutpaisan, **C. Kahattha**, N. Vittayakorn, A. Ruangphanit and W. Pecharapa**,** "Titanium dioxide nanostructures synthesized by sonochemical-hydrothermal process", **Journal of Metals, Materials and Minerals**, Vol. 23,No. 1, pp. 19-24, June 2013**.**

CONFEREN:

1. **Chokchai Kahattha**, and Wisanu Pecharapa, "Physical Properties of Titanium dioxide/Vanadium oxide composites Synthesized by Ball-Milling Process", **Proceedings of the 28th MST Annual Conference, 5-7 January 2011, Chiang Rai, Thailand**
2. **C. Kahattha** and W. Pecharapa, "Characterization of V-doped Titanium Dioxide Synthesized by Sol-gel Precipitation Process", **9th Eco-Energy and Materials Science and Engineering Symposium (EMSES 2011), May 25-28, 2011, Chiangrai.**
3. Narongdet Wongpisutpaisan, **Chokchai Kahattha**, Naratip Vittayakorn, Anucha Ruangphanit, and WisanuPecharapa, "Titanium dioxide nanostructures synthesized by sonochemical – hydrothermal process", **7th International Conference on Materials and Technology (7th - MSAT), June 7-8, 2012, Bangkok, Thailand**
4. **C. Kahattha**, N. Wongpisutpaisan, N. Vittayakorn and W. Pecharapa, "Physical properties of V-doped TiO_2 nanoparticles synthesized by sonochemical-assisted process", **8th Asian Meeting on Electroceramics, July 1-5, 2012, Penang, Malaysia**.
5. **Chokchai Kahattha** and Wisanu Pecharapa, "Effects of Reductant on Physical Properties and Formation of Vanadium Oxide Compounds Prepared by Hydrothermal Route", **8th Asian Meeting on Ferroelectric Materials, Dec 9-14, 2012, Pattaya, Thailand.**
6. **C. Kahattha**, W. Techitdheera, N. Vittayakorn and W. Pecharapa, "Titanium dioxide/Vanadium oxide nanocomposites synthesized via sonochemical and hydrothermal process for energy storage application", **5th IEEE International Nanoelectronic Conference, Jan 2-4, 2013, Singapore.**
7. **C. Kahattha**, N. Vittayakorn and W. Pecharapa, "Effect of sonication time and calcination temperature on physical properties of Titanium dioxide synthesized via sonochemical-assisted process", **The Third International Conference on Engineering, Applied Sciences and Technology (ICEAST 2013), Bangkok, Thailand, August 21-24, 2013.**

Available online at www.sciencedirect.com

SciVerse ScienceDirect

Ceramics International 39 (2013) S389–S393

CERAMICS INTERNATIONAL

www.elsevier.com/locate/ceramint

Physical properties of V-doped TiO_2 nanoparticles synthesized by sonochemical-assisted process

C. Kahattha[a,b], N. Wongpisutpaisan[a], N. Vittayakorn[a,b,c], W. Pecharapa[a,b,*]

[a] College of Nanotechnology, King Mongkut's Institute of Technology Ladkrabang (KMITL), Bangkok 10520, Thailand
[b] Thailand and Center of Excellence in Physics (ThEP Center), CHE, 328 Siayuthtaya RD, Bangkok 10400,Thailand
[c] Department of Chemistry, King Mongkut's Institute of Technology Ladkrabang (KMITL), Bangkok 10520, Thailand

Available online 22 October 2012

Abstract

V-doped TiO_2 nanoparticles were synthesized by sonochemical process using titanium isopropoxide as a titanium source, vanadyl acetylacetonate as a dopant source. Sonication was conducted using sonic horn operated at 20 kHz for 20 min until the completely precipitated product was reached. The as-synthesized precipitates with various vanadium dopant (1–5 mol %) were calcined at 500–1000 °C for 4 h. The relevant physical properties of the nanoparticles were characterized by X-ray diffraction (XRD), Raman spectroscopy, X-ray photoelectron spectroscopy (XPS), scanning electron microscope (SEM) and transmission electron microscope (TEM). The anatase phase TiO_2 nanoparticles can be synthesized by sonochemical process. Post calcinations process results in the anatase-to-rutile phase transformation and the enhancement in crystallinity with increasing temperature. The results also indicate good incorporation of V ions in TiO_2 lattices and significant effect of V dopant on alternation of interplanar spacing of TiO_2.

Keywords: A. Powders: Chemical preparation; B. Microstructure-final; D. TiO_2

1. Introduction

In recent years, titanium dioxide (TiO_2) has attracted considerable interest due to their promising applications in many areas such as smart window, buffer layer in dye-sensitized solar cell, self-cleaning materials, UV-detector, photodegradation and gas sensor. Due to the limitation of its properties such as rather high recombination of photo-generated electron-hole pairs, weak absorption in the visible region and weak magnetic property, the findings of a study examining doping with various elements such as Fe, N, Cu, Ag and Pd could indicate a promising method to resolve these problems [1]. Among transition metal ions, vanadium (V) is an attractive potential candidate as an effective additive into TiO_2 due to the close ionic radius between these two elements. Recently, there have been a number of research works focusing on effective techniques for synthysizing TiO_2 such as hydrothermal process [2], flame spray pyrolysis [3], co-precipitation process [4] and sonochemical process [5]. Among these techniques, the sonochemical process is well suited for the synthesis of these materials because of its simplicity, low equipment cost, ease of synthesis and doping. To our best knowledge, the synthesis of V-doped TiO_2 via sonochemical process in combination with post thermal calcinations has is not available in the literatures.

In this work, we report on the simple synthesis of V-doped TiO_2 nanoparticles by sonochemical precipitation process. The effect of vanadium content and the calcinations temperature on crucial physical properties of as-prepared products were thoroughly scrutinized.

2. Experimental and method

V-doped TiO_2 with various vanadium contents were synthesized by sonochemical-assisted process. Titanium isopropoxide [$Ti(C_6H_{14}O_2)_2$] and vanadylacetylacetonate [$VO(C_5H_8O_2)]_2$ were used as starting source materials for Ti and V, respectively. All chemicals were purchased form

*Corresponding author at: College of Nanotechnology, King Mongkut's Institute of Technology Ladkrabang (KMITL), Bangkok 10520, Thailand. Tel.: +66 81 6116884.
E-mail address: kpewisan@gmail.com (W. Pecharapa).

0272-8842/$ - see front matter © 2012 Elsevier Ltd and Techna Group S.r.l. All rights reserved.
http://dx.doi.org/10.1016/j.ceramint.2012.10.100

Sigma Aldrich. In the synthesis process, certain doping amount of vanadylacetylacetonate was dissolved into designated amount of titanium isopropoxide and stirred at room temperature for 24 h until a transparent pale yellow solution was obtained. The V doping concentration was varied from 1–5 mol %. 10 mL of the stocked solution and 150 mL of deionized water was filled into the chamber and then the mixed liquid was irradiated with high intensity ultrasound (650 W 20 kHz) by a Sonics Model VCX 750 at room temperature in ambient air for 20 min until the completely precipitated product was reached. After cooling down to room temperature, the resulting precipitates were washed with deionized water and ethanol and centrifuged at 5000 rpm for 5 min. After that the cleaned precipitates were calcined at different temperatures from 500–1000 °C for 4 h. The crystal structure and phase identification of the samples were investigated by X-ray diffraction with a monochromatic source of Cu Kα (λ=0.15405 nm). Raman spectroscopy (Thermo Scientific DXR Raman Microscope with 532 nm DPSS laser) was employed to verify the substitution of the Ti sites with V in the TiO_2 lattice. X-ray photoelectron spectroscopy (AXIS Ultra ^{DLD} with dual anode Mg and Al K_α X-ray source) was applied to verify the chemical states of Ti and V. Their morphologies were monitored with JEOL JSM-6340 F field emission scanning electron microscope with an accelerating voltage of 5.0 kV. Transmission electron microscopy images and selected area electron diffraction (SAED) patterns were taken with TECNAI G2 20 transmission electron microscope, using an accelerating voltage of 200 kV.

3. Results and discussion

Fig. 1(a) shows the XRD patterns of the 5 mol% V-doped TiO_2 powders calcined at different temperatures from 500–1000 °C in air for 4 h. Noticeable diffraction peaks positioned at 2θ=25.29°, 37.82°, 48.07°, 53.99° and 55.12° which are observed on the spectra of as-sonochemically-synthesized product and doped sample calcined at 500 °C was attributed to (101), (004), (200), (105) and (211) orientation plane of anatase-TiO_2 [JCPDS89-4921]. This result indicates that as-sonochemically-synthesized powder in anatase phase of TiO_2 can be obtained by single-step sonochemical process without the calcination [6]. Plausible formation mechanism of TiO_2 particles initiated by the sonochemical process is suggested. During sonication, dissolved titanium isopropoxide in deionized water can undergo hydrolysis and condensation process to create hydrolyzed alcoxides, which have numerous amount of functional hydroxyl groups. Simultaneously, rapid collision driven by intense ultrasound energy can sufficiently generate localized high temperature region, which is able to expedite the condensation reactions of hydroxyl groups to produce the nucleation of fine TiO_2 nanoparticles. When the calcinations temperature elevated to 600 °C, the mixture peaks of the anatase and rutile phase were observed with rutile phase being predominant and completely transformed

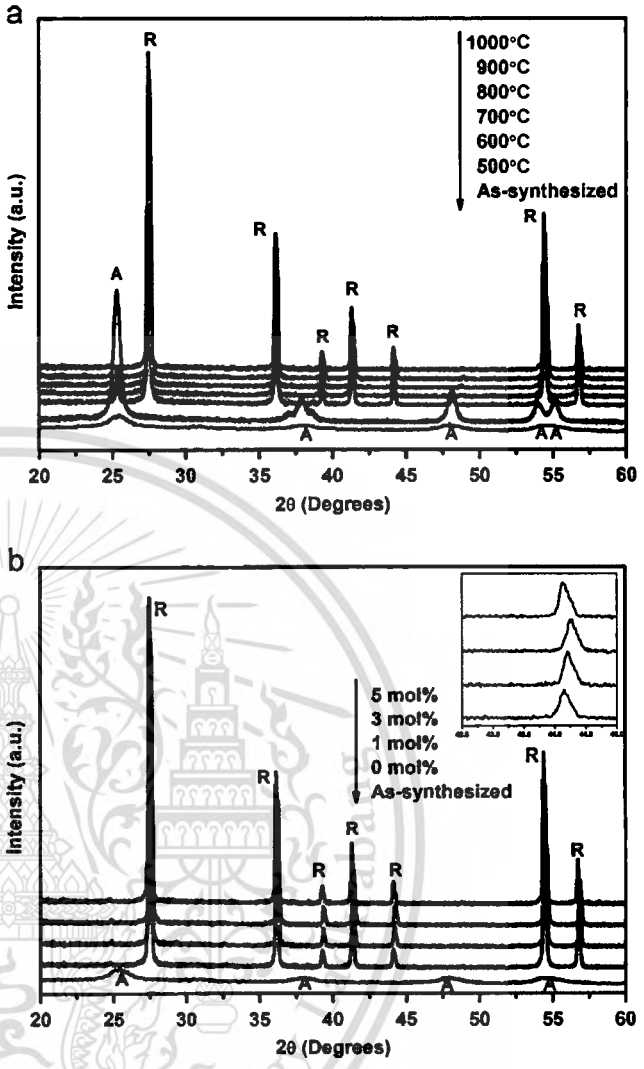

Fig. 1. XRD patterns of the V-doped TiO_2 nanoparticles synthesized by sonochemical process with different (a) calcination temperatures and (b) vanadium doping contents.

to rutile phase as the temperature was over 600 °C. These results indicate that the phase transformation between anatase and rutile phase is activated at calcinations temperature-higher than 500 °C. Fig. 1(b) exhibits the XRD patterns of the V-doped TiO_2 with different V doping contents. As observed in all doped samples, the intense and sharp diffraction peaks situated at 2θ=27.49°, 36.12°, 39.26°, 41.29°, 44.12°, 54.40° and 56.73° are assigned to (110), (101), (200), (111), (210), (211) and (220) plane of rutile phase [JCPDS89-4920]. No characteristic peaks ascribed to vanadium oxides (such as V_2O_5 or VO_2) were detected, indicating that the V ions can suitably be doped into TiO_2 lattice [7]. In addition, the significant shifts of peak positions to higher angle are observed (an inset of Fig.1(b)) as V doping content increases up to 3 mol% thereafter shifts back to lower angle, indicating the alternation of *d*-spacing of TiO_2 with specific V doping content. The inteplanar spacing (*d*-spacing) and crystallite size of the V-doped TiO_2 could be determined by Bragg's law and

the Scherrer equation as shown in Table 1. This alternation in *d*-spacing may be attributed to the proper replacement of smaller ionic radius of V^{4+} (0.72 Å) at specific content on some of Ti^{4+} (0.75 Å) sites leading to the noticeable spacing shrinkage in TiO_2 [8].

Raman spectra of the samples prepared at different calcinations temperature and with different V doping contents are illustrated in Fig. 2(a) and (b), respectively. In Fig. 2(a), for the sample calcined at 500 °C for 4 h, the characteristic peaks at around 399, 516 and 639 cm^{-1} are attributed to B_{1g}, A_{1g} and E_g mode of anatase phase, respectively [9]. The rutile phase was obtained as the calcinations temperature ascended to 600 °C or even higher, the characteristic peaks of rutile phase at 235, 447 and 612 cm^{-1} ascribed to two-phonon scattering, E_g and A_{1g} mode of rutile phase are clearly noticed [9]. These results are in harmony with the results revealed by XRD spectra. Fig. 2(b) displays the Raman scattering of the V-doped TiO_2 with different V doping contents and calcined at 1000 °C for 4 h. All results indicate the scattering peaks around 235, 447 and 612 cm^{-1} corresponded to the characteristic peaks of rutile phase and the intensities of all characteristic peaks decrease with increasing doping content. Furthermore, the scattering peaks associated to the V–O compounds were undetectable. These results also imply the suitable doping of vanadium into rutile TiO_2 [10], that is well agreeable to the presumption from XRD results.

Table 1
Characteristics of V-doped TiO_2 with different condition

V-contents (mol%)	Temperature (°C)	*d*-spacing (Å)	Crystallite size (nm)
0	1000	3.24[R]	51.57[R]
1	1000	3.23[R]	67.31[R]
3	1000	3.22[R]	57.35[R]
5	1000	3.24[R]	67.25[R]
5	500	3.51[A]	15.81[A]
5	600	3.24[R]	46.88[R]
5	700	3.24[R]	57.27[R]
5	800	3.24[R]	61.87[R]
5	900	3.23[R]	61.92[R]

[A]Calculated from (101) orientation plane of anatase.
[R]Calculated from (110) orientation plane of rutile.

Additionally, the chemical composition of V-doped TiO_2 nanoparticle was analyzed by XPS as shown in Fig. 3. The peaks appearing at 458.7 and 464.3 eV are associated with $Ti^{4+}2p^{3/2}$ and $Ti^{4+}2p^{1/2}$, respectively [11]. It is an indication of the existence of Ti^{4+} ions in the sample. For V-doped TiO_2, The peak positions of Ti 2*p* slightly shift to high binding energies, suggesting that V ions are incorporated into TiO_2 lattice [12]. In Fig. 3(b), the peaks appearing at binding energies of 517.2 eV could be ascribed to $V^{4+}2p^{3/2}$ [7]. It is confirmed that the V^{4+} ions exist in the V-doped TiO_2 but the vanishment of V $2p^{1/2}$ binding energy is due to the low level of V doping [7]. This result strongly confirmed that the V^{4+} were appropriately incorporated into TiO_2 lattice and substituted to Ti^{4+} site due to its close ionic radius (Ti^{4+} = 0.75 Å and V^{4+} = 0.72 Å) [8].

The SEM images exhibiting the morphologies of 5 mol% V-doped TiO_2 calcined at different temperatures are demonstrated in Fig. 4. The SEM images disclose that the precipitate powders from sonochemical process are

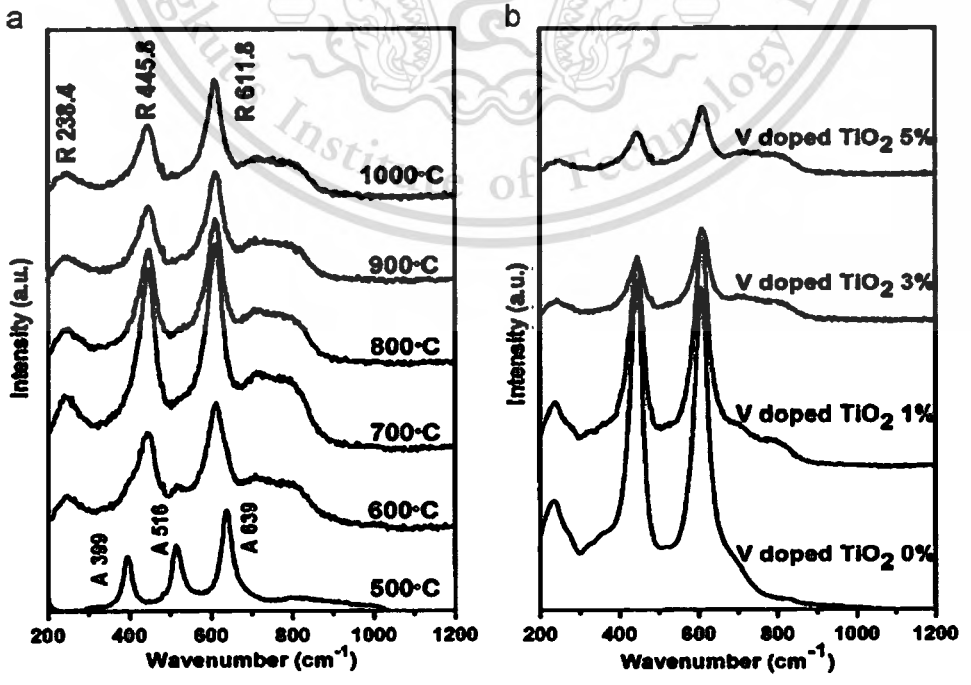

Fig. 2. Raman spectra of the V-doped TiO_2 nanoparticles synthesized by sonochemical process (a) at different calcination temperatures and (b) with vanadium contents (calcined at 1000 °C for 4 h).

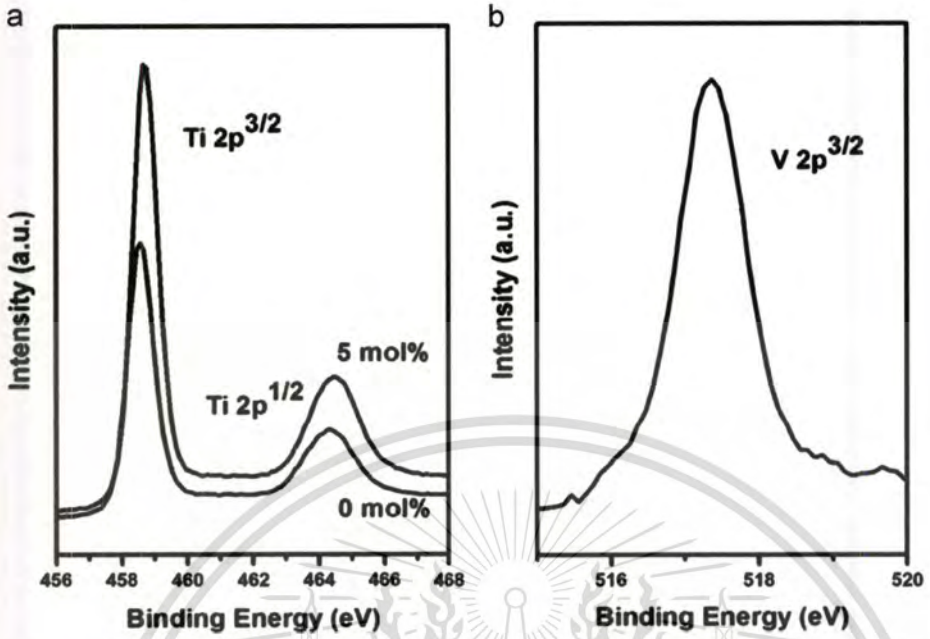

Fig. 3. XPS spectra of the V-doped TiO_2 5 mol% calcined at 1000 °C for 4 h synthesized by sonochemical process in (a) the Ti 2*p* regime and (b) the V 2*p* regime.

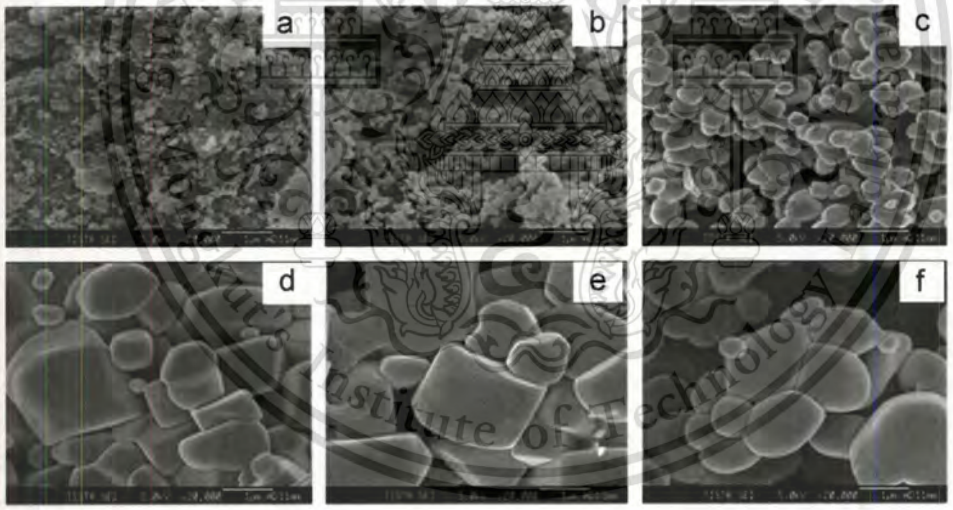

Fig. 4. SEM images of 5 mol% V-doped TiO_2 synthesized by sonochemical process and calcined at (a) 500 °C, (b) 600 °C, (c) 700 °C, (d) 800 °C, (e) 900 °C and (f) 1000 °C.

aggregated from nanosize to microsize after calcinations temperature elevates from 500 °C to 1000 °C. High magnification and Selected Area Electron Diffraction (SEAD) mode of undoped and 5 mol% V-doped TiO_2 nanoparticles are shown in Fig. 5. The results reveal that the samples consist of interplanar spacing along the length direction of 3.27 Å and 3.25 Å for undoped and V-doped TiO_2, respectively. The TEM results revealing the decrease of interplanar spacing of TiO_2 due to V dopant is in good accordance with the values calculated from XRD patterns.

4. Conclusions

In summary, V-doped TiO_2 nanoparticles were successfully synthesized by sonochemical-assisted processs in combination with calcinations process in temperature range of 500–1000 °C. The XRD result disclosed that as-synthesized powder has an anatase phase of TiO_2. It was further notified that the calcinations temperature and the incorporation of V dopant have significant influence on physical properties of the powders. XRD and Raman spectra showed that the transformation of anatase to rutile

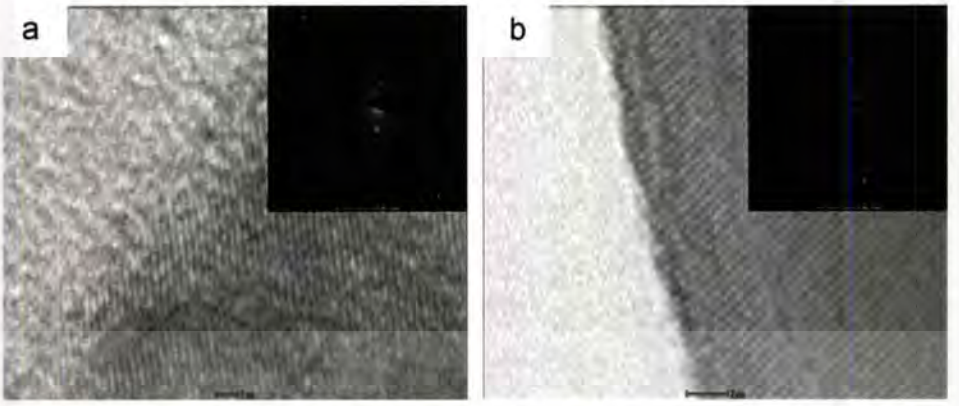

Fig. 5. TEM images of (a) undoped TiO_2 and (b) 5 mol% V-doped TiO_2 synthesized by sonochemical process and calcined at 1000 °C for 4 h (scale bar 1 and 2 nm; the inset images are SEAD mode).

phase was activated after the calcinations was over 500 °C. The amelioration in crystallinity was achieved with increasing calcinations temperature accompanying XRD and SEM results. XPS results revealed the existence of V ion incorporated into the TiO_2 lattice due to the close ionic radius between V^{4+} and Ti^{4+}. Noticeable interplanar spacing alternation was observed as the V doping content increased.

Acknowledgments

This work has partially been supported by the National Nanotechnology Center (NANOTEC), NSTDA, Ministry of Science and Technology, Thailand, through its program of Center of Excellence Network and was financially supported by KMITL research fund. Authors would like to thank Energy Policy and Planning Office, Ministry of Energy, Thailand, for research funding support.

References

[1] K.S. Rane, R. Mhalsiker, S. Yin, T. Sato, K. Cho, E. Dunbar, P. Biswas, Visible light-sensitive yellow $TiO_{2-x}N_x$ and Fe–N co-doped $Ti_{1-y}Fe_yO_{2-x}N_x$ anatasephotocatalysts, Journal of Solid State Chemistry 179 (2006) 3033–3044.

[2] S.S. Mali, P.S. Shinde, C.A. Betty, P.N. Bhosale, W.J. Lee, P.S. Patil, Nanocoral architecture of TiO_2 by hydrothermal process: synthesis and characterization, Applied Surface Science 257 (2011) 9737–9746.

[3] K.K. Akurati, A. Vital, J. –P. Dellemann, K. Michalow, T. Graule, D. Ferri, A. Baiker, Flame-made WO_3/TiO_2 nanoparticles: relation between surface acidity, structure and photocatalytic activity, Applied Catalysis B-Environmental 79 (2008) 53–62.

[4] R. Zanella, S. Giorgio, C.H. Shin, C.R. Henry, C. Louis, Characterization and reactivity in CO oxidation of gold nanoparticles supported on TiO_2 prepared by deposition–precipitation with NaOH and urea, Journal of Catalysis 222 (2004) 357–367.

[5] L.G. Reyes, I.H. Perez, L.D. Barriga-Arceo, H.D. Rosales, E.A. Estrada, R.S. Parra, J.J. Cruz-Rivera, Temperature effects during Ostwald ripening on structural and bandgap properties of TiO_2 nanoparticles prepared by sonochemical synthesis, Materials Science and Engineering B-Solid 175 (2010) 9–13.

[6] C. Yu, J.C. Yu, M. Chan, Sonochemical fabrication of fluorinated mesoporous titanium dioxide microspheres, Journal of Solid State Chemistry 182 (2009) 1061–1069.

[7] X. Lü, J. Li, X. Mou, J. Wu, S. Ding, F. Huang, Y. Wang, F. Xu, Room-temperature ferromagnetism in $Ti_{1-x}V_xO_2$ nanocrystals synthesized from an organic-free and water-soluble precursor, Journal of Alloys and Compounds 499 (2010) 160–165.

[8] Z. Zhang, C. Shao, L. Zhang, X. Li, Y. Liu, Electrospunnanofibers of V-doped TiO_2 with high photocatalytic activity, Journal of Colloid and Interface Science 351 (2010) 57–62.

[9] X. Shen, J. Zhang, B. Tian, Microemulsion-mediated solvothermal synthesis and photocatalytic properties of crystalline titania with controllable phases of anatase and rutile, Journal of Hazardous Materials 192 (2011) 651–657.

[10] D. de la Cruz, J.C. Arevalo, G. Torres, R.G. Bautista Margulis, C. Ornelas, A. Aguilar-Elguezabal, TiO_2 doped with Sm^{3+} by sol–gel: synthesis, characterization and photocatalytic activity of diuron under solar light, Catalysis Today 166 (2011) 152–158.

[11] B. Tian, C. Li, J. Zhang, One-step preparation, characterization and visible-light photocatalytic activity of Cr-doped TiO_2 with anatase and rutile bicrystalline phases, Chemical Engineering Journal 191 (2012) 402–409.

[12] R. Dholam, N. Patel, A. Miotello, Efficient H_2 production by water-splitting using indium-tin-oxide/V-doped TiO_2 multilayer thin film photocatalyst, International Journal of Hydrogen Energy 36 (2011) 6519–6528.

Synthesis of vanadium oxide/titanium dioxide nanocomposites via sonochemical and hydrothermal process and their utilisation for energy storage application

C. Kahattha

College of Nanotechnology,
King Mongkut's Institute of Technology Ladkrabang,
Chalongkrung Rd., Ladkrabang,
Bangkok 10520, Thailand

and

ThEP Center, CHE,
328 Siayuthtaya Rd.,
Bangkok 10400, Thailand
Fax: +66-23298265
E-mail: kahattha@gmail.com

W. Techitdheera

Faculty of Science,
School of Applied Physics,
King Mongkut's Institute of Technology Ladkrabang,
Bangkok 10520, Thailand
Fax: +66-23298265
E-mail: naratipcmu@yahoo.com

N. Vittayakorn

College of Nanotechnology,
King Mongkut's Institute of Technology Ladkrabang,
Chalongkrung Rd., Ladkrabang,
Bangkok 10520, Thailand

and

Advanced Materials Science Research Unit,
Faculty of Science,
Department of Chemistry,
King Mongkut's Institute of Technology Ladkrabang,
Bangkok 10520, Thailand
Fax: +66-23298265
E-mail: wdheera@gmail.com

W. Pecharapa*

College of Nanotechnology,
King Mongkut's Institute of Technology Ladkrabang,
Chalongkrung Rd., Ladkrabang,
Bangkok 10520, Thailand

and

ThEP Center, CHE,
328 Siayuthtaya Rd.,
Bangkok 10400, Thailand
Fax: +66-23298265
E-mail: kpewisan@gmail.com
*Corresponding author

Abstract: This work focuses on the synthesis of V_2O_5/TiO_2 nanocomposites by sonochemical and hydrothermal process. First, titanium dioxide (TiO_2) nanopowders were synthesised by sonochemical process using titanium isopropoxide as a titanium source. Meanwhile, hydrothermal process was employed to modify the structure of commercial V_2O_5 powder to be nanorod-like structure V_2O_5 to increase its specific surface area. Structural and morphological properties of the composites were characterised by X-ray diffraction, scanning electron microscope and transmission electron microscope. The XRD results indicate that the crystallisation of the composite corresponds to anatase and orthorhombic structures of TiO_2 and V_2O_5, respectively. The significant variation of charge storage properties of the composites under ultraviolet irradiation was obtained by varying V_2O_5 content in the composite. Results suggest that V_2O_5 loaded into the nanocomposite plays a key role as a storage material of photoelectrons generated by TiO_2 illuminated by ultraviolet irradiation.

Keywords: TiO_2; V_2O_5; sonochemical; hydrothermal; energy storage.

Reference to this paper should be made as follows: Kahattha, C., Techitdheera, W., Vittayakorn, N. and Pecharapa, W. (2014) 'Synthesis of vanadium oxide/titanium dioxide nanocomposites via sonochemical and hydrothermal process and their utilisation for energy storage application', *Int. J. Nanotechnol.*, Vol. 11, Nos. 1/2/3/4, pp.333–344.

Biographical notes: Chokchai Kahattha received his BS and MS in Applied Physics from King Mongkut's Institute of Technology Ladkrabang (KMITL) in 2005 and 2009, respectively. He is now a PhD student at College of Nanotechnology, King Mongkut's Institute of Technology Ladkrabang. His current researches are focused on the synthesis processes, characterisation techniques of metal oxide-based materials such as ZnO, SnO_2, TiO_2, VO_2 and V_2O_5, composite and transition-doped TiO_2.

Wicharn Techitdheera received his BSc in Physics from Khon Khaen University in 1985, MSc in Physics from Chulalongkorn University in 1990, He is currently an Associate Professor at Department of Physics, King Mongkut's Institute of Technology Ladkrabang (KMITL). His active researches are based on the materials science and computational physics.

Naratip Vittayakorn earned his PhD in Materials Science from Chiang Mai University in 2004. He was a Visiting Scientist at Iowa state university from 2002–2004, and at Oregon state university in 2006. He is currently an Assistant Professor of Material Science in the Department of Chemistry and a Research Scientist in the College of Nanotechnology Ladkrabang, at the King Mongkut's Institute of Technology Ladkrabang, Bangkok, Thailand. He received the Thailand Young Scientist Award from the Foundation for the Promotion of Science and Technology under the Patronage of His Majesty the King (2008). He has over 60 publications in the research areas of ferroelectric, piezoelectric, dielectric and nano-materials.

Wisanu Pecharapa received his BS in Physics from Chiangmai University in 1992, MS in Physics from University of Central Florida, USA in 1997, and PhD in Applied Physics from King Mongkut's Institute of Technology Ladkrabang (KMITL) in 2007. He is currently an Associate Professor and permanent academic staff at College of Nanotechnology, King Mongkut's Institute of Technology Ladkrabang (KMITL). His current researches are focused on the synthesis processes, characterisation techniques of metal oxide-based materials such as TiO_2, ZnO, WO_3, NiO, SnO_2 and their alloys and composite, especially in low-dimensional structures that can be applied for optical, optoelectronics, catalysts and energy applications.

This paper is a revised and expanded version of a paper entitled 'Titanium dioxide/Vanadium oxide nanocomposites synthesized via sonochemical and hydrothermal process for energy storage application' presented at *IEEE international Nanoelectronics Conference (INEC) 2013*, Resort World Sentosa, Singapore, 2–4 January, 2013.

1 Introduction

Vanadium pentoxide (V_2O_5) has been intensively studied in the field of nanomaterial due to its excellent and suitable properties for various applications such as sensors, catalysts, cathode materials for batteries and electrochemical applications [1,2]. For charge storage mechanism of V_2O_5, the intercalation/deintercalation of Li^+ between the vanadium pentoxide layers in the electrode can be explained by the following redox reaction:

$$V_2O_5 + xLi^+ + xe \leftrightarrow Li_xV_2O_5 \quad (1)$$

The high Li^+ intercalation/deintercalation in V_2O_5 is dependent upon the nearly complete redox reaction between V^{4+} and V^{5+} [3]. Previously, many techniques such as sputtering, atmospheric chemical vapour deposition, co-precipitation and hydrothermal method [4,5] have been successfully employed to synthesise functional V_2O_5 nanostructures. Sahana et al. [6] prepared V_2O_5 by spin coating and observed the crucial electrochemical properties of the thin films. Metalorganic, organic and inorganic were selected as the starting precursors in this process. The results indicated that the Li^+ intercalation capacity and Li^+ diffusion coefficient was increased by an order of magnitude in the non-stoichiometric films. Dhayal Raj et al. [7] reported on gas sensing properties of V_2O_5 hollow spheres made up of self-assembled nanorods synthesised by solvothermal method and the corresponding results indicated that V_2O_5 nanorods had superior sensing response for ethanol when compared to that of ammonia. Keng-Che

et al. [8] gave a report on electrochromic properties of V_2O_5 nanowires derived from commercial V_2O_5 powder. The deposition of V_2O_5 nanowires were carried out by thermal evaporation onto ITO substrate and the results indicated that V_2O_5 nanowires were obtained after kept in a pressure of 8×10^{-4} Torr and 650°C. The transmittance spectrum change of V_2O_5 nanowires is 37.4% at 415 nm. It is believed that the properties of V_2O_5 can be enhanced by the incorporation of functional materials in form of compatible composites. Among many metal oxide compounds, TiO_2 has been attracted numerous attentions due to its fascinating properties including wide band gap, excellent response in ultraviolet region, non-toxicity and chemical stability. TiO_2 can efficiently generate photoelectron under UV irradiation, which can effectively assist the optical performance of V_2O_5. Recently, TiO_2 nanostructures have been synthesised by variety of methods such as hydrothermal technique [9], solvothermal technique [10], electrospinning method [11], frame spray pyrolysis [12] and sonochemical process [13]. Among these methods, sonochemical is suitable for synthesis this metal oxide due to its simplicity, short time process and comfort of nanopowder synthesis with high yield. However, few reports on the composite of these two materials originally synthesised by two different methods have been yet acknowledged.

In this work, we report the synthesis of V_2O_5 nanorods by hydrothermal process, TiO_2 nanoparticles by sonochemical process and the composite of these materials. As-prepared composites were utilised as energy storage material. The effect of weight ratio of V_2O_5 : TiO_2 on photoelectrochemical properties of the products was studied and discussed.

2 Material and method

2.1 Synthesis of TiO_2 by sonochemical process

TiO_2 powders were synthesised by sonochemical-assisted process. In the synthesis process, certain amount of titanium isopropoxide was dissolved into solution of absolute ethanol and acetylacetone and then stirred at room temperature for 24 h until transparent pale yellow solution was obtained. 10 mL of the stocked solution and 50 mL of deionised water was filled into the chamber and then the mixed liquid was irradiated with high intensity ultrasound (650 W 20 kHz) by a Sonics Model VCX 750 at room temperature in ambient air for 30 min until the completely precipitated product was reached. After cooled down to room temperature, the resulting precipitates were washed with deionised water and ethanol. After that the cleaned precipitates were calcined at 500°C for 4 h.

2.2 Synthesis of V_2O_5 nanorods by hydrothermal method

The V_2O_5 nanorods were synthesised by hydrothermal method using commercial V_2O_5 powder as the source of vanadium and *n*-butanol, acetylacetone were chosen as the reducing agents. In a typical process, 3.62 g of commercial V_2O_5 powder, 10 mL of *n*-butanol, 10 mL of acetylacetone and 100 mL of deionised water were vigorously magnetically stirred at room temperature for 1 h. The suspension was transferred into a 250 mL Teflon-lined stainless autoclave, which was then filled with deionised water up to 200 mL of total volume. The autoclave was sealed and kept at 120°C for 24 h and

then cooled down to room temperature for 24 h. The obtained dark blue precipitate was filtered and washed for several times with deionised water, acetone and absolute ethanol and dried in air at 80°C for several time, followed by calcinations at 500°C for 4 h.

2.3 Fabrication of V_2O_5/TiO_2 nanocomposite films

In this process, V_2O_5/TiO_2 nanocomposites with different ratio of $V_2O_5 : TiO_2$ were dissolved in the solution of nitric acid, DI water, absolute ethanol and terpineol. After that, the mixed solution was stirred at room temperature for 30 min and assigned as solution A. The solution B was prepared using ethylcellulose dissolved in absolute ethanol and sonicated until the opaque solution was obtained. After that, the final mixed solution between solution A and B was homogenised at 6000 rpm for 30 min and stirred at 120°C until the viscous yellow suspension was obtained. Secondly, the well mixed suspension was slowly dropped and spread onto the FTO glass substrate followed by drying in air at 80°C for 10 min to yield the as-prepared thin film. Finally, the as-prepared composites film was further continued residual removal by heating at 500°C in air for 2 h to obtain the V_2O_5/TiO_2 nanocomposite film. The schematic draw of the device is shown in Figure 1.

Figure 1 The schematic draw of the device using V_2O_5/TiO_2 nanocomposite film as working electrode

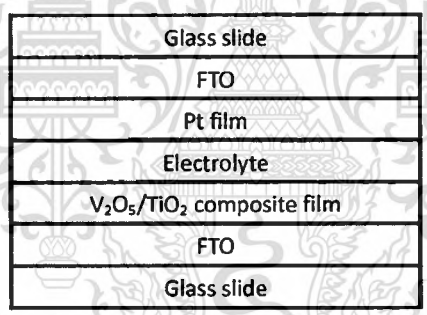

2.4 Film characterisation

The crystal structures of the samples were investigated by X' Pert PRO X-ray diffraction with a monochromatic source of Cu K_α ($\lambda = 0.15405$ nm). Their morphologies were monitored with JEOL JSM-6510 scanning electron microscope with an accelerating voltage of 5.0 kV. Transmission electron microscopy images and selected area electron diffraction (SAED) patterns were carried out by TECNAI G2 20 transmission electron microscope, using an accelerating voltage of 200 kV. Its optical absorption was investigated by Helios γ UV-Vis spectrophotometer.

2.5 Photoelectrochemical measurement

Photoelectrochemical measurement was conducted using Autolab PGSTAT302 with V_2O_5/TiO_2 nanocomposite film as the working electrode and Pt films as the counter electrode. Photocurrent measurement was carried out in the electrolyte of 0.1 M $LiClO_4$

at room temperature. The current-potential curves were measured at a potential sweep rate of 20 mV/s in dark and under sun light irradiated by solar simulator lamp.

3 Result and discussion

The crystalline structure of the V_2O_5/TiO_2 nanocomposite films was investigated by XRD and their corresponding patterns are shown in Figure 2. The noticeable diffraction peaks, which appeared in diffraction spectra of V_2O_5 synthesised by hydrothermal method and TiO_2 synthesised via the sonochemical process attributed to orientation plane of orthorhombic structure of V_2O_5 corresponded to JCPDS file No. 89-061 and anatase phase of TiO_2 corresponded to JCPDS file No. 89-4921. These results indicated that V_2O_5 orthorhombic structure and TiO_2 with pure anatase phase were obtained with calcinations route at 500°C. Meanwhile, dual spectra appeared in the diffraction peaks of V_2O_5/TiO_2 nanocomposite and disappearance of unusual diffraction peaks in the spectra. These results imply that the V_2O_5/TiO_2 nanocomposite can be obtained. The possible mechanisms anticipated to the formation of TiO_2 nanoparticles during sonochemical process are proposed. During the process, titanium isopropoxide dissolved in deionised water may transform to hydrolysed alkoxides via hydrolysis and condensation processes. This intermediate form processes relevant functional groups that can further transform to fine TiO_2 nanoparticles by condensation process by the assistance of rapid collision driven by intense ultrasound energy provided by ultrasonic irradiation [14]. Meanwhile the plausible mechanisms responsible for the formation of V_2O_5 nanorods via hydrothermal process are suggested. First, the starting V_2O_5 powders were dissolved and the oxidation state +5 of vanadium is reduced to +4 by the presence of *n*-butanol and acetylacetone acting as reducing agents. Under hydrothermal, the intermediate species can undergo condensation and nucleation of vanadium oxide nuclei that can rapidly develop to various types of low dimensional nanostructures including nanorods and nanobelts [15]. The SEM image of the nanorod-like V_2O_5 is shown in Figure 3(a). Meanwhile the SEM image of TiO_2 nanoparticles synthesised by sonochemical-assisted process is exhibited in Figure 3(b). Figure 3(c) illustrates the morphology of V_2O_5/TiO_2 nanocomposite with weight ratio 0.9 : 0.1. It is clearly seen that the nanorod-like V_2O_5 with diameter about 200 nm can be synthesised by hydrothermal method. From Figure 3(c), it is observed that TiO_2 nanoparticles are uniformly dispersed in V_2O_5 nanorod matrix. These results implied that V_2O_5/TiO_2 nanocomposite films can be prepared by mixing oxide materials using facile technique.

TEM images and electron diffraction patterns of TiO_2 nanopowders and V_2O_5 nanorod are shown in Figure 4. It clearly seen that the TiO_2 nanoparticles have a quasi-spherical structure with diameter 20–30 nm and exhibit the polycrystallinity after calcination at 500°C as shown in Figure 4(a) and (b). Meanwhile, V_2O_5 nanorods synthesised via hydrothermal method and calcined at 500°C exhibit the single crystalline phase as shown in Figure 4(c) and (d). These result are in good accordance with XRD and SEM results. The optical absorption of TiO_2 and V_2O_5 was investigated by UV-Vis spectroscopy and the corresponding spectra are shown in Figure 5. It clearly seen that the UV light in range 300–400 nm was absorbed by TiO_2 nanoparticles due to the typical optical band gap of TiO_2 [16]. Meanwhile, V_2O_5 can absorb light with photon energy in the range 450–470 nm. This characteristic feature was also observed in previous report [17]. From the result, the absorption in UV region of TiO_2 nanoparticles can initiate the

generation of photoelectrons under illumination, which support the photoelectrochemical process of V_2O_5.

Figure 2 XRD patterns of bare TiO_2, V_2O_5 and V_2O_5/TiO_2 nanocomposite films

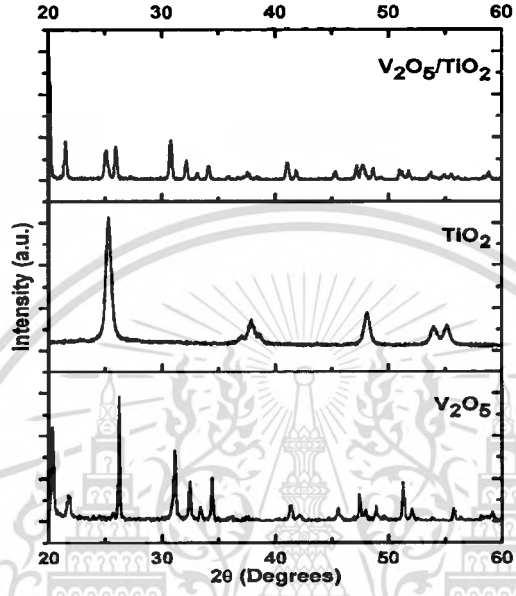

The photoelectrochemical properties of V_2O_5/TiO_2 nanocomposites with different weight ratio are shown in Figure 6. For bare V_2O_5 case, it is noticed that the current density of the film increases when illuminated by solar simulator light due to its absorption properties in the visible region of this material [18]. For all samples, both oxidation and reduction peak are observed in cyclic voltammogram revealing that the V_2O_5 nanorods exhibit charge capacitive behaviour owing to intercalation/ deintercalation of Li^+ in V_2O_5 matrix [17]. Furthermore, the changing of colour on the V_2O_5 nanorods working electrode from brown to dark grey associated with the reduction of oxidation number of V^{5+} to V^{4+} is observed [19]. The increasing of current density in the composites used as working electrode is probably proceeded following the relative energies of the conduction bands of TiO_2 and V_2O_5. Under illumination, photo-generated electrons can easily be transferred from Ti(3d) to V(3d) orbitals, supporting the charges transfer and leading to the higher current density of the device. This presumption is supported by previous work that the performance of N_xTiO_{2-x}/NiO bilayer thin film electrodes was investigated [20]. It was found that the efficient separation of photogenerated charge carriers occurs in the interconnected N_xTiO_{2-x} and NiO thin film. This phenomenon implies that the enhancement in light-induced photoelectron generation can be achieved by the incorporation of TiO_2 into V_2O_5 due to the photoelectron generated by TiO_2 during illumination. The optimised weight ratio of V_2O_5/TiO_2 for superiority in current density is found to be 0.7 : 0.3. Further detailed studies on roles of both materials on the performance of composite are underway so that the better understanding of corresponding processes could be clearly understood.

Figure 3 SEM images of (a) V_2O_5 nanorods, (b) TiO_2 nanoparticles and (c) V_2O_5/TiO_2 nanocomposites (the scale bar = 5 μm)

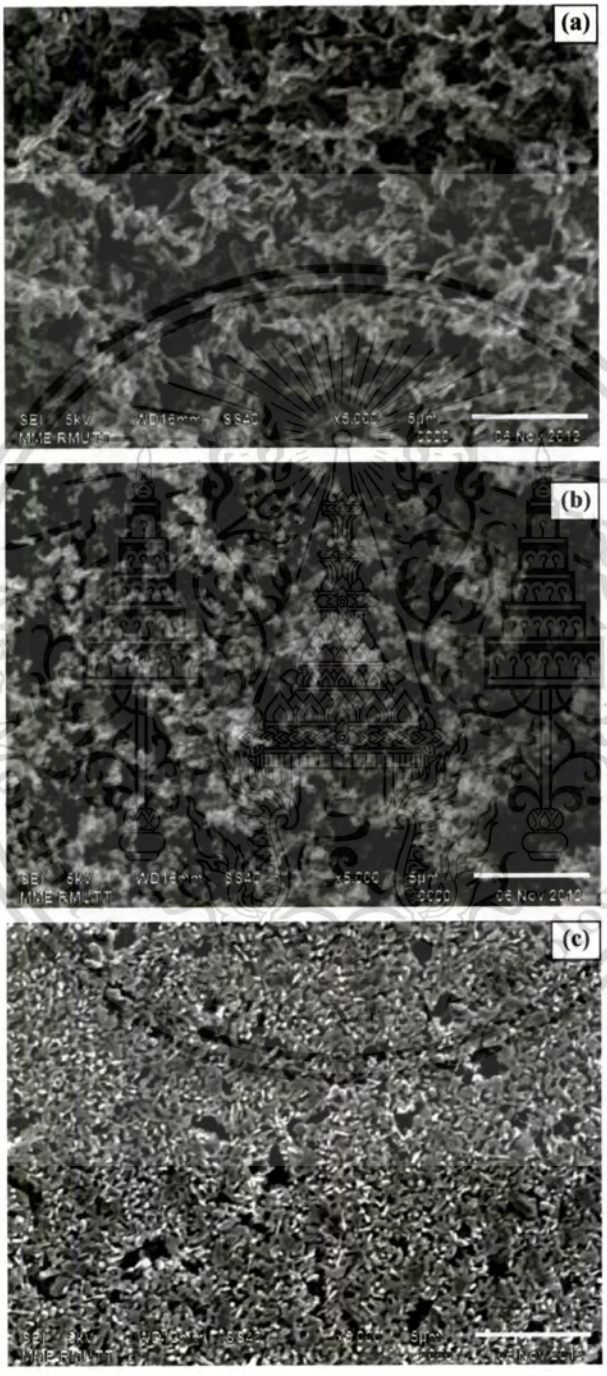

Figure 4 TEM images of (a) TiO_2 nanoparticles, (b) SAED image of TiO_2, (c) V_2O_5 nanorods and (d) SAED image of V_2O_5

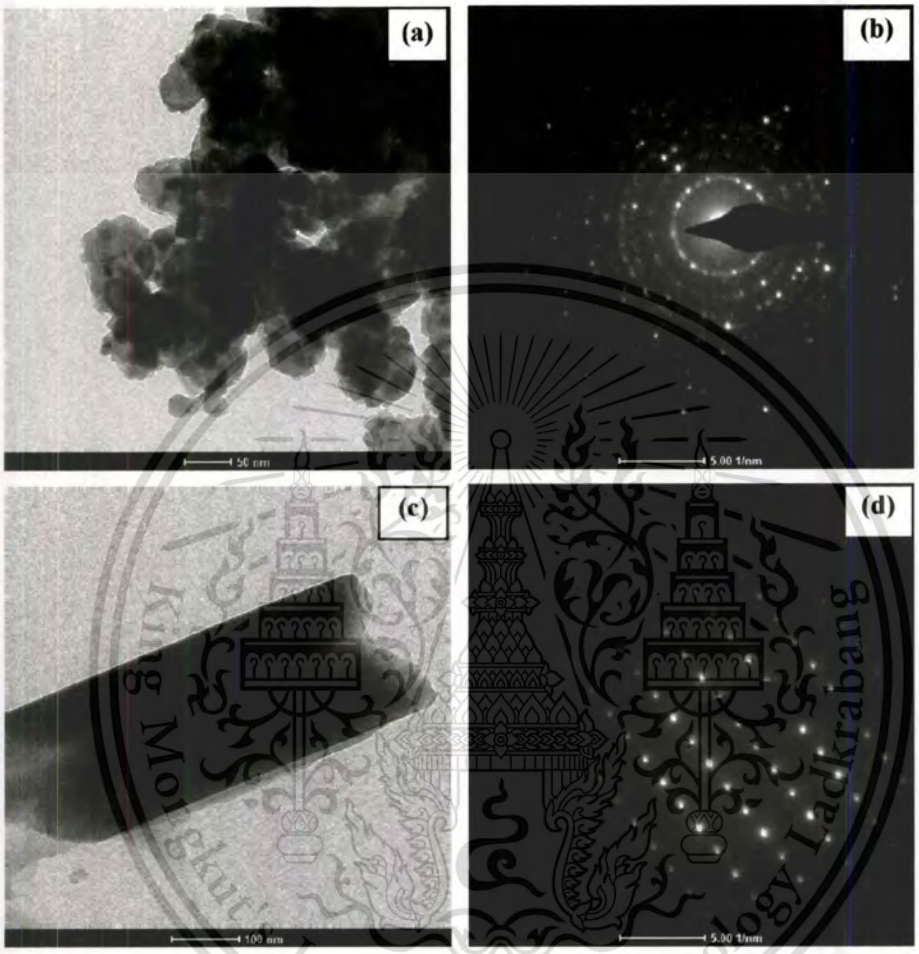

4 Conclusion

In summary, V_2O_5, TiO_2 and V_2O_5/TiO_2 nanocomposite were successfully prepared by hydrothermal, sonochemical and mechanical mixing method, respectively. The XRD results revealed that the diffraction spectrum of nanocomposites film consist of dual diffraction peaks of orthorhombicV_2O_5 and anatase TiO_2 structures. The possible mechanisms for the formation of TiO_2 and V_2O_5 nanostructures are proposed. SEM results indicated that the TiO_2 nanoparticles are well-dispersed in V_2O_5nanorodhost matrix. The photoelectrochemical results suggest that the performance of nanocomposite films utilised as working electrode can be enhanced by loading TiO_2 in V_2O_5 nanorods and the maximum current is about 22 μA at the weight ratio is 0.7 : 0.3. The amelioration in their performance may due to the higher charge transfer in the device with the presence of TiO_2 in the V_2O_5 matrix.

Figure 5 Optical absorption spectra of TiO_2 nanoparticles and V_2O_5 nanorods synthesised by sonochemical and hydrothermal method, respectively

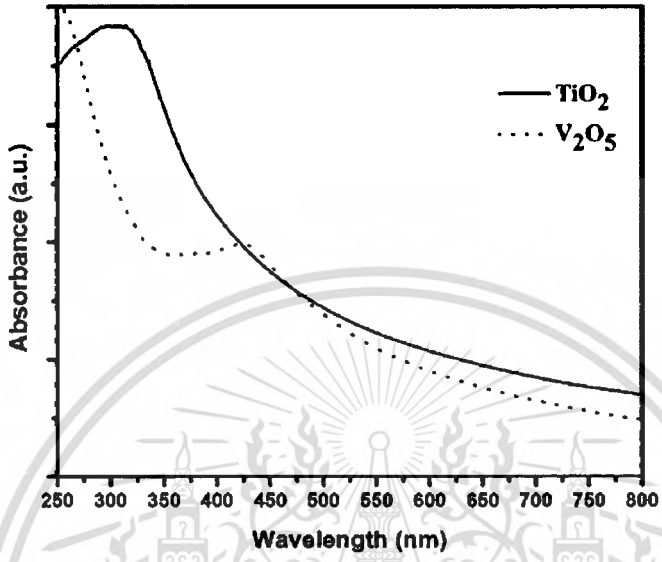

Figure 6 Cyclic voltammograms of V_2O_5/TiO_2 nanocomposites with different weight ratio at scan rate 20 mV/s. (Electrode area was 0.5 × 0.5 cm^2)

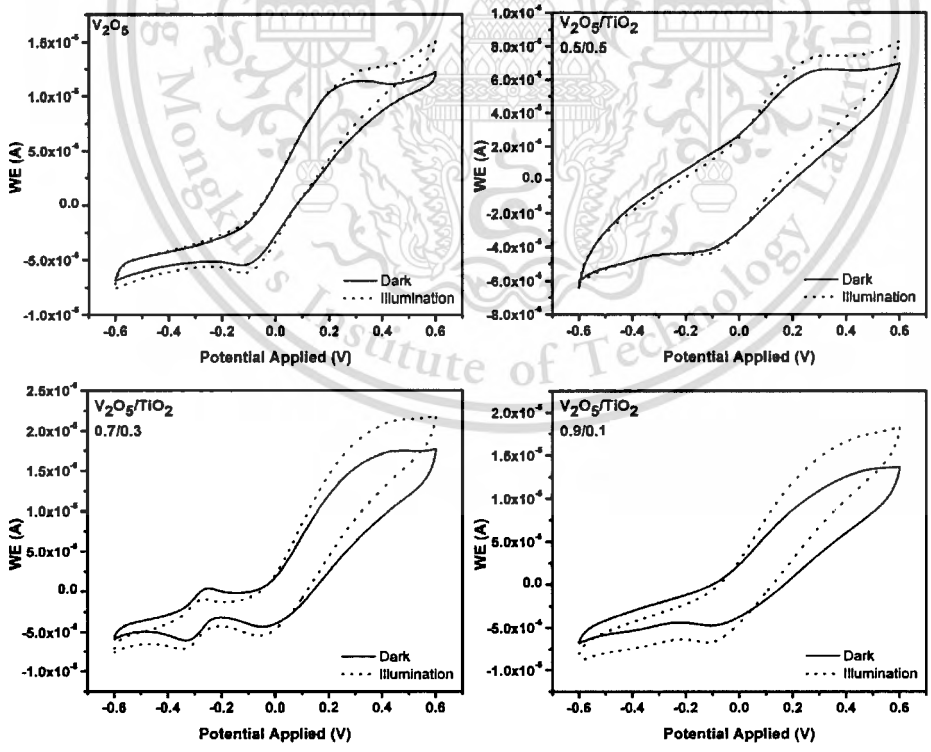

Acknowledgements

This work has partially been supported by the National Nanotechnology Center (NANOTEC), NSTDA, Ministry of Science and Technology, Thailand, through its program of Center of Excellence Network and was financially supported by KMITL research fund. Authors would like to thank Energy Policy and Planning Office, Ministry of Energy, Thailand, for research funding support. Authors would like to thank Rajamangala University of Technology Thanyaburi (RMUTT) for XRD and SEM measurement.

References

1 Lian-Mei, C., Qiong-Yu, L., Yan-Jing, H., Yan, Z. and Xiao-Yang, J. (2009) 'Investigations on capacitive properties of the AC/V_2O_5 hybrid supercapacitor in various aqueous electrolytes', *J. Alloys Compd.*, Vol. 467, Nos. 1–2, pp.465–471.

2 Ivanava, T. and Harizanova, A. (2005) 'Electrochromic investigation of sol-gel derived thin films of TiO_2-V_2O_5', *Mater. Res. Bull.*, Vol. 40, No. 3, pp.411–419.

3 Groult, H., Le Van, K., Mantoux, A., Perrigaud, L. and Doppelt, P. (2007) 'Study of the Li^+ insertion into V_2O_5 films deposited by CVD onto various substrates', *J. Power Sources*, Vol. 174, No. 1, pp.312–320.

4 Navaneetha, K.N. and Edmund, G.S. (2011) 'Low temperature chemical vapor deposition of nanocrystalline V_2O_5 thin films', *Thin Solid Films*, Vol. 519, No. 11, pp.3663–3668.

5 Chuan, C., Dongsheng, G. and Ying, W. (2011) 'Solution processing of V_2O_5-WO_3 composite films for enhanced Li-ion intercalation properties'. *J. Alloys Compd.*, Vol. 509, No. 3, pp.909–915.

6 Sahana, M.B., Sudakar, C., Thapa, C., Lawes, G., Naik, V.M., Baird, R.J., Auner, G.W., Naik, R. and Padmanabhan, K.R. (2007) 'Electrochemical properties of V_2O_5 thin films deposited by spin coating', *Mater. Sci. Eng., B*, Vol. 143, No. 3, pp.42–50.

7 Dhayal Raj, A., Pazhanivel, T., Suresh Kumar, P., Mangalaraj, D., Nataraj, D., Ponpandian, N. (2010) 'Self assembled V_2O_5 nanorods for gas sensors', *Curr. Appl. Phys.*, Vol. 10, No. 2, pp.531–537.

8 Keng-Che, C., Fu-Rong, C. and Ji-Jung, K. (2006) 'V_2O_5 nanowires as a functional material for electrochromic device', *Sol. Energy Mater. Sol. Cells*, Vol. 90, Nos. 7–8, pp.1156–1165.

9 Souvereyns, B., Elen, K., De Dobbelaere, C., Kelchtermans, A., Peys, N., D'Haen, J., Mertens, M., Mullens, S., Van den Rul, H., Meynen, V., Cool, P., Hardy, A. and Van Bael, M.K.. (2013) 'Hydrothermal synthesis of a concentrated and stable dispersion of TiO_2 nanoparticles', *Chem. Eng. J.*, Vol. 223, pp.135–144.

10 Yeji, L., Jinho, C. and Misook, K. (2010) 'Comparison of the photovoltaic efficiency on DSSC for nanometer sized TiO_2 using a conventional sol-gel and solvothermal methods', *J. Ind. Eng. Chem.*, Vol. 16, No. 4, pp.609–614.

11 Touseef, A.M., Shamshi, H., Woon-Seob, S., Hoa Van, B., Hak-Kyo, L., Myung-Seob, K. and Hwang, I.H. (2013) 'TiO_2 nanorods via one-step electrospinning technique: a novel nanomatrix for mouse myoblasts adhesion and propagation', *Colloids Surf., B*, Vol. 101, pp.424–429.

12 Gian, L.C., Elena, S. and Lucio, F. (2008) 'Photocatalytic hydrogen production over flame spray pyrolysis-synthesised TiO_2 and Au/TiO_2', *Appl. Catal., B*, Vol. 84, Nos. 1–2, pp.332–339.

13 Jingjing, G., Shenmin, Z., Zhixin, C., Yao, L., Ziyong, Y., Qinglei, L., Jingbo, L., Chuanliang, F. and Di, Z. (2011) 'Sonochemical synthesis of TiO_2 nanoparticles on graphene for use as photocatalyst', *Ultrason. Sonochem*, Vol. 18, No. 5, pp.1082–1090.

14 Yu, C., Yu, J.C. and Chan, M. (2009) 'Sonochemical fabrication fluorinated of mesoporous titanium dioxide microspheres', *J. Solid State Chem.*, Vol. 182, No. 5, pp.1061–1069.

15 Zhang, Y., Chen, C., Wu, W., Niu, F., Liu, X., Zhong, Y., Cao, Y., Liu, X. and Huang, C. (2013) 'Facile hydrothermal synthesis of vanadium oxides nanobelts by ethanol reduction of peroxovanadium complexes', *Ceram. Int.*, Vol. 39, No. 1, pp.129–141.

16 Jingbing, L., Lin, C., Jinshu, W., Mankang, Z. and Wenxiong, Z. (2010) 'A facile one-step approach to visible-light-sensitive vanadium-doped TiO_2 hollow microspheres', *Mater. Sci. Eng., B*, Vol. 172, pp.142–145.

17 Yan, L.C., Nutan, G., Stevin, S.P., Vanchiappan, A., Grace, W. and Madhavi, S. (2011) 'Morphology, structure and electrochemical properties of single phase electrospun vanadium pentoxidenanofibers for lithium ion batteries', *J. Power Sources*, Vol. 196, No. 2, pp.6465–6472.

18 Boudaoud, L., Benramdane, N., Desfeux, R., Khelifa, B. and Mathieu, C. (2006) 'Structural and optical properties of MoO_3 and V_2O_5 thin films prepared by spray pyrolysis', *Catal. Today*, Vol. 113, Nos. 3–4, pp.230–234.

19 Sooyeun, K. and Minoru, T. (2012) 'Electrochromic windows based on V_2O_5-TiO_2 and poly(3,3-dimethyl-3,4-dihydro-2H-thieno[3,4-b][1,4]dioxepine) coatings', *Sol. Energy Mater. Sol. Cells*, Vol. 107, pp.225–229.

20 Huang, H., Jiang, L., Zhang, W.K., Gan, Y.P., Tao, X.Y. and Chen, H.F. (2010) 'Photoelectrochromic properties and energy storage of $TiO_{2-x}N_x$/NiO bilayer thin films', *Sol. Energy Mater. Sol. Cells*, Vol. 94, No. 2, pp.355–359.

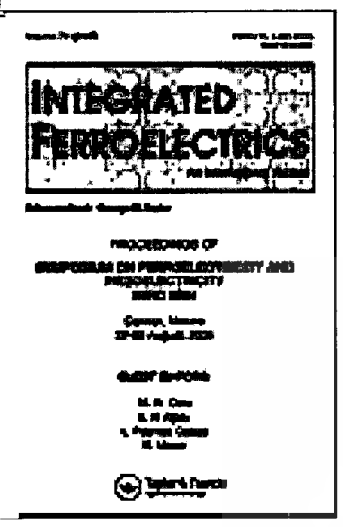

Integrated Ferroelectrics: An International Journal

Publication details, including instructions for authors and subscription information:
http://www.tandfonline.com/loi/ginf20

Effects of Reductant on Physical Properties and Formation of Vanadium Oxide Compounds Prepared by Hydrothermal Route

Chokchai Kahattha [a b] & Wisanu Pecharapa [a b]

[a] College of Nanotechnology , King Mongkut's Institute of Technology Ladkrabang (KMITL) , Bangkok , 10520 , Thailand

[b] Thailand and Center of Excellence in Physics (ThEP Center) , CHE, 328 Siayuthtaya RD, Bangkok , 10400 , Thailand

Published online: 07 Dec 2013.

To cite this article: Chokchai Kahattha & Wisanu Pecharapa (2013) Effects of Reductant on Physical Properties and Formation of Vanadium Oxide Compounds Prepared by Hydrothermal Route, Integrated Ferroelectrics: An International Journal, 149:1, 49-55, DOI: 10.1080/10584587.2013.852927

To link to this article: http://dx.doi.org/10.1080/10584587.2013.852927

Integrated Ferroelectrics, 149:49–55, 2013

ISSN: 1058-4587 print / 1607-8489 online
DOI: 10.1080/10584587.2013.852927

Taylor & Francis
Taylor & Francis Group

Effects of Reductant on Physical Properties and Formation of Vanadium Oxide Compounds Prepared by Hydrothermal Route

CHOKCHAI KAHATTHA[1,2] AND WISANU PECHARAPA[1,2,*]

[1]College of Nanotechnology, King Mongkut's Institute of Technology Ladkrabang (KMITL), Bangkok 10520, Thailand
[2]Thailand and Center of Excellence in Physics (ThEP Center), CHE, 328 Siayuthtaya RD, Bangkok 10400, Thailand

Vanadium oxide nanostructures were successfully synthesized by hydrothermal process using V_2O_5 as a starting source material. The process was conducted at 120°C for 48 h using different reductants including n*-butanol and acetylacetone. The essential physical properties of as-synthesized products were characterized by XRD, FT-IR spectroscopy, SEM and TEM. The XRD and Raman results revealed that the crystalline structure and phase of the samples are highly dependent on the reductant types. The SEM images enclose that as-prepared samples possess different morphologies depending on different reactant. The phase transformation from V_2O_5 to VO_2 can be also carried out by this process with assistance of these reactants.*

Keywords Reductant; vanadium oxide and hydrothermal

1. Introduction

Since the last few decades, numerous materials such as ZnO, TiO_2, CuO, MnO_2 and VO_2 have been synthesized or fabricated in various forms of one-dimensional (1D) nanostructures such as nanowire, nanotube and nanorod [1]. Due to uniqueness in nanostructure, 1D material has been attracted great attention for wide varieties of applications such as magnetic, electrical and optical technologies [2]. Among these materials, VO_2 has been considered as smart material for many applications due to its fascinating structure that can be transformed from a semiconductor to a metal at moderate transition temperature at about 70°C. Above this transition temperature, it adopts the tetragonal rutile structure and is typically metallic. On contrary, it is in semiconductor behavior with monoclinic structure at below transition temperature. Conversion in electrical properties pushes large changes in optical properties. At lower transition-temperature the monoclinic structure is transparent in infrared region, whereas the tetragonal rutile structure is reflective at higher transition temperature. Because of this interesting property, it has been widely utilized in many applications such as humidity sensor [3], thermochromic window [4] and optical switching devices [5]. More recently, there have been a number of research works focusing on the effective techniques for synthesizing VO_2 such as radio frequency sputtering [6], thermal

Received December 9, 2012; in final form August 25, 2013.
*Corresponding author. E-mail:·kpewisan@gmail.com

reduction [7], ion beam sputtering [8], atmospheric pressure chemical vapor deposition [9] and hydrothermal process [10]. Wentao Jiang *et al.* [11] synthesized three different VO_2 nanostructures using hydrothermal process with different concentration of oxalic acid at 180°C and studied the capacitance performance. It was found that the urchin-like VO_2 had the highest lithium ion intercalation. Kimson C. Kam *et al.* [12] synthesized VO_2 nanorods via the hydrothermal process using NH_4VO_3 as the vanadium source and investigated the thermochromic properties of as-synthesized nanorods. They found that the thermochromic transition temperature of the VO_2 nanorods is about 10°C higher compared to bulk VO_2. Tina F.-R. Shen *et al.* [13] employed the hydrothermal process for synthesizing VO_2 at different hydrothermal treatment temperatures and different thermal treatment under ambient argon. They found that VO_2 were obtained as hydrothermal treatment temperature was above 160°C and the thermal treatment was a crucial process to change its structure. From literatures, it is notified that the formation of VO_2 structures depends strongly on the environment and crucial conditions of hydrothermal process such as reducing agent, pH, hydrothermal treatment temperature and thermal treatment temperature.

In this present study, we report the synthesis of VO_2 nanorods by hydrothermal method without thermal treatment process. The effect of reducing agent types on physical properties and formation of as-prepared products were investigated and discussed.

2. Experiments

All chemicals were reagent grade and used as purchased without further purification. Vanadium pentoxide (V_2O_5), *n*-butanol ($C_4H_{10}O$) and acetylacetone ($C_5H_8O_2$) were purchased from Sigma-Aldrich. VO_2 nanorods were synthesized by hydrothermal method using V_2O_5 as the source of vanadium and *n*-butanol, acetylacetone as the reductants. Firstly, 3.62 g of commercial V_2O_5 powder, 10 mL of *n*-butanol, 10 mL of acetylacetone and 200 mL of deionized water were vigorously magnetic stirred at room temperature for 1 h. The suspension was then transferred into a 250 mL Teflon-lined stainless autoclave. Secondly, the autoclave was sealed and kept at 120°C for 48 h with vigorously magnetic stirred and then cooled down to room temperature for 24 h. Finally, the obtained dark blue precipitate was filtered and washed with deionized water, acetone and absolute ethanol for several times and dried in air at 80°C. The crystal structures of the samples were investigated by X' Pert PRO X-ray diffraction with a monochromatic source of Cu K_α ($\lambda = 0.15405$ nm). Chemical bonding of the materials was characterized by Fourier transform infrared spectroscopy (FTIR) in the range of 400–4000 cm^{-1}in the transmittance mode. Their morphologies were monitored with JEOL JSM-6510 scanning electron microscope (SEM) with an accelerating voltage of 5.0 kV. Transmission electron microscopy (TEM) images and selected area electron diffraction (SAED) patterns were taken with TECNAI G2 20 transmission electron microscope, using an accelerating voltage of 200 kV.

3. Results and Discussion

XRD patterns of as-synthesized vanadium oxide via the hydrothermal process at 120°C for 48 h using different reductant agents are shown in Fig. 1. In the case of *n*-butanol as the reductant agent, the XRD pattern displays multi-diffraction peaks of mixed structures. The diffraction peaks positioned at $2\theta = 26.1°$ and 47.3° are attributed to (110) and (600) orientation plane of orthorhombic structure of V_2O_5 [JCPDS file No. 89-2482]. This result suggests that the complete transformation of VO_2 phase could not be carried out by only *n*-butanol reducing agent. In contrast, the diffraction peaks of VO_2 are appeared in the XRD

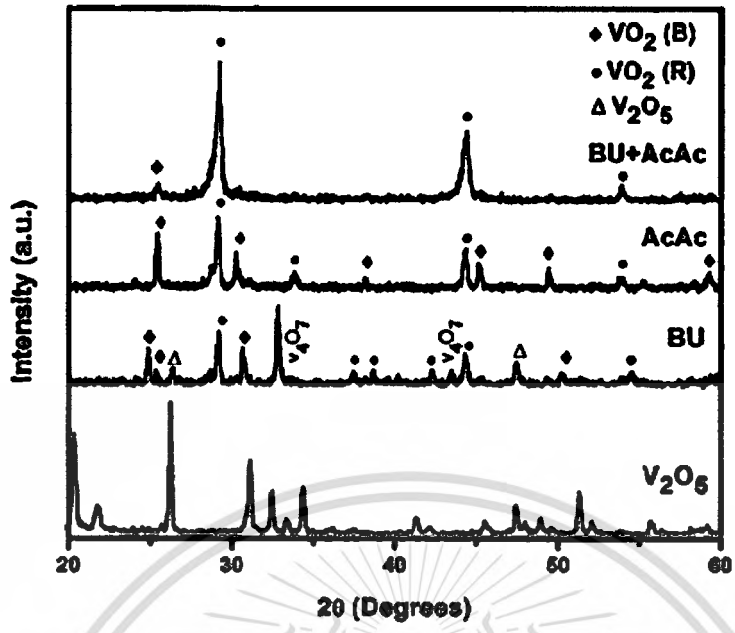

Figure 1. XRD patterns of the commercial V_2O_5 powders and VO_2 synthesized by hydrothermal method at 120°C for 48 h using different reducing agents.

pattern of the as-synthesized product from process using acetylacetone as the reductant agent. The disappearance of diffraction peaks of V_2O_5 indicates that the starting materials can be completely transformed into VO_2 with hydrothermal process using acetylacetone as the reductant agents. However, the diffraction peaks reveal the mixture phases of VO_2 (B) and VO_2 (R) with the monoclinic structures [14–15]. In the case of dual reductant *n*-butanol and acetylacetone, the prominent diffraction peaks situated at around $2\theta = 28.0°$, 44.0° and 53.0° are assigned to (011), (021)/(012) and (102) orientation plane of VO_2 (R), respectively. In addition, a noticeable peak at around $2\theta = 25.4°$ is attributable to (110) orientation plane of VO_2 (B). Based on XRD results, it can be deduced that *n*-butanol, acetylacetone and temperature are the important factors in the transformation of V_2O_5 to VO_2.

The chemical bonding of the starting materials and as-synthesized VO_2 powders carried out by hydrothermal process at 120°C for 48 h using dual reductant agents are shown in Fig. 2. The prominent band situated at about 3460 and 1650 cm^{-1} are associated to the stretching and bending vibration mode of absorbed H_2O and O—H groups by KBr molecules, respectively [16]. The characteristic peaks of V_2O_5 are identified at around 1025, 830, 598 and 480 cm^{-1}. The peak at 1025 cm^{-1} relates to V=O stretching vibration mode, while the broad peak at around 830 cm^{-1} is attributed to coupled vibration mode between V=O and V—O—V [17]. The 1000 cm^{-1}peak observed in VO_2, which generally exists in many vanadium oxide compounds corresponds to anointer mediate oxidation state between V^{5+} in V_2O_5 and V^{4+} in VO_2. It is attributed to the stretching mode of short V=O bonds that are also present in VO_2 [18]. The signal peak positioned at around 540 cm^{-1} in the FTIR spectrum of VO_2 is assigned to the vibrational bending mode of V—O—V [19], These FTIR results are in good accordance with the presumption from XRD results.

The SEM images as seen in Fig. 3 illustrate the morphologies of the V_2O_5 and VO_2 nanorods synthesized via the hydrothermal process at 120°C for 48 h using dual reducing agents. It clearly seen that the hydrothermal process not only evidently transform its crystal

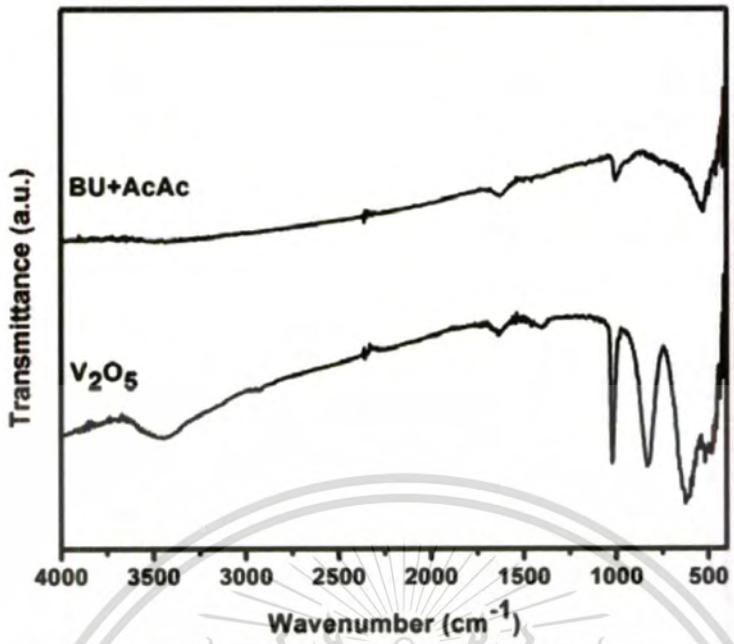

Figure 2. FTIR spectra of the commercial V_2O_5 powders and VO_2 powders synthesized by hydrothermal method at 120°C for 48 h using dual reducing agents.

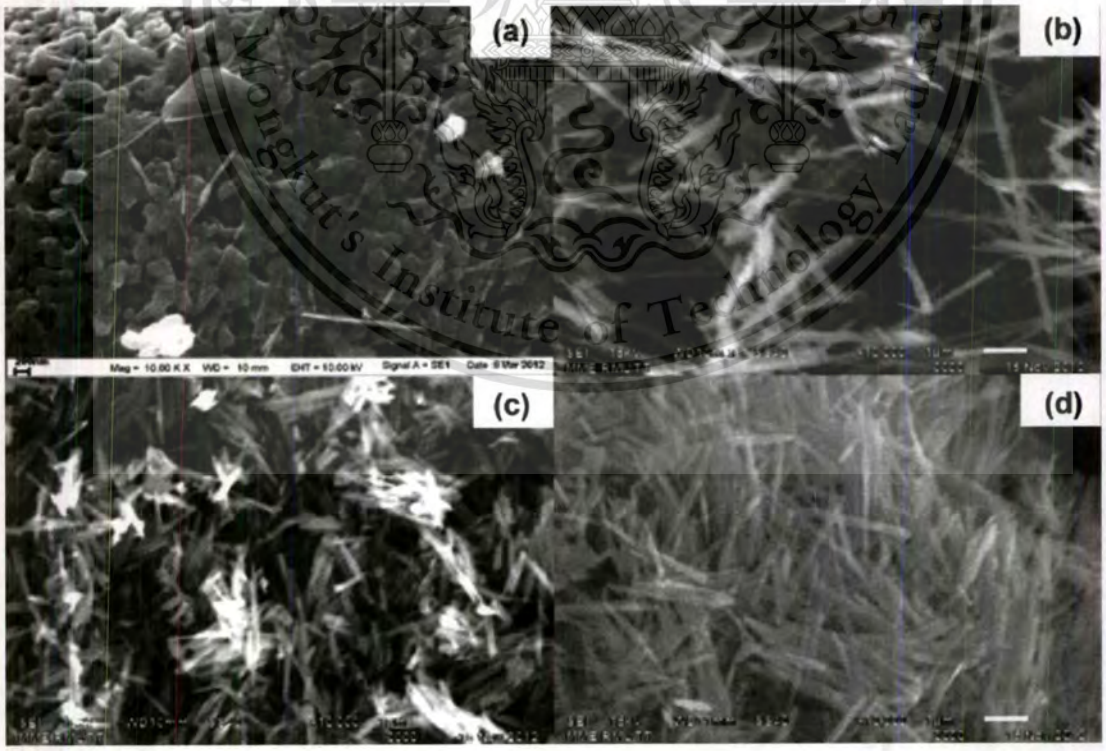

Figure 3. SEM images of (a) commercial V_2O_5 powders and VO_2 nanorods synthesized by facile hydrothermal method at 120°C for 48 h using (b) *n*-butanol as areductant, (c) acetylacetone as a reductant and (d) dual *n*-butanol and acetylacetone as reductants.

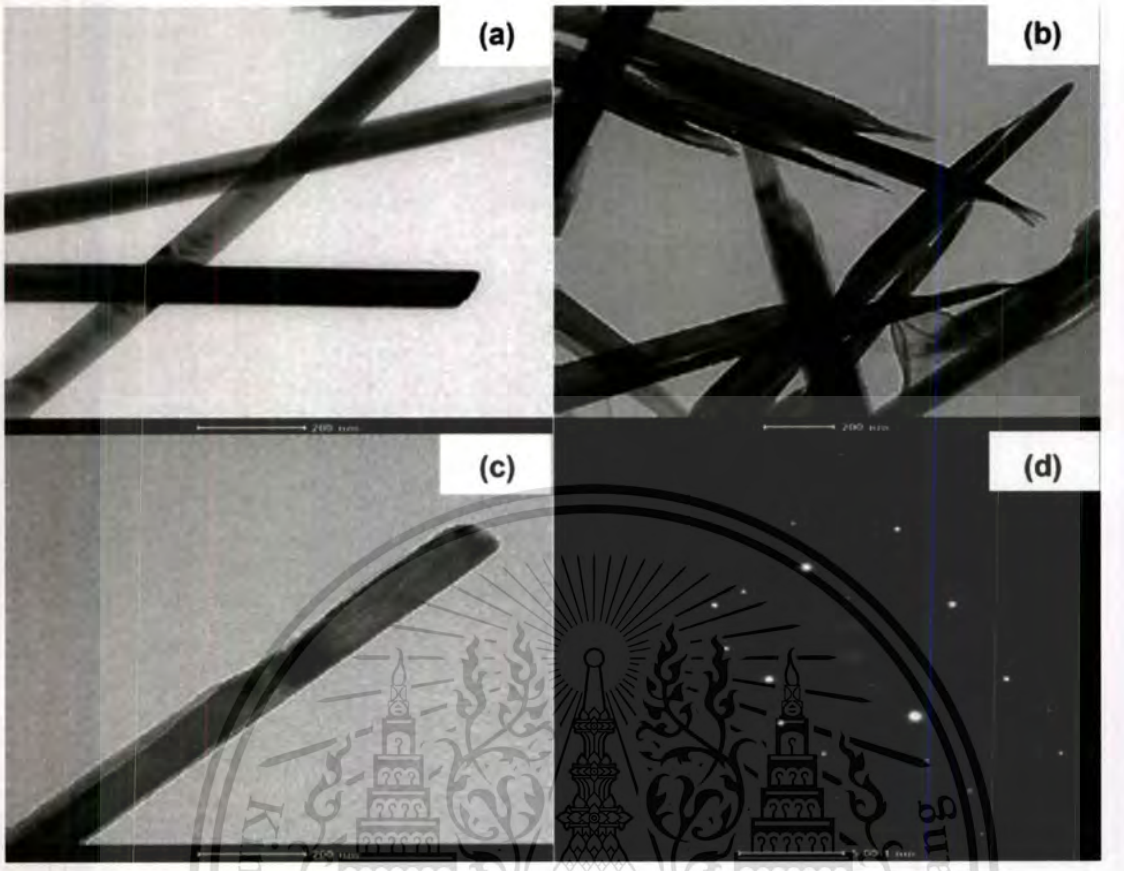

Figure 4. TEM images of VO_2 nanorods synthesized by facile hydrothermal method at 120°C for 48 h with (a) *n*-butanol as the reductant, (b) acetylacetone as the reductant, (c) dual *n*-butanol and acetylacetone as the reductants and (d) SAED image the sample using dual reductants.

structure of V_2O_5 to VO_2 but also change physical structure of this material from brain-like to nanorod-like with strong influence of reductant types on size dimension of the rods.

TEM image of as-synthesized sample using *n*-butanol as the reductant as seen in Fig. 4(a) exhibits uniform rod-like structure with diameter of about 80 nm and length over 10 μm. Meanwhile, Fig. 4(b) shows the leaf-like structure of the sample using acetylacetone as a reductant, that appears to be an ultra thin cut of the parallelepiped with a diameter of 100 nm and a length of 2 μm. For the sample obtained by using dual *n*-butanol and acetylacetone as the reductants (Fig. 4c) exhibits the short-rod like structure with a diameter of 80 nm and a length 2–3 μm. Selected area electron diffraction (SAED) image as observed in Fig. 4(d) can confirm that the as-synthesized VO_2 possesses high degree of crystallization. From SEM and TEM results, it is affirmed that the one-dimensional VO_2 can be synthesized by single-step hydrothermal method without any further post-treatment.

4. Conclusion

In summary, VO_2 nanorods were successfully synthesized by facile hydrothermal method at 120°C for 48 h using *n*-butanol and acetylacetone as potential reductants. The XRD results revealed that the as-synthesized nanorods have the mixed phase of VO_2 (B) and VO_2 (R) monoclinic structure. SEM and TEM results disclosed that the dimension, size and shape of the as-synthesized samples highly depend on the type of reductant agents which are the

key factors for synthesizing metastable low dimensional VO_2 structures that could be the potential structure applied for thermochromic and optoelectronic devices.

Acknowledgments

This work has partially been supported by the National Nanotechnology Center (NANOTEC), NSTDA, Ministry of Science and Technology, Thailand, through its program of Center of Excellence Network and was financially supported by KMITL research fund. Authors would like to thank Energy Policy and Planning Office, Ministry of Energy, Thailand, for research funding support.

References

1. Jai Singh, Sandip S. Patil, Mahendra A. More, *et al.*, Formation of aligned ZnO nanorods on self-grown ZnO template and its enhanced field emission characteristics. *Appl. Surf. Sci.* **256**, 6157–6163 (2010).
2. Chuanhui Xia, Chenguo Hu, Peng Chen, *et al.*, Magnetic properties and photoabsorption of the Mn-doped CeO_2 nanorods. *Mat. Res. Bull.* **45**, 794–798 (2010).
3. Jinhua Li, and Ningyi Yuan, Temperature sensitivity of resistance of VO_2 polycrystalline films formed by modified ion beam enhanced deposition. *Appl. Surf. Sci.* **233**, 252–257 (2004).
4. M. Benkahoul, M. Chaker, J. Margot, *et al.*, Thermochromic VO_2 film deposited on Al with tunable thermal emissivity for space applications. *Sol. Energ. Mat. Sol. C.* **95**, 3504–3508 (2011).
5. KuangYue Tsai, Fong-Hsu Wu, Han-Ping D. Shieh, *et al.*, Optical switching properties of VO2 films driven by using WDM-aligned lasers. *Mater. Chem. Phys.* **96**, 331–336 (2006).
6. Sébastien Saitzek, Frédéric Guinneton, Guillaume Guirleo, *et al.*, VO_2 thin films deposited on silicon substrates from V_2O_5 target: Limits inoptical switching properties and modeling. *Thin Solid Films.* **516**, 891–897 (2008).
7. Ji Qi, Guiling Ning, and Yuan Lin, Synthesis, characterization, and thermodynamic parameters of vanadium dioxide. *Mat. Res. Bull.* **43**, 2300–2307 (2008).
8. Xingjian Yi, Changhong Chen, Luqin Liu, *et al.*, A new fabrication method for vanadium dioxide thin films deposited by ion beam sputtering. *Infrared. Phys. Techn.* **44**, 137–141 (2003).
9. P. Evans, M. E. Pemble, and D. W. Sheel, *et al.*, Multi-functional self-cleaning thermochromic films by atmospheric pressure chemical vapour deposition. *J. Photoch. Photobio. A.* **189**, 387–397 (2007).
10. Shidong Ji, Feng Zhang, and Ping Jin, Selective formation of VO_2(A) or VO_2(R) polymorph by controlling the hydrothermal pressure. *J. Solid. State. Chem.* **184**, 2285–2292 (2011).
11. Wentao Jiang, Juan Ni, Ke Yu, *et al.*, Hydrothermal synthesis and electrochemical characterization of VO_2(B) with controlled crystal structures. *Appl. Surf. Sci.* **257**, 3253–3258 (2011).
12. Kinson C. Kam, and Anthony K. Cheetham, Thermochromic VO_2 nanorods and other vanadium oxides nanostructures. *Mat. Res. Bull.* **41**, 1015–1021 (2006).
13. Tina F.-R. Shen, Ming-Hong Lai, Thomas C.-K. Yang, *et al.*, Photocatalytic production of hydrogen by vanadium oxides under visible light irradiation. *Journal of the Taiwan Institute of Chemical Engineers.* **43**, 95–101 (2012).
14. Haihong Yin, Ke Yu, and Zhengli Zhang, Morphology-control of VO_2(B) nanostructures in hydrothermal synthesis and their field emission properties. *Appl. Surf. Sci.* **257**, 8840–8845 (2011).
15. Shidong Ji, Feng Zhang, and Ping Jin, Phase transition of single crystal VO_2(R) nanorods in solution revealed by reversible change in surface charge state and structure. *Mater. Lett.* **65**, 708–711 (2011).
16. Lijuan Mao, and Chunyan Liu, A new route for synthesizing VO_2(B) nanoribbons and1D vanadium-based nanostructures. *Mat. Res. Bull.* **43**, 1384–1392 (2008).

17. Zhou Ke-chao, Cao Du-meng, and Li Zhi-you, Soft-chemical synthesis and high-temperature electrochemical characteristics of VO_2. *Trans. Nonferrous Met. Soc. China.* **16**, 517–521 (2006).
18. Nagaraju Ganganagappaa, and Ashoka Siddaramannab, One step synthesis of monoclinic VO_2 (B) bundles of nanorods: Cathode for Li ion battery. *Mater Charact.* **68**, 58–62 (2012).
19. J.-C. Valmalette, and J.-R. Gavarri, High efficiency thermochromic VO_2(R) resulting from the irreversible transformation of VO_2 (B). *Mat. Sci Eng. B.* **54**, 168–173 (1998).

Advanced Materials Research Vol. 802 (2013) pp 252-256

doi:10.4028/www.scientific.net/AMR.802.252

Effect of Sonication Time and Calcination Temperature on Physical Properties of Titanium Dioxide Synthesized via Sonochemical-assisted Process

Chokchai Kahattha[1,2,3,a], Naratip Vittayakorn[1,2,3,b] and Wisanu Pecharapa[1,2,3,c]

[1] College of Nanotechnology, King Mongkut's Institute of Technology Ladkrabang (KMITL), Bangkok 10520, Thailand

[2] Thailand and Center of Excellence in Physics (ThEP Center),CHE,328 Siayuthtaya RD, Bangkok 10400,Thailand

[3] Department of Chemistry, King Mongkut's Institute of Technology Ladkrabang(KMITL), Bangkok 10520, Thailand

[a]kahattha@gmail.com, [b]naratipcmu@yahoo.com, [c]kpewisan@gmail.com

Keywords: Sonochemical, TiO_2, Snatase

Abstract. Titanium dioxide nanoparticles (TiO_2) were successfully synthesized via a sonochemical-assisted process using titanium isopropoxide as the titanium sources and calcination process at 300-500 °C. The effect of sonication time and heat treatment temperature on structural and nanostructure properties of the nanoparticles were characterized by X-ray diffraction (XRD), Raman spectroscopy, scanning electron microscope (SEM) and transmission electron microscope (TEM). The XRD and Raman results indicated that the crystalline of as-sonochemically synthesized TiO_2 nanoparticles corresponded to anatase phase of TiO_2 after sonication for 30 mim. The high quality crystalline anatase phase and increasing of crystalline size can be obtained after calcinations process.

Introduction

Titanium dioxide (TiO_2) has attracted great attention in many practical applications such as optical electrode [1], gas sensor [2], self-cleaning windows [3], UV-detector [4] and photodegradation [5]. Recently, there have been a number of research works focusing on the effective techniques for synthysizing TiO_2 such as sol-gel technique [6], hydrothermal [7], flame spray pyrolysis [8] and sonochemical process [9]. Among these techniques, the sonochemical process has been attracted for the synthesis of these materials because of its simplicity. The chemical effects of ultrasound do not come from a direct interaction with molecular species. However, sonochemistry arises from acoustic cavitation namely the formation, growth, and implosive collapse of bubbles in a liquid. Cavitational collapse generates high intense local heating (about 5000 K), high pressures (about 1000 atm), and high heating and cooling rates (>10^9 K/s). The chemical effects of ultrasound have been explained as the consequence of localized hot spots created during bubble collapse. The collapse of bubbles caused by cavitation produces intense local heating and high pressures, with very short lifetimes. Cavitation can create extraordinary physical and chemical conditions in otherwise cold fluid [10]. The major advatage of this technique, apart from its fast quenching rate and operation at ambient conditions, is that it is a simple and energy efficient process.

In this work, we report on the simple synthesis of TiO_2 nanoparticles by sonochemical-assisted process and investigation of the effect of sonication time and calcinations temperature on its physical properties using X-ray diffraction (XRD), Raman spectroscopy, scanning electron microscope (SEM) and transmission electron microscope (TEM).

Materials and methods

TiO2 nanoparticles were synthesized by sonochemical-assisted process. Titanium isopropoxide [Ti(C6H14O2)2] were used as starting source materials for Ti. The chemical precursor was purchased from Sigma Aldrich without purification. In the typical synthesis process, titanium

isopropoxide was dissolved in 20 mL of absolute ethanol and stirred at room temperature for 2 h. Furthermore, deionized water was filled into stocked solution until the total volume at 100 mL and stirred for 2 h. The stocked suspension was filled into the chamber and then the mixed liquid was irradiated with direct immersion of high intensity ultrasound titanium horn (750 W 20 kHz) by a Sonics Model VCX 750 at room temperature in ambient air for 10-30 min until the completely precipitated product was reached. After cooled down to room temperature, the resulting precipitates were washed with deionized water and ethanol. After that the cleaned precipitates were calcined at different temperatures from 300-500 °C for 4 h. The crystal structure and phase identification of the samples were investigated by X-ray diffraction with a monochromatic source of Cu Kα (λ=0.15405 nm) and Raman spectroscopy (Thermo Scientific DXR Raman Microscope with 532 nm DPSS laser). Their morphologies were monitored with JEOL JSM-5410LV scanning electron microscope with an accelerating voltage of 20.0 kV. Transmission electron microscopy images and selected area electron diffraction (SAED) patterns were taken with TECNAI G2 20 transmission electron microscope, using an accelerating voltage of 200 kV.

Results and discussions

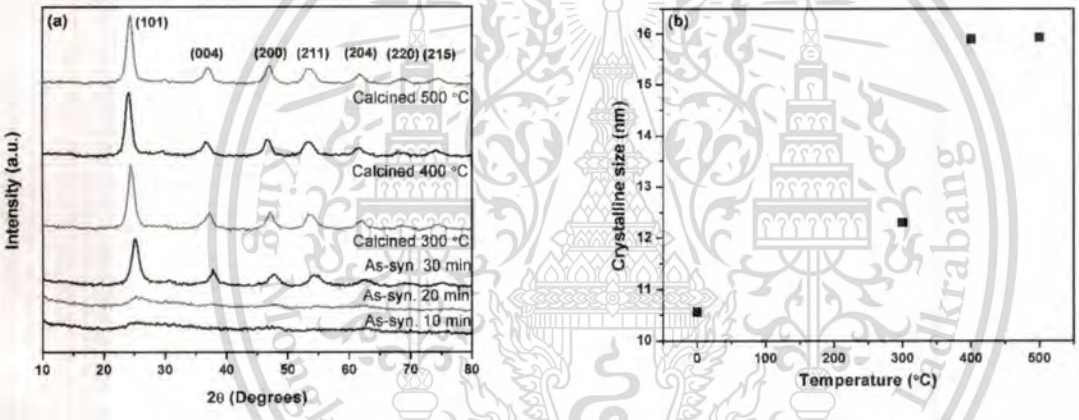

Figures. 1 (a) XRD patterns of the as-synthesized with various sonication time and calcined TiO_2 nanoparticles and (b) the crystalline size as a function of calcinations temperature.

The structural properties of as-synthesized and TiO_2 powders synthesized by sonochemical-assisted method with different sonication times and calcinations temperature were investigated by XRD patterns as shown in Fig. 1(a). The XRD patterns of the product obtained with sonication times for 10 and 20 min do not show any sharp diffraction peaks with characteristics of crystalline phase. When the sonication time rise to 30 min, the sample shows prominent diffraction peaks situated at 2θ = 25.3°, 37.8°, 48.1°, 55.2°, 62.8°, 70.5° and 75.2°, which correspond to (101), (004), (200), (211), (204), (220) and (215) orientation plane with tetragonal structure of anatase phase (JCPDS File No. 89-4921), respectively. This result implies that as-sonochemically synthesized powder in anatase phase of TiO_2 can be produced by one-step sonochemical process using sonication time above 30 min without the heat treatment process [11]. After heat treatment process, it is observed that there is increasing intensity of the diffraction peaks. This result indicates that the high quality crystalline anatase phase can be obtained by calcinations process and crystalline size as a function of calcinations temperature is shown in Fig. 1(b).

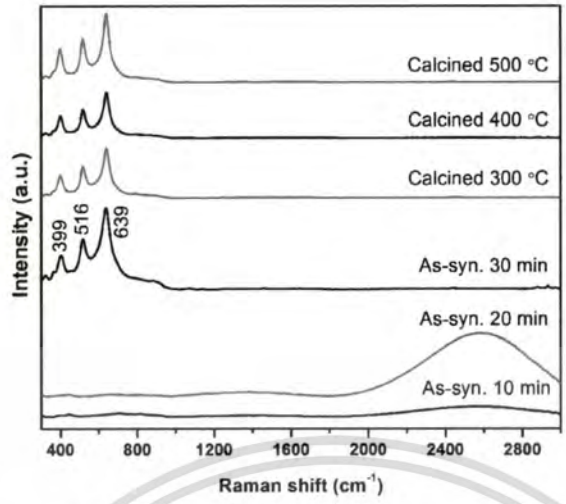

Figures. 2 Raman spectra of the as-synthesized and calcined TiO_2 nanoparticles with various sonication times and calcinations temperatures.

Raman spectra of the samples synthesized at different sonication times and calcinations temperatures are illustrated in Fig. 2. In Fig. 2, there is no characteristic peaks of TiO_2 in Raman spectra of as-sonochemically obtained powder with sonication times for 10 and 20 min. Meanwhile, the samples sonicated with high intensity ultrasound for 30 min and calcined at 300-500 °C for 4 h, the characteristic peaks at around 399, 516 and 639 cm^{-1} are attributed to B_{1g}, A_{1g} and E_g mode of anatase phase, respectively [12]. These results are in agreement with the results revealed by XRD spectra. From XRD and Raman results, the formation mechanism of anatase TiO_2 particles initiated by sonochemical-assisted process is proposed. During stirred with magnetic stirrer, dissolved titanium isopropoxide in deionized water can proceed hydrolysis and condensation process to create functional hydrolyzed alcoxides, which have great amount of Ti-OH. Simultaneously, rapid collision driven by high intensity ultrasound energy can sufficiently generate localized high temperature region, which is able to expedite the condensation reactions of hydroxyl groups to produce the nucleation of fine TiO_2 nanoparticles [13].

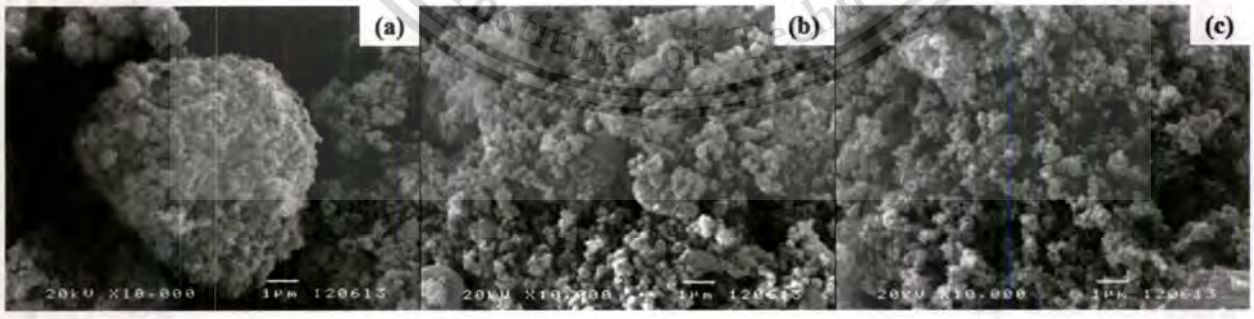

Figure. 3 SEM images of TiO_2 synthesized by sonochemical-assisted process with (a) sonication time 10 min, (b) sonication time 30 min and (c) calcined at 500 °C for 4 h.

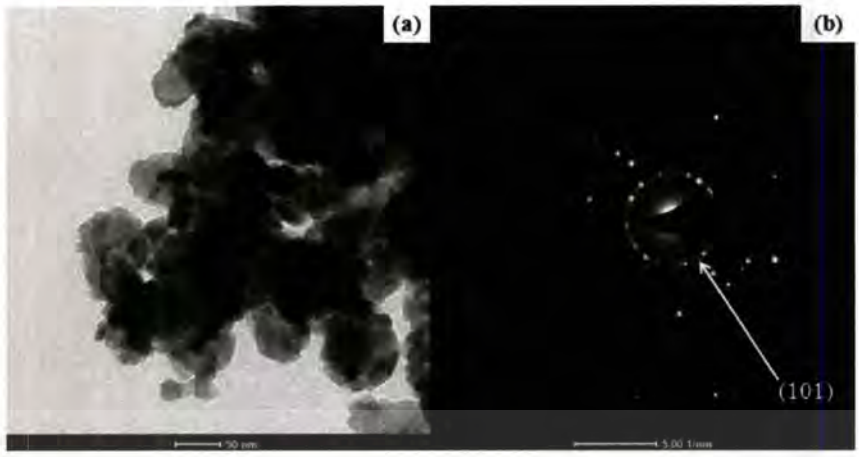

Figure. 4 (a) TEM and (b) SAED images of TiO_2 synthesized by sonochemical-assisted process and calcined at 500 °C for 4 h.

The SEM images illustrate the morphologies of TiO_2 synthesized by sonochemical-assisted process and calcined at 500 °C for 4 h as demonstrated in Fig. 3. The SEM images disclose that the high intensity ultrasound can be reduced size of the powders from microsize to nanosize regime. High magnification and Selected Area Electron Diffraction (SEAD) mode of as-calcined TiO_2 nanoparticles are shown in Fig. 4. It clearly seen that the fine TiO_2 nanoparticles have a quasi-spherical structure with diameter 20-30 nm and show the polycrystalline structure after calcined at 500 °C.

Summary

In summary, TiO_2 nanoparticles were successfully synthesized by sonochemical-assisted process. The XRD and Raman results revealed that as-synthesized powder has an anatase phase of TiO_2 after sonication for 30 min. Furthermore, the calcinations temperature has significant influence on crystalline size. SEM and TEM results indicated that the quasi-spherical polycrystalline nanopowder with diameter 20-30 nm can be produced by sonochemical-assisted processand calcination at 500 °C.

Acknowledgments

This work has partially been supported by the National Nanotechnology Center (NANOTEC), NSTDA, Ministry of Science and Technology, Thailand, through its program of Center of Excellence Network and was financially supported by KMITL research fund. Authors would like to thank Energy Policy and Planning Office, Ministry of Energy, Thailand, for research funding support.

References

[1] G. Waldner, M. Pourmodjib, R. Bauer, M. Neumann-Spallart, Photoelectrocatalytic degradation of 4-chlorophenol and oxalic acid on titanium dioxide electrodes, Chemosphere. 50 (2003) 989–998.

[2] Zachary M.S., Amit B., Susmita, B., Titanium dioxide thin films for high temperature gas sensors, Thin Solid Films. 519 (2010) 434–438.

[3] N.P. Mellott, C. Durucan, C.G. Pantano, M. Guglielmi, Commercial and laboratory prepared titanium dioxide thin films for self-cleaning glasses: Photocatalytic performance and chemical durability, Thin Solid Films. 502 (2006) 112-120.

[4] Yangang, H., Gang, W., Mang, W., Hongzheng, C., Hybrid ultraviolet photodetectors with high photosensitivity based on TiO_2 nanorods array and polyfluorene, Appl. Surf. Sci. 256 (2009) 1530-1533.

[5] M.V. Diamanti, M. Ormellese, E. Marin, A. Lanzutti, A. Mele, M.P. Pedeferri, Anodic titanium oxide as immobilized photocatalyst in UV or visible light devices, J. Hazard. Mater. 186 (2011) 2103–2109.

[6] M. Bestetti, D. Sacco, M.F. Brunella, S. Franz, R. Amadelli, L. Samiolo, Photocatalytic degradation activity of titanium dioxide sol–gel coatings on stainless steel wire meshes, Mater Chem Phys. 124 (2010) 1225-1231.

[7] S. Song, J. Tu, Z. He, F. Hong, W. Liu, J. Chen, Visible light-driven iodine-doped titanium dioxide nanotubes prepared by hydrothermal process and post-calcination, Appl. Catal. A:Gen. 378 (2010) 169-174.

[8] G. L. Chiarello, E. Selli, L. Forni, Photocatalytic hydrogen production over flame spray pyrolysis-synthesised TiO_2 and Au/TiO_2, Appl. Catal. B: Environ. 84 (2008) 332-339.

[9] C. Yu, Q. Fan, Y. Xie, J. Chen, Q. shu, J. C. Yu, Sonochemical fabrication of novel square-shaped F doped TiO_2 nanocrystals with enhanced performance in photocatalytic degradation of phenol, J. Hazard. Mater. 237–238 (2012) 38-45.

[10] X. K. Wang, C. Wang, W. L. Guo, J. G. Wang, A novel single-step synthesis of N-doped TiO_2 via a sonochemical method, Mater. Res. Bull. 46 (2011) 2041-2044.

[11] C. Yu, J. C. Yu, M. Chan, Sonochemical fabrication of fluorinated mesoporous titanium dioxide microspheres, J. Solid. State. Chem. 182 (2009) 1061–1069.

[12] L. González-Reyes, I. Hernández-Pérez, F.C. Robles Hernández, Effect of coarsening of sonochemical synthesized anatase on BET surface characteristics, Chem. Eng. Sci. 66 (2011) 721-728.

[13] K. Prasad, D.V. Pinjari, A.B. Pandit, S.T. Mhaske, Phase transformation of nanostructured titanium dioxide from anatase-to-rutile via combined ultrasound assisted sol–gel technique, Ultrason. Sonochem. 17 (2010) 409-415.